Sculpting Shadows

Thomas William Clark

SCULPTING SHADOWS

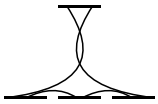

On the Spatial Structuring of Fields & Atoms:

A Tale of Light and Darkness

Thomas William Clark
MPhys

October 2016

Submitted in partial fulfillment of the requirements for the degree of Doctor of Philosophy

to the

School of Physics & Astronomy
College of Science and Engineering
University of Glasgow

ABSTRACT

Whether in art or physics, two dimensions are better than one. And in this context, we consider the spatial shaping of optical fields and atomic polarisations.

This work begins with a comprehensive review of how to accurately and arbitrarily modulate transverse beam profiles using six different methods. The methods are presented in the context of a general complex input beam and the shaping and measuring of the input beam with a single SLM is discussed and demonstrated.

A simple setup is then considered that allows for the rapid switching between arbitrary profiles, using only a single holographic component and an acousto-optical modulator (AOM). In this setup, a switching speed of approximately 10 kHz is demonstrated explicitly, limited by the current detection system, but where speeds of up to 20 MHz are estimated to be possible.

The following discussion then concentrates on the spatial structure of atoms, reviewing the conceptual tools needed to measure and interpret an atomic cloud in the presence of a magnetic field from fundamental concerns, both in theory and in practice: assuming a classical light field and a quantum atomic system. The specific implementation of both a magneto-optical trap and a holographically-shaped dynamic dark SpOT follows.

The crux of the work then concerns how polarisation-structured light can be used to create spatial patterns of transparency (spatial EIT) within an atomic cloud. Beginning with a review of EIT in general, with particular focus on an $F = 1 \rightarrow F = 0$ transition, the spatial modulation of absorption, dispersion, polarisation rotation and change in ellipticity is predicted for systems in the presence of a transverse magnetic field. The depth of this magnetic field dependency is then explored in some detail, where the relationship between observed patterns and applied magnetic field suggests the possibility of a visual magnetometer. The final section then considers how linearly polarised light and a q-plate was used to demonstrate spatially dependent transparency in a real atomic cloud.

CONTENTS

[1] angular momentum probability surface

LIST OF TABLES

LIST OF FIGURES

[2]Faraday rotator

PREFACE

A Note on the Text

In this work, the author would like to acknowledge the chance, however small, that some liberty may have been taken in regards to the customary styles of scientific discourse. Although great care has been taken to make the content accessible to the majority of scientists, and even the odd mathematician, it is the strong opinion of this author that without recognised wonder or joy in the discoveries that research brings, there is little value to the enterprise: and instead, we doom ourselves to a fate of slavish book-keeping. Therefore, if the reader finds themselves at the wrong end of misplaced levity, or over-exaggeration; it is a simple scribbler's hope that such irreverence will be borne in good grace. For science is a serious business and heaven forbid that the field of optics is taken lightly…

Thomas W. Clark
Glasgow, Scotland
October 2016

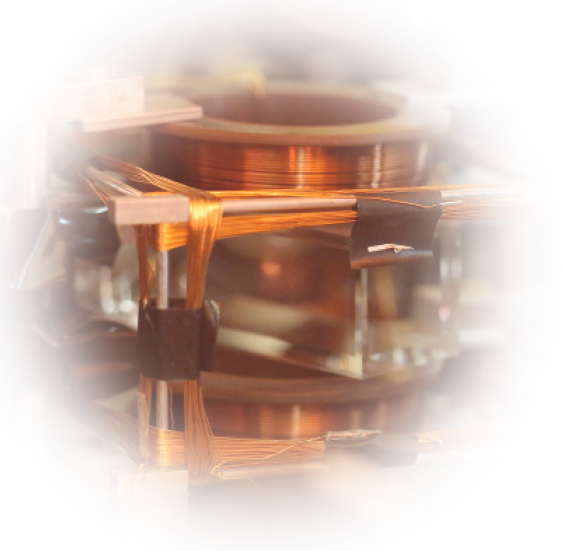

ACKNOWLEDGEMENTS

It was a particular insight of T.S. Eliot that it takes being *in over your head* to know how tall you are. And yet more importantly, the same can be said for the height of your friends. In this respect, I would like to thank the many people, kith and kin, who through position and patience, remain far-enough above to make me feel small, while having been close-enough to appreciate the irony.

In the lab

First on the list, is my perennial last author: Sonja Franke-Arnold. With every thesis, there is an expectation to thank your supervisor, but here I would like to offer my sincere gratitude: to someone who has not just given me a great opportunity, but who has given me the tools, motivation and occasional push to bring it to its full. Whether in national conference or homely Burns' supper, Sonja has been a great mentor who as well as giving me many new insights into the world of atoms, has had to put up with more Hungarian weddings than any boss should have to bear.

Next in line, is the sure-footed scotsman with a surprisingly good french accent. Just outside the burdens of supervisorship, Neal Radwell had the (until now) thankless task of teaching practical physics to a thoroughly absent-minded pupil. I just want to say here that as much as I know how frustrating it must have been, I really appreciate the effort you made and the time you took to help me along the way. As a parting gift, I can now reveal that I was indeed your secret santa. Having never seen Alan Partridge though, I can safely say that your contribution to the last four years was immensely helpful: neither ordinary nor French.

It would however be remiss to think that the role of lab-underling is without its particular challenges. Such is the case, I would also like to thank both Graeme Walker and Ádám Selyem: my predecessor and successor respectively, who together were a great help in finding both my feet and an extra pair of hands.

In the office

It may come as a surprise to those outside the fold, but it's hard to think of a friendlier working environment than being kept in the basement with an optics research team. Whether you feel like an ancient Egyptian board game, unicycle jousting or the simple challenge of trying to uncover why there's an office disco ball, there's definitely something for everyone. In fact, I can honestly say, every single person I've bumped into in the last four years has had something to add to this story: something for which I can only offer my sincere thanks.

Although I struggle to think of a person who hasn't had to endure my awkward questions or pontification, I'd particularly like to thank Matt Edgar, Daniele Giovannini, David Phillips and Johannes Courtial for all of the handy tips and tricks they've had to spare over the years; and of course the mysterious Miles, whose enthusiastic influence transcends his bodily presence.

I would also like to thank the great Graham Gibson for both his practical help and particular brand of heart-warming cynicism; something which has kept me company on many a fine morning. The banterful procrastination of one Sara Restuccia also didn't go unnoticed and her tales of vengeful cats and temperamental mountains won't go unmissed. In fact the office was a proud source of alien culture, with even the likes of Paisley represented by both Peter Morris and Euan Cowie. I would particularly like to thank Peter for doing his homeland proud: giving his desk-mate a level of care not extended to his own body. The other half of the ghostly dream-team has much to answer for, but of all the wit and wisdom of the lyrical Reuben Aspden, I will particularly remember coming back to the office and hearing that I had eloped with a Hungarian princess.

I would also like to thank my longest-serving peer (and at times swimming coach), monsieur Oxburgh. I greatly appreciated both his mathsy skills and incisive honesty, but most of all for keeping us all on our toes with his many unexpected questions.

In-between

There are of course, many other people who helped in this work and any complete list is doomed to failure. But here, I would also like to thank the workshop, who usually (but not always) had to take time out of *Call of Duty* to answer my requests. I also would like to thank the cleaning staff, who had more enthusiasm in the morning than should be allowed; the whistling janitors, who's musical tones provided much light entertainment and

Lucy Murray, who's outstanding administration makes it hard to believe she works for a university.

A shout-out also has to be made to the guys at Strathclyde for lending me both their lab and their time on many occasions and of course my funders: the engineering and physical sciences research council, without whom I couldn't have bought so much cake. It should also be declared, that the typesetting of this thesis was inspired by and adapted from the work of Eivind Uggedal [1]. Any complaints therefore about the margin size should of course be directed there ...

In-house

Although the many people mentioned above, both explicitly and otherwise, made sacrifices for the production of this thesis, there are still those for whom the end of office hours offered no escape.

I would like to thank all of those at Sandyford Henderson for being a great support, encouragement and motivating force for both getting me settled in Glasgow and for getting this thesis on the move. I would also like to thank Dr Philip Andrew of 22 Caird drive. Although he might be regretting it now, his storage of things was a great help in getting my thesis submitted and his beardy banter played no insignificant role in making my life and times in Glasgow something to remember.

For many years now, it has been something of a small dream of mine to reach this point. I don't particularly know the why, but the vague idea of getting a PhD has lingered in the back of my head for a long time: before I even set out on the first steps of my first degree. I would speculate that the misty vision had its origins in some form of unhelpful pride, but even since, it has limped on regardless, with, I have to say, varying degrees of enthusiasm. At this point in the proceedings though, I can safely say that not only would it not have happened without those closest to me, but it would have meant nothing too. It is not beyond the scope of anyone to write up pages of knowledge for some titular reward, but it is beyond many to remain faithful to those they are most responsible for. And for that, I dedicate this small work, however unprofound, to those sculptors who have and continue to shape the essence of my life. My quiet confidante, my steadfast sister, my mushy mum, my doting dad; this thesis is for you. And for the author of forms himself, for whom light from the shadows springs.

DECLARATION OF THE AUTHOR

There have been many helpers along the way, and the support and compassion of those recognised previously have been the foundation for this work: in ways both material and otherwise. In this light however, it is with no intended disrespect that I officially declare that the final content, structure and composition of this work is the result of my own hands, except where reference is given to others; and to my knowledge it has not been presented in any previous application for a degree at this or any other institution.

SETTING THE SCENE

1

One does not become enlightened by imagining figures of light, but by making the darkness conscious.

C.G. Jung

Space and Shape

The world may have begun in light, but the darkness was not far behind. In life; in light; it ever follows, foreshadows or fades. It can affect us in an unlimited number of ways. Yet it is rarely questioned. And never structured. For if it is without form, then what can we frame?

And yet, now gently ebbing in the wake of gravitational waves, the scope and structure of the natural world have never seemed less remote. For beneath the ripples, lay another confirmation: that the universe is a structured entity; or, that space itself can be shaped.

If space can move from background to focus, then perhaps the shade can do likewise?

Shape and Shadow

In this work, we consider the sculpting of shadows, but before we continue further, it is expedient to lay out both the scope and structure of the work at hand. Despite choosing to begin with a little drama, it is not the intention of this discourse to garner praise above its station. Our travels will be light and modest and the probing questions are simply a way of providing a little interest, where the content is otherwise dry.

Our destination then is not astrophysical in scale, but atomic. Beginning with a consideration of the spatial shaping and switching of optical fields, we will then demonstrate how the absorption profile of an atomic cloud can be moulded, such that the transverse form is independent of the atoms' spatial distribution. And in this respect, we will demonstrate how atomic shadows can be shaped.

To best understand the context, let us consider the normal situation. The shadows of our everyday life are predictable. If we shine a beam at an object, then the light has four broad choices: to miss, to scatter, to be absorbed or to pass straight through. Accordingly, we are familiar with the situation in Figure 1.1.

Very recently however, two of these processes have been demonstrated in the extreme. Published simultaneously, Corzo *et al.* [2] and Sorensen *et al.* [3] have both demonstrated how only a few thousand atoms can be used to give powerful reflection: such that up to 75% of light can be reflected from just 2000 atoms. The work of Sorensen *et al.* is captured in Figure 1.2 (Left), where the central red light is reflected from a line of atoms held in an optical fibre. On the right of Figure 1.2 however, we see how carbon nano-tubes can be used to create the most absorptive material in the world [4, 5]: where the material absorbs 99.97 % of visible light. So dark, that it is incredibly difficult to make out any of the three-dimensional structure.

The fourth optical option, is that of transparency. Although a certain element of transparency can be observed in daily life, in this work we will only consider the effect in terms of coherent population trapping [6, 7] or, very similarly, electromagnetically induced transparency (EIT) [8, 9]. In these situations, it is not simply the case that atoms can lose some of their opacity, but rather

Figure 1.1: An overview of the macroscopic absorption process. The light that interacts with the object is absorption or scattered, such that a dark outline is formed in its wake.

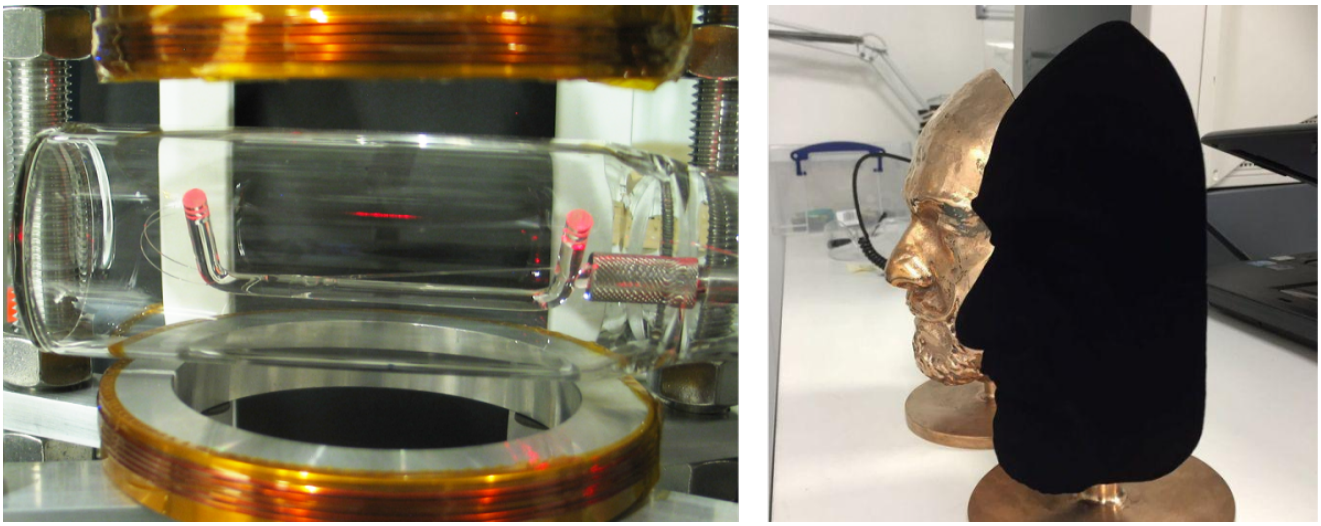

Figure 1.2: On the left, red light in an optical fibre is clearly visible, despite being reflected from only a few thousand atoms [3, 10]. On the right however, a carbon nano-tube structure is shown with 99.96absorption in the visible spectrum [5].

that they can be made completely transparent: to a theoretically perfect level. In this work, we will consider atomic profiles with both regions of absorption and transparency, therefore covering the third and fourth options.

Publication History

While this thesis is an original composition, we note here that much of the underlying work is already in the public domain. Some care has been taken to distance the current work from the publication content, but with the same or similar figures and analysis, there is always a risk of implicit or explicit self-plagiarism. Where there is any doubt however, this list forms a base reference for the content as a whole. Furthermore, in recognition that time and teamwork are not always linear quantities, we consider here the work in its original completion order: with a brief commentary on author contributions.

Past

- N. Radwell, D. Brickus, **T.W. Clark** and S. Franke-Arnold
  High speed switching between arbitrary spatial light profiles [11]

To the best of my knowledge, this project was suggested and supervised by Franke-Arnold and the initial software and results were completed by Brickus, with support from Radwell. After this, Radwell completed the majority of the remaining experimental results before being joined by Clark. Clark was involved in the modularisation of the experimental code, the last runs of the experiment and in the analysis that followed.

The content is heavily adapted from this paper, from which only the third figure was taken without modification.

- N. Radwell, **T.W. Clark**, B. Piccirillo, S.M. Barnett and S. Franke-Arnold
  Spatially Dependent Electromagnetically Induced Transparency [12]
  This experiment was initially proposed by Radwell. It was largely directed by Franke-Arnold, but within the laboratory, Radwell took the leading role. The experimental system and results were jointly developed by Radwell and Clark, and the initial (incomplete) theory was composed by Clark, with support from Franke-Arnold. A crucial contribution was made by Barnett, which allowed for a first solution, that was then developed by Clark and verified by Franke-Arnold. The q plate was created by Piccirillo.

  This paper forms the foundation for the contents of Chapter 4 (p. 111), but only the last figure has been used without modification.

- **T.W. Clark**, R.F. Offer, S. Franke-Arnold, A.S. Arnold and N. Radwell
  Comparison of beam generation techniques using a phase only spatial light modulator [13]
  This project was suggested and supported by Franke-Arnold and Arnold, and latterly led by Radwell. The majority of the theoretical simulation and generation was developed by Radwell and the experimental software was developed by Clark, based on the work of Radwell, and supplemented by Offer. The experimental results were taken by Clark and Offer and the analysis was largely completed by Clark and Radwell.

  Section 2.3 is heavily derived from this paper, with all of the graphs being adapted, but reused.

Pending

These works are currently in the process of being prepared for publication. Such is the case, their titles may be subject to change.

- Á. Selyem, **T.W. Clark**, N. Radwell and S. Franke-Arnold
  Holographically controlled three-dimensional electron shelving
  This work formed a large part of the time taken on the PhD, but due to time constraints, does not feature in the current discourse.
- **T.W. Clark** and S. Franke-Arnold
  Magnetism and spatial EIT
  This manuscript will build on the theoretical work undertaken for the EIT paper above, where rather than a simple application of Fermi's golden rule, there is a consideration of the full Bloch equation system under different regimes, as covered in Chapter 3 and Chapter 4.
  This work has so far been undertaken by Clark alone, in the last months of the PhD process, but is currently under discussion with Franke-Arnold.

Thesis Layout

Having outlined the topic and listed the work already published, we now proceed to the structure of the thesis as a whole.

Chronology

Rather than present the work chronologically, as outlined above, we will advance conceptually, both in the overall structure and for the internal logic of the chapters. Furthermore, rather than discuss the historical events, we present the arguments with the full knowledge of hindsight, as if everything had been planned perfectly in advance. As a particular example, it will become apparent that there is far more theory for the spatial EIT process than experimental results. This is due to the theory being developed after the initial results, and because construction work prevented a return to the experiment. The decision was made to avoid these reflections within the text however, for the sake

of internal coherence. Full details of the developments can be obtained on request.

Structure

With this in mind, our discussion will come in three main topics, split into two parts: a drama in three acts.

The first part features a single chapter and will cover the structuring of light on its own: considering both the basic properties, the generation of holograms and an application to the fast switching between different spatial modes.

The second part of the thesis will include the remaining two main chapters, and concerns both atomic systems themselves as well as their interaction with both optical and static magnetic fields. The first chapter will largely feature the theoretical underpinning of the chapter to follow. Beginning with very general and abstract concerns, the chapter will increasingly bridge the gap between theory and practice, detailing how atomic observables can be both modelled theoretically and obtained experimentally, before concluding with a summary of the constructed experimental system. The second chapter in this part is the crux of this work. Those with less confidence in their attention span can skip to this chapter, for if you are only going to read one, then this is it!

Finally, the narrative will come to a close in chapter five. A brief summary of both the obtained results and the possible future developments will be given, before finishing on some closing remarks.

And so, now we consider the main story: where the fields are not green and the clouds are not grey. Trusting that some revelation, however small, will make such a journey worthwhile; either useful in practice or reminiscion, it is hoped that it will constitute a narrative of interest; a simple tale worthy of the telling.

PART I

LIGHT & FLIGHT: THE SHAPING AND SWITCHING OF COMPLEX FIELDS

OPTICAL STRUCTURE AND THE SHAPING OF COMPLEX FIELDS

2

We live in a world of light. Crossing the vastness of space, and defying our notions of time, these rippling waves of energetic information reveal the spatial forms of all physical objects. Together with the eyes, they invite both perspective and structure: giving shape to all that we see. A sentiment proclaimed most eloquently by Ralph Waldo Emerson:

> *The eye is the best of artists. By the mutual action of its structure and of the laws of light, perspective is produced, which integrates every mass of objects, of what character soever, into a well colored and shaded globe, so that where the particular objects are mean and unaffecting, the landscape which they compose, is round and symmetrical. And as the eye is the best composer, so light is the first of painters. There is no object so foul that intense light will not make beautiful.*

The ability of light to reveal spatial shape therefore, is surely without question, but what of the fields themselves? Can such ephemeral entities be constructed or carry their own spatial design?

Outline

The truth of the matter is that it is not difficult to structure light - at least in principle. Simply take an image and hold it loosely in a wandering beam[1]. On reflection; in colour, intensity and spatial relationship; you now have a travelling beam of immense complexity. It *really* is not difficult to structure a beam of light. At the risk of a premature end to this thesis however, there are limitations to such an approach.

1. N.B. This can be done with the mind's eye, without loss of generality…

2.1 Optical Structure

Despite our every-day experiences, the idea that light itself can be shaped is often overlooked. Amongst the general public, the revelation is the principle, but, even amongst scientists, the *extent* to which this can be done can still raise a few eyebrows. In this regard, we begin by exploring the fundamental properties of an optical wave, outlining the terms and considering their relative implications for spatial design.

2.1.1 The wave equation

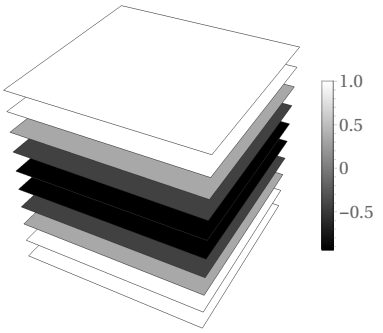

Figure 2.1: The propagation of a plane wave according to $\psi(\boldsymbol{r}) = \cos(\boldsymbol{k}\cdot\boldsymbol{r} - \omega t)$, where the planes represent the transverse profile of the beam at successive values of z over a full wave cycle, coloured according to relative amplitude.

When considering the fundamentals of light and electrical architecture, there are few places to begin other than *Maxwell's equations*. Considering only light itself, the equations reduce to:

$$\begin{aligned} \boldsymbol{\nabla}\cdot\boldsymbol{E} &= 0, & \boldsymbol{\nabla}\times\boldsymbol{E} &= -\frac{\partial}{\partial t}\boldsymbol{B}, \\ \boldsymbol{\nabla}\cdot\boldsymbol{B} &= 0 & \text{and } \boldsymbol{\nabla}\times\boldsymbol{B} &= \mu_0\epsilon_0\frac{\partial}{\partial t}\boldsymbol{E} \end{aligned} \tag{2.1}$$

where the variables carry their standard definitions. From these equatons, we find:

$$\boldsymbol{\nabla}\times(\boldsymbol{\nabla}\times\boldsymbol{E}) = -\frac{\partial}{\partial t}(\boldsymbol{\nabla}\times\boldsymbol{B}) \tag{2.2}$$

$$\therefore \boldsymbol{\nabla}(\boldsymbol{\nabla}\cdot\boldsymbol{E}) - \nabla^2\boldsymbol{E} = -\mu_0\epsilon_0\frac{\partial^2}{\partial t^2}\boldsymbol{E} \quad \text{and thus we recover:}$$

$$\nabla^2\boldsymbol{E} = \frac{1}{c^2}\frac{\partial^2}{\partial t^2}\boldsymbol{E}, \tag{2.3}$$

where the magnetic wave equation can be derived similarly. Perhaps one of the three most profound discoveries in modern physics, along with the associated special relativity and quantum mechanics, it can be safely assumed that this equation has been well-studied. The simplest solution is usually given by

$$\boldsymbol{E}(\boldsymbol{r},t) = \mathcal{E}(\boldsymbol{r})\hat{\underline{e}}\, e^{i[\boldsymbol{k}\cdot\boldsymbol{r}-\omega t+\varphi]}, \tag{2.4}$$

and this serves as a concise summary of all of the fundamental properties we can expect in an electrical field. The pre-factor is of course the electric field amplitude, which can have arbitrary spatial dependence in itself; $\boldsymbol{k}$ is the wave propagation vector;

ω and t represent the angular frequency and time elapsed respectively; φ represents any other phase offset, which can be spatially or temporally dependent and $\hat{\underline{e}}$ defines the complex axis of oscillation, otherwise known as the polarisation of the field.

The real part of this expression is plotted in Figure 2.1 for $t = \varphi = 0$, $\lambda = 1$, $r = x \in [0, 1]$ and $\hat{\underline{e}} = 1, 0$ and represents one of the simplest possible three-dimensionsal waves. The expression in Eq. 2.4 is, aptly, normally known as a *plane wave*, but such a designation can lead to problems. As we will discuss later, these solutions are rightly prioritised above others because all macroscopic optical phenomena can be described with their superposition. The problem however, arises when we fail to realise the extent of the simplification and forget that other solutions are possible too. More strictly, these structures are only *harmonic* plane waves and in general, any solution that satisfies

$$\boldsymbol{E}(\frac{\boldsymbol{k}\cdot\boldsymbol{r}}{k} \mp ct) \tag{2.5}$$

is possible, where $\boldsymbol{E}$ is twice differentiable. Furthermore, as the wave equation is linear in electric field, then the principle of superposition applies and the general form is then

$$\boldsymbol{E}(\boldsymbol{r}, t) = C_1\boldsymbol{E}(\frac{\boldsymbol{k}\cdot\boldsymbol{r}}{k} - ct) + C_2\boldsymbol{E}(\frac{\boldsymbol{k}\cdot\boldsymbol{r}}{k} + ct) \tag{2.6}$$

where $C_{1,2}$ are arbitrary constants. In this case, the functional form hasn't been specified at all, and so the amplitude can be defined at will. What has been constrained however, are the *phase* properties of the field.

The surfaces joining all points of equal phase are known as the *wavefronts* and of all three-dimensional waves, only a plane wave can move through space with an unchanging profile. If instead we consider *spherical* symmetry, $\boldsymbol{E}(\boldsymbol{r}) = \boldsymbol{E}(r, \theta, \phi) = \boldsymbol{E}(r)$, then the most general solution can be written as

$$\boldsymbol{E}(\boldsymbol{r}, t) = \frac{C_1}{r}\boldsymbol{E}(r - ct) + \frac{C_2}{r}\boldsymbol{E}(r + ct), \tag{2.7}$$

where $C_{1,2}$ perform the same function, but are not necessarily equal to the plane wave case. The specific harmonic expression

then follows as

$$\boldsymbol{E}(\boldsymbol{r}, t) = \frac{\mathcal{A}}{r} e^{ik[r \mp ct]}, \tag{2.8}$$

where $\mathcal{A}$ is known as the *source strength*. Therefore, depending on the symmetry imposed on the system, we can find other solutions to the wave equation, but analytical results get more difficult the further we diviate from these two test cases. Even for the case of *cylindrical* wavefronts, no general solution has been found, but for sufficiently large r the field can be approximated by

$$\boldsymbol{E} \simeq \frac{\mathcal{A}}{\sqrt{r}} e^{ik[r \mp ct]}. \tag{2.9}$$

The drop off in r and $r^{1/2}$ for spherical and cylindrical systems respectively can be interpreted as a consequence of energy conservation, but it also means that when experienced in the limit of a large distance from the source, the wavefronts will approximate plane wave solutions.

In any case, the phase of a wave is intimately connected to the spatial shape of the field and this is something that we will take advantage of throughout this thesis. There are however more direct ways to change the profile.

2.1.2 *Amplitude*

The plane wave solutions seen so far are illustrative and certainly of fundamental importance, but they have the unfortunate property that they cannot exist. This follows from energy conservation; the solutions are unbounded in space, and so the energy extends across the wavefront, stretching to infinity. Real solutions however, are defined by their boundaries.

Transverse Modes

The full derivation of bounded field patterns is beyond the scope of our discussion, but the spatial properties are of interest and so we will consider a brief outline of their origins. Returning to the wave equation, we assume that the solution is *separable* in space and time, $E(\boldsymbol{r},t) = E(\boldsymbol{r})E(t)$, such that the equation reduces to

$$\left[\nabla^2 + k^2\right] E(\boldsymbol{r}) = 0 \tag{2.10}$$

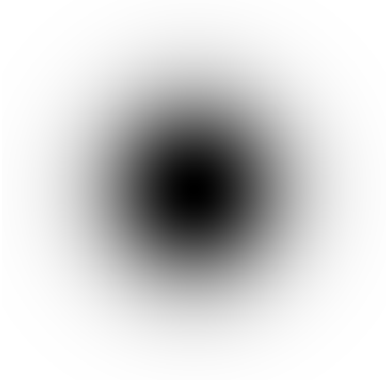

Figure 2.2: The transverse intensity profile of a fundamental Gaussian at $z = 0$.

for spatial terms: known as the *Helmholtz* equation. Following our opening discussion, we recall that plane waves are the only three-dimensional beams that can propagate with an unchanging profile and so we focus on plane-wave-like solutions. Eq. 2.10 can be simplified under the *paraxial* approximation, where we assume that the angle between the wave-vector and the optical axis is small *i.e.* $\left|\frac{\partial^2}{\partial z^2}E(\boldsymbol{r})\right| \ll \left|k\frac{\partial}{\partial z}E(\boldsymbol{r})\right|$. This allows the solution to separated further, such that

$$\boldsymbol{E}(\boldsymbol{r},t) = \mathcal{E}_0 \;\; u(\boldsymbol{r})\underline{\hat{e}} \;\; e^{-i[kz-\omega t]} \tag{2.11}$$

and the wave equation for normalised amplitude u is then

$$\nabla_{\mathrm{T}}^2 u(\boldsymbol{r}) - i\,2k\frac{\partial}{\partial z}u(\boldsymbol{r}) = 0, \tag{2.12}$$

where ∇_{T}^2 contains the transverse components of the Laplacian. The problem with our earlier plane wave solutions was that they weren't bounded in space. If we consider the opposite situation, and instead specify that our solution has the smallest possible divergence and transverse extent, then we obtain [14].

$$u(\boldsymbol{r}) = \frac{w_0}{w(z)}\, e^{\frac{-r^2}{w(z)^2}} e^{-i[k\frac{r^2}{2R(z)} - \psi(z)]}, \tag{2.13}$$

where the $z-$*dependent* parameters are the

Rayleigh range $$z_R = \pi \frac{w_0^2}{\lambda}; \tag{2.14}$$

Beam width $$w(z) \equiv w_0 \sqrt{1 + \left[\frac{z}{z_R}\right]^2}; \tag{2.15}$$

Radius of curvature $$R(z) \equiv z\left[1 + \left[\frac{z_R}{z}\right]^2\right] \text{ and} \tag{2.16}$$

Gouy phase $$\psi(z) \equiv \arctan(\frac{z}{z_R}). \tag{2.17}$$

Here, z is measured from the focus of the beam, where the *beam width* $w(z) = w_0$ is minimised. Functionally, the beam width describes the change in radius of the beam as it propagates, but mathematically, it is defined as the distance at which the field drops to $1/e$ of it's peak value. The Rayleigh range z_R is then defined as the distance at which the width is $\sqrt{2}$ larger than the *beam waist* w_0. As we will see, this corresponds to the distance at which the intensity profile doubles and serves as a physically meaningful unit for discussing propagation distances.

Comparing Eq. 2.13 with the spatial component of Eq. 2.4(p. 10), we note that, overall, elements of the harmonic plane wave have survived, but the additional real factors cause the amplitude to scale with distance from the origin: where on propagation, the width function causes the transverse profile to increase; but radially, the intensity is now bounded and decays with the ubiquitous Gaussian profile (Figure 2.2). Although near the beam waist we approach the planar wave fronts derived previously, the situation here is more complicated. In general, the wave fronts are no longer planes perpendicular to the propagation axis, but curved surfaces that develop according to $R(z)$: where the curvature tends to zero both at infinity and at the beam waist.

The additional subtlety in the phase structure is the inclusion of the Gouy phase, which accounts for the rapid phase change of a beam when passing through its waist. This additional phase can actually be considered a quantum effect [15, 16]. As Eq. 2.13 was based on a search for the smallest, least divergent bounded

profile, then a beam with a radius on the scale of its waist comes under the governance of the uncertainty principle.

Overall, we have established that realistic spatial solutions to the wave equation depart strongly from the idealised plane wave introduced previously. The beam however, is *self-consistent* in that only its size, as opposed to shape, changes on propagation. This property makes Eq. 2.13 an example of a transverse *mode* of free-space propagation. It is not however, the only solution.

Further, *higher-order*, modes can be found by considering solutions with larger and wider divergences and beam radii respectively. Such solutions however are strongly dependent on the boundary conditions, and in practice the constraints set by the propagation medium, *i.e.* whether or not the beam is travelling within a laser resonator, optical fibre or other wave guide system, result in many varying patterns.

The two most widely used decompositions however, are the *Hermite-Gaussian* (HG) and *Laguerre-Gaussian* (LG) mode families.

Laguerre-Gaussian Modes

As suggested, the LG and HG family of modes can be derived by searching for freely-propagating solutions of the wave equation with steadily increasing products of divergence and beam size. What distinguishes the two systems from one another, is the symmetry decomposition. For HG beams, we would consider a cuboidal coordinate system, whereas for LG beams we consider a cylindrical system. For our purposes, we consider the LG decomposition, such that the normalised transverse profiles can be written

$$u_{lp} = \sqrt{\frac{2p!}{\pi(p+|l|)!}}\frac{1}{w(z)}\underbrace{\left[\frac{r\sqrt{2}}{w(z)}\right]^{|l|}\left[\frac{2r^2}{w(z)^2}\right]L_p^{|l|}\left(\frac{2r^2}{w(z)^2}\right)}_{\text{Transverse modulation}}\underbrace{e^{-\frac{r^2}{w(z)^2}}e^{-i\left[k\frac{r^2}{2R(z)}-\psi(z)\right]}}_{\text{Gaussian factors}}e^{-il\phi}, \tag{2.18}$$

where the dimensions of m^{-1} are consistent with a normalisation in cylindrical coordinates *i.e.* $\int r^2 \left|u_{lp}\right|^2 drdzd\phi = 1$. These profiles are characterised by $l \in \mathbb{Z}$ and $p \in \mathbb{N}$, and are written in terms of the generalised Laguerre polynomials $L_p^{|l|}$. The results bear a lot in common with Eq. 2.13, and this is no co-

Figure 2.3: The transverse intensity profile of Laguerre-Gaussian beams for $(l,p) = (0,0);(0,1);(1,0)$ and $(1,1)$ at $z = 0$ where the rows and columns are specified by l and p respectively.

incidence. Defined by l and p, the modes are doubly infinite and the presence of the first factor means that they form a complete orthonormal basis set for describing any freely-propagating paraxial transverse mode. The previous result is then known as the *fundamental mode* and is almost always the lowest order solution of any mode system.

For larger values of $|l|$ however, we see that the Gaussian amplitude factors are modulated by the Laguerre polynomials and, distinctively, there is now a phase winding of the amplitude around the azimuth of frequency l. This phase dependence then affects the field amplitude as for $l \neq 0$ there is a singularity along the propagation axis. To satisfy the paraxial wave equation therefore, the amplitude along this axis cannot exist and is suppressed.

The effect of the p index is not so easily observed from the equation alone, but the net effect of all of these contributions is to create a field pattern with $p+1$ radial nodes and a single longitudinal node along the propagation axis, whose radius increases with $w_0\sqrt{l/2}$. The results of plotting the intensity profile, $\mathrm{LG}_{lp}\mathrm{LG}^*_{lp}$, for $l, p \in [0,1]$ are shown in Figure 2.3.

Furthermore, although it is not normally measurable for lower-orders, the full expression for the Gouy phase depends on the total mode number N according to

$$\psi(z) = (N+1)\arctan(\frac{z}{z_R}), \tag{2.19}$$

where $N = |l| + 2p$.

The full field can then be specified by $E(\boldsymbol{r},t) = u(\boldsymbol{r})\underline{\hat{e}}\ e^{-i[kz-\omega t]}$, where we haven't yet considered the polarisation dependence.

2.1.3 *Polarisation*

Fundamental to the spatial structuring of any non-longitudinal wave is the concept of polarisation. From the wave equation, we know that the interplay of electric and magnetic fields suppresses wave oscillations along the axis of propagation[2] and this means the wave can usually be decomposed into two dimensions. The choice of decomposition however, is in the eye of the beholder.

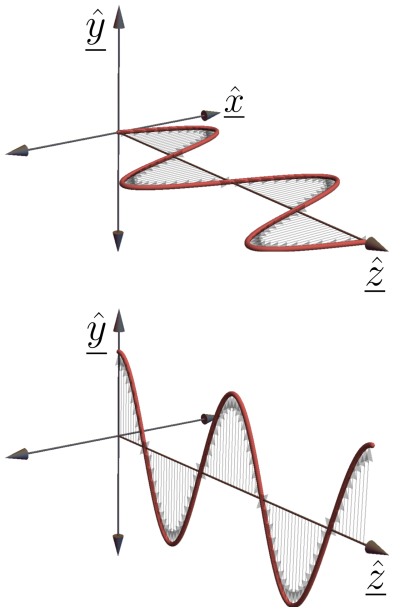

Figure 2.4: A schematic outline of horizontal and vertical polarisation over two optical wavelengths.

Definitions

Addressing this inherent ambiguity, we define here the conventions used throughout this discourse.

First of all, an optical field is fundamentally electro-magnetic in origin and so we must decide whether we are referring to the electric or magnetic component. As suggested by our choice of wave equation, we will follow the now standard practice in optics of using the polarisation of the electric field when discussing the beam as a whole.

Geometrically, the oscillation can then broadly be broken down into whether it is *linear*, *circular* or an *elliptical* superposition of both. Linear polarisation is relatively easy to define. For a chosen axis, the electric field oscillates back and forth with no preferred direction and the basis vectors are usually referred to as *horizontal* and *vertical* respectively, as compared with the axis of propagation. For our purposes, we will consider all propagation to be along the positive $\hat{z}$-axis, unless otherwise specified and thus, for a right-handed coordinate system, horizontally and vertically polarised light will be taken as the $\hat{x}$ and $\hat{y}$ axes respectively. (Figure 2.4). For circularly polarised light, the electric field rotates at the angular frequency around the propagation axis, but there are two widely-used conventions for labelling the rotation. The traditional optics convention however, is to consider clockwise rotation of an oncoming beam as *right circularly polarised* and this is the convention used throughout this work. The only exception being when we discuss offset magnetic fields, which can be analysed by rotating the axis of quantisation.

As we will be spending considerable time discussing the interaction of polarised light with atoms, it is instructive to also

2. This is not necessarily true in practice, but outside of strong focussing [17], is a good approximation.

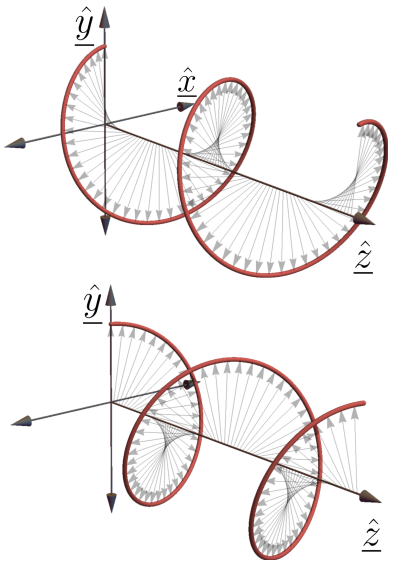

Figure 2.5: An illustration of left(top) and right(bottom)-circularly polarised light over two wavelengths.

consider a full division of polarisation across 3D space. In these situations therefore, any field linearly or circularly polarised perpendicular to the chosen quantisation axis, can be collectively referred to as σ-polarised light and any field parallel to quantisation will be known as π-polarised light, where the relation to the Cartesian bases can be summarised as:

$$|\sigma_+\rangle = \frac{1}{\sqrt{2}}\left[|x\rangle + i|y\rangle\right] \text{ (Left)}, \tag{2.20a}$$

$$|\sigma_-\rangle = \frac{1}{\sqrt{2}}\left[|x\rangle - i|y\rangle\right] \text{ (Right) , and} \tag{2.20b}$$

$$|\pi\rangle = |z\rangle. \tag{2.20c}$$

It is not enough to be able to characterize light however; if we are to shape polarisation, we must be able to move between the different states.

Wave plates and the Jones formalism

The easiest way to alter the polarisation state of laser beams is to use a wave plate. As can be seen from Eq. 2.20, the only difference between σ_+ and σ_- is one of relative phase between the Cartesian axes. Also known as wave retarders, optical wave plates operate by slowing perpendicular polarisation components with respect to one another to change these relative phases.

The phase-shifts required to change the polarisation are on the order of fractions of a wavelength and so are necessarily limited to small frequency ranges. The two most common plates are the half- and quarter-wave devices which aptly induce a relative phase offset of π and $\pi/2$ between the two perpendicular axes. By rotating these devices however, we can control how this phase difference affects our incoming light, such that the combination of both plates can be used to move an incoming beam throughout all transverse polarisation space.

Mathematically, these polarisation effects can be modelled with the *Jones* formalism. In this framework, the transverse component of a plane wave can be represented as:

$$\boldsymbol{E}(x,y) = \begin{bmatrix} E_{0x}e^{i\phi_x} \\ E_{0y}e^{i\phi_y} \end{bmatrix} e^{i(kz-\omega t)},$$

where the pre-factor is known as the *Jones vector* and $\phi_{x,y}$ represent generic phases in x and y. Normalising appropriately, we can then associate vectors and operators with our beams and optical elements respectively such that:

$$|\sigma_-\rangle = \frac{1}{\sqrt{2}}\begin{bmatrix} 1 \\ -i \end{bmatrix}, \qquad \frac{\hat{\lambda}}{2} = \begin{bmatrix} \cos 2\theta & \sin 2\theta \\ \sin 2\theta & -\cos 2\theta \end{bmatrix}, \tag{2.21}$$

$$|\sigma_+\rangle = \frac{1}{\sqrt{2}}\begin{bmatrix} 1 \\ +i \end{bmatrix}, \qquad \frac{\hat{\lambda}}{4} = \frac{1}{\sqrt{2}}\begin{bmatrix} i+\cos 2\theta & \sin 2\theta \\ \sin 2\theta & i-\cos 2\theta \end{bmatrix}$$

and where the fast axes of the wave plates are at an angle θ with respect to the horizontal. From these matrices, we can see that a half wave plate allows for the rotation of linear polarisation and the inversion of the handedness of circularly polarised light. A quarter-wave plate however, has complex terms and so can be used to transform between linearly and circularly polarised light, confirming that a combination of the two can be used to explore all polarisation states.

A big advantage of the Jones method with respect to other methods of monitoring the polarisation is that if we allow both vector elements to remain complex, then we can keep track of both relative and overall phases: information that is essential when considering interaction with other fields. The disadvantage of this approach however, is that the polarisation is then necessarily not expressed in terms of measurable quantities and as such, does not necessarily provide an intuitive understanding of the polarisation state. A more geometric way of expressing the polarisation state is through the *polarisation ellipse*.

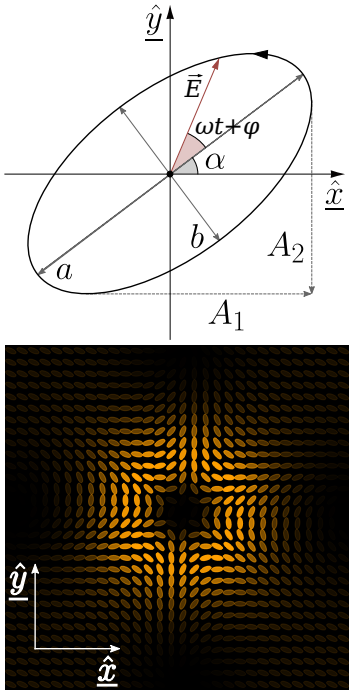

Figure 2.6: An illustrative overview of a polarisation ellipse (above) and an example of the formalism extended to describe a non-trivial vector-vortex beam (below). Here, the transverse beam structure is indicated by a series of ellipses. The colour and transparency indicate the polarisation circularity and beam intensity respectively, with hue moving from red to blue proportional to how far the polarisation is from 100% $|\sigma_-\rangle$.

The polarisation ellipse

If the base polarisation states can be represented as lines and circles, then it's not unreasonable that any superposition can be described as an ellipse. The complex polarisation vector can be expressed in terms of the relative amplitudes and phases between two polarisation axes *i.e.*

$$\hat{\underline{e}} = \left[A_1\hat{\underline{e}}_1 + A_2 e^{i\phi_{rel}}\hat{\underline{e}}_2\right], \tag{2.22}$$

where A_i are normalised so that $A_1^2 + A_2^2 = 1$. If we then consider the case where $\hat{\underline{e}}_i$ are the principal axes of an ellipse, then we

can define the semi-major a and semi-minor b axes as the largest and smallest relative amplitudes respectively, where the relative phase between them is $\pm\pi/2$. As a and b are normalised appropriately, then we can parametrise the vector trigonometrically without loss of generality. Such that,

$$\hat{\underline{e}} = [\cos\epsilon\ \hat{\underline{e}}_1 + i\sin\epsilon\ \hat{\underline{e}}_2]\,, \tag{2.23}$$

where $\epsilon = \pm\arctan b/a$ defines the *ellipticity* of the ellipse. To account for the angular offset, then we simply consider Eq. 2.22 rotated α rad about the axis of propagation. The polarisation can then be expressed up to an overall phase factor in terms of the measurable quantities α and ϵ *i.e.*

$$\hat{\underline{e}} = [\cos\alpha\cos\epsilon - i\sin\alpha\sin\epsilon]\,\hat{\underline{x}} + [\sin\alpha\cos\epsilon + i\cos\alpha\sin\epsilon]\,\hat{\underline{y}}, \tag{2.24}$$

where $\hat{\underline{e}}_1$ and $\hat{\underline{e}}_2$ have been taken as the Cartesian unit vectors $\hat{\underline{x}}$ and $\hat{\underline{y}}$. Spatially dependent polarisation patterns can then be represented by splitting a beam profile into a grid, where each cell contains an ellipse of eccentricity ϵ, rotated α radians from the $\hat{\underline{x}}$-axis. Furthermore, by colour-coding the ellipse according to ϵ and varying the transparency with beam intensity, we can characterise the polarisation profile of any vector beam.

2.1.4 Phase

Of all the fundamental properties of light, the notion of *phase* is perhaps the most distinctive and yet probably the most difficult to define. For our purposes, we will often refer to the argument of any oscillating function as the phase of the function and so in more words the phase is simply an indicator of the overall progress of a waveform when compared to a full cycle. In the literature, there is often a silent confusion between this usage and reference to the *phase offset*, but in our discussions we should try to avoid this where possible. As introduced previously, the phase of any optical field is closely linked to the overall architecture and is in general a function of both space and time. The real vitality of the concept however, is when we consider the interaction of two or more fields.

2.1.5 *Interference*

The electromagnetic wave equation (Eq. 2.3(p. 10)) is a linear system in $\boldsymbol{E}$ and so falls under the *superposition principle*: such that a linear combination of solutions is also a solution. Mathematically, the solutions $f(x)$ then have the properties

$$f(x_1 + x_2) = f(x_1) + f(x_2) \text{ and} \tag{2.25a}$$ Additivity

$$f(ax) = af(x). \tag{2.25b}$$ Homogeneity

For the case of optical radiation, superposition is the foundation for interference: allowing us to express the interaction of two waves as a linear sum. Consequently, phase effects are not observable until we consider the *intensity* profile of the field, which can be defined as the time-averaged value of the Poynting vector *i.e.*

$$\langle S \rangle_t \equiv \frac{1}{2\eta} |E|^2, \tag{2.26}$$

where η is the effective impedance of the medium. For an electric field *in vacuo*, the intensity is then

$$\mathcal{I} = \frac{1}{2}\epsilon_0 c |E|^2, \tag{2.27}$$

where the constants carry their usual definitions [3]. The addition of two monochromatic harmonic waves with spatial phase can then be written as

$$\boldsymbol{E}(\boldsymbol{r},t) = \boldsymbol{\mathcal{E}}_1(\boldsymbol{r},t)e^{i[\varphi_1(\boldsymbol{r})-\omega t]} + \boldsymbol{\mathcal{E}}_2(\boldsymbol{r},t)e^{i[\varphi_2(\boldsymbol{r})-\omega t]}, \tag{2.28}$$

where the observed interference pattern is

$$\boldsymbol{\mathcal{I}}(\boldsymbol{r}) \propto \int \boldsymbol{E}(\boldsymbol{r},t) \cdot \boldsymbol{E}^*(\boldsymbol{r},t)dt \tag{2.29}$$

$$= \boldsymbol{\mathcal{I}}_1(\boldsymbol{r}) + \boldsymbol{\mathcal{I}}_2(\boldsymbol{r}) + 2\sqrt{\boldsymbol{\mathcal{I}}_1\boldsymbol{\mathcal{I}}_2}\cos\left[\varphi_1(\boldsymbol{r}) - \varphi_2(\boldsymbol{r})\right], \tag{2.30}$$

where we have assumed that the two fields have the same polarisation. The *interferogram* above is the starting point for measuring the relative phase between two beams and here, we use it to emphasise that only the relative phase of the interaction is of any importance. If the relative phase is allowed to fluctuate over the integration time however, the oscillation will average to zero and so Eq. 2.30 is strongly dependent on maintaining spatial *coherence*.

3. The intensity is often stated without the impedance terms and although some care has been taken to avoid this throughout the discourse, there is no guarantee that some occurrences haven't been overlooked. In practise however, this is not usually a problem as intensity measurements are normalised or in arbitrary units.

Although the above analysis will presumably be very familiar, we include it here to underline how the beam intensity can be directly manipulated by careful choice of the spatial phase: something which will be of great importance in § 2.3 (p. 29) and illustrative for the work discussed in Chapter 4 (p. 111).

2.2 Spatial Shaping

Having recovered the elementary relationship between relative spatial phase and intensity, we now have two broad paths for constructing spatially-dependent beams: the direct control of amplitude through manipulation of spatial boundaries, or the interaction of fields with differing phase-structures: where we include polarisation effects in this category too[4].

4. An approach that will be justified later in the section.

It is tempting to immediately right-off the former as a viable tool, but, as can be seen in the later discussion of optical trapping, there are often practical applications for this approach. Perhaps counter-intuitevly, recent developments also suggest that it may be possible in the near future to create digitally-specified laser profiles, cutting out much of the need for later shaping. Reardless of these potential possibilities however, we will now consider how to move from the fundamental Gaussian to more complex structures, beginning with the simplest optical components.

2.2.1 Geometry

Similarly to the imposition of amplitude boundary conditions, the easiest way to change the light intensity through phase manipulation is transmission through a shaped medium. In § 2.1.2 (p. 15) we saw that there are modes of propagation that take on the profile of annular rings and these LG modes, foundationally Gaussian functions weighted by Laguerre polynomials, are formed from rotational symmetry around the axis of travel. Of relevance however, is that the vortex is not a result of the mode restrictions, but of the single contribution to the phase: $e^{il\phi}$. It follows therefore that vortex beams can be created from the fundamental mode by imparting such a phase.

These are not the only type of vortex beams however. A very recent discovery has uncovered a new category. Whereas a typical optical vortex is created when light twists around a dark hole (or line), it is now known that there are *spatiotemporal* optical vortices: which form a ring, or toroid, around a self-focusing light pulse [18].

Historically, LG beams were perhaps first considered by Goubau and Schwering in 1961 [19], but it was the work of Allen, Beijersbergen, Spreeuw and Woerdman [20] that gave them their foremost application. Crucial to this demonstration however, was the conversion between HG and LG field profiles. Such a transformation was discussed by Tamm and Weiss [21] in the contex of optical resonators, where cylindrical lenses were used to introduce astigmatism and the broken symmetry led to required change in boundary conditions. Abramochkin and Volostnikov [22] recognised that passing the beam through a cylindrical lens was enough to perform the conversion and as Allen explained, the purpose of the cylindrical lens was to establish focussing along only one of the axes, creating a spatial phase difference with the other according to the propagating Gouy phase.

Simpler methods exist however, with perhaps the most conceptually simple being the spiral phase plate [23]; where a helically shaped component acts as an azimuthally varying resistance, directly inducing the required phase profile.

A very recent discovery however, has shown that an even simpler method is possible: where the phase profile is created from total internal reflection in a glass cone [24]. In addition to its simplicity, a great advantage of this technique, is that the Fresnel coefficients are largely wavelength independent in the optical spectrum and so the procedure works reliably across the visible spectrum.

2.2.2 Q-Plate

In our later experiments however, we generate a superpositon of structured light using a novel birefringent waveplate with spatially varying optical axis [25]. Defined by topological charge q, this *q–plate* acts as a spin-to-orbital angular momentum con-

verter and transforms incoming linearly polarised light into right and left circularly polarised beams with azimuthally varying phase difference. The q-plate is conceptually similar to other waveplates, but relies on electrically powered liquid–crystals to form an azimuthally wound polarisation with a pattern defined by its topological charge q and which consequently can impart an OAM of $l = 2q$. The action of the q–plate can then be defined by $\hat{Q}(x, y)$: such that

$$\hat{Q}(x,y) = \begin{bmatrix} \cos 2\alpha(x,y) & \sin 2\alpha(x,y) \\ \sin 2\alpha(x,y) & -\cos 2\alpha(x,y) \end{bmatrix} \text{ and} \tag{2.31}$$

$$\therefore \hat{Q}(x,y)\sigma_- = e^{i2q\phi + i2\alpha_0}\sigma_+ \tag{2.32}$$

for $\alpha(x, y) = \alpha_0 + q\phi$ and $\phi = \tan^{-1} y/x$. Hence, we see explicitly that the action of an arbitrary q–plate is identical to that of a half-wave plate, with the addition of a spatially dependent phase retardation.

From Eq. 2.18, we recognise this retardation as a helical mode with $l = 2q$ and note that the sign is dependent on the polarisation handedness.

Having recovered the elementary relationship between spatial phase and intensity, we now outline how this effect can be harnessed for the creation of more sophisticated spatial patterns: beginning with the fundamentally elegant *diffraction grating*.

2.2.3 *Diffraction Gratings*

Fundamentally, a diffraction grating is a periodic structure that is used to deflect light in specific directions. Properly configured however, it can also be used to modulate light in intensity and frequency and as a knowledge of diffraction gratings underlies the following discussion, we consider its mechanism in some detail.

Such gratings can ordinarily operate either by amplitude or phase modulation. In this work however, we will only consider gratings that operate on the phase. Specifically, although diffraction gratings can affect the absolute phase of light in a way that is not obvious [26], the standard grating equation approach is sufficient for our purposes.

Considering the general case of light incident in three dimensions, we can obtain the full grating equation for conical diffraction from geometry [27] [5], such that

$$Gr_\Delta = \cos\phi\,[\sin\theta_{\text{in}} + \sin\theta_{\text{out}}] \tag{2.33}$$

and G is the groove frequency, r_Δ is the optical path difference and ϕ is the azimuthal angle of standard spherical coordinates. From this we can immediately recover the law of reflection:

$\theta_{\text{out}} = -\theta_{\text{in}}$ for $r_\Delta = \phi = 0$ and the special case: (2.34)

$$Gr_\Delta = 2\sin\theta_{\text{in}} \tag{2.35}$$

(Littrow Configuration)

for $\theta_{\text{out}} = \theta_{\text{in}}$, where we again assume that the light is contained within the x–z plane, such that $\phi = 0$. This arrangement is known as the *Littrow Configuration* and has special significance in the construction and frequency tuning of an ECDL[6].

For constructive interference, and perpendicular incidence, the grating equation then reduces to

$$\sin\theta_{\text{in}} + \sin\theta_{\text{out}} = Gm\frac{\lambda}{n} \tag{2.36}$$

where $m \in \mathbb{Z}$ and λ is the incident wavelength. In most situations however, it is desirable to maximize the amount of light in a particular order and this can be achieved by applying a slope to the grating, where the individual facets are inclined by the *blaze angle* Θ_{blaze} [7]. Under this condition, there is a new, phase-matched, law of reflection within the medium with respect to the grating angle. Therefore, for an angle of incidence defined by $\theta_{\text{B}} = \theta_{\text{in}} - \Theta_{\text{blaze}} = \theta_{\text{out}} + \Theta_{\text{blaze}}$, all of the power is diffracted into one order according to

$$\sin\theta_{\text{B}} = m\frac{G\lambda}{2n}. \tag{2.37}$$

(Bragg's Law)

For illustration, this result can also be written in vector notation, where we follow the treatment of Blanche [28]. If we consider two beams incident at θ_{B} and $-\theta_{\text{B}}$ with respect to the diffraction

5. We adopt the common sign convention, where angles measured between the normal and direction of incidence are positive.

7. So-named because the grating would shine brightly on alignment.

[6] external-cavity diode laser

plane normal $\underline{\hat{n}_K}$, then we can decompose their k-vectors:

$$\begin{aligned} \boldsymbol{k}_\pm &= \boldsymbol{k}_\pm \cdot \underline{\hat{n}_K} + \boldsymbol{k}_\pm \cdot \underline{\hat{K}} \\ &= |\boldsymbol{k}_\pm| \cos(\pm\theta_\mathrm{B})\, \underline{\hat{n}_K} + |\boldsymbol{k}_\pm| \cos(\frac{\pi}{2} \mp \theta_\mathrm{B})\, \underline{\hat{K}} \\ &= |\boldsymbol{k}| \left[\cos\theta_\mathrm{B}\, \underline{\hat{n}_K} \pm \sin\theta_\mathrm{B}\, \underline{\hat{K}}\right] \end{aligned} \tag{2.38}$$

for $|\boldsymbol{K}| \equiv 2\pi G$ and $|\boldsymbol{k}| = \frac{2\pi n}{m\lambda}$. In this context, $\boldsymbol{K}$ is known as the *grating vector*, and can be used to define Bragg's law more concisely:

(*K*-vector closure)

$$\boldsymbol{K} = \boldsymbol{k}_1 - \boldsymbol{k}_2 \tag{2.39}$$

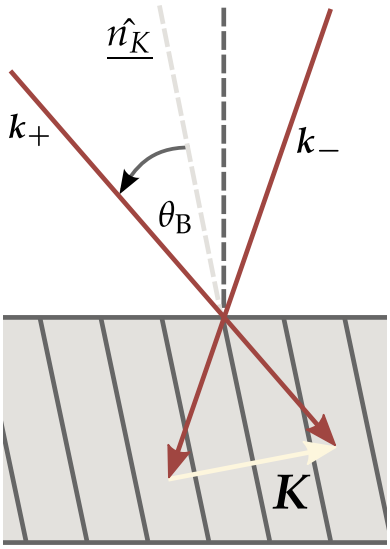

Figure 2.7: An overview of the *K*-vector closure relation.

and $+, - \to 1, 2$. In our discussion above, we have considered grating effects from a rather idealised perspective: where the interaction is between individual ray-vectors and planes. In practice however, macroscopic regimes demand a multitude of both, such that the thickness of the gratings has to be taken into account. Bragg's law was first derived in the context of volumetric materials and so thick gratings are said to operate in the *Bragg regime*. In this regime, interference from the assorted layers constrains the energy to one order of diffraction. Thin gratings on the other hand, which we will focus on, come under the *Raman-Nath regime*, marked in practice by the possibility of many diffraction orders. The separation of the two regimes however is not discrete, but can be distinguished by the Klein and Cook formalism:

$$\frac{2\pi k_0 d}{n\Lambda^2 \cos\theta} = \begin{cases} < 1 & \to \text{Thin} \\ > 10 & \to \text{Thick,} \end{cases}$$

where d is the thickness of the grating medium in metres.

Regardless of the thickness however, Eq. 2.39(p. 26) shows how changing a diffraction grating can redirect the spatial components of incident light. It follows that a spatially dependent diffraction grating could then be of some interest.

2.2.4 *Holography*

A hologram can be defined as the source pattern that, under illumination, reproduces a desired complex field. Working with this

definition, we can see how a standard diffraction grating is itself a specific example of a hologram and considering the previous results, we begin to see how optical fields can be specified more generally.

The groundwork of holographic imaging was developed by Gabor [29] in the context of electron microscopes, but, by showing that both the intensity and phase of a beam could be reconstructed, the principles are the same for coherent light. In the context of laser systems, the complex modulation of the field can actually be used to emulate the effect of almost all of the most commonly used optical components. Fundamentally, this is achieved by considering a hologram as a large complex superposition, where in principle each point can be treated as an individual grating that varies with orientation and periodicity.

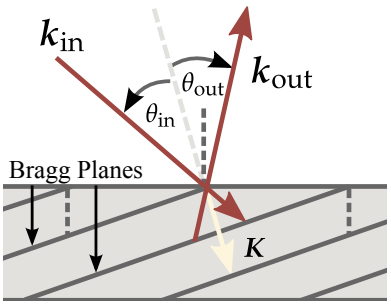

Figure 2.8: An overview of the K-vector closure relation, as applied to a reflection grating.

2.2.5 *Computer-Generated Holograms*

Traditionally, holographic imaging and shaping was heavily restricted by technology and required physical exposure and capture with photographic plates *e.g.* onto Silver Halide emulsions. Today however, holograms can be computer-generated and displayed on demand, where the limited bit depth is more than compensated by the ability to digitally specify an arbitrary pattern.

This flexibility means we have complete control over our generation method, as we will consider in the next section, but for our purposes we will only consider *Fourier*, rather than Fresnel type holograms; where our methods are limited to the *Fraunhofer approximation*. In this limit, the intended field patterns will be realised in the far-field, requiring a lens to bring the image closer than infinity, and in general we will only consider two-dimensional field patterns.

2.2.6 *SLM*

Of the many devices capable of carving a beam of light, there are none that have the range and application of a spatial light

modulator (SLM[8]). Although the expression has literal meaning, in academic literature it refers specifically to a set of electronic devices that can modify either the phase or amplitude in a discretized manner. In this context, there are then two broad categories of device: the LCoS[9] and the MOEMS[10] [28]. In the reported work, we are concerned specifically with the Hamamatsu LCOS X13138-01 [30].

Considering only LCoS devices, these SLMs operate by the spatial manipulation of birefringent liquid-crystal molecules; where applying the appropriate voltage rotates the crystals *in situ*. After configuration, an SLM can then induce a spatially dependent lag in the field propagation, usually up to a few wavelengths, where the phase pattern is specified by computer. Explicitly therefore, LCoS SLMS are phase-only systems, but in practice this can be extended.

[8] spatial light modulator
[9] liquid crystal on silicon
[10] micro-opto-electro mechaical system

2.3 Digital Holograms

Digital holography allows the near-arbitrary shaping of spatial profiles, but its very flexibility invites uncertainty. There is no unique way of creating a general field. In this section therefore, we investigate six methods of hologram generation, rated according to obtained field quality and power. Furthermore, we consider how all of the methods can be adapted to account for arbitrary input, how the incoming beam can be both measured and shaped using the same SLM as well as exposing the output field's non-linear dependence on spatial filtering and intensity compensation.

As discussed above, an LCoS SLM can allow full spatial control of the phase over several wavelengths and so here we will focus on how such a device can be adapted to arbitrarily modulate the amplitude. Even within these constraints however, there remain many different practices and so we further consider only single-pass deterministic methods, where the primary goal is geometric accuracy. Under these conditions, the majority of the methods perform acceptably well, but subtle differences arise when forming differing field patterns, both under near-field imaging conditions and on propagation. These results, as well as practical concerns like hologram computation cost and available phase range will naturally dictate the choice of method in any particular application, but overall we note the surprising reliability of naïve amplitude scaling: a method that was only included as a benchmark for later discussion.

2.3.1 *Amplitude shaping*

Following our discussion of phase gratings, we recall that the diffraction efficiency is strongly dependent on grating depth and thus, if we could control the grating depth, we could deflect a tunable portion of the light away from straight reflection. Using an SLM, we can emulate the phase effect of almost any optical element and so by computationally modifying the phase profile of a phase grating, and spatially selecting the first-order deflection, precise amplitude control can be achieved, independent of the

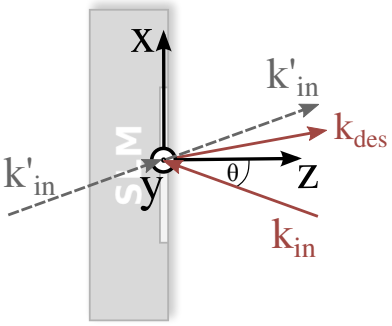

Figure 2.9: The ray vector operation of a reflective LCoS SLM, where k'_{in} is drawn in the cases of both transmission and reflection for illustration.

desired phase[11]. Mathematically therefore, we suppose that a phase-only hologram $H = H(\boldsymbol{r}_\mathrm{T})$ is used to create a desired field $E_\mathrm{des} = \mathcal{E}_\mathrm{des}(\boldsymbol{r})e^{i\varphi_\mathrm{des}(\boldsymbol{r}_\mathrm{T})}$ from an input field $E_\mathrm{in} = \mathcal{E}_\mathrm{in}(\boldsymbol{r}_\mathrm{T})e^{i\varphi_\mathrm{in}(\boldsymbol{r}_\mathrm{T})}$. Imposing that the field after the SLM should be spatially separated from the zeroth-order reflection, then

$$E_\mathrm{in}e^{i\boldsymbol{k'}_\mathrm{in}\cdot\underline{\hat{r}}} \times e^{iH} = E_\mathrm{des}e^{i\boldsymbol{k}_\mathrm{des}\cdot\underline{\hat{r}}} \ , \tag{2.40}$$

where $\underline{\hat{r}} = (\underline{\hat{x}}, \underline{\hat{y}}, \underline{\hat{z}})$, $\boldsymbol{r}_\mathrm{T} = (x, y)$ and $\boldsymbol{k'}_\mathrm{in}$ and $\boldsymbol{k}_\mathrm{des}$ are the wavevectors of the input and desired beam respectively when considering the SLM in a transmissive picture with angle of incidence $\theta = 0$ (Figure 2.9). The effect of the hologram, ignoring a uniform attenuation[12], then follows as:

$$e^{iH} = \frac{E_\mathrm{des}}{E_\mathrm{in}}e^{i(\boldsymbol{k}_\mathrm{des}-\boldsymbol{k'}_\mathrm{in})\cdot\underline{\hat{z}}}, \tag{2.41}$$

such that collecting the terms yields

$$e^{iH} = \mathcal{E}_\mathrm{rel}e^{i\varphi_\mathrm{tot}} \tag{2.42}$$

where the relative field amplitude $\mathcal{E}_\mathrm{rel} \equiv \mathcal{E}_\mathrm{des}/\mathcal{E}_\mathrm{in}$ and total relative phase $\varphi_\mathrm{tot} \equiv \varphi_\mathrm{des} - \varphi_\mathrm{in} + (\boldsymbol{k}_\mathrm{des} - \boldsymbol{k'}_\mathrm{in}) \cdot \underline{\hat{z}}$ lie in the intervals $[0, 1]$ and $[-\pi, \pi]$ respectively; we are assuming a small angle between $\boldsymbol{k}_\mathrm{des}$ and $\boldsymbol{k'}_\mathrm{in}$ and where from now on, the spatial dependence is implied. In our setup, the spatial offset is achieved by applying a phase grating φ_grat of the form

$$\varphi_\mathrm{grat} = \mathrm{Mod}(\frac{2\pi x}{\Lambda}, 2\pi), \tag{2.43}$$

where the $\Lambda = 2\pi/(\boldsymbol{k}_\mathrm{des} - \boldsymbol{k'}_\mathrm{in})$ is the grating period (taken in our experiments and simulations to be $\Lambda = 4$ pixels).

The problem of hologram design then reduces to solving Eq. 2.42 for H.

The form of Eq. 2.42 suggests that any solution will be intrinsically complicated. If we simply set the SLM phase to φ_tot, then we can in principle transform any incoming phase field to any profile that we might desire, along with any corresponding spatial offset. The amplitude however, will be completely unaffected and herein lies the problem [13]. As suggested, this can be mitigated by careful control of the grating height. Once again,

11. The filtering also significantly improves the mode purity, by spatially decoupling the shaped and unshaped light.

12. A result of the reflection of the beam from the SLM surface.

13. Although it's true that the electric field will be unaffected, the *intensity* need not be. On propagation, any phase discontinuity will necessitate areas of darkness, as already considered in the case of Laguerre-Gaussian beams.

there are many methods for generating holograms of this form and although analytical solutions may appear to be exact we note that various experimental effects, including spatial filtering and SLM pixelation, render all methods imperfect. A numerical and experimental comparison of a selection of such methods are therefore outlined below.

Method A

The first method was included as a simple benchmark. Acknowledging that φ_{tot} needs to be scaled spatially, then we consider the situation where φ_{tot} is spatially scaled by the relative amplitude $\mathcal{E}_{\text{rel}}$ *i.e.*

$$H = \mathcal{E}_{\text{rel}}\varphi_{\text{tot}} \tag{2.44}$$

For a grating depth of 2π, theoretically all light can be diffracted into the first order, but as the grating depth decreases, light is removed from the first order and appears in the zeroth order. In this way, the scaling function is used to encode the relative amplitude between the desired and incoming beams. This naïve approach assumes a direct linear relationship between grating depth and amplitude, which although incorrect, produces surprisingly good results. The technique is widely used, often even without taking into account the spatial shape of the input beam.

Method B

Proposed by A. Arnold, the next method is a recent suggestion, first implemented by the author, R.F. Offer and N. Radwell[13], and doesn't follow the above line of reasoning. Taking inspiration from the early techniques of holography, it relies not on the relative phase and amplitude, but on the complex argument of the superposition of the initial and desired fields. Just as traditional holograms were created by interfering scattered light intensities with a coherent reference beam, we consider instead the phase information inherent in the superposition of the two fields *i.e.*

$$H = \arg(NE_{\text{dg}} + E_{\text{in}}) \tag{2.45}$$

where $E_{\text{dg}} = \mathcal{E}_{\text{des}} e^{i(\varphi_{\text{des}} + \varphi_{\text{grat}})}$ and N is a normalisation factor to ensure E_{dg} never exceeds E_{in}. It should be noted that this hologram encodes both phase and amplitude information as it sums the fields before taking the argument.

Method C

An expansion on the principles behind method A, the technique of Davis *et al.*[31] addresses the fact that the diffraction efficiency is not linear with grating height. Fourier analysis suggests that the amplitude of light diffracted into the first order is actually given by

$$A = e^{i[1-f(A)]\pi} \operatorname{sinc}(\pi\,[1 - f(A)]), \tag{2.46}$$

where $f(A)$ is not yet determined scaling function. Omitting the exponential term, numerical inversion of Eq. 2.46 then gives

$$f(A) = 1 - \frac{1}{\pi} \operatorname{sinc}^{-1}(A), \tag{2.47}$$

where sinc^{-1} is appropriately defined for $A \in [0, \pi]$. The hologram is then the product of this function and the total relative phase:

$$H = \left[1 - \frac{1}{\pi} \operatorname{sinc}^{-1}(\mathcal{E}_{\text{rel}})\right] \varphi_{\text{tot}}. \tag{2.48}$$

Method D

The omission of the phase term however, can lead to amplitude information leaking into the phase profile. As highlighted by Bolduc *et al.*[32], it was then suggested that this could be accounted for by re-expressing the hologram as

$$H = M\,[\varphi_{\text{tot}} - \pi M] \tag{2.49}$$

where $M = 1 + \frac{1}{\pi} \operatorname{sinc}^{-1}(\mathcal{E}_{\text{rel}})$.

Method E

Another approach to generating holograms was proposed by Arrizòn*et al.*[33]. They show that, in order to create the desired

output field in the first order of the diffraction pattern, $f(\mathcal{E}_{\text{rel}})$ must be obtained from

$$J_0[f(\mathcal{E}_{\text{rel}})] = \mathcal{E}_{\text{rel}} \tag{2.50}$$

where J_0 is the zeroth-order Bessel function and $f(\mathcal{E}_{\text{rel}})$ can be recovered by numerical inversion. The resulting hologram is then given by

$$H = \varphi_{\text{tot}} + f(\mathcal{E}_{\text{rel}}) \sin(\varphi_{\text{tot}}) \tag{2.51}$$

where f is obtained from $J_0(\ f(\mathcal{E}_{\text{rel}})\ ) = \mathcal{E}_{\text{rel}}$.

Method F

Arrizòn*et al.*[33] also considered holograms of the form

$$H = f(\mathcal{E}_{\text{rel}}) \sin(\varphi_{\text{tot}}) \tag{2.52}$$

where $f(\mathcal{E}_{\text{rel}})$ is deduced from $J_1(\ f(\mathcal{E}_{\text{rel}})\ ) = a\mathcal{E}_{\text{rel}}$ and a is a constant between 0 and 0.5819, the maximum of the first order Bessel function. A particular strength of this hologram is that it can be implemented on an SLM with reduced phase range.

2.3.2 *Input intensity correction*

Having extended the above methods to account for the incoming profile, we now consider how to use this extra freedom in practice. Before we can compensate for the incoming beam however, we need to ensure that the SLM itself isn't introducing any errors to the system. Assuming that the incident wavefront has negligible deviation from a plane wave, then we first ensure that the SLM is performing optimally.

Aberration Correction

A perfect SLM would have an optically flat front surface. In reality however, small surface imperfections lead to an astigmatic output beam, even when the SLM is switched off. The effect of this is most pronounced in the far field and is therefore easily observable at the focus of a lens. In general, this astigmatism can be corrected by first characterising these astigmatisms using

Zernike mode decomposition and then correcting for these by applying the appropriate inverse phase [34, 35]. Here however we find that the introduced astigmatism is very well approximated by a cylindrical lens and can be corrected by incorporating an appropriate cylindrical lens into the holograms (Figure 2.10).

Incident intensity measurement

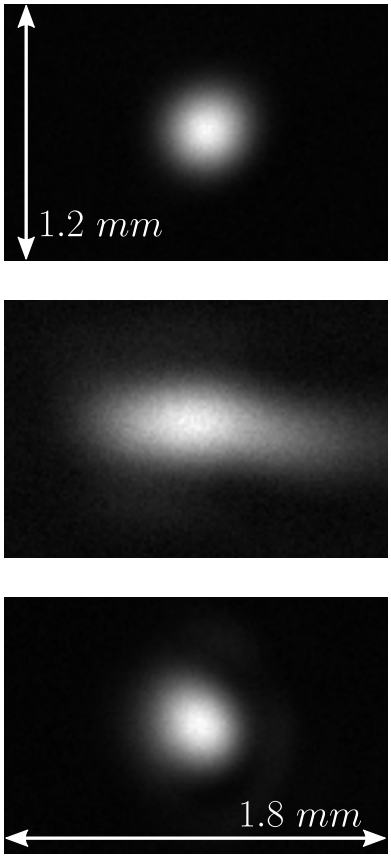

Figure 2.10: The intensity profile of the beam taken at the focus of a 750 mm focal length lens for the beam before the SLM (top), the beam after the SLM (middle) and the beam after the SLM (bottom) when a cylindrical lens of focal length 11 m at an angle of 96 degrees to the vertical is added to the hologram.

Generally speaking, the use of an SLM presupposes that the incoming beam will not be complicated. This being the case, and where the system is well-aligned, then it will often be sufficient to assume a zeroth-order Gaussian as the input or whatever mode most closely approximates the incoming field. Including these assumptions in our hologram calculations greatly improve the field quality when compared to a harmonic plane wave, but a more general system would allow for experimental imperfections. The easiest way of measuring an incoming beam's intensity profile would be to take an image with a camera, positioned at the exact location of the SLM - however this is experimentally inconvenient and requires rescaling and thorough alignment. To avoid these issues a more general and, as far as the author is aware, original method was used.

Single-pixel imaging techniques [36, 37] effectively turn the SLM into an in situ camera, giving an image of the input beam which has perfect pixel registration and scaling, however at the cost of resolution. A sequence of patterned masks are displayed, such that each mask blocks a particular spatial region of the input field and the remaining light is measured with a power meter. By using an orthogonal set of masks, namely the Hadamard set, full spatial information of the intensity field can be recovered, with N^2 measurements required to reconstruct an image with $N \times N$ resolution. We use this method to record an image with 32×32 resolution and use bicubic interpolation to expand this up to the 600×600 resolution of the SLM. This image is then used as the input intensity profile for all future hologram generation.

Following the discussion previously, we present an experimental analysis of the consequences of assuming differing intensity profiles for the incoming beam. In order to fully test our

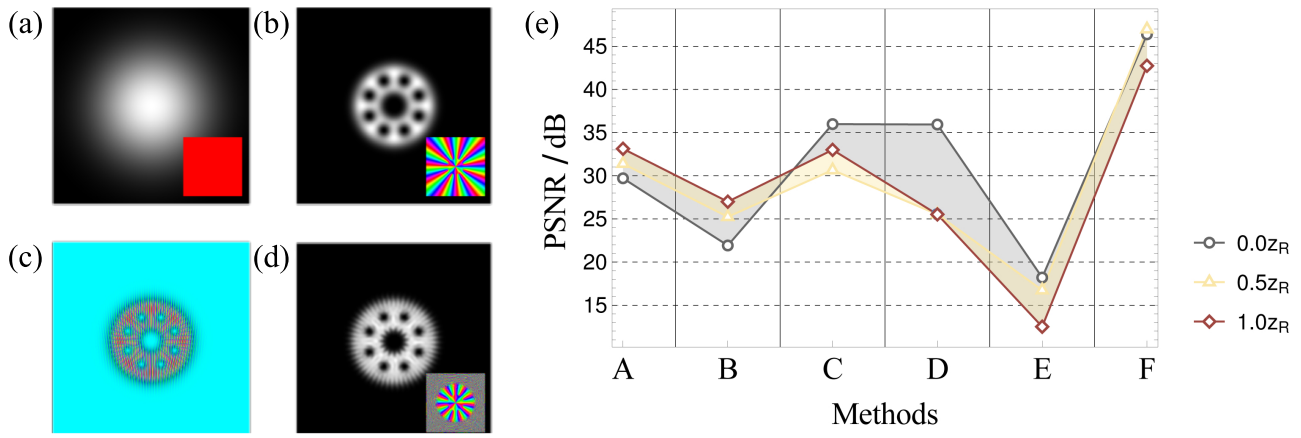

Figure 2.11: (a) Intensity and phase (inset) of the input Gaussian beam. (b) Intensity and phase (inset) of the desired beam (here shown for an *optical Ferris wheel*). (c) Hologram generated using method A, where the 8-bit greyscale is converted to phase by the SLM. (d) Intensity and phase (inset) of the beam generated by the input beam in (a) and the hologram in (c). The phase insets use phase ranges from $-\pi$ to π periodically (red to red on a standard colour wheel). (e) Numerical evalution of the mode quality for the six different hologram generation methods, shown for imaging plane (0.0 z_R) and further propagation by half (0.5 z_R) and a full Rayleigh range (1.0 z_R).

correction technique, we consider the worst case scenario of an unfibred, misaligned beam. As we can see from the figure, assuming a Gaussian input profile is an improvement on assuming a plane wave, but the dramatic increase in quality is seen when we use the measured profile, as obtained using the single-pixel techniques discussed earlier.

2.3.3 *Numerical Model*

To assess the methods outlined above we define a set of test beams including 3 patterns based on Laguerre-Gauss (LG) [38] modes and their superpositions and 1 photographic image. LG modes contain optical vortices associated with dark regions in amplitude and a winding in phase. They are characterised by two parameters, a winding number ℓ and a radial order p, however for this investigation we restrict ourselves to modes with $p = 0$ and define a Laguerre-Gaussian mode of order ℓ to be LG_ℓ.

Within this set we have chosen three test beams: a simple fundamental Gaussian LG_0, a single Laguerre-Gaussian mode of moderate order (LG_{10}) and a spatially intricate superposition of LG modes $|LG_3 + \alpha LG_{11}|^2$; $\alpha = |\frac{11}{3}|^{\frac{1}{4}}$, known as an optical Ferris wheel [39]. A final test is made with a non-propagating field

shape: a scene of an appropriately named *laser class* sailboat.

In our simulations, we use the LabVIEW development environment to both generate the holograms and to predict the resulting intensity and phase profiles after spatial filtering and propagation. We begin by defining the input beam E_{in} and the desired beam E_{des}(as shown in Figure 2.11(a) and Figure 2.11(b) respectively) and use these to calculate H according to the methods outlined above (see Figure 2.11(c) for an example hologram). The output field is then given by applying the hologram phase to the input field such that:

$$E_{\text{out}} = E_{\text{in}} e^{iH}. \tag{2.53}$$

As discussed, our desired beam is produced in the first diffracted order of the grating which has to be separated from the rest of the field. This is achieved by spatially filtering the beam in the far field, where the diffraction orders are well separated. Numerically, we model this by taking the Fourier transform of E_{out} and multiplying the resulting field by a circular mask (set to 1 mm diameter for these results), setting all of the values outside the circular region to zero. The exact size of this filter plays a significant role in the beam quality and is discussed in more depth in the final section on experimental details. Using an inverse Fourier transform on the filtered data then gives the amplitude and phase of the new light field at the imaging plane of the SLM, as shown for method A in Figure 2.11(d). We note that after the selection of the first order, we subtract the grating phase from the field in order to remove the associated tilt, where of course in practice the selected order will continue to propagate at an angle to the pure reflection.

Using this model, we predict the intensity profile of the light at the imaging plane of the SLM as well as for propagation of 0.5 and 1.0 Rayleigh ranges, for methods A-F.

To measure the accuracy of each method we compare the generated intensity with the desired beam. The methods should be able to accurately reproduce both intensity and phase, and while we do not measure the phase profiles directly, the intensity measurements after propagation reflect the phase accuracy. For the laser modes we perform a 2D fit of the intensity data with

the relevant function ($|LG_0|^2$, $|LG_{10}|^2$ or $|LG_3 + \alpha LG_{11}|^2$), specifying the waist and setting the centre position, offset, rotational phase and amplitude as free parameters. For the photograph, we instead use the Mathematica ImageAlign function to scale and align the reference image with the intensity data.

The intensity data is then compared to the fitted function by employing the Peak Signal-to-Noise Ratio (PSNR) as a quality metric [40]. The PSNR is a well-established metric, originally employed by signal engineers and later maintained as a tool to quantify the quality of reconstruction of lossy compression codecs. We note that, in order to compare the different results, the data has to be normalised with respect to each other and as such, the background (taken from the numerical fits) was first subtracted before normalising the data. The normalisation was accomplished by dividing each image by its corresponding fitted amplitude and rescaling the data and fit such that each fit has the same maximum value. The data however was allowed to go outside the boundaries of the fit.

We then employ the PSNR quality metric, which is based on the mean square error (MSE) given by:

$$MSE = \frac{1}{mn} \sum_{i=0}^{m-1} \sum_{j=0}^{n-1} [I(i,j) - K(i,j)]^2 \tag{2.54}$$

where I is the perfect m by n monochrome reference image and K is the approximation under study. This allows us to define the PSNR per decibel:

$$PSNR = 10 \log_{10} \left(\frac{MAX_I^2}{MSE} \right) \tag{2.55}$$

where MAX_I is the maximum value of I. We apply this metric to the data for each generation method, desired image and propagation distance

The results are plotted in Figure 2.11(e), where we infer that all of the methods, with the significant exception of method E, should produce reasonable results. Method F in particular, somewhat surprisingly, should give the best results for all propagation distances by approximately 10 dB, with method C predicted to yield the next best overall results. Additionally, we see that

method D's performance should deteriorate steeply after half a Rayleigh range of propagation and yet maintain the same beam quality after a full Rayleigh range. Finally, we note that naïve amplitude scaling, method A, is predicted to do quite well, very slightly outperforming method C outside of the imaging plane.

Mode quality with aperture

All of the generation methods presented rely on spatially filtering the desired mode in the first order diffracted spot. Whereas other beam shaping techniques explicitly rely on the use of apertures [41], we simply wish to remove all of the unwanted parts of the field. We find that the exact size of this spatial filter has a significant impact on the quality of the mode and we use our numerical simulation to investigate this effect more rigourously.

We generate a hologram for the Ferris wheel mode using method A and monitor the beam quality as we increase the size of our spatial filter. The results are plotted in Figure 2.12(a) and here we see that where the aperture is not cutting the beam (contrary to the first data point), a lower filter radius can significantly improve the mode quality. Additionally, we see that under the same conditions there is an associated pseudo-linear decrease in power, but with a very shallow gradient. In most situations therefore, we would assume that the quality gain justifies the small loss in power. For illustration, we also visualize the full Fourier plane (Figure 2.12(b)) and a subection of the Fourier plane including the spatial filter size with respect to the first order (Fig. Figure 2.12(c). The resulting intensity patterns are also displayed in the right hand column of Figure 2.12(b) and Figure 2.12(c).

Mode quality with thresholding

We have stated previously that producing an accurate E_{out} requires knowledge of E_{in}. Methods (A-D and F) modulate the grating in order to remove power where it is not wanted. As a consequence, on a pixel by pixel basis, the desired beam amplitude cannot exceed the input beam amplitude. If perfect beam accuracy is desired then this forces the output beam to be scaled

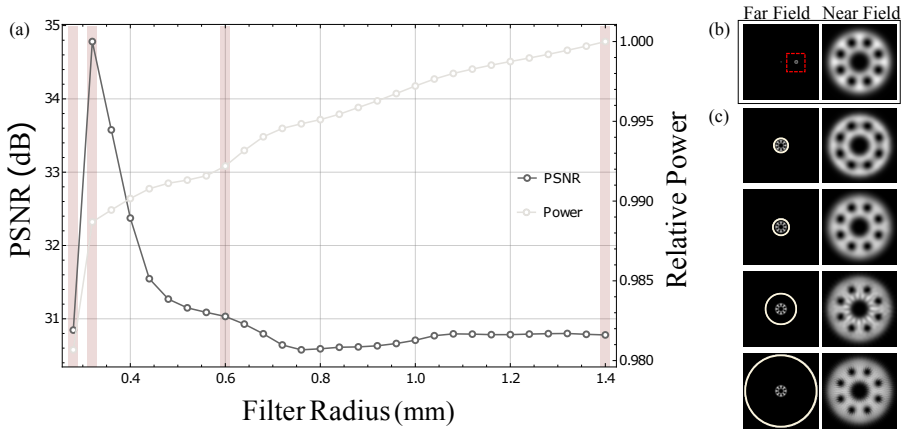

Figure 2.12: (a) The Ferris wheel PSNR and total power as the size of the spatial filter is adjusted, where the red bars highlight the data points that have been visualised in (c). (b) The full far- and near-field intensity profiles associated with filter size 0.6 mm where the red dashed box indicates the sub-region used in the left column of (c). (c) Far- and near-field intensity profiles associated with the filter sizes marked in pink in (a), with the filter boundary marked with a white circle.

in intensity such that E_{out} never exceeds E_{in} at any position, thereby limiting the amount of light in the output mode. For high power applications this is undesired and we therefore propose a method which can increase the output power at the expense of some beam accuracy. This can be achieved by misrepresenting the form of E_{in} used for the calculation of the relative field.

The peak value of the relative field and therefore the output power is limited by the low amplitude regions of E_{in}. Therefore if these low amplitude values are removed, by setting all values below a particular threshold to the threshold value, the total power in the output mode will increase. This however misrepresents the input beam and therefore reduces the accuracy of the mode generation, as is shown in Figure 2.13. It should be noted that the data shown previously in this paper was taken with a threshold level of 0.01, i.e. 1%, serving only to remove the effects of the noise associated with our intensity measurement. Figure 2.13 clearly shows two regimes; a stable region for a threshold value below 0.2 and a transition to a scaling region beyond. This transition point depends on the relative size of E_{in} and E_{des} and can be understood to occur when E_{des} begins to overlap with the thresholded region (flat parts in the top row of Figure 2.13(b)). In the latter region we see that it is possible to trade beam generation accuracy for more power.

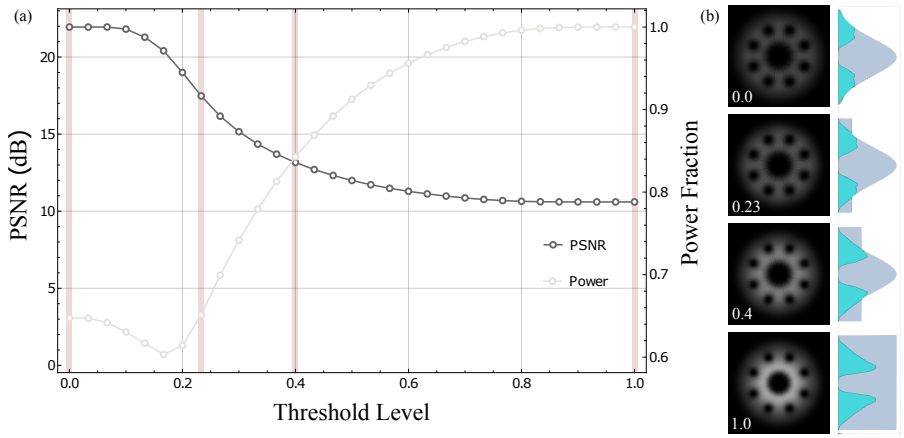

Figure 2.13: (a) The PSNR and associated beam power of the simulated Ferris wheels with respect to the intensity threshold level. Four key threshold levels are highlighted by a red bar, corresponding to the images in (b). (b) 2D intensity profiles and central cross sections of the assumed input beam (grey) and the generated beam (blue).

2.3.4 *Experimental setup*

The experimental setup is shown in Figure 2.14. The light (generated from a 776 nm Toptica DL100) passes through a single-mode fibre, to spatially filter the beam, before passing through a beam expanding telescope which increases the beam waist to 4.65 mm. The beam is then reflected off an SLM (Hamamatsu LCOS X13138-01) at approximately three degrees before it propagates through a final telescope. In the Fourier plane of this telescope we filter the first order with an aperture set to a diameter of ~ 1 mm. The intensity patterns are then recorded on a camera (Point Gray Chameleon CMLN-13S2M-CS) at the image plane of the SLM, followed by measurements 0.5 and 1.0 Rayleigh ranges away from this image plane.

2.3.5 *Experimental Results*

The hologram generation methods are tested by displaying each hologram consecutively and recording the obtained intensity patterns in three different planes as described in the experimental set-up section. Figure 2.15 shows a full set of images for the Ferris wheel beam, including the simulation of the intensity in the image plane in the top row as well as the measured intensity pattern in the image plane of the SLM (second row), after

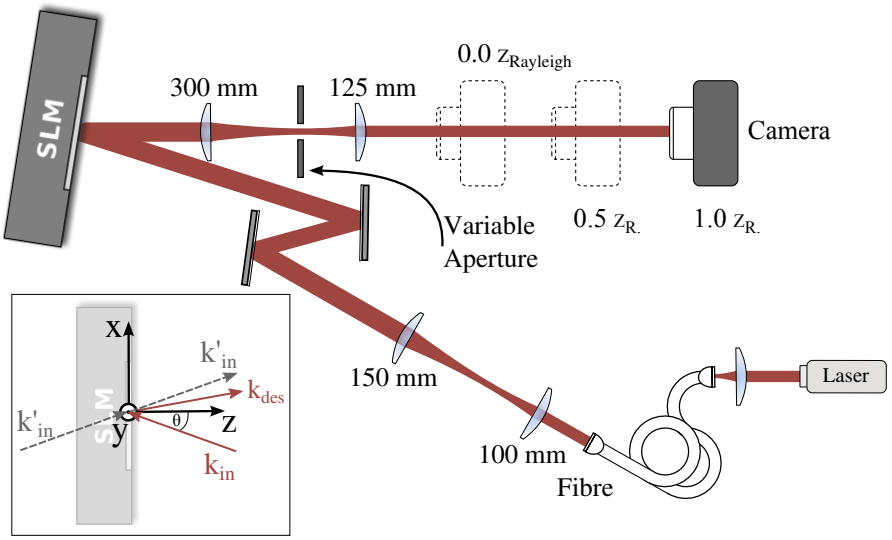

Figure 2.14: A fibre-coupled 776 nm laser (with 4.9 µm $1/e^2$ mode field diameter) is first expanded to a waist of 4.65 mm before illuminating the centre of the SLM, where the inset highlights the axes and wavevectors of interest. The output beam is then Fourier filtered before being imaged at one of three propagation distances.

propagating half a Rayleigh range (285 mm, third row) and after propagating a full Rayleigh range (569 mm, bottom row). These are all intensity measurements however the propagation images reveal the accuracy of the phase reproduction as any phase imperfections will result in a deviation from the desired mode. Similar measurements have been taken for the Gaussian beam (LG_0), the Laguerre-Gaussian beam (LG_{10}) and the photograph; a subset of which are shown in Figure 2.16.

We perform a quantitative analysis of the generation methods by assessing them against two criteria: the accuracy of beam generation and the distribution of power. Applying the PSNR metric to the experimental data, as for the numerical results, we obtain Figure 2.17.

Power Distribution

In many applications we are not only concerned with the spatial mode quality, but require as much power as possible. Our second assessment criteria is therefore to find how much power there is in the desired mode for each method. We first measure the total power at the output compared to the total power impinging on the SLM, which gives the total efficiency. We define the *mode*

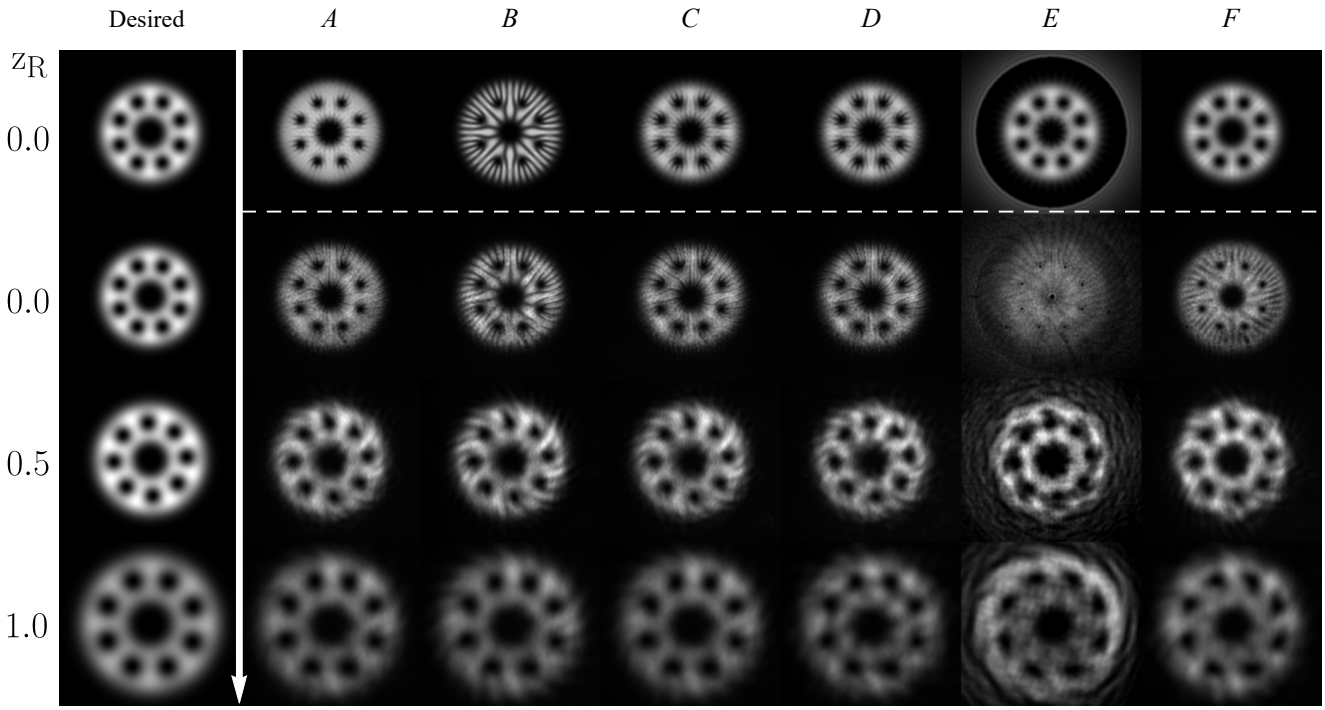

Figure 2.15: An overview of the measured beam intensities for an optical Ferris wheel shaped according to each hologram generation method (horizontal) and propagation distance (vertical) respectively. The first row shows the simulated prediction for each method and the first column indicates the desired field intensity for 0.0, 0.5 and 1.0 Rayleigh ranges.

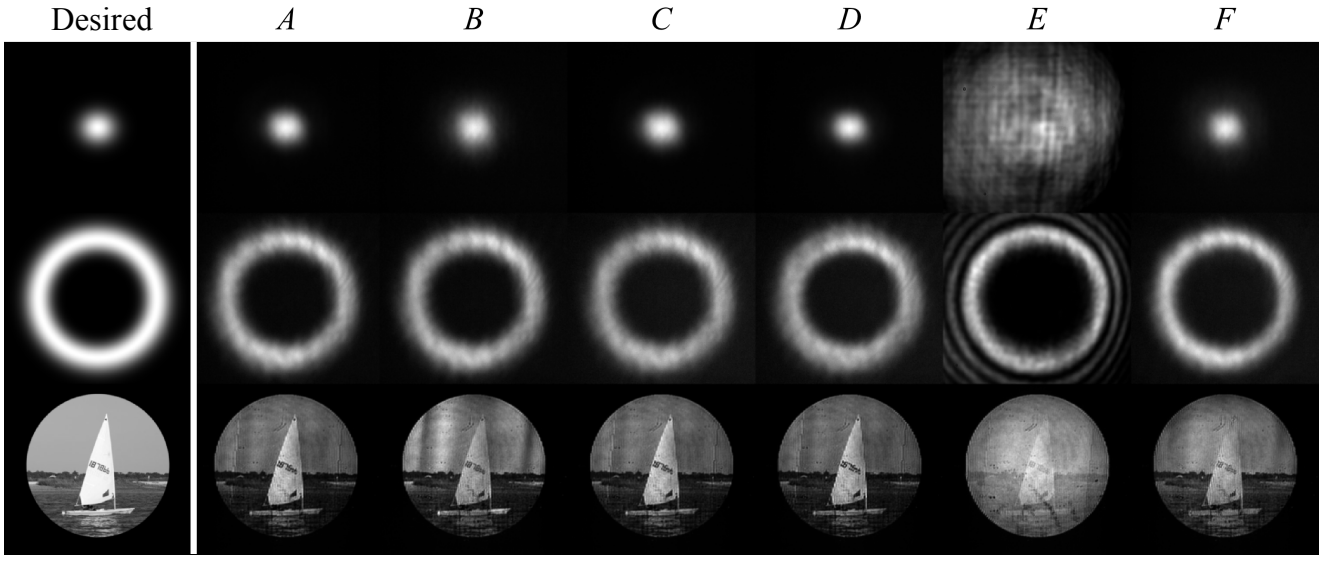

Figure 2.16: An overview of the measured beam intensities for a fundamental Gaussian, an LG_{10} and an arbitrary image according to each hologram generation method. The first column indicates the desired pattern, the first and middle row show the measured beam after one Rayleigh range of propagation and the bottom row shows an arbitrary scene in the image plane of the SLM.

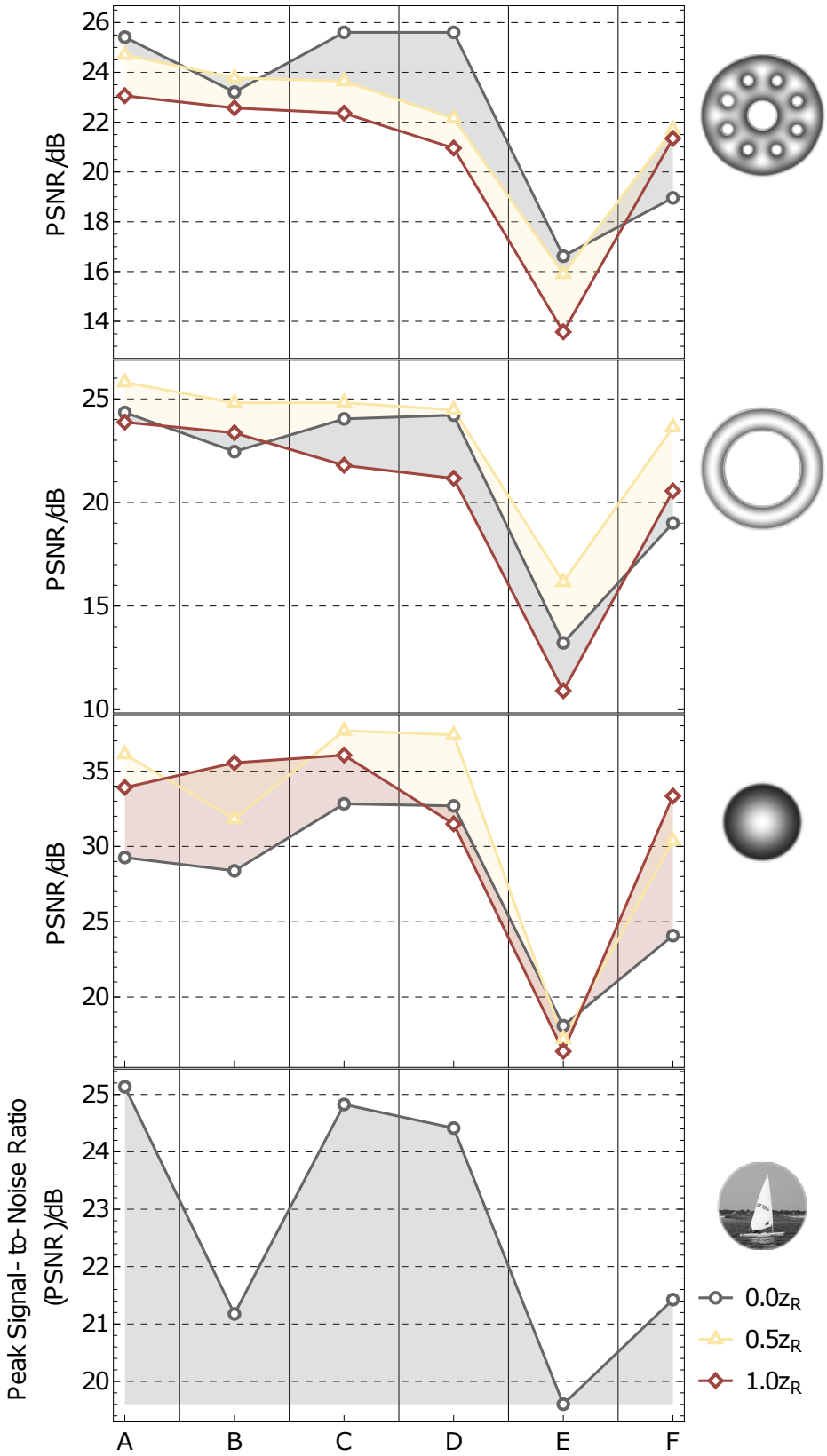

Figure 2.17: An estimation of the constructed field quality, as determined by the peak signal-to-noise ratio for the three propagating modes and the arbitrary pattern.

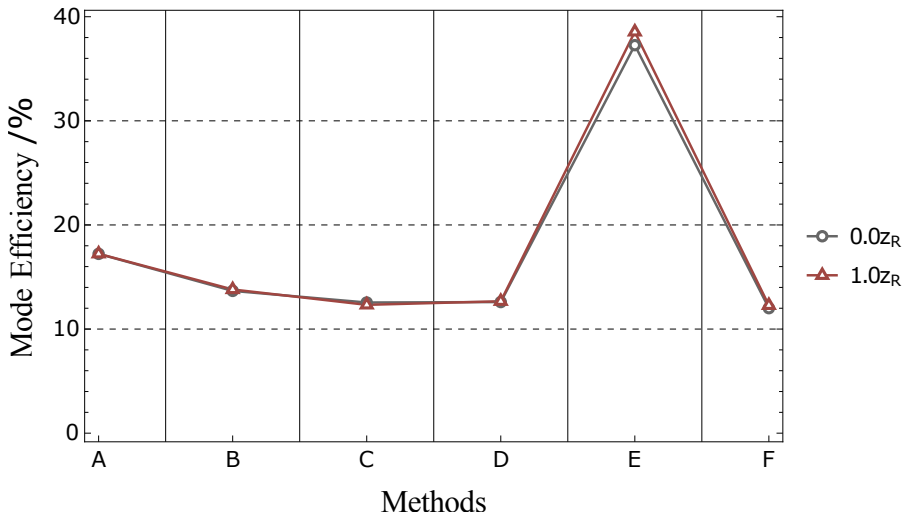

Figure 2.18: The variation in mode efficiency across the different hologram generation methods, as measured for different propagation distances of an optical Ferris wheel. The total power after the spatial filter for each method is scaled by the associated cross-correlation between each mode and its fit, before being expressed as a percentage of the measured input power of 26.4 mW.

efficiency as the fraction of this power which contains our desired mode, determined by calculating the projection of our generated mode onto our desired mode (details can be found in Section 3A of [42]). Using the Ferris wheel as our test beam, the results are illustrated in Figure 2.18.

2.3.6 *Discussion*

We begin by considering the ability for each of the methods to produce an accurate representation of the intensity of the desired modes. Inspection of Figure 2.17 reveals that methods A-D and F perform well in general, with only method E showing a clear dip in quality. We attribute this deviation to a high sensitivity to small imperfections in the input phase, which we assume to be flat. This is perhaps natural as the method does not modulate the depth of the grating, instead relying on interference to achieve intensity modulation, and therefore shows increased sensitivity to phase.

Taking a closer look at the creation of the Ferris wheel mode (top of Figure 2.17) we can see that in general the mode is best in the image plane and the quality degrades slightly as it propagates, showing a small deviation from the desired phase.

Looking at specific methods, the absolute best performance is achieved by methods C and D, very closely followed by method A. The strong performance of methods C and D is not surprising, however our naïve benchmark, method A, performs extremely well for all propagation distances. Method B is a little less accurate in the image plane, but seems to be more robust to propagation; with method F also propagating well, indicating an accurate generation of the phase profile.

Turning to the LG_{10} mode generation (second row of Figure 2.17) we once again see that all methods except for method E perform similarly well. Once again method A performs surprisingly well, with the other methods very close behind. The Gaussian mode generation again shows similar results (third row of Figure 2.17). Turning finally to the recreation of the boat (bottom row of Figure 2.17) we see methods A,C and D performing well with the other methods falling close behind, with a range of only 5 dB. We note in particular that the relatively poor performance of method B here seems to arise from a sensitivity to our aberration correction, which can be seen by the presence of an overall cylindrical lens pattern (see Figure 2.16 bottom row).

We next consider the power in the desired mode. The mode efficiencies of the six hologram generation methods are shown in Figure 2.18 and we see that method E contains the most power with more than 35% of the input power, while the other methods all contain between 12% and 18%. It should be noted that these numbers are specific to the exact input beam and desired mode, with an upper limit being placed on the mode efficiency equal to the projection of the input beam onto the output mode, which in this case is 53%. These numbers can therefore be increased by appropriate tuning of the input and output modes to optimise overlap.

From this analysis we can draw several conclusions; for the generation of laser modes, if beam accuracy is your primary concern, methods C and D perform very well. Surprisingly however, these methods do not significantly outperform our naïve method A. While this result may be specific to the modes chosen here, this is a significant result particularly in applications where hologram generation has to be performed quickly, as method A

does not involve the numerical inversion present for methods C and D.

If one cares primarily about the power present in the desired mode then method E is the clear winner, however this comes at the cost of significant loss in beam quality. For small, but significant gains in power, method A may also be of interest.

2.3.7 Conclusions

We have tested six different methods of digital hologram generation and find that all are capable of producing high quality beams. Experimental testing of each method's ability to generate a Gaussian mode, LG modes and an arbitrary image reveals the strengths of each particular method; we find that method A, though the simplest and most naïve performs extremely well in all tests and would be well suited to applications requiring fast calculations of holograms. Methods B, C and D all perform very well across all tests with C and D having a slight advantage in the generation of arbitrary images. Method E, while producing a low quality mode, provides the most power and method F performs well and requires a reduced phase range, making it useful for low-cost SLMs.

In addition we have stressed the importance of accounting for the form of the input beam and introduced a new way of detecting this *in situ.* We also find that the intensity profile of the input beam can place restrictions on the output power when the desired beam is large and have introduced and demonstrated a method to increase the output power at the expense of beam generation accuracy. Finally we have shown that the spatial filter size plays a crucial role in the beam generation accuracy and have shown that optimal filtering can achieve an increase in beam generation accuracy without significant loss of power.

We believe that these results will be useful across the many applications which rely on digital holograms, including optical trapping, atomic potential shaping, microscopy and beyond.

2.4 High-Speed Switching

By this point in our narrative, we have explored many optical properties, but we have held ourselves in space only; in this section however, we turn to more temporal concerns.

In general, the laser light used throughout this work is generated using a carefully controlled ECDL [14], which has a typical linewidth of approximately 1 MHz. Our discussions therefore have and often will implicitly assume monochromatic beams. Consequently, we are not concerned with the profile or temporal structure of our beams, but it is essential to be able to change their frequencies and for this purpose, we use an acousto-optical modulator (AOM[15]).

14. The exception is the switching experiment detailed in this section which uses a commercial Helium-Neon laser.

As we will find however, an AOM is also particularly suited to swift changes in direction. Thus, having first outlined its basic properties and mode of operation, we will segue into a brief summary of how a coupled hologram-AOM system can be used for rapid data-transfer, a summary of which has been published previously [11]. We will consider the system in the context of three alphabets; covering both arbitrary intensity patterns and Laguerre-Gaussian modes.

2.4.1 Acousto–Optical Modulators (AOMs)

Following our overview in § 2.2.3 (p. 24), an AOM can be summarised as a time-dependent diffraction grating. As sound waves are essentially ripples of pressure through a medium, the grating is formed from electrically generated acoustic waves that create alternating regions of high and low refractive index. The time-dependence however, comes from the motion of the sound waves. In general, AOMs use travelling waves that propagate through the medium and, at up to two orders of magnitude faster than through air, the sound waves provide a significant frequency shift [16].

16. For frequency-preserving diffraction, a standing wave can be used, but for the majority of AOM models a travelling wave is assumed.

The specifications of AOMs vary widely with model, but beam shifts of up to 500 MHz (double-passed) are now possible

[15] acousto-optical modulator

in practice [43]. Although, we will only consider shifts in the range of 70 to 130MHz. The transfer of frequency can be understood with appeal to the Doppler effect, such that light which is scattered in the direction of the travelling wave increases and that scattered oppositely decreases in frequency: where the associated energy is gained or lost from phonon excitations.

As an AOM is specifically a volumetric grating, it operates in the Bragg regime [17] and would be expected to concentrate the diffracted energy in only one order. In practice however, the wavefronts (both acoustic and optical) are not infinitely wide and so other orders do appear. As the grating is a phase effect however, then the efficiency can be extremely high: ranging from 99% in principle to approximately 80-90% in practice [28].

17. In fact, AOMs are often referred to as *Bragg cells*.

Although we focus here on the possible frequency shifts, an AOM can also be used to modulate the intensity and spatial deflection. Intensity changes are primarily the result of diffraction efficiency, which can be altered by changing the amplitude of the applied sound wave. Of particular importance to our later discussion however, is the spatial deflection inherent with a diffraction grating. By changing the frequency of the applied sound, we change the spacing of our grating and, from our previous derivations Eq. 2.39(p. 26), this can be seen to change the diffraction direction. Both the phase and even the polarisation [44] of an incoming beam can also be affected, but these effects play no part in our discussion.

2.4.2 Switching Overview

With the introduction of special relativity, there is now a theoretical speed-limit for single-pass data transfer, but in optical communications such concerns are unlikely to ever bring contentment: with data capacity already a fast-developing problem. An increase in capacity can be achieved either by increasing the number of transmitted photons or by increasing the dimensionality of the degree of freedom [45]: allowing the transmission of more information per photon. Intuitively, it follows that the ability to structure light spatially would allow for more efficient information transfer and complex images have indeed been shown to

be highly efficient messengers [46, 47]. Furthermore, our early discussion of spatial profiles indicated that transverse mode families form an infinite or doubly infinite state space and as such, there have been many recent proposals on high dimensional light processing, particularly on the use of LG decompositions [48, 49, 50]. The natural consequence of a large character base however, is the need for high-speed modulation.

The works of both Bozinovic *et al.* [51] and Wang *et al.* [52] have brought data rates into the terabit regime and fast space-division multiplexing in a single-fibre has been demonstrated by Richardson, Fini and Nelson [53] but, by their nature, such methods require N communication channels, with separate source and detection systems, for N modes: drastically restricting application in the single-photon realm.

Considering the devices introduced previously, LG-based beams can be created using SLMs, but even the very best LCoS systems operate on the order of 1 kHz [54] [18], where DMD[19]s can achieve 4 kHz [55]. Slussarenko *et al.*, have proposed a system based on q-plates and EOM[20]s that would in principle operate on the order of hundreds of MHz but the multi-stage setup required also suffers from scalability problems [56].

18. For comparison, the device used throughout this chapter has a refresh rate of 60Hz.

In contrast, we consider how an AOM can be concisely configured for scalable, detection-limited switching rates of 10 kHz, with the potential for rates up to 20 MHz. Using only a single channel, such a system is also free from the detrimental scaling outlined above and is fully compatible with quantum communication protocols.

Most encoding methods suffer from having to dynamically shape the spatial profile per character request; an intrinsically slow process. If the data alphabet is pre-defined however, the only relevant time scale is the inter-character switching rate and this is the principle underlying the experiment. Using the SLM from our previous discussion (§ 2.3 (p. 29)), an array of holograms can be addressed with a single AOM, where the data rate is then determined by the rise time and driving electronics.

[19] digital micromirror device
[20] electro-optical modulator

2.4.3 Setup

The experimental setup, as illustrated in Figure 2.19, was based on what is known as an *extended double-pass* configuration. As outlined above, the spatial deflection of the AOM can be controlled by electronic modulation of the acoustic frequency and this is what allows us to address a pre-defined array of holograms. To create a single communication channel however, the SLM is aligned in the Littrow configuration (Eq. 2.35(p. 25)), such that no matter the deflection angle of the AOM, the first order from the SLM always retraces its path through the AOM. The remaining problem, is the separation of the output and input beams, but this is taken care of with polarisation optics.

More specifically, the spatial deflection of the AOM was controlled with the LabVIEW programming environment and an associated National Instruments DAq[21]. The AOM (Crystal Technology 3080-122, central modulation frequency 80 MHz) deflection angle was found to vary with drive frequency at 0.19 mrad/MHz and thus, for a usable modulation frequency of $60 - 100$MHz, a total deflection range of 7.9 mrad. We should also note that although the second pass reverses the angle of deflection, the beam receives a frequency shift based on the propagation direction of the sound wave rather than that of the optical beam, leading to a doubling of the imparted frequency. If this frequency shift is a problem however, standing wave AOMs can be used to completely remove this effect.This particular SLM (Hamamatsu LCoS) provides full control of the phase and amplitude with a resolution of 800×600 pixels and a pixel size of 20 µm, but in practice this could be replaced by any fixed holographic element where the data characters are appropriately separated in space: greatly reducing cost and complexity. The setup would be of little use however, if we could not distinguish been the incident and outgoing fields, a distinction made with polarisation. The input beam is therefore horizontally polarised before entering the beam-shaping system and a Faraday rotator (FR) is subsequently used both as an optical isolator and to ensure that returning fields exit the correct side of the polarising

[21] data acquisition device

beam splitter. As we will later explore in in our discussion of atoms, the FR uses a magnetic field to induce a 45° rotation of our incident light. Unlike wave plates however, it does not obey reversibility and so on counter-propagation the beam undergoes a further 45° rotation, that allows the light to exit the system. An SLM however, is strongly polarisation dependent and so to optimise the efficiency a half-wave plate is used to temporarily counter the effects of the rotator.

The combined result of these effects is that by changing the driving frequency of the AOM, light is diffracted from a hologram of choice and output in a single channel; the channel output was then initially observed on a CCD camera, as highlighted in Figure 2.20.

2.4.4 *Results*

As illustrated in Figure 2.20, the setup was utilised for three sets of holograms: $l = [0, 3], p = 0$; $l = 0, p = [1, 4]$ and $l = 0, p = 0$ with four intensity masks in the shape of Latin characters. Considering the resulting camera images, the predicted and measured intensity profiles are largely in agreement, but suffer from astigmatism and uneven intensities. At the time of the original

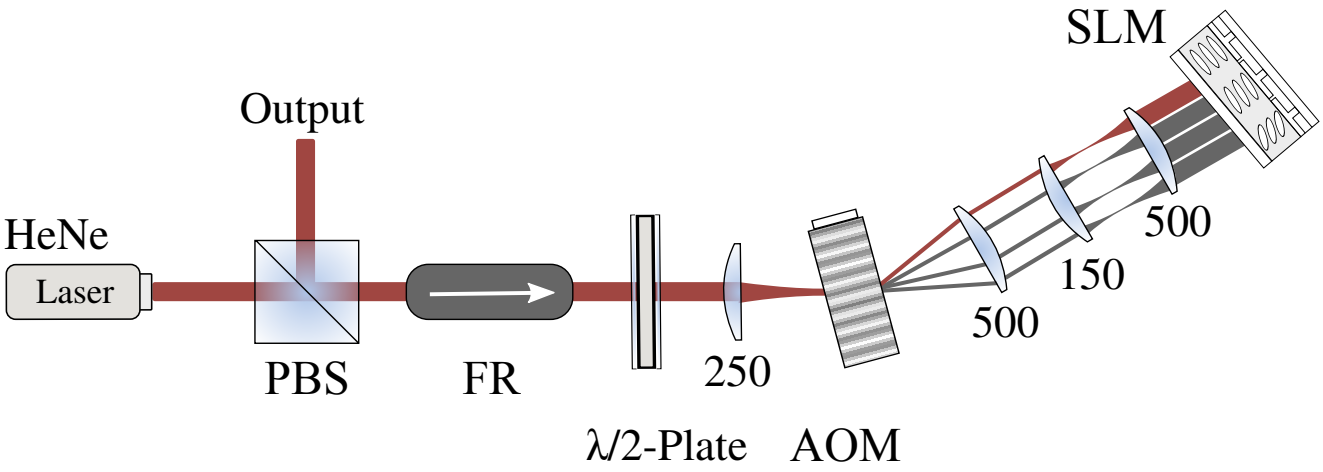

Figure 2.19: An overview of the apparatus used for switching. A horizontally polarised Helium-Neon laser is first passed through a polarising beam splitter (PBS), Faraday rotator (FR) and half-wave plate before being focused through an acousto-optical modulator (AOM). The light is then magnified to cover the area of a single hologram, dictated by the AOM drive frequency, before being diffracted back from the SLM through the polarisation optics. For clarity, the lens focal lengths are given in mm, the beam waist at the AOM is calculated as 150 µm and the red path indicates the currently selected deflection.

paper, the imperfections were attributed to a combination of astigmatism imparted by the AOM crystal and minor system misalignment that couldn't be removed with optimisation of the associated focusing parameters. With hindsight however, it is likely that the SLM aberration discovered in the previous section and the unoptimised implementation of the hologram algorithms were dominating factors. An unfortunate consequence of the order in which the experiments were carried out.

The indicated measurement times suggest a modest data rate for the system, but is really limited to the detection rate of the CCD camera rather than the generation rate. To test the system at higher speeds and to obtain more quantitative results, the CCD image was restricted to a single line of pixels. This was detected at a rate of 500Hz, but was still far below what we might have expected.

Restricting the camera output to a single line of pixels however, highlights the trade-off inherent with increasing detection rates. Although, we can assume that the rest of the profile is maintained at these speeds, there is certainly experimental dissatisfaction in making these assumptions. Necessarily however, the camera was replaced with a quadrant photodiode (New Focus 2901). This device directly outputs an x (y) signal, which internally is the difference between both left (upper) and right (lower) quadrants. These x and y coordinates give the centre of intensity of an incident beam and can in principle be read at up to 100 kHz. Such detection rates come with severely deteriorated signal quality however, and it was expedient to construct a more appropriate character alphabet. Instead of the profiles outlined above, each letter was designed to fill two quadrants of the QPD[22]. The letters were the left, right, lower and upper half of the input beam respectively and they can be generated by deflecting only the corresponding halves of the beam using the holograms shown in the insets of Figure 2.21. Following the method outlined above, these simplified letters were then similarly selected in tandem at a rate of 10 kHz, with the signal position in x and y recorded as a function of time (Figure 2.21).

[22]quadrant photo diode

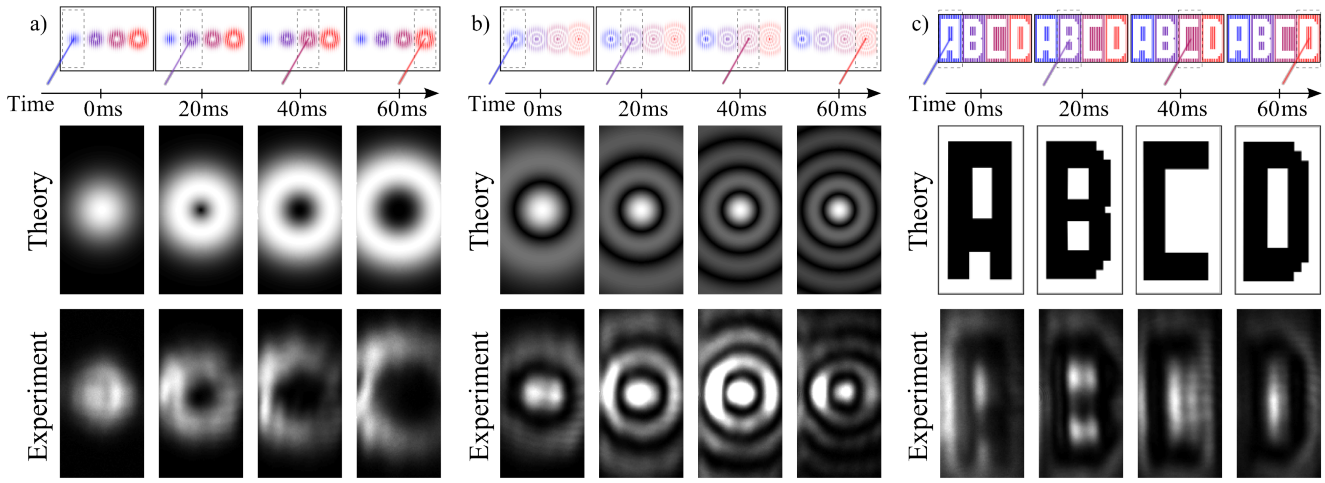

Figure 2.20: Hologram arrays, theoretical predictions and beam profiles for three different alphabets. The alphabet in a) has an azimuthal number l, varying from 0 to 3 (left to right) and b) has a radial number p varying from 1 to 4 (left to right). The alphabet in c) uses an intensity mask of the letters: 'A' to 'D'. The data in the bottom row of a) and c) was intensity scaled such that the maximum intensity is white. The data in the bottom row of b) for the $p = 2, 3$ and 4 modes was enhanced by a factor 2, 3 and 4 respectively to emphasise the low intensity features.

Figure 2.21 then confirms that outside of the switching times the signal settles to a stable value, suggesting successful switching between the profiles every 100 µs. Although orders of magnitude below what can be expected of an AOM, these results were taken at the extreme end of the QPD detection bandwidth and faster detectors are necessary to prove these predictions beyond reasonable doubt. Such a result however, brings our data rate into the same range as those listed previously and underlines the potential of the system for future development.

2.4.5 *Technical Discussion*

Having demonstrated the principle for high-speed encoding, we now analyse these results in the context of efficiency, data transfer rate and scalability.

Regarding the efficiency, the main source of loss is diffraction. Both the SLM and AOM distribute incident light across many orders, although with experimental Bragg conditions this can be greatly offset. Nevertheless, each interaction loses approximately 15% of the light and including the double pass through the AOM, this results in an efficiency approaching 61% overall.

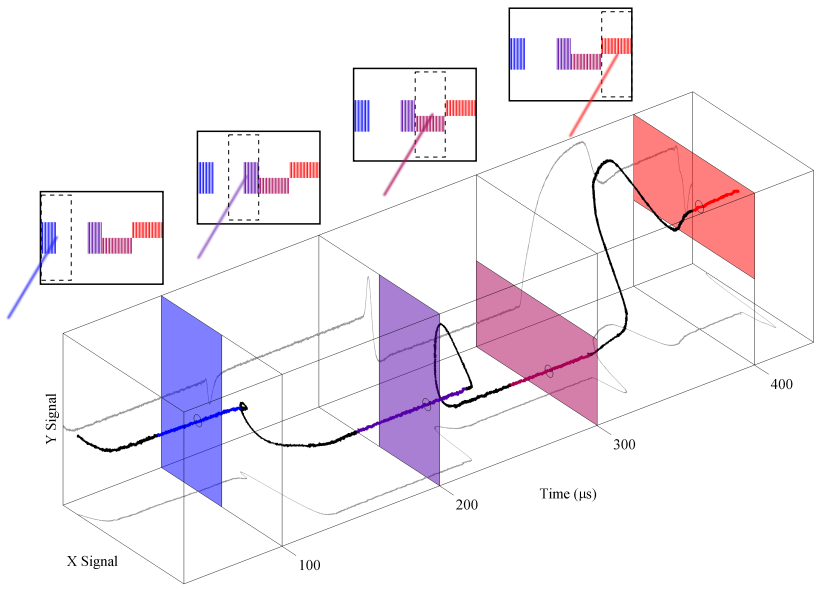

Figure 2.21: Trajectory of the QPD signal in time. The semi-transparent planes indicate the pattern in which the beam is shaped at a particular time and the grey projected lines are the projection of the trajectory onto the axes.

The data transfer rate is the product of the *modulation rate* and the *data capacity* of the signal, where the modulation rate is limited both by the *rise time* of the AOM and the *photon transit time*.

The transit time is simply the round-trip time for the photon between leaving and returning to the AOM[23], while the rise time varies with beam size in the AOM: such that the modulation rate is then determined by the optical path length and choice of lenses in the system respectively.

23. This is the time required before the AOM grating frequency can be changed. If it was switched any earlier, then the returning photon would not be brought back into the original propagation axis.

The data capacity is conceptually more intuitive, increasing with increasing number of letters in the system, but it suffers from the limitations of the *data capacity factor* $\log_2(N_c)$, where N_c is the number of characters in the alphabet. This factor accounts for the associated number of bits required to contain the same amount of data. Unfortunately however, addressing the same hologram means that larger alphabets require a smaller beam size at the SLM and this leads to competing concerns as the SLM and the AOM are in conjugate Fourier planes. Larger beam waists in the AOM therefore mean slower modulation rates, with the net result that an increase in data capacity results in a decrease in modulation rate.

The data transfer rate clearly has a complicated relationship with the alphabet size, resulting in a rate peak at between three and four characters.

This presents a system user with a choice. Previously, we noted that our single-channel system doesn't suffer from the same multiplexing scalability problems and this remains true if we desire maximum efficiency. A loop-hole around our previous argument however, is that if we allow differing character beams to overlap and latterly use a spatial filter then we can sacrifice efficiency for larger beams with improved data rates. This however, would introduce a $1/N_c$ scaling efficiency and so the choice is whether or not the user desires optimum efficiency or speed: ultimately deciding whether or not the system is applicable to quantum or classical applications.

2.4.6 *Switching Conclusions*

Therefore, we have developed a prototype spatial modulator for communication, which has full control over phase and intensity of the character alphabet. This has been verified to 10 kHz, but faster detection and driving electronics could potentially lead to encoding rates that exceed 20 MHz. This could involve ultrafast cameras, an LG modesorter [57] or SLMs linked to avalanche photodiodes. In either case, we suggest that the mechanism might find application in high-dimensional quantum communication [48, 58, 59, 60].

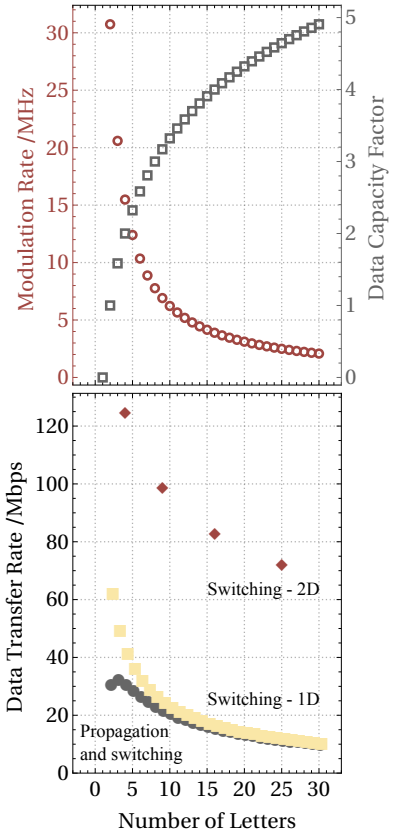

Figure 2.22: The predicted modulation rate, data capacity factor and data transfer rate as a function of alphabet size.

2.5 Light Conclusions

Throughout this chapter we have discussed the various spatial parameters inherent in a beam of light; we have detailed a selection of the many existing methods used to both generate and sculpt beams with spatially intricate profiles and we have reviewed the generation of holograms designed for amplitude-shaped intensity patterns. We have also seen how a single hologram component and an AOM, can be used to establish a rapid encoding channel for arbitrary spatial modes.

PART II

ART & ATOMS:
THE THEORY AND PRACTISE OF STRUCTURED LIGHT IN ATOMS

ATOMIC STRUCTURE AND THE CREATION OF A HOLOGRAPHIC TRAP

3

Is this a pencil or a sphere? [a]

Although the confusion of physicists between spheres and everday-objects is now a well known phenomenon, the question perhaps loses some of its absurdity when applied to a single atom: the oversimplification now a little too close to home. Atomic interactions however, are strongly spatially dependent, particularly in the quantum realm, and so by failing to ask such questions we lose physical insight into the underlying mechanisms. The question however, is what do we gain by trying to answer them?

[a] This approach to the introduction was inspired by more technical comments made by Wolfgang Ketterle in his OpenCourseWare MIT lectures[61].

Outline

In this chapter, we introduce and define the underlying tools needed for detailed investigation of relevant atomic properties: both theoretical and experimental. We begin by analysing the spatial structure of atoms, highlighting how this relates to both rotation, orbital angular momentum and magnetic field, before studying the mathematics used in later chapters to make theoretical predictions. Following these discussions, we will outline how such properties can be related to laboratory results, before concluding with an overview of the experimental system implemented in practice.

3.1 Atomic Space

To consider an atom's geometric dependence should not be an unusual thing. Assuming a central field, then the separated solution of the hydrogenic Schrödinger equation is

$$\psi_{nlm}(\boldsymbol{r}) = R_{nl}(r)Y_{lm}(\theta,\phi) \tag{3.1}$$

where, n, l and m denote the principal quantum, orbital angular momentum and magnetic quantum numbers respectively and the two functions represent the radial and angular components of the wavefunction. This crucial result however is in many ways well known, but is often less well remembered or is the limit of experimentalists' familiarity with spatial structure. The link between space, angular momentum and magnetic field is often not considered at all. Following the theme of this discourse however, we will take some time to expand on these relationships, before progressing to outline their interaction with semi–classical fields.

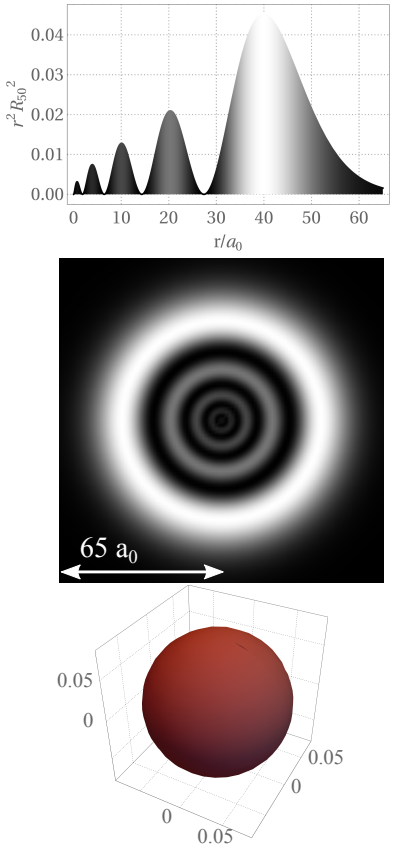

Figure 3.1: The radial and spherical harmonic probability distributions for the $n = 5, l = 0$ Hydrogen wavefunction.

As expounded previously, it is generally the spatial structuring of light that allows us to understand the shape of the world around us, but even when considering a macroscopic object, it can often be difficult to gauge the depth or curvature from one glance. In these incidences, it is rotation which breaks the symmetry. Images can be taken from different angles, such that the object is reconstructed from projections, or even the *shadows* left behind[1]. Rotation itself however, is a macroscopic phenomenon and can fundamentally be defined by a unitary operator:

$$\mathcal{D}[\mathcal{R}_{\underline{\hat{n}}}(d\theta)] \equiv 1 - i\frac{d\theta}{\hbar}\,\hat{\mathrm{O}}\cdot\underline{\hat{n}}, \tag{3.2}$$

where $\mathcal{R}_{\underline{\hat{n}}}(d\theta)$ represents an infinitesimal rotation about the axis $\underline{\hat{n}}$ and $\hat{\mathrm{O}} \in \{\boldsymbol{S}, \boldsymbol{L}, \boldsymbol{J}, \boldsymbol{I}, \boldsymbol{F}\}$ is the angular momentum operator. As the mathematical generator of rotation, clearly any restriction in angular momentum, would affect the system's ability to rotate and thus, the spatial distribution measurable. In this context, the eponymous consequence of quantum mechanics, that angular momentum is discretised, has renewed meaning. The standard m_i rules *e.g.* $m_{\mathrm{L}} = -l, -l+1, \ldots, 0, \ldots, l-1, l$ can be interpreted as the limitations placed on spatial orientation under measurement. Returning to our opening question then, how do we know

1. This process can be cleverly simulated through the use of active projection of structured light [62], but the principle remains the same

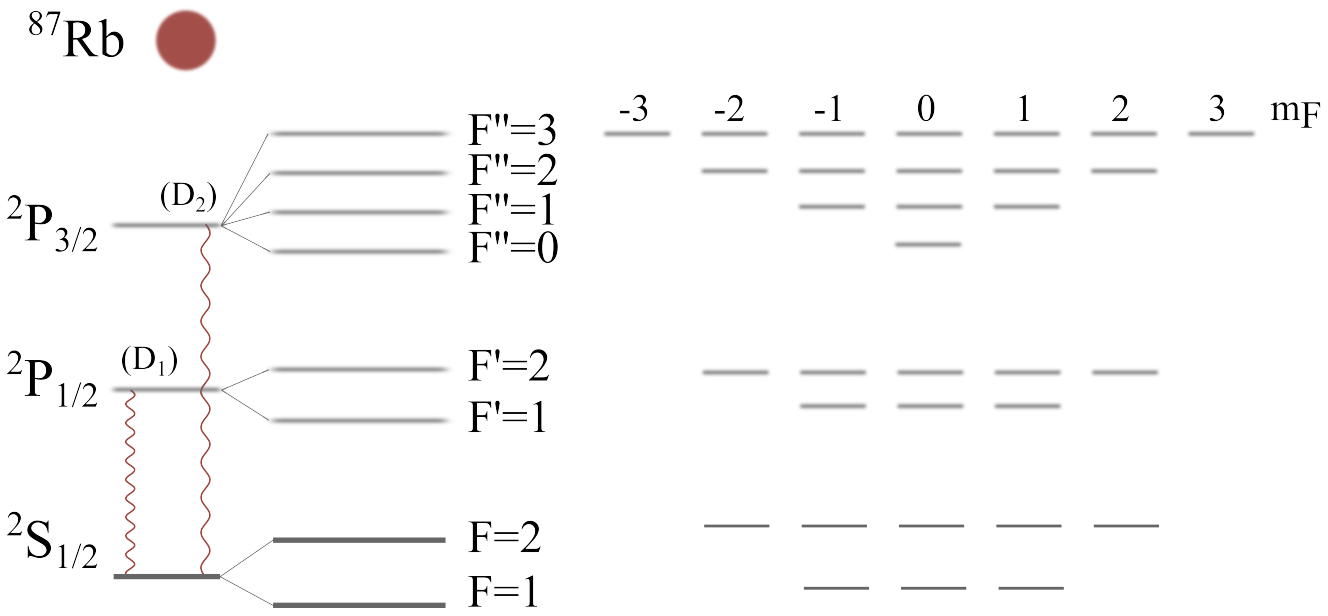

Figure 3.2: An outline of the atomic level scheme for Rubidium-87, where the leftmost levels illustrate the fine structure lines of the D_1 and D_2 transitions, the middle set of levels represent the Hyperfine expansion and the right-most levels denote the possible spatial projections.

if an object is a pencil or a sphere? Well, we can consider its excitation into different angular momentum states. If it has no orbital angular momentum, then we can't know if it's an elongated object; the wave function is completely symmetric and so for the purposes of measurement the object is a sphere. The only way to know, is to localise the object in space with an angular wave packet: itself, a superposition of states with different angular momenta. If the object is a dipole, then we need to be able to rotate it at least twice. If the object is elliptical then we need three angles to measure it. If the angular momentum is restricted therefore, then there is a limit to what we can know and so the distinction between a sphere and a pencil (ellipsoid), may not be possible, but conversely, if we can increase the available angular momentum, then there are more spatial possibilities.

There is a reason however, why the spatial orientation is called the magnetic quantum number.

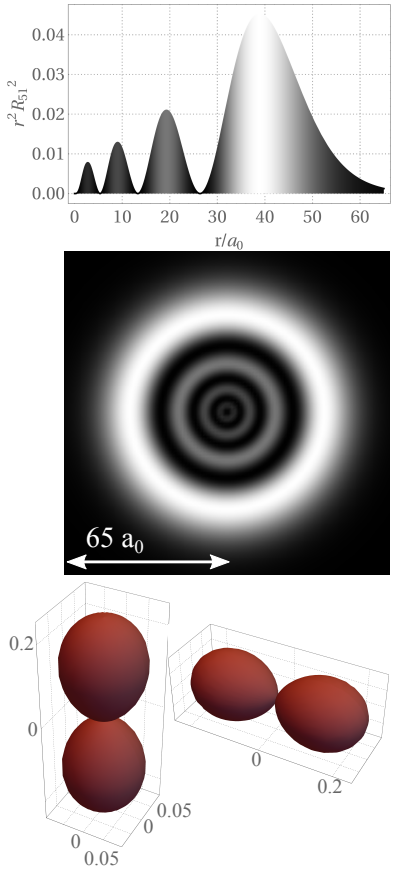

Figure 3.3: The probability distributions for the $n = 5, l = 1$ wavefunction, including each positive orientation.

3.1.1 *Magnetic dipole moment*

The close relationship between magnetic field and angular momentum is fundamental and can be seen implitcitly in Maxwell's

equations. In the absence of magnetic monopoles, it takes a moving charge to produce or to feel a magnetic field. Thus, magnetism requires the motion of electricity and the motion of electricity is in essence, the angular momentum of an electron.

Following the treatment of Griffiths [63], we can effectively describe a magnetic field by introducing the vector potential. Just as with Gauss' law in electrostatics, where $\boldsymbol{\nabla} \times \boldsymbol{E} = 0$ leads to the electrostatic potential $\boldsymbol{E} = -\boldsymbol{\nabla} V$, Gauss' law for magnetostatics, $\boldsymbol{\nabla} \times \boldsymbol{B} = \mu_0 \boldsymbol{j}$, allows us to define the vector potential according to $\boldsymbol{B} = \boldsymbol{\nabla} \times \boldsymbol{A}$ and choosing $\boldsymbol{\nabla} \cdot \boldsymbol{A} = 0$.

Such a choice is known as the *Coulomb gauge*, as is of course only one of infinitely many ways of accounting for the extra degree of freedom of the vector potential. An example of a gauge Taking $\boldsymbol{j}$ to be zero at infinity, we can then write the corresponding vector potential:

$$\boldsymbol{A}(\boldsymbol{r}) = \frac{\mu_0}{4\pi} \int_{\mathcal{V}} \frac{\boldsymbol{j}(\boldsymbol{r'})}{s} d\mathcal{V}, \tag{3.3}$$

where we recall that $\boldsymbol{r'}$ is the position vector of the current source and $s = |\boldsymbol{r} - \boldsymbol{r'}|$ is the distance between the source and the point of observation, $\boldsymbol{r}$.

This can be seen formally from Ampère's law:

$$\begin{aligned} \boldsymbol{\nabla} \times \boldsymbol{B} &= \mu_0 \boldsymbol{j} \\ \therefore \boldsymbol{\nabla} (\boldsymbol{\nabla} \cdot \boldsymbol{A}) - \nabla^2 \boldsymbol{A} &= \mu_0 \boldsymbol{j} \\ \therefore \nabla^2 \boldsymbol{A} &= -\mu_0 \boldsymbol{j} \end{aligned} \tag{3.4}$$

and noticing that this is now just the superposition of three scalar Poisson's equations.

The simplest example of electricity in motion is a single closed loop of constant current I and this can be expressed as

$$\boldsymbol{A}(\boldsymbol{r}) = \frac{\mu_0 I}{4\pi} \oint \frac{1}{s} d\boldsymbol{l'} \tag{3.5}$$

$$= \frac{\mu_0 I}{4\pi} \sum_{n=0}^{\infty} \frac{1}{r^{n+1}} \oint r'^n P_n(\cos\gamma) d\boldsymbol{l'} \tag{3.6}$$

$$= \frac{\mu_0 I}{4\pi} \left[\underbrace{\cancel{\frac{1}{r}\oint d\boldsymbol{l'}}}_{\text{Monopole}} + \underbrace{\frac{1}{r^2}\oint r' \cos\gamma d\boldsymbol{l'}}_{\text{Dipole}} + \underbrace{\frac{1}{r^3}\oint r'^2 \left[\frac{3}{2}\cos^2\gamma - \frac{1}{2}\right] d\boldsymbol{l'}}_{\text{Quadropole}} + \ldots \right]$$

where γ is the angle between the source and observation vectors and we recall that the monopole term must necessarily vanish as $\boldsymbol{\nabla} \cdot \boldsymbol{B} = 0$. The dominant term in this expression is then the dipole contribution:

$$\begin{aligned} \boldsymbol{A}_{\text{dip.}}(\boldsymbol{r}) =& \frac{\mu_0}{4\pi}\frac{1}{r^2} I \oint r' \cos\gamma d\boldsymbol{l'} \qquad (3.7) \\ =& \frac{\mu_0}{4\pi}\frac{1}{r^2} I \oint \left(\underline{\hat{r}} \cdot \boldsymbol{r'}\right) d\boldsymbol{l'} \qquad \text{As } \gamma = \angle r\ \mathcal{O}\ r' \\ =& \frac{\mu_0}{4\pi}\frac{1}{r^2} I \boldsymbol{a'}_{\perp} \times \underline{\hat{r}}, \end{aligned}$$

and therefore,

$$\boldsymbol{A}_{\text{dip.}}(\boldsymbol{r}) = \frac{\mu_0}{4\pi} \left[\frac{\boldsymbol{d}_{\text{B}} \times \underline{\hat{r}}}{r^2}\right]. \tag{3.8}$$

Here, we have defined the magnetic dipole moment:

$$\boldsymbol{d}_{\text{B}} \equiv I \int d\boldsymbol{a} \tag{3.9}$$

such that $\boldsymbol{a}$ is the vector area of the loop, with direction defined by the right-hand rule. In standard spherical coordinates, the dipole field is then

$$\begin{aligned} \boldsymbol{B}_{\text{dip.}}(\boldsymbol{r}) =& \boldsymbol{\nabla} \times \boldsymbol{A} \qquad (3.10) \\ =& \frac{\mu_0}{4\pi} \left(\boldsymbol{\nabla} \times \mathrm{d}_{\text{B}} \frac{\sin\theta}{r^2} \underline{\hat{\phi}}\right) \\ =& \frac{\mu_0}{4\pi} \frac{\mathrm{d}_{\text{B}}}{r^3} \left[2\cos\theta \underline{\hat{r}} + \sin\theta \underline{\hat{\theta}}\right]. \qquad (3.11) \end{aligned}$$

With substitution, the generalised field by for a current loop is then

$$\boldsymbol{B}_{\text{dip.}}(\boldsymbol{r}) = \frac{\mu_0}{4\pi} \frac{1}{r^3} \left[3\left(\boldsymbol{d}_{\text{B}} \cdot \underline{\hat{r}}\right) \underline{\hat{r}} - \boldsymbol{d}_{\text{B}}\right]. \tag{3.12}$$

From Eq. 3.12, the magnetic field of a current loop is completely defined by the geometric distribution of the magnetic dipole moment and this itself is simply the spatial orientation of a current.

Assuming a classical orbit of the electron around a positively charged core at rest, such that the internal magnetic field of the atom is determined by:

$$\begin{aligned} |\boldsymbol{d}_{\mathrm{B}}| &= I a_{\perp} \\ &= \left(e f_{\mathrm{rev}}\right)\left(\pi R^2\right) \\ &= \frac{e}{2M_{\mathrm{e}}} L \end{aligned} \tag{3.13}$$

where R is the radius of the orbit, f_{rev} is the frequency of revolution and L is the orbital angular momentum. Vectorially, this can be expressed concisely as

$$\boldsymbol{d}_{\mathrm{B}} = -\gamma_{\mathrm{gy}} \boldsymbol{L}, \tag{3.14}$$

where $\gamma_{\mathrm{gy}} \equiv \frac{e}{2M_{\mathrm{e}}}$ is the gyromagnetic ratio.

This comes from classical mechanics, where we can recall that the momentum of a gyroscope precesses at a frequency

$$\begin{aligned} \omega &= \frac{v}{R} \\ &= \left[\frac{d\,|\boldsymbol{L}|}{dt}\right]\left[\frac{1}{|\boldsymbol{L}| \sin\theta}\right] \end{aligned} \tag{3.15}$$

In a magnetic field, the torque, τ, on the dipole moment is given by $\tau = |\boldsymbol{d}_{\mathrm{B}} \times \boldsymbol{B}|$ and so we can define the *Larmor frequency*:

$$\Omega_{\mathrm{L}} \equiv \frac{\mathrm{d}_{\mathrm{B}}\, B}{L} = \gamma_{\mathrm{gy}} B. \tag{3.16}$$

With quantised angular momentum however,

$$\mathrm{d}_{\mathrm{B}L} = -d_{\mathrm{Bohr}} \sqrt{l[l+1]} \tag{3.17a}$$

$$(\mathrm{d}_{\mathrm{B}L})_z = -d_{\mathrm{Bohr}} m_{\mathrm{L}} \tag{3.17b}$$

where we have officially introduced the angular momentum projection on the quantisation axis, m_{L}. The classical form has survived with the *Bohr magneton*, d_{Bohr}, equal to $\hbar\, \gamma_{\mathrm{gy}}$.

3.1.2 *Fine structure*

So far, we have tacitly assumed that we are working with a completely isolated set of atomic energy levels and in the non-relativistic limit, such a system can be described by Eq. 3.1(p. 60)

where the energy is completely determined by the principal quantum number. In practice however, this is not the case and even in our experimental semi-classical limit, these predictions are not accurate enough.

The first broad set of corrections to this regime can be found directly from Dirac's relativistic Schrödinger equation and the difference is known as the *fine structure* [2], in homage to its improvement on the Bohr model. Modelling this correction as a perturbation in the non-relativistic results, there are three components: the kinetic energy, Darwin and spin-orbit terms. The kinetic energy correction is a straightforward account of the effects of special relativity, and will not be considered here in any more detail. The Darwin term is an offset that only affects orbitals where $l \neq 0$; it is a result of the electron being in constant oscillation, such that the interaction is *smeared* out over its Compton wavelength [64]. Of most importance to our discussion however, is the spin-orbit interaction.

2. These do not include the Lamb shift [64].

Spin-orbit coupling

The previous subsection outlined how the orbital motion of the electron is intimately related to the magnetic field. In quantum mechanics of course, an electron also has angular momentum due to its spin and this can be written similarly to Eq. 3.17:

$$\mathrm{d}_{\mathrm{B}S} = -\,\mathrm{g}_{\mathrm{S}}\, d_{\mathrm{Bohr}} \sqrt{s[s+1]} \tag{3.18a}$$

$$(\mathrm{d}_{\mathrm{B}S})_z = -\,\mathrm{g}_{\mathrm{S}}\, d_{\mathrm{Bohr}} m_{\mathrm{S}}, \tag{3.18b}$$

where g_{S} is known as the *Landé g-factor* for S. This factor can approximately taken as equal to 2, as again derived from the Dirac equation[3] and suggests that the electron spin is twice as effective as the orbit in generating a dipole moment. Including the effects of spin, the electron now has a total magnetic dipole moment

3. A small correction can be made to this factor using QED, but for our purposes, this is not important.

$$\boldsymbol{d}_{\mathrm{B}e} = -\frac{d_{\mathrm{Bohr}}}{\hbar}\left[\boldsymbol{L} + 2\boldsymbol{S}\right]. \tag{3.19}$$

The orbiting electron then experiences a net motional magnetic field from the interaction of its internally generated dipole with

the moment of rotation. And competing fields come with an energetic cost.

The Zeeman effect

Despite using the word *cost*, the spin-orbit correction is an effect of relative orientation and can either add or subtract from the unperturbed energy [4].

The coupling was first observed in the splitting of spectroscopic lines in the presence of a magnetic field and is also governed by the relative orientation of the vectors: where the perturbation $\hat{H}_Z$ is given by[5]

$$\hat{H}_Z = -\boldsymbol{d}_{B_e} \cdot \boldsymbol{B}_{ext}. \tag{3.20}$$

The form of the theoretical interaction is then dependent on the relative strengths of the couplings, influencing our choice of eigenstate. In the weak-field limit, the coupling of the spin and orbital parts is stronger than their individual couplings to the applied field and, geometrically, it is instructive to consider them as one coupled vector, $\boldsymbol{J} = \boldsymbol{S} + \boldsymbol{L}$, that subsequently couples to the magnetic field as a whole. In the opposite case of a field stronger than their mutual interaction however, then each dipole moment will couple to the field individually: such that the eigenstate is described with both angular momenta. In this work however, we only consider atomic rubidium. As a heavier alkali atom, rubidium has a large fine-structure splitting, of approximately 7 THz [65, 66], and so is well out of the range of any magnetic field we will consider. Such is the case, we will always assume the weak-field limit, unless stated otherwise.

In this limit, our approach to Eq. 3.20 is to find the average dipole moment along the total angular momentum $\boldsymbol{J}$ before considering the ensuing projection along the magnetic field. An average is necessary as the spin g-factor in Eq. 3.19 misaligns the dipole moment from the vector $\boldsymbol{J}$. The component parallel to $\boldsymbol{J}$ is well defined by the precession however, which cancels out the perpendicular term. This can be expressed more generally by the

4. This is in contrast to the kinetic energy and Darwin terms, which are always negative and positive respectively.

5. Here, we use a sign convention consistent with our choice of positive Landé factor, to ensure that the magnetic moment is directed anti-parallel to the angular momentum.

Wigner-Eckart projection theorem applied to $\boldsymbol{J}$:

$$\begin{aligned} \left\langle J, m_J \right| \hat{\mathbb{O}} \left| J, m_J \right\rangle &= c \left\langle J, m_J \right| \boldsymbol{J} \left| J, m_J \right\rangle \\ \implies c &= \frac{\left\langle J, m_J \right| \hat{\mathbb{O}} \cdot \boldsymbol{J} \left| J, m_J \right\rangle}{\left\langle J, m_J \right| \boldsymbol{J} \cdot \boldsymbol{J} \left| J, m_J \right\rangle} \end{aligned} \tag{3.21}$$

$$\therefore \ \left\langle J, m_J \right| \hat{\mathbb{O}} \left| J, m_J \right\rangle = \frac{\left\langle J, m_J \right| \hat{\mathbb{O}} \cdot \boldsymbol{J} \left| J, m_J \right\rangle}{\left\langle J, m_J \right| \boldsymbol{J^2} \left| J, m_J \right\rangle} \left\langle J, m_J \right| \boldsymbol{J} \left| J, m_J \right\rangle \tag{3.22}$$

where $\hat{\mathbb{O}}$ is an arbitrary vector operator, c is an arbitrary constant and $\boldsymbol{J}$ is conserved[6].

With this result, the Hamiltonian can be calculated according to

$$\begin{aligned} \hat{H}_{\mathrm{ZJ}} &= -\frac{\left\langle J, m_J \right| \boldsymbol{d}_{\mathrm{B}e} \cdot \boldsymbol{J} \left| J, m_J \right\rangle}{J\left[J+1\right]} \boldsymbol{J} \cdot \boldsymbol{B}_{\mathrm{ext}} \\ &= -\frac{\left\langle J, m_J \right| \boldsymbol{L} \cdot \boldsymbol{J} \left| J, m_J \right\rangle + 2 \left\langle J, m_J \right| \boldsymbol{S} \cdot \boldsymbol{J} \left| J, m_J \right\rangle}{J\left[J+1\right]} d_{\mathrm{Bohr}} \boldsymbol{J} \cdot \boldsymbol{B}_{\mathrm{ext}}. \end{aligned} \tag{3.23}$$

As the fraction on the left is just a number however, we can use this to define the Landé g-factor for $\boldsymbol{J}$, such that

$$\mathrm{g_J} = \frac{3}{2} + \frac{S\left[S+1\right] - L\left[L+1\right]}{2J\left[J+1\right]} \tag{3.24}$$

as derived from the vector relation[7] $\boldsymbol{v}_1 \cdot \boldsymbol{v}_2 = \frac{1}{2}\left[\boldsymbol{v}_3^2 - \boldsymbol{v}_1^2 - \boldsymbol{v}_2^2\right]$.

The shift in energy associated with the Zeeman effect can then be written as

$$\hat{H}_{\mathrm{ZJ}} = d_{\mathrm{Bohr}}\, \mathrm{g_J}\, \boldsymbol{J} \cdot \boldsymbol{B}_{\mathrm{ext}}, \tag{3.25}$$

such that the atomic energy states are split into eigenstates of $\boldsymbol{J}$. Further perturbations however, can change the situation, such that J is no longer degenerate in the other angular momenta. The vacuum effects described by QED is one such perturbation and is known as the *Lamb* shift. This shift only affects the spin-state however; if we consider the magnetic dipole moment of the nucleus, then we have to consider even more coupling.

6. This projection result is actually equivalent to the classical vector model in the case of diagonal matrix elements [64]. In this case it is the coherence that distinguishes the quantum realm.

7. ($\boldsymbol{v}_3 = \boldsymbol{v}_1 + \boldsymbol{v}_2$)

3.1.3 Hyperfine Structure

The final layer of structure that we will consider, is the *Hyperfine* level scheme. This refinement is a result of the magnetic

dipole moment of the nucleus $\mathrm{d}_{\mathrm{B}N}$, which varies with different isotopes. The total atomic magnetic moment is then the sum of the electronic and nuclear moments:

$$\begin{aligned} \boldsymbol{d}_{\mathrm{Btot}} &= -\,\mathrm{g_J}\, d_{\mathrm{Bohr}} \boldsymbol{J} + \mathrm{g_I}\, \mathrm{d}_{\mathrm{B}N}\, \boldsymbol{I} \\ &\simeq -\,\mathrm{g_J}\, d_{\mathrm{Bohr}} \boldsymbol{J} \end{aligned} \tag{3.26}$$

as $\mathrm{d}_{\mathrm{B}N} \ll d_{\mathrm{Bohr}}$[8] and where $\boldsymbol{I}$ represents the nuclear spin.

As $\boldsymbol{I}$ has a negligible contribution to the total dipole, it can be assumed that the magnetic interaction energy is solely dependent on $\boldsymbol{J}$. The inter-momentum coupling however is significant and carries interaction energy [9] $A\boldsymbol{I}\cdot\boldsymbol{J}$, where A_{HF} is the species and level-dependent hyperfine constant [10] [64]. In analogy to strong spin-orbit coupling, we then introduce a new momentum,

$$\boldsymbol{F} \equiv \boldsymbol{J} + \boldsymbol{I}. \tag{3.27}$$

The Zeeman effect can then be described in the hyperfine weak-field limit, where the interaction with an external field $\boldsymbol{B}$ is weaker than the hyperfine interaction, following the same reasoning of the previous subsection.

The effective Hamiltonian in this limit is then:

$$\begin{aligned} \hat{H}_{\mathrm{ZF}} &= \mathrm{g_J}\, d_{\mathrm{Bohr}} \frac{\langle F, m_F | \, \boldsymbol{J}\cdot\boldsymbol{F} \, | F, m_F \rangle}{F\,(F+1)} \boldsymbol{F}\cdot\boldsymbol{B} \\ &= \mathrm{g_J}\, d_{\mathrm{Bohr}} \frac{F\,[F+1] + J\,[J+1] - I\,[I+1]}{2F\,[F+1]} \boldsymbol{F}\cdot\boldsymbol{B}. \end{aligned} \tag{3.28}$$

Which of course can be written with an appropriate Landé factor as

$$\hat{H}_{\mathrm{ZF}} = g_F d_{\mathrm{Bohr}} \boldsymbol{F}\cdot\boldsymbol{B}. \tag{3.29}$$

As we hope to evaluate this expression explicitly, finding the Hamiltonian is reduced to the task of finding an expression for $\boldsymbol{F}\cdot\boldsymbol{B}$. Using the angular momentum operators in spherical polar coordinates for quantisation in $\hat{z}$, we can write:

8. For context, the nuclear moment is given by $\mathrm{d}_{\mathrm{B}N} = d_{\mathrm{Bohr}} \frac{M_{\mathrm{e}}}{M_{\mathrm{P}}} \simeq \frac{d_{\mathrm{Bohr}}}{1836}$ [64].

9. (In the magnetic dipole approximation.)

10. With units of h Hz.

$$
\begin{aligned}
\boldsymbol{F}\cdot\boldsymbol{B} &= F_{\mathrm{x}}B_x + F_{\mathrm{y}}B_y + F_{\mathrm{z}}B_z \\
&= \hbar B\left(\frac{1}{\sqrt{2}}\begin{pmatrix}0&1&0\\1&0&1\\0&1&0\end{pmatrix}\sin\theta\cos\phi + \frac{1}{\sqrt{2}}\,i\begin{pmatrix}0&-1&0\\1&0&-1\\0&1&0\end{pmatrix}\sin\theta\sin\phi\right. \\
&\qquad \left. + \begin{pmatrix}1&0&0\\0&0&0\\0&0&-1\end{pmatrix}\cos\theta\right) \\
&= \hbar B\begin{pmatrix}\cos\theta & \frac{1}{\sqrt{2}}\sin\theta e^{-i\phi} & 0\\ \frac{1}{\sqrt{2}}\sin\theta e^{i\phi} & 0 & \frac{1}{\sqrt{2}}\sin\theta e^{-i\phi}\\ 0 & \frac{1}{\sqrt{2}}\sin\theta e^{i\phi} & -\cos\theta\end{pmatrix},
\end{aligned}
\tag{3.30}
$$

such that the final perturbation is

$$
\hat{H}_{\mathrm{ZF}} = g_F d_{\mathrm{Bohr}}\hbar B\begin{pmatrix}\cos\theta & \frac{1}{\sqrt{2}}\sin\theta e^{-i\phi} & 0\\ \frac{1}{\sqrt{2}}\sin\theta e^{i\phi} & 0 & \frac{1}{\sqrt{2}}\sin\theta e^{-i\phi}\\ 0 & \frac{1}{\sqrt{2}}\sin\theta e^{i\phi} & -\cos\theta\end{pmatrix}. \tag{3.31}
$$

The weakness of the nuclear interaction however, makes the coupling of $\boldsymbol{J}$ and $\boldsymbol{I}$ much finer than that of $\boldsymbol{S}$ and $\boldsymbol{L}$: and so maintaining the weak-field limit requires much smaller magnetic fields. As we will be dealing exclusively with the $5^2S_{1/2}$ and $5^2P_{3/2}$ levels of ^{87}Rb however, the ground and excited state values of A_{HF} are approximately $h \times 3.4\,\mathrm{GHz}$ and $h \times 85\,\mathrm{MHz}$ respectively [65]. The interaction energies, Bd_{Bohr}, equal to these values correspond to external field strengths of approximately 5000 G and 60 G respectively. As our discussion will only consider fields less than ten Gauss, then we are safely within the weak-field regime and F remains a good quantum number.

3.2 A Semi–classical Model of Atom-Light Interaction

We now consider the underlying principles and mathematical tools behind our model of atomic state interaction. Here, we assume that the electric dipole coupling is the only driver of light interaction and that in contrast to the magentic fields con-

sidered previously, the coupling can be modelled entirely classically. We will first trace an appropriate set of operator definitions and terminology before proceeding in application to explore the physical observables. Although the initial considerations present illustrative examples for the case of a two-level atom, it is hoped that it is clear the concepts highlighted are introduced without loss of generality, unless stated otherwise.

3.2.1 *Foundations*

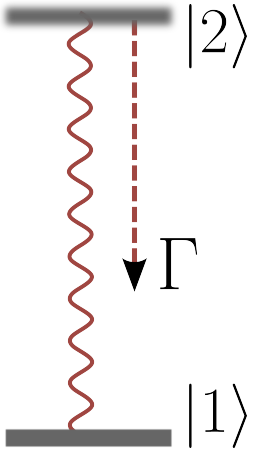

Figure 3.4: A schematic diagram of an atom with two available states of energy where: $\hat{H}_0|i\rangle = U_i|i\rangle$ and Γ is the rate of spontaneous decay from the excited to the ground state.

We begin by considering a two-level model of an atom in which there are two available energy states: the ground state $|1\rangle$ and the excited state $|2\rangle$. These states have a corresponding difference in their associated eigenvalues: $\hbar\omega_{\Delta E} = U_2 - U_1 = \hbar\omega_0$ and are illuminated with a classical light field as demonstrated in Figure 3.4. Throughout this section we operate under the assumption that all applied fields are monochromatic, linearly polarised and that the light can be appropriately modelled as interacting with an individual atom: a physically sensible regime for polarised laser-light applied to a dilute gas.

Let $|i\rangle\langle j|$ be an operator that removes an electron from level j and creates an electron in level i respectively. From this we note that $\hat{\mathbb{I}}$ is $\sum_i |i\rangle\langle i|$ such that:

$$\left(\sum_i |i\rangle\langle i|\right)|\psi(t)\rangle = \Big(|1\rangle\langle 1| + |2\rangle\langle 2|\Big)\Big(\alpha_1(t)|1\rangle + \alpha_2(t)|2\rangle\Big) \tag{3.32}$$

$$\begin{aligned} &= \alpha_1(t)|1\rangle + \alpha_2(t)|2\rangle \\ &= |\psi(t)\rangle \\ &= \hat{\mathbb{I}}|\psi(t)\rangle \end{aligned}$$

where $\alpha_i(t)$ are the probability amplitudes, $|\psi(t)\rangle$represents an arbitrary two-level system and the wave functions are normalised conventionally.

We can now usefully re-express the Hamiltonian by applying

$\hat{\mathbb{I}}$ to both sides:

$$\begin{aligned}\hat{H}_0 &= \left(\sum_i |i\rangle\langle i|\right) \hat{H}_0 \left(\sum_j |j\rangle\langle j|\right) \\ &= \sum_i \sum_j |i\rangle U_{\mathrm{j}} \delta_{ij} \langle j| \\ &= \sum_i U_{\mathrm{i}} |i\rangle\langle i|\end{aligned} \tag{3.33}$$

where δ_{ij} is the Kronecker delta and we recall that $\langle i | \hat{H}_0 | j \rangle = U_{\mathrm{j}} \delta_{ij}$ is the expectation value of the foundational atomic Hamiltonian. Therefore, for our two-level system:

$$\hat{H}_0 = U_1 |1\rangle\langle 1| + U_2 |2\rangle\langle 2|. \tag{3.34}$$

For the uninitiated, this is indeed a powerful result as it suggests that we do not always need to know the form of the operator, but rather only the possible energy eigenvalues, which in principle could be measured by experiment.

3.2.2 *The light-matter interaction*

Having considered the atomic Hamiltonian, we can introduce the substance of the topic at hand. Within our semi-classical approximation, we consider the application of a Maxwellian electric field, $\boldsymbol{E}$, which creates a dipole consisting of two point charges of equal magnitude, q, and opposite sign.

Such an arrangement will naturally produce a torque that aligns with the field, similarly to the case of the magnetic dipole, and this satisfies $\boldsymbol{\tau} = \boldsymbol{d}_{\mathrm{E}} \times \boldsymbol{E}$, where we recall that $\boldsymbol{d}_{\mathrm{E}} = q\,\boldsymbol{r}_{\mathrm{d}}$ is the electric dipole moment and $\boldsymbol{r}_{\mathrm{d}}$ is defined as the displacement from the negative to the positive charge. The interaction energy, or potential energy U of the interaction, can then be calculated by considering the work done on the system:

$$\begin{aligned}U_\Delta &= \int_{\theta_i}^{\theta_f} \tau \, d\theta \\ &= \mathrm{d}_{\mathrm{E}}\, \mathcal{E} \left[\cos\theta_i - \cos\theta_f\right]\end{aligned} \tag{3.35}$$

where $U_\Delta = U_{\mathrm{f}} - U_{\mathrm{i}}$.

Consequently, the interaction energy can be written as

$$\hat{H}_{\mathrm{d_E}} = -\boldsymbol{d}_{\mathrm{E}} \cdot \boldsymbol{E}, \tag{3.36}$$

which is the electrical analogue of the magnetic relationship used throughout the previous section.

3.2.3 *The Rabi frequency*

The interaction Hamiltonian can then be expanded in a similar fashion to that of our atomic Hamiltonian.

$$\hat{H}_{\mathrm{d_E}} = \left(\sum_i |i\rangle\langle i|\right) \hat{H}_{\mathrm{d_E}} \left(\sum_j |j\rangle\langle j|\right) \tag{3.37}$$

$$\begin{aligned} &= |1\rangle \langle 1| \hat{H}_{\mathrm{d_E}} |1\rangle \langle 1| + |1\rangle \langle 1| \hat{H}_{\mathrm{d_E}} |2\rangle \langle 2| \\ &\quad + |2\rangle \langle 2| \hat{H}_{\mathrm{d_E}} |1\rangle \langle 1| + |2\rangle \langle 2| \hat{H}_{\mathrm{d_E}} |2\rangle \langle 2| \end{aligned} \tag{3.38}$$

Naturally, we can no longer express the Hamiltonian of the system with reference only to the energy level values. We can however, exclude the $\langle i| \hat{H}_{\mathrm{d_E}} |i\rangle$ terms as $\hat{H}_{\mathrm{d_E}}$ has the odd parity of the dipole moment: leading to a symmetric integration over an odd function. This leaves the two off-diagonal terms:

$$\begin{aligned} &\langle 1| \hat{H}_{\mathrm{d_E}} |2\rangle = \mathcal{E} \langle 1| \underline{\hat{e}} \cdot \boldsymbol{d}_{\mathrm{E}} |2\rangle \cos \omega t \text{ and} \\ &\langle 2| \hat{H}_{\mathrm{d_E}} |1\rangle = \langle 1| \hat{H}_{\mathrm{d_E}} |2\rangle^* \end{aligned} \tag{3.39}$$

for incident field $\boldsymbol{E} = \mathcal{E} \cos \omega t \underline{\hat{e}}$. These equations can be expressed much more concisely:

$$\begin{aligned} &\langle 1| \hat{H}_{\mathrm{d_E}} |2\rangle = -\hbar \Omega_{\mathrm{R}} \cos \omega t \\ &\langle 2| \hat{H}_{\mathrm{d_E}} |1\rangle = -\hbar \Omega_{\mathrm{R}}^* \cos \omega t \end{aligned} \tag{3.40}$$

where Ω_{R} is defined for this toy two level system as:

$$\Omega_{\mathrm{R}} = \frac{1}{\hbar} \mathcal{E} \langle 1| \underline{\hat{e}} \cdot \boldsymbol{d}_{\mathrm{E}} |2\rangle \tag{3.41}$$

and is known as the *Rabi Frequency*. This is analogous to the magnetic frequency introduced previously, but whereas the Larmor frequency is a measure of precession of the atomic angular momenta around the magnetic field axis, the Rabi frequency represents the oscillation frequency of the state populations. The rate is governed by the dipole moment and, for a real system, is subject to angular momentum constraints. Any transition

with a non-zero transition dipole moment integral is known as *electric-dipole allowed*, to which we will limit our discussions.

3.2.4 *Rotating wave approximation*

To describe the interacting system as a whole, we must of course consider the Schrödinger equation:

$$i\hbar\frac{\partial}{\partial t}|\psi\rangle = \left[\hat{H}_0 + \hat{H}_{\mathrm{d_E}}\right]|\psi\rangle \tag{3.42}$$

with symbols defined as previously. Our system can then be written as:

$$i\hbar\begin{pmatrix}\dot{\alpha}_1|1\rangle\\ \dot{\alpha}_2|2\rangle\end{pmatrix} = \hbar\begin{pmatrix}\omega_1 & -\Omega_{\mathrm{R}}\cos\omega t\\ -\Omega_{\mathrm{R}}\cos\omega t & \omega_2\end{pmatrix}\begin{pmatrix}\alpha_1|1\rangle\\ \alpha_2|2\rangle\end{pmatrix} \tag{3.43}$$

where $\dot{\alpha}_i$ represents the partial time derivative of the probability amplitude associated with state $|i\rangle$ and $U_{\mathrm{i}} = \hbar\omega_{\mathrm{i}}\ \forall i \in\{1,2\}$.

Such a system has an explicit time dependence in the Hamiltonian, but this can be removed using an important physical simplification known as the *rotating-wave approximation*. This follows from the recognition that the Euler expansion of an oscillation is a sum of oppositely signed frequencies that contribute unevenly to the interaction and the following mathematical analysis follows the example of Auzinsh *et al.* [67]. If we consider a unitary transformation[11] that follows one frequency in time, then the remaining term will be too off-resonant to contribute meaningfully to the interaction. Mathematically, we define an effective Hamiltonian by

$$\hat{H}_{\mathrm{eff}} = \hat{U}^{*T}\hat{H}\hat{U} - i\hbar\hat{U}^{*T}\frac{\partial}{\partial t}\hat{U}, \tag{3.44}$$

where $\hat{U}$ is not to be confused with the energy of the system. Although the first term is the standard form of the unitary transformation, we include the second term to avoid changes to the Schrödinger equation [12]. If we consider the transformation defined by

$$\hat{U} = \begin{pmatrix}1 & 0\\ 0 & e^{-i\omega t}\end{pmatrix}, \tag{3.45}$$

11. This is a bijective transformation that only changes the representation of an operator *i.e.* a change of form rather than function.

12. This accounts for the non-inertial nature of the transformation, similarly to the extra terms introduced in a classically accelerating frame.

then the Hamiltonian can be re-expressed as

$$\hat{H} = \hbar \begin{pmatrix} \omega_1 & -\frac{1}{2}\Omega_{\mathrm{R}}\left[1+e^{-2i\omega t}\right] \\ -\frac{1}{2}\Omega_{\mathrm{R}}\left[1+e^{2i\omega t}\right] & \omega_2 - \omega \end{pmatrix}. \tag{3.46}$$

The ground state energy can be defined to zero without loss of generality and this means the system degeneracy is determined by the level of detuning between the applied field and the excited state. For nearly resonant light, the interaction is then composed of a constant contribution at half the Rabi-frequency and a largely detuned contribution oscillating in time. If ω is much greater than the line width of the transition, then these terms can be ignored: removing the time dependence of the Hamiltonian [13].

13. The factor of a half in the final result has a physical interpretation: highlighting that half of the interaction energy has been removed.

3.2.5 *The density operator*

Another important mathematical tool is the *density operator*, which can be considered a generalisation of the wave function to describe a statistical ensemble of several quantum states *i.e.*

$(p_i \geq 0; \sum_i p_i = 1)$

$$\hat{\rho} \equiv \sum_i p_i |\psi_i\rangle\langle\psi_i|. \tag{3.47}$$

Here, p is the relative probability of finding the system in a state $|i\rangle$, such that $\hat{\rho}$ can be used to describe both *mixed* and *pure* states. In practice, the density operator provides a concise means of calculating the expectation values of the system and will prove essential in nearly all of the more in-depth analysis that will follow. For a cloud of non-interacting atoms, the system can be described by

$$\hat{\rho} = \frac{1}{N_{\mathrm{a}}} \sum_{i=1}^{N_{\mathrm{a}}} |\psi_i\rangle\langle\psi_i| \tag{3.48}$$

where N_{a} is the total number of atoms and ψ_i represents an individual atomic wave function. The expectation value of any

operator on an atomic vapour can then be described by

$$\begin{aligned}\overline{\langle \psi_i | \hat{\mathrm{O}} | \psi_i \rangle} &= \frac{1}{N_\mathrm{a}} \sum_{i=1}^{N_\mathrm{a}} \langle \psi_i | \hat{\mathrm{O}} | \psi_i \rangle \\ &= \sum_n \frac{1}{N_\mathrm{a}} \sum_{i=1}^{N_\mathrm{a}} \langle n | \psi_i \rangle \langle \psi_i | \hat{\mathrm{O}} | n \rangle \\ &= \sum_n \langle n | \left[\frac{1}{N_\mathrm{a}} \sum_{i=1}^{N_\mathrm{a}} |\psi_i\rangle\langle\psi_i| \right] \hat{\mathrm{O}} | n \rangle\end{aligned} \tag{3.49}$$

where we have used the completeness theorem to expand the system in an arbitrary set of basis states. Therefore,

$$\overline{\langle \psi_i | \hat{\mathrm{O}} | \psi_i \rangle} = \mathrm{Tr}\left(\rho \hat{\mathrm{O}}\right), \tag{3.50}$$

where Tr is the trace operator and the expectation value of any observable is then the trace of the density matrix multiplied by the observable's operator. Simply using the product rule, the density matrix then provides a very useful form for the Heisenberg equation:

$$i\hbar \frac{\partial}{\partial t}\rho = \hat{H}_\mathrm{I}|\psi\rangle\langle\psi| - |\psi\rangle\langle\psi|\hat{H}_\mathrm{I} \tag{3.51}$$

or rather:

$$i\hbar \frac{\partial}{\partial t}\rho = \left[\hat{H}_\mathrm{I}, \rho\right] \tag{3.52}$$

where $[\cdots, \cdots]$ denotes the commutator relation. The diagonal elements, ρ_{ii}, of the resulting density *matrix* can be interpreted as the *populations* or probabilities of occupation of the associated states $|i\rangle$ and the off-diagonal terms, $\rho_{ij} : i \neq j$, represent the *coherences*.

3.2.6 The Master Equation in the Lindblad Form

So far in our exposition, we have considered the hamiltonian of an atom and its interaction with a light field: which stimulates transitions between the possible states. We have not however, considered or included the possibility of spontaneous transition between states due to relaxation: an undoubtedly familiar concept which will play a crucial role in our later analysis. Therefore, we proceed by demonstrating how such considerations can be rigorously implemented in our model.

When considering any system within the realms of quantum mechanics; we must concede, whether or not we share Planck's distaste, the loss of the concept of a truly closed system. This follows naturally from the uncertainty relation: a principle which hightlights that even held within a vacuum, there is the possibility of energy fluctuations and thus, physical interactions are possible. Naturally, such problems complicate the matter, but an evidentially justified descriptive simplification comes in the form of the *Markov Approximation* [68]. Such a regime makes the assumption that although any system will be coupled to its surroundings, it is generally the case that the environment fluctuation is so transient, that the correlation is made before any other event takes place in the system. Consequently, the relaxations can be modelled as only depending on the system properties:

$$\frac{\partial}{\partial t}\hat{\rho} = -\frac{i}{\hbar}\left[\hat{H}_{\mathrm{I}}, \hat{\rho}\right] + \Lambda\hat{\rho} \tag{3.53}$$

where Λ is a linear operator to be determined. Using the Stenholm approach [69], as outlined in discussion with Professor Oppo of Strathclyde university, then the system can be described by

$$\frac{\partial}{\partial t}\rho = -\frac{i}{\hbar}\left[\hat{H}_{\mathrm{I}}, \rho\right] + \sum_{i,j}\lambda_{ij}|j\rangle\langle i|\rho|i\rangle\langle j| - \frac{1}{2}\sum_{i,j}\lambda_{ij}|i\rangle\langle i|\rho - \frac{1}{2}\rho\sum_{i,j}\lambda_{i,j}|i\rangle\langle i| \tag{3.54}$$

which is the *master equation* in the Lindblad Form. This equation allows every possible form of interaction, but for our purposes we only want to consider a system with spontaneous decay from the excited to the ground state and *transit* decay from every state: representing the rate that atoms leave the beam path. If we then also assume that for every atom that has decayed from the beam path, another takes its place, Eq. 3.54 simplifies to

$$\frac{\partial}{\partial t}\rho = -\frac{i}{\hbar}\left[\hat{H}_{\mathrm{I}}, \hat{\rho}\right] - \frac{1}{2}\left[\hat{\Gamma}\hat{\rho} + \hat{\rho}\hat{\Gamma}\right] + \hat{\Lambda}, \tag{3.55}$$

where $\hat{\Gamma} = \gamma|g\rangle\langle g| + [\gamma + \Gamma]\,|e\rangle\langle e|$ and $\hat{\Lambda}$ now describes the repopulation: $\Lambda = \frac{1}{N_g}\left[\gamma + \Gamma\rho_{e,e}\right]|g\rangle\langle g|$ for all ground states g and excited states e, where N_g is the number of ground states available to the excited state through selection rules.

The density matrix is therefore central to a modern description of atomic systems, but its domain and interpretation are equally complex. For our purposes however, there is a way of visualising its content in one there-dimensional plot.

This can be seen by the following considerations, where $\hat{a}_i^\dagger \hat{a}_j = |i\rangle\langle j|$ for conciseness. The starting point is to consider the most general linear transformation involving our hermitian operator $\left(\hat{a}_j^\dagger \hat{a}_i\right)^\dagger$:

$$\Lambda\rho = c\rho + \hat{B}\rho + \rho\hat{C} + \sum_{i,j} \lambda_{ij} \hat{a}_j^\dagger \hat{a}_i \rho \hat{a}_i^\dagger \hat{a}_j \tag{3.56}$$

where c is a complex number, and $\hat{B}$ and $\hat{C}$ are operators. If we are considering all of the possible energy levels, then the trace: $\mathrm{Tr}\,(\rho) = 1$.
Therefore from (3.53) and (3.56):

$$\frac{\partial}{\partial t}\mathrm{Tr}\,(\rho(t)) = \mathrm{Tr}\left(-\frac{i}{\hbar}\left[\hat{H}_\mathrm{I}, \rho\right]\right) + \mathrm{Tr}\left(c\rho + \hat{B}\rho + \rho\hat{C} + \sum_{i,j} \lambda_{ij} \hat{a}_j^\dagger \hat{a}_i \rho \hat{a}_i^\dagger \hat{a}_j\right) = 0 \tag{3.57}$$

To continue further, we make use of the fact that the density matrix is self-adjoint:

$$\begin{aligned}\frac{\partial}{\partial t}\rho^\dagger &= \left(-\frac{i}{\hbar}\left[\hat{H}_\mathrm{I}, \rho\right]\right)^\dagger + (\Lambda\rho(t))^\dagger \\ &= \frac{i}{\hbar}\left(\rho^\dagger \hat{H}_\mathrm{I}^\dagger - \hat{H}_\mathrm{I}^\dagger \rho^\dagger\right) + (\Lambda\rho(t))^\dagger \\ &= -\frac{i}{\hbar}\left[\hat{H}_\mathrm{I}, \rho\right] + (\Lambda\rho(t))^\dagger\end{aligned} \tag{3.58}$$

where we recall the standard properties of the adjoint: $(xy)^\dagger = y^\dagger x^\dagger$ and $(x^\dagger)^\dagger = x$.
Therefore, from (3.53) and the hermitian nature of the density matrix:

$$(\Lambda\rho(t))^\dagger = c^*\rho + \rho\hat{B}^\dagger + \hat{C}^\dagger\rho + \sum_{i,j} \lambda_{ij} \left(\hat{a}_i^\dagger \hat{a}_j\right)^\dagger \rho \left(\hat{a}_j^\dagger \hat{a}_i\right)^\dagger = \Lambda\rho(t) \tag{3.59}$$

which, in conjunction with (3.56), implies some very useful results. Although it is strictly not necessary, it implies that $\lambda^* = \lambda$ i.e. that λ is real, but crucially: we have the implication that the operators are both hermitian and identical and that c is real.
Returning to (3.57), substituting for $\hat{B} = \hat{C}$ and using the distributive property of the trace operator, we have:

$$\begin{aligned}-\frac{i}{\hbar}\mathrm{Tr}\left[\hat{H}_\mathrm{I}\rho - \rho\hat{H}_\mathrm{I}\right] + \mathrm{Tr}\left[c\rho + \hat{B}\rho + \rho\hat{B} + \sum_{ij} \lambda_{ij} \hat{a}_j^\dagger \hat{a}_i \rho \hat{a}_i^\dagger \hat{a}_j\right] &= 0 \\ \implies \mathrm{Tr}\left[\rho\left(c + 2\hat{B} + \sum_{i,j} \lambda_{ij} \hat{a}_i^\dagger \hat{a}_j \hat{a}_j^\dagger \hat{a}_i\right)\right] &= 0\end{aligned} \tag{3.60}$$

where the second line is obtained by using the cyclic rule of the trace operator. This implies that $\hat{B} = -\frac{1}{2}\sum_{ij} \lambda_{ij} \hat{a}_i^\dagger \hat{a}_i - \frac{c}{2}$ and thus, a final substitution yields the result.

3.2.7 *Visualising Atomic Polarisation*

From the birth of quantum mechanics, energy level diagrams have traditionally provided much needed insight into an atom's electronic structure, but their less than three-dimensional nature is a fundamental limitation. Auzinsh, Rochester and Budker however, have introduced an artful visualisation tool that can illustrate the full ground state coherences of an atomic density matrix across all of space [70, 71] and this will prove a concise way of expressing the properties of our atomic systems. The following outline is a brief summary of the introduction to these *angular momentum probability surfaces* given in chapter 5 of *Optically Polarized Atoms* [67].

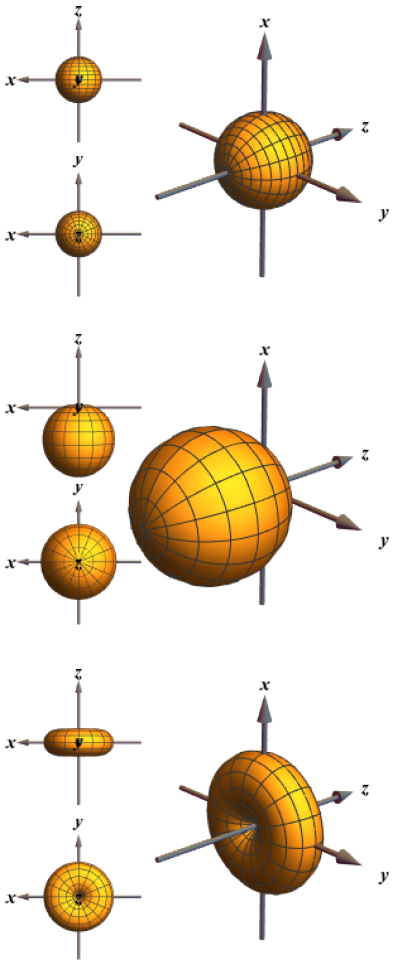

Figure 3.5: Examples of the angular momentum probability surfaces for a normalised F=1 ground state in the case of $\rho_{-1,-1}$=$\rho_{0,0}$=$\rho_{+1,+1}$=1/3 (top), $\rho_{+1,+1} = 1$ (centre) and $\rho_{0,0} = 1$ (bottom).

Overview

From our usual notion of quantised angular momentum, the spatial constraint is perhaps understandable. In general, the maximum information that we can have is one projection of the electron's angular momentum, $m_F\hbar$, and when compared to the magnitude of the total momentum $\sqrt{F(F+1)}\hbar$, the uncertainty principle ensures that it is always less: a testament to the idea that the whole is greater than the sum of its parts. With a density matrix however, the expectation value of obtaining a projection m_F is given by $\rho_{m_F,m_F} = \langle F, m_F | \hat{\rho} | F, m_F \rangle$, where the quantisation axis is often implicitly assumed to be along the axis of light propagation. Experimentally, there is usually good reason to assume a static quantisation axis, but theoretically, we are free to choose. The insight of Auzinsh *et al.* is that the probability of measuring the *maximum* possible angular momentum projection $m_F = F$ can be used as a characterisation of any particular quantisation axis. A three-dimensional probability distribution can then be created by rotating the quantisation axis around the origin for all azimuthal and polar angles and performing the same calculation: where the distance between the surface and the origin represents the probability.

Calculation

Mathematically, the state vector with quantisation axis defined by (ϕ, θ) can then be expressed by

$$\begin{aligned} |F, m_F, (\phi, \theta)\rangle =& \mathcal{D}(\phi, \theta, 0)|F, F\rangle \\ =& \sum_{m'_F} D^{(F)}_{m'_F, F}(\phi, \theta, 0)|F, m'_F\rangle \end{aligned} \tag{3.61}$$

where $\mathcal{D}(\alpha, \beta, \gamma) = e^{-iF_z\frac{\alpha}{\hbar}} e^{-iF_y\frac{\beta}{\hbar}} e^{-iF_z\frac{\gamma}{\hbar}}$ is the general quantum mechanical rotation in terms of the Euler angles and the total angular momentum and

$$D^{(F)}_{m'_F, m_F}(\alpha, \beta, \gamma) = \left\langle F, m'_F \right| \mathcal{D}_{\underline{\hat{z}}}(\alpha)\mathcal{D}_{\underline{\hat{y}}}(\beta)\mathcal{D}_{\underline{\hat{z}}}(\gamma) \left| F, m_F \right\rangle \tag{3.62}$$

are the explicit matrix elements of the quantum-mechanical rotation operators in the Zeeman basis, known as the *Wigner D-functions*.

The probability of finding the maximum projection of angular momentum along the (θ, ϕ) direction is then given by

$$\rho_{F,F}(\theta, \phi) = \sum_{m,m'} D^{(F)*T}_{m,F}(\phi, \theta, 0)\rho_{m,m'} D^{(F)}_{m',F}(\phi, \theta, 0), \tag{3.63}$$

where we let $m = m_F$ for clarity.

Application

With Eq. 3.63, the AMPS can then be used to interpret the distribution of atomic population across a Zeeman ground state. Taking the example of an $F = 1$ ground state, if each sub-level is equally populated, then the maximum projection, $\rho_{F,F}(\theta, \phi) = 1/3$,

has no spatial dependence and this symmetry is reflected in the AMPS (Figure 3.5:top). For circularly-polarised light interacting with a stretched state however, the steady-state condition will see all of the atoms pushed into one outer ground state, such that $\rho_{F,F}(\theta, \phi) = \sin^4\frac{\theta}{2}$ or $\cos^4\frac{\theta}{2}$ for $m_F = \mp 1$ respectively. This is represented in the probability surface (Figure 3.5:middle) as a bulge in $\mp z$. Graphically therefore, there is only one preferred direction and the quantisaton axis is clear. Similarly for $F = 0$, $\rho_{F,F}(\theta, \phi) = \frac{(\sin\theta)^2}{2}$ and whereas the atoms can be seen

to have no preferred direction, there is a preferred axis along z (Figure 3.5:Bottom).

Clearly, the surface plots can be used to illustrate the rotational symmetry properties of the density matrix and the great virtue of this approach is that it is independent of the choice of basis. Pragmatically, they can then be used to find the quantisation axes of a system that produce the simplest possible density matrices. Conceptually however, they provide a concise insight into how we can expect an atomic cloud to interact with light. The symmetry of the atomic polarisation state determines the spatial optical properties of the medium, where for example the axial symmetry around the beam axis implies that the absorption and refractive index will be independent of light polarisation.

What may not be apparent from the simplified examples given above, is that the AMPS, somewhat surprisingly, have a bijective relationship with the Zeeman density matrix of a state *i.e.* they represent a complete knowledge of the modelled system. In contrast to electron density plots, these surfaces do not contain radial information, which may seem like a disadvantage, but this allows them to be used in the context of any angular momentum state, rather than being limited to a single electron configuration.

3.3 Observables

In the last section, we took some time to (re-)familiarise ourselves with the mathematics behind semi-classical light-atom interaction, particularly in introducing and motivating the system density matrix. In this section, we continue this theme, but shift our focus from mechanism to measurement of quantum properties; a paradigm perhaps closer to the heart of the experimental physicist. Acknowledging that the term *observable* carries a certain theoretical baggage, we persevere with the understanding that we are considering the term in its loosest form, simply recognising that not all optical and atomic properties were created equal in regards to ease of access. In this spirit, we consider an outline of the theory and technology needed to extract semi-classical information: as motivated for a laboratory setting.

3.3.1 Optical Observables

Following our characterisation of light as being cardinally described by a combination of amplitude and phase, and given that light is generally our sole measurement tool, then we seek to model all observables in terms of these quantities. Naturally therefore, we are interested in absorption and dispersion of light as it passes through a medium and this can be modelled efficiently through the refractive index. If we consider a non-zero optical phase as the result of a refractive index in a medium, then we can write

$$\underbrace{e^{i[kz-\omega t]}}_{\text{Plane wave}} = \underbrace{e^{i[k_0 z-\omega t+\varphi(z)]}}_{\text{Plane wave with explicit phase}} = \underbrace{e^{i[nk_0 z-\omega t]}}_{\text{Plane wave with explicit medium}}$$

$$\implies n = 1+\frac{\varphi(z)}{k_0 z}, \tag{3.64}$$

where n is the refractive index and k_0 stands for the original wavevector. If we let n carry an imaginary component, such that $n = n_{\mathrm{R}} + in_{\mathrm{I}}$, then we can also account for the absorption *i.e.*

$$\begin{aligned} e^{i[nk_0 z-\omega t]} &= e^{i[n_{\mathrm{R}}k_0 z+in_{\mathrm{I}}k_0 z-\omega t]} \\ &= \underbrace{e^{-n_{\mathrm{I}}k_0 z}}_{\text{Absorption}}\ \underbrace{e^{i[n_{\mathrm{R}}k_0 z-\omega t]}}_{\text{Plane wave}}, \end{aligned} \tag{3.65}$$

where the result is a plane wave of the same form, modulated in amplitude according to both propagation and the value of n_{I}[14]. Such is the case, we now have a simple, if abstract, way of linking the optical observables with an atomic medium, giving an incredibly concise description of the material phenomena. Differentiating, we can motivate the choice of n_{I} further:

$$\frac{d}{dz}\left[\mathcal{E}e^{-n_{\mathrm{I}}k_0 z}e^{i[n_{\mathrm{R}}k_0 z-\omega t]}\right] = \left(\frac{1}{\mathcal{E}}\frac{d\mathcal{E}}{dz} - n_{\mathrm{I}}k_0 + in_{\mathrm{R}}k_0\right)\left[\dots\right], \quad (3.66)$$

where separating the real part allows us to characterise the absorption as

$$n_{\mathrm{I}} = -\frac{1}{k_0\mathcal{E}}\frac{d\mathcal{E}}{dz}; \quad (3.67)$$

the unitless fractional change in electric field with propagation. If we explicitly consider the case of an optically thin medium, then the phase after some distance z will change linearly such that Eq. 3.64(p. 82) becomes:

$$n_{\mathrm{R}} = 1 + \frac{1}{k_0}\frac{d\varphi}{dz}, \quad (3.68)$$

and where we now have an explicit link between the material's characteristics and the change in field and phase of the incoming light. Macroscopic observables, such as polarisation rotation and ellipticity, can then be effectively derived from these values. For example, if we consider a linearly polarised field with two circular components, then the acquired phase shift can be expressed:

$$\begin{aligned}\varphi_\Delta =& \varphi_+ - \varphi_- \\ =& k_0 z\left[n_+ - n_-\right]\end{aligned} \quad (3.69)$$

which leads to an optical rotation of

$$\alpha = \frac{1}{2}k_0 z\,\mathrm{Re}(n_+ - n_-) \quad (3.70)$$

and an ellipticity determined similarly. For our purposes, we define the ellipticity

$$\epsilon \equiv \frac{E_{\sigma_+} - E_{\sigma_-}}{E_{\sigma_+} + E_{\sigma_-}} \quad (3.71)$$

and therefore, the change in ellipticity for a plane wave under-

14. The first exponential factor may look curiously similar to the Beer-Lambert law, but we will consider this in more detail later in this section.

going absorption in the circular polarisation components can be written

$$\epsilon_\Delta = \frac{e^{-\operatorname{Im}(n_+)k_0 z} - e^{-\operatorname{Im}(n_-)k_0 z}}{e^{-\operatorname{Im}(n_+)k_0 z} + e^{-\operatorname{Im}(n_-)k_0 z}} \tag{3.72}$$

$$= -\tanh(\frac{1}{2}k_0 z \operatorname{Im}(n_+ - n_-)). \tag{3.73}$$

therefore, for small angles,

$$\epsilon_\Delta \simeq -\frac{1}{2}k_0 z \operatorname{Im}(n_+ - n_-) \tag{3.74}$$

Having considered the case of a z-dependent plane wave, we have shown how the refractive index can be used to concisely model a material's effect on an incoming field: the imaginary part model's the material's capacity for absorbing or amplifying the light and the real part encompasses the material's ability to change the phase or dispersion of the beam and the combination of the two can describe the effect this has on the field's polarisation. When considering more complicated fields however, it is worth stressing that this intrinsic relationship between absorption and dispersion is incredibly general. If we follow a rigorous derivation of the Kramers-Kronig relations, such as presented [72, 73], then we see that the existence of one strictly implies the existence of the other; the only assumption being causality. In fact, the relationship is so general that it applies to any mathematically causal and dispersive response function, so we should expect our more general results to model loss and dispersion in similar ways. To investigate these generalised fields, we will need to consider the problem from a more fundamental basis.

Maxwell's Equations We first consider Maxwell's equations for matter-interaction in their most general form:

$$\begin{aligned} \boldsymbol{\nabla} \cdot \boldsymbol{D} &= \rho_\mathrm{f}, & \boldsymbol{\nabla} \times \boldsymbol{E} &= -\frac{\partial}{\partial t}\boldsymbol{B}, \\ \boldsymbol{\nabla} \cdot \boldsymbol{B} &= 0 & \text{and } \boldsymbol{\nabla} \times \boldsymbol{H} &= j_\mathrm{f} + \frac{\partial}{\partial t}\boldsymbol{D} \end{aligned} \tag{3.75}$$

where the variables carry their standard definitions, with constitutive relations defined $\boldsymbol{D} \equiv \epsilon_0 \boldsymbol{E} + \boldsymbol{P}$ and $\boldsymbol{H} \equiv \frac{1}{\mu_0}\boldsymbol{B} - \boldsymbol{M}$, as outlined elsewhere. From these equatons, assuming there are no

free charges, free currents or magnetisation, we find:

$$\left.\begin{array}{l}\rho_{\mathrm{f}}\\ \boldsymbol{j}_{\mathrm{f}}\\ \boldsymbol{M}\end{array}\right\} = 0.$$

$$\begin{aligned}\boldsymbol{\nabla}\times(\boldsymbol{\nabla}\times\boldsymbol{E}) &= -\mu_0\frac{\partial}{\partial t}(\boldsymbol{\nabla}\times\boldsymbol{H}) \\ &= -\mu_0\frac{\partial}{\partial t}\left[\frac{\partial}{\partial t}(\epsilon_0\boldsymbol{E}+\boldsymbol{P})\right] \\ &= -\frac{1}{\epsilon_0 c^2}\left[\frac{\partial^2}{\partial t^2}(\epsilon_0\boldsymbol{E}+\boldsymbol{P})\right]\end{aligned} \tag{3.76}$$

and thus:

$$\boldsymbol{\nabla}\times(\boldsymbol{\nabla}\times\boldsymbol{E}) + \frac{1}{c^2}\frac{\partial^2}{\partial t^2}\boldsymbol{E} = -\frac{1}{\epsilon_0 c^2}\frac{\partial^2}{\partial t^2}\boldsymbol{P} \tag{3.77}$$

where the double derivative of polarization density can be seen to act as a source for the radiation field.

Approximations Using a vector identity, the above can be expressed as:

$$\begin{aligned}\boldsymbol{\nabla}(\boldsymbol{\nabla}\cdot\boldsymbol{E}) - \nabla^2\boldsymbol{E} + \frac{1}{c^2}\frac{\partial^2}{\partial t^2}\boldsymbol{E} &= -\frac{1}{\epsilon_0 c^2}\frac{\partial^2}{\partial t^2}\boldsymbol{P}. \\ \therefore \nabla^2\boldsymbol{E} - \frac{1}{c^2}\frac{\partial^2}{\partial t^2}\boldsymbol{E} &\simeq \frac{1}{\epsilon_0 c^2}\frac{\partial^2}{\partial t^2}\boldsymbol{P},\end{aligned} \tag{3.78}$$

where we make use of the assumption that $\boldsymbol{\nabla}\cdot\boldsymbol{E} \simeq 0$ for the problems of interest. Factoring out the z, t dependency for the electric field, we can write:

$$\left(\frac{\partial}{\partial z}+\frac{1}{c}\frac{\partial}{\partial t}\right)\left(\frac{\partial}{\partial z}-\frac{1}{c}\frac{\partial}{\partial t}\right)\boldsymbol{E} + \nabla_{\mathrm{T}}^2\boldsymbol{E} = \frac{1}{\epsilon_0 c^2}\frac{\partial^2}{\partial t^2}\boldsymbol{P} \tag{3.79}$$

, where ∇_{T}^2 collects the transverse components of the Laplacian. For slowly–varing field intensities transverse to the laser axis, we can consider a field:

$$\begin{aligned}\boldsymbol{E}(\boldsymbol{r},t) &= \mathcal{E}(\boldsymbol{r},t)\cos(kz-\omega t+\varphi(\boldsymbol{r},t))\underline{\hat{e}} \\ &= \mathcal{E}(\boldsymbol{r},t)\frac{1}{2}\left[e^{i[kz-\omega t+\varphi(\boldsymbol{r},t)]} + e^{-i[kz-\omega t+\varphi(\boldsymbol{r},t)]}\right]\underline{\hat{e}}\end{aligned} \tag{3.80}$$

and assume a corresponding polarisation density:

$$\boldsymbol{P}(\boldsymbol{r},t) = \mathcal{P}(\boldsymbol{r},t)\frac{1}{2}e^{-i[kz-\omega t+\varphi(\boldsymbol{r},t)]}\underline{\hat{e}} + c.c. \tag{3.81}$$

where we assume that the polarisation maintains the same phase. Therefore,

$$\frac{\partial}{\partial z}\boldsymbol{E}(\boldsymbol{r},t) = \frac{1}{2}\frac{\partial}{\partial z}\mathcal{E}(\boldsymbol{r},t)e^{-i[kz-\omega t+\varphi(\boldsymbol{r},t)]}\underline{\hat{e}} - i\left[k + \frac{\partial}{\partial z}\varphi(\boldsymbol{r},t)\right]\boldsymbol{E}(\boldsymbol{r},t) + c.c. \text{ and} \tag{3.82}$$

$$\frac{\partial}{\partial t}\boldsymbol{E}(\boldsymbol{r},t) = \frac{1}{2}\frac{\partial}{\partial t}\mathcal{E}(\boldsymbol{r},t)e^{-i[kz-\omega t+\varphi(\boldsymbol{r},t)]}\underline{\hat{e}} + i\left[\omega - \frac{\partial}{\partial t}\varphi(\boldsymbol{r},t)\right]\boldsymbol{E}(\boldsymbol{r},t) + c.c. \tag{3.83}$$

, where $\frac{\partial}{\partial t}\boldsymbol{P}(\boldsymbol{r},t)$ is given similarly and $\varphi(\boldsymbol{r},t)$ is a spatially and temporally varying phase difference. The slowly–varying nature of these fields can be expressed explicitly as:

$$\begin{aligned}
&\frac{\partial}{\partial z}\mathcal{E} \ll k\mathcal{E}\,,\ \frac{\partial}{\partial t}\mathcal{E} \ll \omega\mathcal{E}, \\
&\frac{\partial}{\partial z}\varphi \ll k\,,\ \frac{\partial}{\partial t}\varphi \ll \omega \text{ and} \\
&\frac{\partial}{\partial z}\mathcal{P} \ll k\mathcal{P}\,,\ \frac{\partial}{\partial t}\mathcal{P} \ll \omega\mathcal{P}.
\end{aligned} \tag{3.84}$$

Therefore,

$$\left(\frac{\partial}{\partial z} - \frac{1}{c}\frac{\partial}{\partial t}\right)\boldsymbol{E}(\boldsymbol{r},t) \simeq -2ik\boldsymbol{E}(\boldsymbol{r},t) \text{ and} \tag{3.85a}$$

$$\frac{\partial^2}{\partial t^2}\boldsymbol{P}(\boldsymbol{r},t) \simeq \omega^2\boldsymbol{P}(\boldsymbol{r},t). \tag{3.85b}$$

Combining these equations, we can write the paraxial wave equation for a field with slowly varying amplitudes and phase:

$$-2ik\left[\frac{\partial}{\partial z}\boldsymbol{E} + \frac{1}{c}\frac{\partial}{\partial t}\boldsymbol{E}\right] + \nabla_{\mathrm{T}}^2\boldsymbol{E} = -\frac{\omega^2}{\epsilon_0 c^2}\boldsymbol{P} \tag{3.86}$$

where we now implitcitly assume the spatial and temporal dependencies. Or, equivalently, as

$$\frac{\partial}{\partial z}\boldsymbol{E} + \frac{1}{c}\frac{\partial}{\partial t}\boldsymbol{E} + \frac{i}{2k}\nabla_{\mathrm{T}}^2\boldsymbol{E} = -\frac{1}{2\epsilon_0}i\,k\boldsymbol{P}. \tag{3.87}$$

Therefore, in the limit where the transverse component can be neglected, deconstructing into parts allows us to write:

$$\frac{\partial}{\partial z}\mathcal{E} + \frac{1}{c}\frac{\partial}{\partial t}\mathcal{E} = -\frac{k}{2\epsilon_0}\,\mathrm{Im}(\mathcal{P}) \tag{3.88a}$$

$$\frac{\partial}{\partial z}\varphi + \frac{1}{c}\frac{\partial}{\partial t}\varphi = -\frac{k}{2\epsilon_0}\mathcal{E}^{-1}\,\mathrm{Re}(\mathcal{P}). \tag{3.88b}$$

As expected, we now have a coupled set of equations that allow us to model the absorption and disepersion of the propagating light beams, where the imaginary part of our material response describes loss and the associated real component reveals the dispersive nature of the system. It may not be immediately clear how this result relates to our discussion of the refractive index, but the index is of course a macroscopic quantity and to relate this to our mathematical model we can break it down into its fundamental quantities:

$$\begin{aligned} n \equiv \frac{c}{v} = \frac{c}{\left(\frac{1}{\sqrt{\epsilon\mu}}\right)} &= \sqrt{\frac{\epsilon\mu}{\epsilon_0\mu_0}} \\ &\simeq \sqrt{\epsilon_{\mathrm{r}}} \\ &= \sqrt{1+\chi_{\mathrm{E}}}, \end{aligned} \tag{3.89}$$

where we have used the velocities implied by the wave equation and the assumption that the magnetic permeability doesn't deviate from that of a vacuum. The polarisation of the atoms can then be written as

$$\begin{aligned} \boldsymbol{P} &= \epsilon_0 \chi_{\mathrm{E}} \cdot \boldsymbol{E} \\ &= \epsilon_0 \left(n^2 - 1\right) \boldsymbol{E}. \end{aligned} \tag{3.90}$$

Relating to the Density Matrix To complete our journey from macro- to micro-scopic concerns, we define polarisation density:

$$\begin{aligned} \boldsymbol{P}(\boldsymbol{r}, t) &\equiv N_{\mathcal{V}} \sum_i \langle i | \, \boldsymbol{d}_{\mathrm{E}} \, \hat{\rho} \, | i \rangle \\ &= N_{\mathcal{V}} \sum_i \langle i | \, \boldsymbol{d}_{\mathrm{E}} \left(\sum_j |j\rangle \langle j| \right) \hat{\rho} \, | i \rangle \\ &= N_{\mathcal{V}} \sum_{i,j} \boldsymbol{d}_{\mathrm{E}ij} \, \hat{\rho}_{\mathrm{ji}} \end{aligned} \tag{3.91}$$

where $N_{\mathcal{V}}$ is the atomic number density; $\boldsymbol{d}_{\mathrm{E}}$ and $\hat{\rho}$ are the dipole and density operators respectively and ij refers to the transitions between states i and j. Therefore, adapting our previous definition and the above, we obtain:

$$\begin{aligned} N_{\mathcal{V}} \sum_{i,j} \boldsymbol{d}_{\mathrm{E}ij} \, \hat{\rho}_{\mathrm{ij}}(\boldsymbol{r}, t) &= \sum_{ij} \mathcal{P}_{ij} \frac{1}{2} \left(e^{i[kz - \omega t + \varphi(\boldsymbol{r},t)]} + e^{-i[kz - \omega t + \varphi(\boldsymbol{r},t)]} \right) \underline{\hat{e}}_{\mathrm{ij}} \\ \implies \mathcal{P}_{ij} &\simeq 2 N_{\mathcal{V}} \hat{\rho}_{\mathrm{ij}} e^{i[kz - \omega t + \varphi(\boldsymbol{r},t)]} \, \boldsymbol{d}_{\mathrm{E}ij} \cdot \underline{\hat{e}}_{\mathrm{ij}} \end{aligned} \tag{3.92}$$

i.e.

$$\mathcal{P}_{ij} = 2N_{\mathcal{V}}\mathcal{D}_{ij}\hat{\rho}_{\mathrm{ij}}e^{i[\omega_{\mathrm{ij}}t - k_{ij}z + \Phi_{ij}]} \tag{3.93}$$

where θ_{ij} are the dipole phases, $\Phi_{ij} = \varphi_{\mathrm{ij}} - \theta_{ij}$, $\mathcal{D}_{ij} = e^{i\theta_{ij}}\,\boldsymbol{d}_{\mathrm{E}ij}\cdot\hat{\underline{e}}_{\mathrm{ij}}$, $\mathcal{D}_{ij}$ are real and $\hat{\underline{e}}_{\mathrm{ij}}$ is the directional unit vector. Therefore:

$$\frac{\partial}{\partial z}\mathcal{E}_{\mathrm{ij}} + \frac{1}{c}\frac{\partial}{\partial t}\mathcal{E}_{\mathrm{ij}} = -\frac{k_{\mathrm{ij}}}{2\epsilon} \quad \times\ 2N_{\mathcal{V}}\mathcal{D}_{ij}\left[\mathrm{Im}(\hat{\rho}_{\mathrm{ij}})\cos\Theta_{ij} + \mathrm{Re}(\hat{\rho}_{\mathrm{ij}})\sin\Theta_{ij}\right] \tag{3.94}$$

$$\frac{\partial}{\partial z}\varphi_{\mathrm{ij}} + \frac{1}{c}\frac{\partial}{\partial t}\varphi_{\mathrm{ij}} = -\frac{k_{\mathrm{ij}}}{2\epsilon}\mathcal{E}_{\mathrm{ij}}^{-1} \quad 2N_{\mathcal{V}}\mathcal{D}_{ij}\left[\mathrm{Re}(\hat{\rho}_{\mathrm{ij}})\cos\Theta_{ij} - \mathrm{Im}(\hat{\rho}_{\mathrm{ij}})\sin\Theta_{ij}\right] \tag{3.95}$$

where $\Theta_{ij} = \omega_{\mathrm{ij}}t - k_{ij}z + \varphi_{\mathrm{ij}}$. In general, the density matrix elements are time–dependent, but we consider the environment such that the atoms maintain a steady-state. Therefore:

$$\frac{\partial}{\partial z}\mathcal{E}_{\mathrm{ij}} = -\frac{N_{\mathcal{V}}k_{\mathrm{ij}}\mathcal{D}_{ij}}{\epsilon} \quad \times\left[\mathrm{Im}(\hat{\rho}_{\mathrm{ij}})\cos\Theta_{ij} + \mathrm{Re}(\hat{\rho}_{\mathrm{ij}})\sin\Theta_{ij}\right] \tag{3.96}$$

$$\frac{\partial}{\partial z}\varphi_{\mathrm{ij}} = -\frac{N_{\mathcal{V}}k_{\mathrm{ij}}\mathcal{D}_{ij}}{\epsilon}\,\mathcal{E}_{\mathrm{ij}}^{-1}\ \left[\mathrm{Re}(\hat{\rho}_{\mathrm{ij}})\cos\Theta_{ij} - \mathrm{Im}(\hat{\rho}_{\mathrm{ij}})\sin\Theta_{ij}\right]$$

Neglecting dipole phase and under the assumption that the time dependent optical frequency has been removed (*e.g.* in the context of the rotating wave approximation), then these expressions simplify:

$$\frac{\partial}{\partial z}\mathcal{E}_{\mathrm{ij}} = -\frac{N_{\mathcal{V}}k_{\mathrm{ij}}}{\epsilon}\,\boldsymbol{d}_{\mathrm{E}ij}\cdot\hat{\underline{e}}_{\mathrm{ij}} \quad \times\left[\mathrm{Im}(\hat{\rho}_{\mathrm{ij}})\cos\varphi_{\mathrm{ij}} + \mathrm{Re}(\hat{\rho}_{\mathrm{ij}})\sin\varphi_{\mathrm{ij}}\right] \tag{3.97}$$

$$\frac{\partial}{\partial z}\varphi_{\mathrm{ij}} = -\frac{N_{\mathcal{V}}k_{\mathrm{ij}}}{\epsilon}\,\boldsymbol{d}_{\mathrm{E}ij}\cdot\hat{\underline{e}}_{\mathrm{ij}}\,\mathcal{E}_{\mathrm{ij}}^{-1}\ \left[\mathrm{Re}(\hat{\rho}_{\mathrm{ij}})\cos\varphi_{\mathrm{ij}} - \mathrm{Im}(\hat{\rho}_{\mathrm{ij}})\sin\varphi_{\mathrm{ij}}\right]$$

3.3.2 *Atomic Observables*

Now that we have considered their impact on incoming light, our focus moves to what we can learn about the media themselves. For this purpose, there are two main tools: that of fluorescence and absorption imaging which together, with some analysis, allow access to all of the key properties of the atoms. We consider

their derivation here in the context of a two level atom, and this serves the joint purposes of both general erudition and as an example of how the model and calculations were developed in Chapter 4 (p. 111).

Fluorescence

Fluorescence is ubiquitous, both in daily and atomic life. Defined as the scattering rate of an atomic system, we can connect our density matrix model with macroscopic observables by first reconsidering a two level atom interacting with an x-polarised electric plane wave defined by $\boldsymbol{E} = \mathcal{E}\cos(\omega t)\underline{\hat{x}}$. Under these conditions, the bare Hamiltonian can be immediately written as

$$\hat{H} = \begin{pmatrix} 0 & -\hbar\Omega_{\mathrm{R}}\cos(\omega t) \\ -\hbar\Omega_{\mathrm{R}}\cos(\omega t) & U_{\mathrm{e}} \end{pmatrix} \tag{3.98a}$$

$$\widehat{\hat{H}} = \hbar \begin{pmatrix} 0 & -\frac{1}{2}\Omega_{\mathrm{R}} \\ -\frac{1}{2}\Omega_{\mathrm{R}} & -\omega_{\Delta eo} \end{pmatrix} \tag{3.98b}$$

where we have used the rotating wave approximation laid out previously (§ 3.2.4 (p. 73)). The relevant master equations, without considering transit decay, can then be written as

$$\frac{d\hat{\rho}_{\mathrm{gg}}}{dt} = -i\left[-\frac{1}{2}\Omega_{\mathrm{R}}\hat{\rho}_{\mathrm{eg}} + \frac{1}{2}\Omega_{\mathrm{R}}\hat{\rho}_{\mathrm{ge}}\right] + \Gamma\hat{\rho}_{\mathrm{ee}} \tag{3.99a}$$

$$\frac{d\hat{\rho}_{\mathrm{ge}}}{dt} = -i\left[-\frac{1}{2}\Omega_{\mathrm{R}}\hat{\rho}_{\mathrm{ee}} + \omega_{\Delta eo}\hat{\rho}_{\mathrm{ge}} + \frac{1}{2}\Omega_{\mathrm{R}}\hat{\rho}_{\mathrm{gg}}\right] - \frac{1}{2}\Gamma\hat{\rho}_{\mathrm{ge}} \tag{3.99b}$$

$$\frac{d\hat{\rho}_{\mathrm{eg}}}{dt} = -i\left[+\frac{1}{2}\Omega_{\mathrm{R}}\hat{\rho}_{\mathrm{ee}} - \omega_{\Delta eo}\hat{\rho}_{\mathrm{eg}} - \frac{1}{2}\Omega_{\mathrm{R}}\hat{\rho}_{\mathrm{gg}}\right] - \frac{1}{2}\Gamma\hat{\rho}_{\mathrm{eg}} \tag{3.99c}$$

$$\frac{d\hat{\rho}_{\mathrm{ee}}}{dt} = -i\left[\frac{1}{2}\Omega_{\mathrm{R}}\hat{\rho}_{\mathrm{eg}} - \frac{1}{2}\Omega_{\mathrm{R}}\hat{\rho}_{\mathrm{ge}}\right] - \Gamma\hat{\rho}_{\mathrm{ee}}. \tag{3.99d}$$

First considering the system in the absence of relaxation, the time-dependent solutions, assuming that all of the atoms are initially in the ground state, are given as

$$\hat{\rho}_{\mathrm{gg}} = \frac{\Omega_{\mathrm{R}}^2\cos(\Omega t) + \Omega + \omega_{\Delta eo}^2}{2\Omega} \tag{3.100a}$$

$$\hat{\rho}_{\mathrm{ge}} = \frac{\Omega_{\mathrm{R}}}{2\Omega^2}\left[-\omega_{\Delta eo} + \omega_{\Delta eo}\cos(\Omega t) - i\Omega\sin(\Omega t)\right] \tag{3.100b}$$

$$\hat{\rho}_{\mathrm{eg}} = \hat{\rho}_{\mathrm{ge}}^{*} \tag{3.100c}$$

$$\hat{\rho}_{\mathrm{ee}} = \frac{\Omega_{\mathrm{R}}^2}{\Omega^2}\sin^2(\frac{1}{2}\Omega t) \tag{3.100d}$$

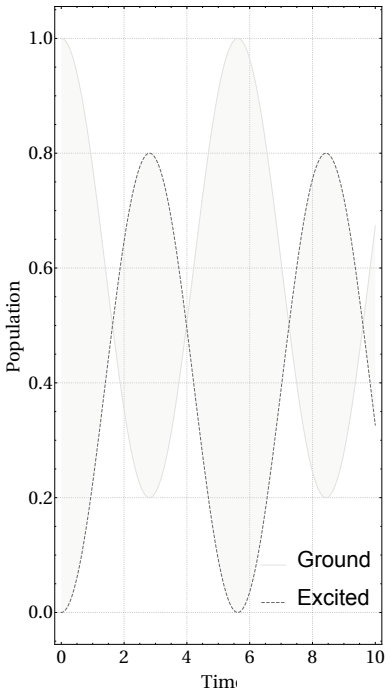

Figure 3.6: The state occupation probability of a time-dependent two level atom under the action of a light field detuned from resonance. In the absence of relaxation, the probability oscillates periodically between the ground and excited states: illustrating the physical significance of the Rabi frequency. Assuming $\Omega_{\mathrm{R}} = 1$, a non-zero detuning, $\omega_{\Delta e0} = 1/2$, prevents the excited state from full population.

where we have defined $\Omega^2 \equiv \Omega_R^2 + \omega_{\Delta eo}^2$ as the *generalised Rabi frequency*. Having introduced the concept of the Rabi frequency as an abstract encapsulation of the dipole moment (§ 3.2.3 (p. 72)), here we explicitly observe its physical significance as an oscillation of the population levels. The system undergoes continuous absorption and emission at frequency $\frac{\Omega_R}{2}$, with a relative strength decided by the detuning (Figure 3.6).

If we include spontaneous decay however, then the effects of damping can bring the system to a time-independent steady-state:

$$\hat{\rho}_{gg} = \frac{1}{\mathcal{D}}\left[\Omega_R^2 + \Gamma^2 + 4\omega_{\Delta eo}^2\right] \tag{3.101a}$$

$$\hat{\rho}_{ge} = \frac{1}{\mathcal{D}} - \Omega_R\left[i\Gamma + 2\omega_{\Delta eo}\right] \tag{3.101b}$$

$$\hat{\rho}_{eg} = \hat{\rho}_{ge}^* \tag{3.101c}$$

$$\hat{\rho}_{ee} = \frac{1}{\mathcal{D}}\Omega_R^2 \qquad \text{where } \mathcal{D} = 2\Omega_R^2 + \Gamma^2 + 4\omega_{\Delta eo}^2. \tag{3.101d}$$

The competition inherent in this configuration between the Rabi frequency and decay then motivates the introduction of a *saturation parameter* $\kappa = \frac{\Omega_R^2}{\Gamma^2}$. Plotting the state populations for resonant light (Figure 3.7), we recover the result that a two-level system cannot be used for population inversion, unlike the idealised case outlined above. Furthermore, κ can be seen to qualify different regimes of interaction, where for $\kappa < 1$ the population development is largely linear with saturation and for $\kappa > 1$ the population fractions both asymptote towards .5.

The fluorescence of the system is then a combination of these effects, where the fluorescence rate $\mathcal{F}$ is the excited state population probability multiplied by the decay rate *i.e.*

$$\mathcal{F} = \Gamma\hat{\rho}_{ee}. \tag{3.102}$$

Therefore, for a two-level atom subject to spontaneous decay and in the limit of negligible transit relaxation,

$$\mathcal{F} = \Gamma\frac{\Omega_R^2}{2\Omega_R^2 + \Gamma^2 + 4\omega_{\Delta eo}^2}. \tag{3.103}$$

The task remaining, is then to relate this result to experimental parameters. Our main optical observable is the light intensity

and so combining the freely-propagating expression defined previously (Eq. 2.27(p. 21)) with our definition of the Rabi frequency (Eq. 3.41(p. 72)),

$$\mathcal{I} = \Omega_{\mathrm{R}}^2 \left[\frac{1}{2} \epsilon_0 c \hbar^2 \frac{1}{\langle 1 | \hat{\underline{\epsilon}} \cdot \boldsymbol{d}_{\mathrm{E}} | 2 \rangle^2} \right]. \tag{3.104}$$

The intensity is then proportional to the square of the Rabi frequency and the inverse of the square of the dipole matrix element. This matrix element contains the details of the interactions, but it is a geometric property and so can be taken as a constant. Similarly to κ we can define the saturation intensity by

$$\frac{\mathcal{I}}{\mathcal{I}_{\mathrm{sat}}} \equiv \frac{2\Omega_{\mathrm{R}}^2}{\Gamma^2} \tag{3.105}$$

where $\mathcal{I}_{\mathrm{sat}}$ does not depend on the electric field and the choice of factor is purely for convenience. This allows us to rewrite our expression for the fluorescence in terms of experimental parameters and so

$$\mathcal{F} = \frac{\Gamma}{2} \frac{\mathcal{I}/\mathcal{I}_{\mathrm{sat}}}{1 + \mathcal{I}/\mathcal{I}_{\mathrm{sat}} + [2\omega_{\Delta eo}/\Gamma]^2}, \tag{3.106}$$

where we note that this rate applies to a single atom. Experimentally, the fluorescence signals are collected either using a photodiode or a camera, where the power P of the signal is given as

$$\begin{aligned} P_{PD} =& \text{Total emission rate} \times \text{Fraction of signal collected} \\ =& \text{photon energy} \times \text{emission rate} \times \frac{\text{collection angle}}{4\pi} \times \eta \end{aligned} \tag{3.107}$$

and so

$$P_{sig} = \hbar\omega \times N_{\mathrm{a}} \cdot \mathcal{F} \times \frac{\eta \Omega_{\mathrm{ca}}}{4\pi}, \tag{3.108}$$

where N_{a}, Ω_{ca} and η are the number of atoms in the signal, collection angle and detector efficiency respectively. Although in this context, care should be taken not to confuse the collection angle with the Rabi frequency. Rearrangement then gives an expression for the number of atoms in the system,

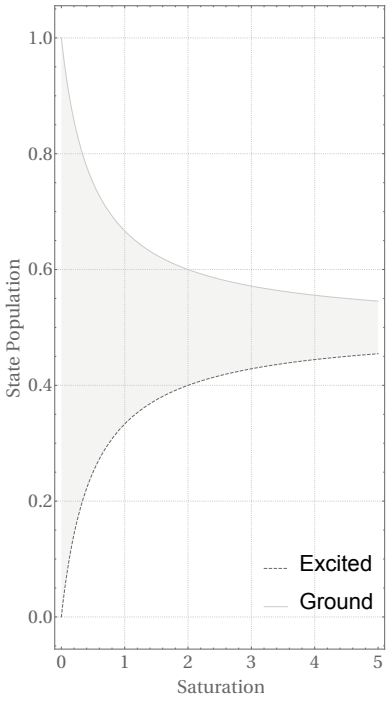

Figure 3.7: In the presence of relaxation, a two-level system is sufficiently damped to yield steady-state populations. The populations are then determined by the relative strengths of the two effects, such that increasing the Rabi frequency asymptotically brings the occupations to convergence.

$$N_{\mathrm{a}} = P_{sig}\frac{1}{\hbar\omega\mathcal{F}}\frac{4\pi}{\eta\Omega_{\mathrm{ca}}}. \tag{3.109}$$

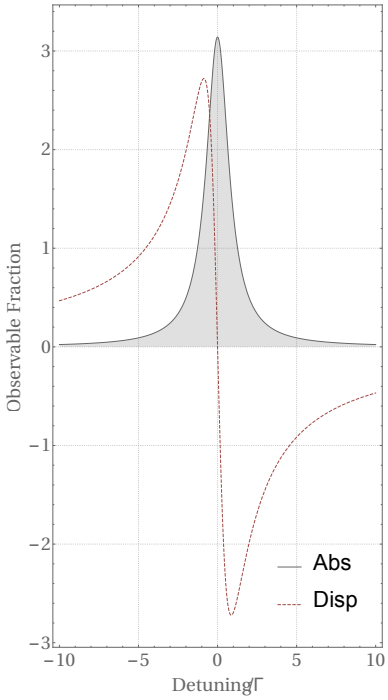

Figure 3.8: The calculated absorption and dispersion of a two-level system with respect to detuning per natural line width.

In practice therefore, fluorescence imaging only requires an appropriate camera for the given wavelength, situated according to normal imaging rules, and can be used to estimate the number of atoms in a cloud. We can also then use the spatial information in the image to estimate the widths and so in principle, a full atomic density measurement can be performed. In practice, fluorescence imaging is not the most accurate method for obtaining atom number or density values, but its passive nature usually allows real-time display of atomic clouds, either when confined to a vapour cell or to a standard MOT[15]. Therefore, this approach was only used for rough apparatus alignment and optimisation, with final values calculated using the methods outlined further below. The frequency dependence of the fluorescence signal however, has proven invaluable for choosing the applied laser frequencies and more details of this process can be found in the context of *saturation absorption spectroscopy*. For the most accurate measurements of atom number, density and temperature however, we must consider the absorption of the system.

Absorption

In the previous subsection, we took some time to outline how absorption features in the semi-classical model as it is the most straightforward property to access and the most fundamental way to interact with our atoms. The rigorous derivation (Eq. 3.98a(p. 89))(in the limit of a thin-medium) for absorption per unit path length and atomic density is then

$$\frac{1}{N_{\mathcal{V}}}\frac{1}{\mathcal{E}k}\frac{\partial}{\partial z}\mathcal{E}_{\mathrm{ij}} = \frac{1}{\epsilon}\frac{\mathrm{d}_{\mathrm{E}ge}}{\mathcal{E}}\ \mathrm{Im}(\hat{\rho}_{\mathrm{ge}}) \tag{3.110}$$

, where we recall that our coupling electric field was assumed to be plane and linearly polarised in $\underline{\hat{x}}$ and where this expression is actually the fractional change in electric field: thus either absorption or gain depending on the appropriate sign.

[15] magneto optical trap

The matrix element can then be expanded in terms of the lifetime and geometry according to:

$$\left|\langle g_i, J \,\|\mathrm{d_E}\|\, e, J' \rangle\right|^2 = \frac{3}{4}\hbar k_0^3 \left(2J'+1\right) \mathrm{Br_i}\Gamma \tag{3.111}$$

where Br is the *branching ratio* of the excited state [67, 74]. Therefore, for our system,

$$\frac{1}{N_\mathcal{V}}\frac{1}{\mathcal{E}k}\frac{\partial}{\partial z}\mathcal{E}_{\mathrm{ij}} = \frac{1}{\epsilon}\frac{3k_0^3\Gamma}{4\Omega_\mathrm{R}}\left(2J'+1\right)\mathrm{Br_i}\ \mathrm{Im}(\hat{\rho}_{\mathrm{ge}}). \tag{3.112}$$

The dispersion can be expanded similarly, where both profiles can be seen in Figure 3.8 as a function of detuning.

In practice however, a more phenomenological approach to absorption is needed to relate these results to laboratory measurements.

Experimentally, the rate of change of beam intensity with propagation can be defined by

$$\frac{d\mathcal{I}(x,y,z)}{dz} \equiv -a(x,y,z)\mathcal{I}(x,y,z) \tag{3.113}$$

$$\implies \mathcal{I}(x,y,z) = \mathcal{I}(x,y,0)e^{-\int_0^z a(x,y,z')dz'} \tag{3.114}$$

by integrating factor

The absorption coefficient, a, [16]is a macrocscopic parameter, but to express it in terms of single atom interactions we can rewrite it as

$$a(x,y,z) = \sum_{i=1}^{\text{all species}} \sigma_\mathrm{i} N_{\mathcal{V}\mathrm{i}}(x,y,z') \tag{3.115}$$

where the index i represents a distinct atomic species, $N_\mathcal{V}$ is the atomic number density[17] and σ is known as the absorption cross-section: an element specific characterisation of the absorption probability for a given species[18]. This allows us to write

$$\frac{\mathcal{I}(x,y,z)}{\mathcal{I}(x,y,0)} = e^{-\sum_i \sigma_\mathrm{i}\int_0^z N_{\mathcal{V}\mathrm{i}}(x,y,z')dz'}, \tag{3.116}$$

the Beer-Lambert law for light intensity [19]. There are many different ways of modelling the attenuation coefficient and this is reflected across the literature. For ease of comparison, we therefore note that

$$\text{Transmittance} = \frac{\mathcal{I}(x,y,z)}{\mathcal{I}(x,y,0)} = e^{-az} = e^{-\mathrm{OD}} = 10^{-\mathcal{A}}, \tag{3.117}$$[20]

16. The coefficient is often called the attenuation as the loss could also have been due to scattering. We make the assumption however, that the absorption is the only appreciable mechanism.

17. $N_\mathcal{V} = \frac{N}{\mathcal{V}}$

18. If you're wondering why it's called the cross section, the units are m^2.

19. care should be taken in using this law out of context[75]

20. *cf.* $e^{-n_1 k_0 z}$, the cofactor introduced previously.

where OD is known as either the *optical depth* or *optical density* equivalently, and $\mathcal{A}$ is known as the *absorbance*. Rearranging, and allowing for background noise, we then have an expression for the optical depth,

$$\mathrm{OD} = \ln\left(\frac{\mathcal{I}(x,y,0) - \mathcal{I}_{\text{back.}}}{\mathcal{I}(x,y,z) - \mathcal{I}_{\text{back.}}}\right) = \sum_i \sigma_{\mathrm{i}} \int_0^z N_{\mathcal{V}\mathrm{i}}(x,y,z')dz' \tag{3.118}$$

which, in the limit of one atomic species, allows us to express the atomic density in the $\underline{\hat{x}}$-$\underline{\hat{y}}$ axis as

$$N_{\mathcal{V}}(x,y) \equiv \int_0^z N_{\mathcal{V}}(x,y,z')dz' = \frac{\mathrm{OD}}{\sigma}. \tag{3.119}$$

The scattering cross-section σ_{sc} can be defined [64] as

$$\begin{aligned}
\sigma_{\mathrm{sc}} \equiv & \frac{\text{emission power}}{\text{incident intensity}} && (3.120)\\
= & \frac{\hbar\omega_0 \mathcal{F}}{\mathcal{I}_0} && (3.121)\\
= & \left[\frac{\hbar\omega_0\Gamma}{2\mathcal{I}_{\text{sat}}}\right]\left[1 + \mathcal{I}/\mathcal{I}_{\text{sat}} + \left[2\omega_{\Delta eo}/\Gamma\right]^2\right]^{-1} && (3.122)\\
\equiv & \frac{\sigma_0}{1 + \mathcal{I}/\mathcal{I}_{\text{sat}} + \left[2\omega_{\Delta eo}/\Gamma\right]^2} && (3.123)
\end{aligned}$$

where σ_0 is appropriately defined as the resonant weak field cross-section. The number of atoms can then be obtained by integrating over $\underline{\hat{x}}$ and $\underline{\hat{y}}$ on the camera images while taking into account the camera and imaging configurations *i.e.*

$$N_{\mathrm{a}} = \mathcal{M}\ p.p. \sum_{x,y} N_{\mathcal{V}}(x,y) \tag{3.124}$$

for magnification $\mathcal{M}$ and pixel pitch$p.p.$.

To calculate the atomic density in three dimensions we need the volume of the cloud. Fitting one of our intensity images to a two-dimensional Gaussian distribution, we can recover the standard deviations in x and y (σ_x, σ_y). We can then assume that the standard deviation in z is the same as that of x due to symmetry of the magnetic field and use this in the expression for the amplitude of the three-dimensional equation to estimate a peak value for the atomic density:

$$N_{\mathcal{V}} = \frac{N_{\mathrm{a}}}{[2\pi]^{\frac{3}{2}}\sigma_x\sigma_y\sigma_z}. \tag{3.125}$$

Therefore, atomic number information can be retrieved by imaging an outgoing probe beam both with and without the presence of an atomic cloud. Logarithmically comparing the probe beam's shadow to its image then returns an absorption coefficient. We should note however, that efficient absorption imaging requires a closed transition and so care must be taken in choosing both the frequency and the polarisation of the applied light. An interesting recent development however, suggests that it is now possible to specify the atomic number in some configurations [76].

The temperature on the other hand, was calculated by considering the ballistic expansion of the cloud in the absence of applied fields. The expansion of the widths is given by [77, 78]

$$\sigma_i^2(t) = \sigma_{i0}^2 + \frac{k_{\mathrm{B}}T_{\mathrm{i}}}{M}t^2 \quad \forall i \in \{x, y, z\}, \tag{3.126}$$

and so by reloading the trap and allowing the cloud to expand for varying time intervals, the temperature can be obtained from a line of best fit. Combining the density and temperature measurements, the phase-space density can then be calculated according to

$$PSD = N_{\mathcal{V}}\left[\frac{\hbar}{\sqrt{2\pi M k_{\mathrm{B}}T}}\right]^3. \tag{3.127}$$

Atomic Spectroscopy

So far in our discussion, we have assumed that we have access to an approximately monochromatic beam near the resonance of our atomic transitions, but without justification of how this is achieved in practice.

In order to reliably and accurately know the frequency of the lasers, a technique known as *hyperfine pumping* was employed. As can be seen in Figure 3.9(Left), a field is passed through a beam sampler[21], is retro-reflected through a glass chamber containing rubidium and is detected at the photo–diode: the output of which is connected to an oscilloscope. The photodiode

21. The beam sampler is polarisation dependent and so with a half-wave plate the signal can be adjusted to reflect from $\sim 0 - 15\%$ of the beam.

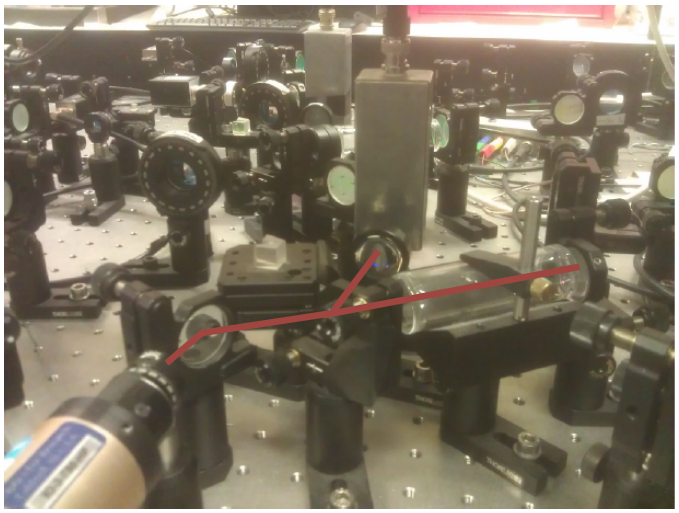

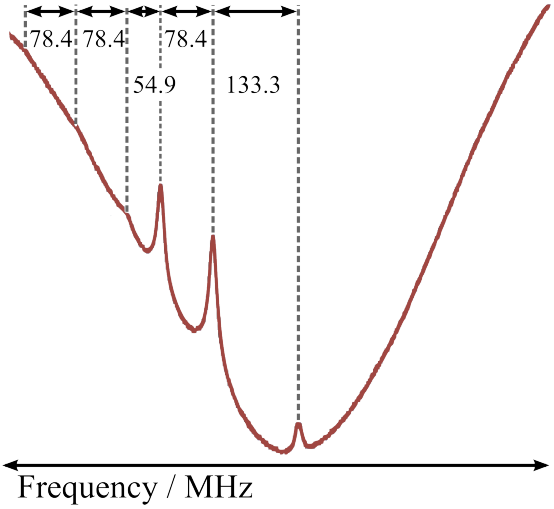

Figure 3.9: An example of the setup required for hyperfine spectroscopy (Left) and an associated oscilloscope trace (Right), annotated with relative frequencies.

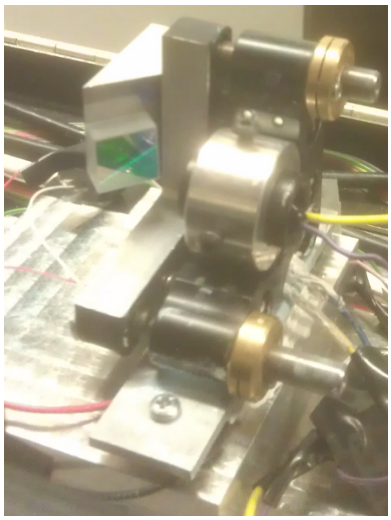

Figure 3.10: One of the extended cavity diode lasers used throughout the spatial EIT project. The diode laser and collimating lens are contained in the black plastic cylinder and held in an optical mirror mount: aligned with a suspended reflection grating. Embedded in the mirror mount is a piezo device that allows very fine tuning of the laser-grating angle.

trace is then generated by the combination of pump and probe fields (incident and reflected beams). If the laser frequency is far from resonance, then the Doppler effect ensures that the pump and probe beams interact with different atoms. If the laser is near-resonant with a transition however, then both the pump and probe fields interact with atoms that are close to stationary: resulting in sharp spikes of photo–current.

Traditionally, such an arrangement is known as *saturated absorption spectroscopy* [64]: as the pump beam is understood to excite atoms out of reach of the reflected beam. The work of Smith and Hughes [79] however, demonstrates that the saturation of the transition is actually a relativity small factor in the resulting trace. In contrast, the authors show that transient pumping between hyperfine levels is the dominant contribution.

Such a system allows for an accurate selection of the laser frequency by electronic feedback to a laser. The particular lasers used throughout the spatial EIT project were tailor-made extended-cavity diodes, as described by Arnold, Wilson and Boshier [80] and imaged in Figure 3.10. The diode is aligned in the Littrow configuration (Eq. 2.35(p. 25)) with respect to an external reflection grating (1800 lines/mm), such that changing the extended cavity length modulates the combined laser feedback. In our system, the laser and grating are attached to opposite ends of a

mirror mount, and adjusted using a small piezo.

Connecting the piezo to a signal generator, the piezo can be expanded and contracted quickly enough to provide a real–time transmittance trace for a spread of frequencies: as shown in Figure 3.9(Right). The frequency of the laser however is also temperature dependent and thus, the laser mount is thermo–electrically cooled with appropriate feed–back electronics: with further fine–tuning of the temperature carried out by altering the amount of current through the laser.

3.4 Cooling and Trapping

Having discussed the intricacies of what can be measured, we now consider the possibilities of what can be made. The starting point of any investigation in atomic physics is, naturally, to have a localised source of atoms. The most stable way of securing atoms of a particular species is to contain them explicitly in a glass cell. The processes involved in this are now well established and so vapour cells are now widely available and commerciably viable. The main disadvantage of this containment however, is that the atoms maintain thermal equilibrium with their surroundings and so are otherwise a long way from an ideal quantum environment. The ability to establish cold atom traps from first principles is therefore a mainstay of almost every atomic lab and the work previously undertaken was no exception.

For our purposes, we first consider the conceptual tools and purposes underpinning the basic MOT and SpOT[22], before reflecting on the creation of a dynamic dark SpOT: the particular configuration relevant to the experimental results presented in the next chapter.

3.4.1 The Scattering Force

If we are to build then we need a force and so we consider how an applied field can impact our atoms, as appropriate to our previous results [23].

23. This overall approach is adapted from *Atomic Physics* [64].

[22] spontaneous-force optical trap

To begin with, we consider Newton's second law as applied to a quantum system:

$$\frac{d\langle \hat{\boldsymbol{p}} \rangle}{dt} = -\langle \boldsymbol{\nabla} U \rangle \tag{3.128}$$

where $\hat{\boldsymbol{p}}$ and U are the linear momentum and energy respectively and $\langle \cdot \rangle$ represents our expectation value. We restrict ourselves to the semi-classical approach, such that the quantum mechanical dipole energy $U = -\frac{1}{2}\,\boldsymbol{d}_{\mathrm{E}} \cdot \boldsymbol{E}$ is induced[24] by a classical electric field. From our previous discussions,

$$\begin{aligned}\langle \mathrm{d}_{\mathrm{E}} \rangle &= \sum_i \langle i |\, \mathrm{d}_{\mathrm{E}}(kz - \omega t)\hat{\rho}\, | i \rangle \\ &= e^{i[kz-\omega t]} \langle g |\, \mathrm{d}_{\mathrm{E}}\, | e \rangle\, \hat{\rho}_{\mathrm{ge}} + H.c. \\ &= \mathrm{d}_{\mathrm{E}ge} \left[\left(\hat{\rho}_{\mathrm{ge}} + \hat{\rho}_{\mathrm{eg}}\right) \cos(kz - \omega t) + i \left(\hat{\rho}_{\mathrm{ge}} - \hat{\rho}_{\mathrm{eg}}\right) \sin(kz - \omega t) \right],\end{aligned} \tag{3.130}$$

where we have assumed that the induced dipole carries the same complex phase as a z-propagating incident field. The force in this direction can then be written as

$$\begin{aligned}F_{\mathrm{z}} &= -\frac{\partial}{\partial z} U \\ &= -\frac{1}{2} \langle \mathrm{d}_{\mathrm{E}} \rangle \frac{\partial}{\partial z} \langle E \rangle \\ &= -\frac{1}{2} \langle \mathrm{d}_{\mathrm{E}} \rangle \left[\frac{\partial}{\partial z} \mathcal{E} \cos(kz - \omega t) + k\mathcal{E} \sin(kz - \omega t) \right],\end{aligned} \tag{3.131}$$

which, after time-averaging, can be expressed as

$$\langle F_{\mathrm{z}} \rangle_t = -\frac{1}{2}\, \mathrm{d}_{\mathrm{E}ge} \left[\frac{\partial}{\partial z} \mathcal{E} \left(\hat{\rho}_{\mathrm{ge}} + \hat{\rho}_{\mathrm{eg}}\right) + ik\mathcal{E} \left(\hat{\rho}_{\mathrm{ge}} - \hat{\rho}_{\mathrm{eg}}\right) \right]. \tag{3.132}$$

Separating the two terms, expressing the field in terms of the Rabi frequency and including our density matrix values, then we obtain expressions for both the *dipole* and the *scattering* force *i.e.*

$$F_{\mathrm{di.}} = -\hbar \left[\frac{\partial}{\partial z} \Omega_{\mathrm{R}} \right] \frac{\Omega_{\mathrm{R}} \omega_{\Delta e}}{\Omega_{\mathrm{R}}^2 + \Gamma^2/2 + 2\omega_{\Delta e}^2} \tag{3.133}$$

and

$$F_{\mathrm{sc.}} = \hbar k \Gamma \frac{\Omega_{\mathrm{R}}^2}{2\Omega_{\mathrm{R}}^2 + \Gamma^2 + 4\omega_{\Delta e}^2}. \tag{3.134}$$

Therefore, in the absence of a Rabi gradient in z, the quadrature

24. It is the induction of the dipole that leads to the factor of a half *i.e.*

$$\begin{aligned}U &= -\int_0^E \boldsymbol{d}_{\mathrm{E}}(\boldsymbol{\mathcal{E}}) \cdot d\boldsymbol{\mathcal{E}} \\ &= -\frac{1}{2}\, \boldsymbol{d}_{\mathrm{E}} \cdot \boldsymbol{E}\end{aligned} \tag{3.129}$$

where the induced dipole is proportional to $\boldsymbol{E}$.

component of the net force dominates. Recalling our expression for the scattering rate, we see that this force is simply the rate of momentum impacting on the atoms from decay: justifying both the name and the out of phase nature of this phenomenon. Furthermore, if we again re-express our equation in terms of saturation intensity (Eq. 3.106(p. 91)), and consider the limit of infinitely powerful input, then the maximum possible force is

$$F_{\text{sc. max}} = \hbar k \frac{\Gamma}{2}. \tag{3.135}$$

If we insert the decay rate and transition wavelength for absorption across the D_2 line in Rb-87, then the maximum acceleration a_{max} is $\sim 1 \times 10^5\,\text{m}\,\text{s}^{-2}$. Considering this is four orders of magnitidue greater than the gravitational field, then an applied field, even in the absence of strong focussing or shaping, can be used to heavily influence the positions of our atoms, the first requirement of a trap.

If we then consider the symmetric application of six identical lasers aligned along the three Cartesian axes, where each is pointing towards the origin, then each beam applies a force on the atom towards the centre. Superficially, this may seem equivalent to having no force on the atoms, but we have neglected the Doppler effect and thus, such arguments only apply to atoms at rest. Recalling that a *moving* atom will experience a higher frequency from opposing light, and a lower frequency from supporting light, then there is an imbalance in the forces. Specifically, if our applied light fields are deliberately detuned from rest resonance, then we create a situation such that any atom moving away from the centre experiences a relatively greater opposing force. This system configuration is known as an *optical molasses*. Ideally therefore, the atomic kinetic energy within the beam intersection decreases to zero over time. The reality however is quite different, for two main reasons.

First of all, although varying the detuning of the applied fields allows us to slow moving atoms, it is an exclusive process. Detune too much and the force on low velocity atoms is not enough; detune too little and the force on higher velocity atoms is not sufficient to induce interaction. In this case, the system forces

us to choose, creating a *capture range* for our atomic velocities.

And secondly, the ideal limit ignores the effect of fluctuations. The two main sources of fluctuations are spontaneous emission and absorption. Although the net force due to spontaneous emission averages to zero, fluctuations in this force lead to a three-dimensional random walk of recoil velocities in the atom, such that the atom is kept from absolute cooling. The fluctuations in absorption are similar, but are due to the probabilistic nature of the scattering rate. For every time increment, the specific number of absorbed photons will vary and this leads to an additional random walk in velocity, but constrained to one-dimension per beam due to the more directed nature of the force. The combination of these effects leads to a predicted minimum value for the temperature T_{D}:

$$T_{\mathrm{D}} = \frac{1}{2}\frac{\hbar}{k_{\mathrm{B}}}\Gamma \tag{3.136}$$

where T_{D} is known as the Doppler temperature. The details of this derivation can be found in *Atomic Physics* [64], but as it is only valid for $\mathcal{I} \ll \mathcal{I}_{\mathrm{sat}}$, we will not consider it here.

3.4.2 A Magneto-Optical Trap

The ability to slow our atoms by force is a necessary, but not sufficient, condition for building a trap. For steady confinement we also need to introduce a spatial dependence to the force, in order that atoms are held in a localised region of interest.

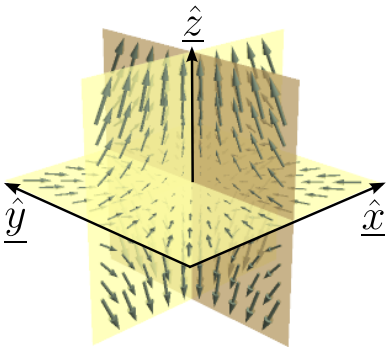

Figure 3.11: A 3D overview of the vector field created by two coils in the anti-Helmholtz configuration, where the magnetic field is given by $\boldsymbol{B} = (-x/2, -y/2, z)$.

Principles

There are many ways of introducing such a dependence, but perhaps the most straightforward approach is to use magnetic fields to break the spatial symmetry. At the beginning of the chapter, we exposed how an applied magnetic field affects the atomic energy levels and a key feature of these discussions was that the magnetic field can be used to reveal spatial structure in the system. As the magnetic field is increased, the projections of the angular momentum reveal the precession of the Larmor frequency and this directly leads to a change in resonance energy

of the atomic transitions which is direction dependent. Using a similar principle therefore, the introduction of a spatially dependent magnetic field can be used to affect different atomic polarisations differently and thus, careful selection of the polarisation of our crossed fields can be used to strongly favour one set of resonances over another. Subsequently, the combined effect preferentially scatters the light, cooling and and pushing the atoms towards the trap centre.

Particulars

The mechanism of the MOT is outlined in Figure 3.11. The symmetry that we are looking for is a radial signal that increases with distance from a central point and such a field can be created with only two coils of wire. The arrangement in this case is known as the *Anti-Helmholtz configuration*, where identical coils are separated and aligned antisymmetrically, such that their currents flow in opposing directions. In this setup, the magnetic fields cancel at the centre, but for small distances around this point the fields increase linearly with radius and this imposes a detuning between the differing circular polarisations, as outlined in Figure 3.12 [25]. Starting with a small detuning, we see that as the atoms get further from the centre, the degeneracy of interaction is broken more strongly, such that there is more scattering and hence a proportionally greater force. Crucially, as the magnetic field is antisymmetric across quadrants, the opposite detunings are imposed for atoms travelling in the negative axis, and so for correctly chosen polarisations, there is always a restoring force. Although this shares certain conceptual similarities with an optical Molasses, the key differences are that the opposing force is dependent on the atoms' distance from the origin, and also that the system is strongly polarisation dependent. Furthermore, we emphasise here that this is not what is usually termed a magnetic trap. By definition, the magnetic field is a foundational component, but the fields are often only on the order of 10 G and so do not meaningfully contribute to the force on the atoms. Another consideration is that the laboratory environment is not itself isolated from magnetic fields, whether

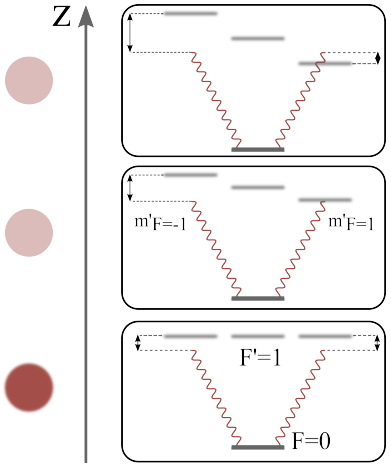

Figure 3.12: A one-dimensional projection of the atomic energy levels as an atom leaves the centre of a magnetic quadropole field.

25. Where we note that for ^{87}Rb, the combination of angular momentum causes the $m_F = -1$ and $m_F = +1$ states to rise and fall in energy respectively on application of a positive magnetic field.

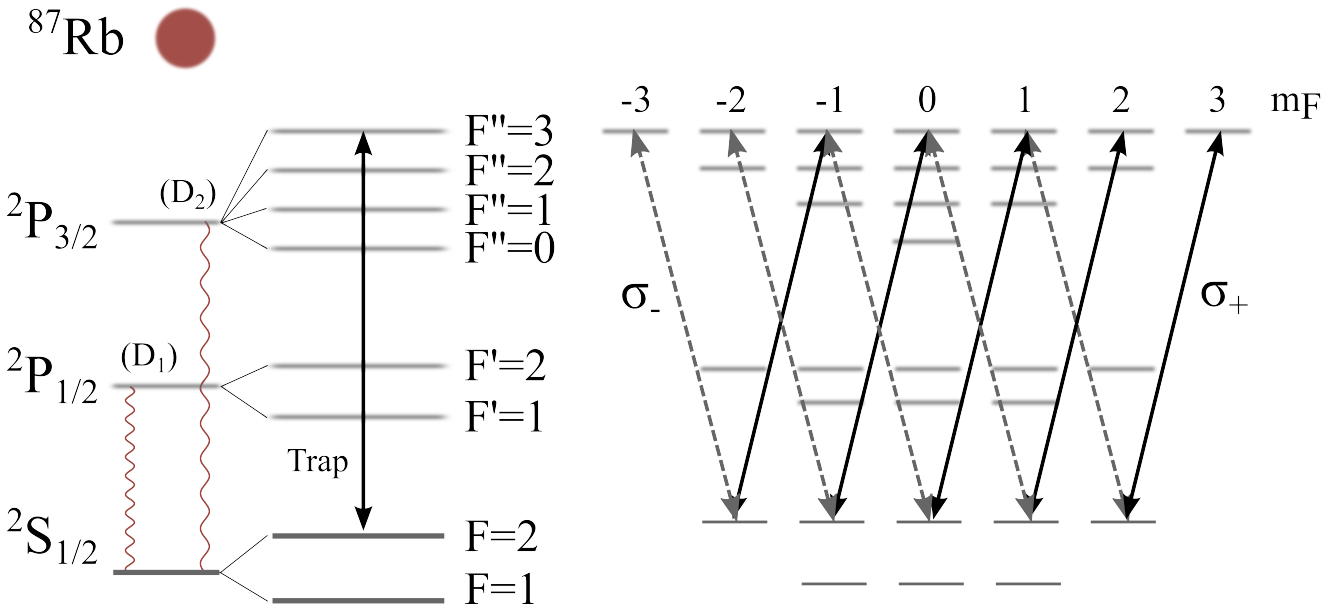

Figure 3.13: An outline of the atomic level scheme for Rubidium-87, highlighting the trapping transition and associated couplings for circularly polarised light.

local or geomagnetic, and so an additional set of coils have to be arranged and adjusted around the trapping setup to cancel out these fields. These coils are known as the *compensation coils*. With all of these considerations in mind however, it is now theoretically possible to create a MOT, but as is often the case, the reality of atomic transitions complicates things.

So far, we have tacitly assumed that we are working with a completely isolated set of atomic transitions, but of course this is not possible. If we consider the energy level structure for an alkali metal, the two lowest-frequency transitions are usually sufficiently separated by spin-orbit coupling to be treated independently, but the hyperfine splitting is very interconnected and this makes it impossible to form a trap using only one frequency. This can be seen from the selection rules for electric dipole transitions:

$$\Delta F = 0, \pm 1;\ F + F' \geq 1 \text{ and } \Delta m_F = 0, \pm 1, \tag{3.137}$$

as derived from symmetry considerations and where F' represents an excited state. Under these constraints, continually applied circularly polarised light will move the atomic population to either projection extreme of $|F = I + \frac{1}{2}\rangle$, forming a *stretched*

state (Figure 3.13). It is perhaps tempting to think an applied field on the $|F = I + \frac{1}{2}\rangle \rightarrow |F' = I + \frac{3}{2}\rangle$ transition would then simply oscillate back and forward without interruption, but such a field can also excite atoms to $|F' = I + \frac{1}{2}\rangle$ and this state can decay to the $|F = I - \frac{1}{2}\rangle$ ground state. Although this off-resonant excitation is far less probable, lost atoms cannot reenter the cycle and thus, steady-state conditions ensure all atoms find their way to the ground state: outside the field's influence. In general therefore, two lasers are needed to establish and maintain a MOT, where the second is superimposed with the first, but coupled between the lower ground state and an excited state whose relaxation coincides with $|F = I + \frac{1}{2}\rangle$. The complete beam configuration is outlined in Figure 3.15 for the specific case of ^{87}Rb, where the choice of *repumping* transition is informed by later work, as discussed in subsection 3.4.3.

Practice

Having considered the theoretical subtleties, we now highlight how a MOT can be established in practice. At the outset, we should note that the fundamentals of this system were first implemented by A. Vernier [81] before subsequent development by G. Walker and N. Radwell [82, 83], as directed and guided by S. Franke-Arnold. My particular role therefore was, in conjunction with Dr Radwell, to optimise, maintain and extend the system for applied experiments: particularly regarding the experiments described in Chapter 4 (p. 111). As this experiment focussed on the spatial patterns however, we will not explicitly consider the experimental optimisations in detail.

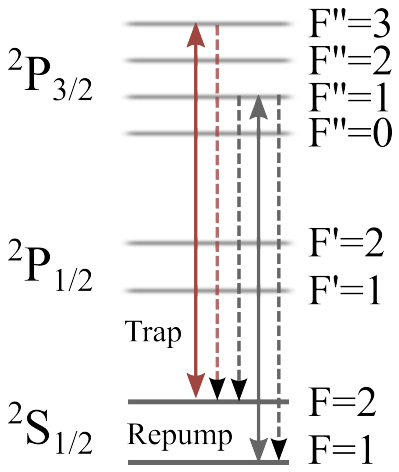

Figure 3.15: The beam configuration used for establishing a MOT in Rubidium-87, as related to this work.

The key practical considerations for creating a MOT are then what atomic species to load into the trap; how to source and arrange the two relevant coupling frequencies; what parameters to use for the two magnetic field coils; and how to electronically facilitate the whole process.

The system at Glasgow exclusively uses atomic Rubidium, as this allows for trapping frequencies close that of a standard CD read/write beam: greatly lowering the cost of the lasers. The refined coupling frequencies however are a matter of choice a

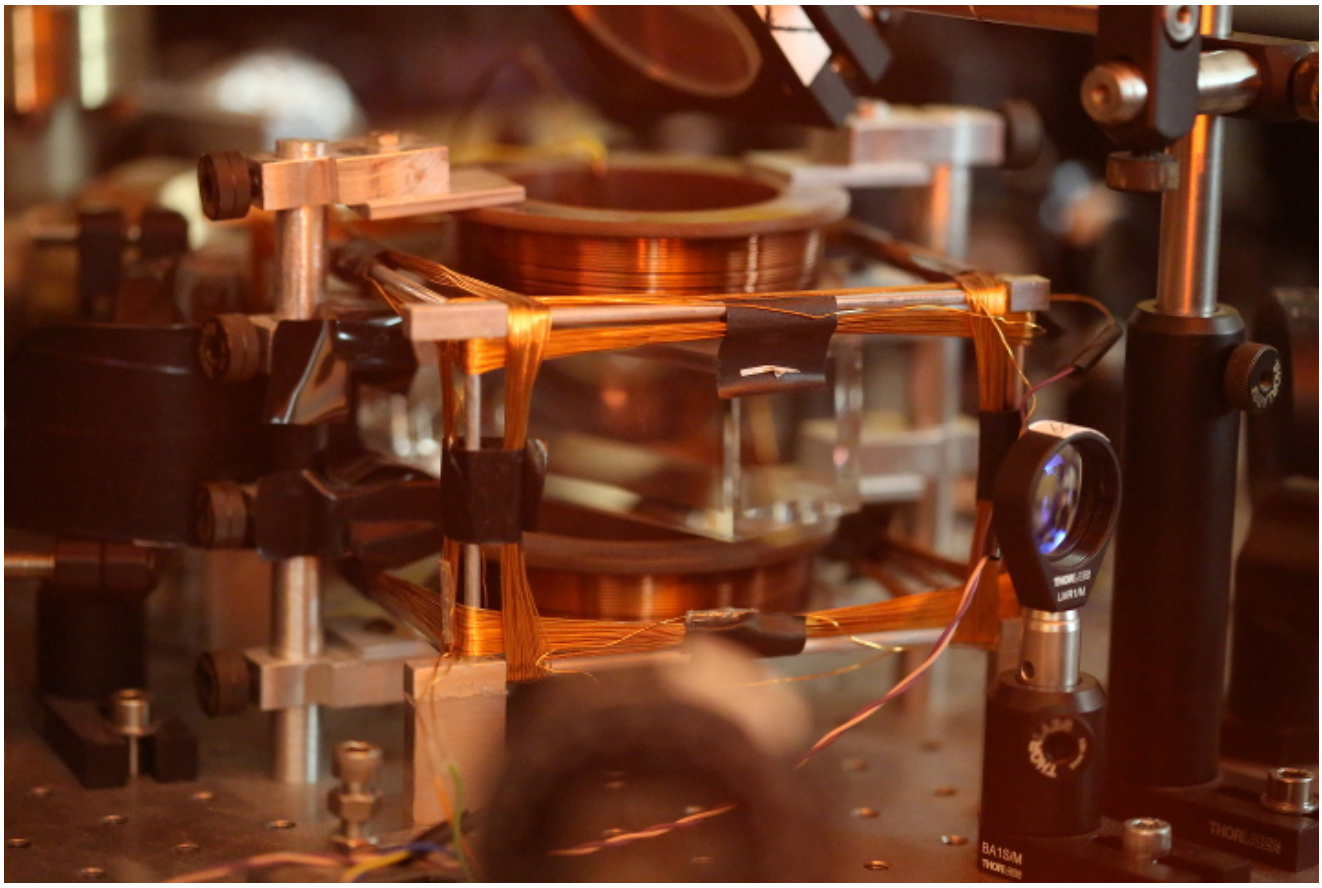

Figure 3.14: An image of the magneto-optical trap created in practice (courtesy of Ádám Selyem), where the atomic cloud is clearly visible at the centre of the glass chamber. The quadrupole field and the compensation/bias fields are created with the circular and rectangular coils respectively.

matter of choice a matter of choice a matter of choice a matter of choice a matter of choice a matter of choice.

Coupling frequencies

As outlined above, there is an obvious choice for trapping in an alkali metal and for our Rubidium system this is the $5^2S_{\frac{1}{2}}F = 2 \rightarrow 5^2P_{\frac{3}{2}}F = 3$ transition, where the applied field is appropriately circularly polarised to allow for cooling and trapping. The natural choice of repump transition is more ambiguous, but for our purposes, the transition $5^2S_{\frac{1}{2}}F = 1 \rightarrow 5^2P_{\frac{3}{2}}F = 1$ was used, in the understanding that we will soon be including an additional field. The trap beam was then configured as described above, but for convenience, the counter-propagating arms of the MOT were created with mirrors, rather than with separate sources, and the

repump was only overlapped with the trap beam in the $x - z$ plane.

The source of both frequencies are the locked, custom-made ECDL lasers discussed above (§ 3.3.2 (p. 95)), with offsets and detunings introduced by AOMs. Following the outline above, the trap frequency was red detuned by 17 MHz to maximise the atom number (using absorption imaging), while the repumping laser was held at resonance. The associated AOM parameters are listed in Table 3.4.

For the creation of the MOT, the $\frac{1}{e^2}$ beam radii of the trapping and repump fields were circa 1.0 and 0.6 cm respectively, with associated powers of approximately 6.5 mW per arm and 1 mW respectively.

Magnetic coils

The circular trap coils used throughout were 8 cm in diameter, 6.9 cm separated and wound with 130 turns. The optimised current was found to be 2.4 A [82] and this leads to a field gradient of approximately 10 G/cm. From the hyperfine Zeeman shift (§ 3.1.3 (p. 67)), the MOT coils then cause a shift of approximately 7.0 MHz cm^{-1} and 9.3 MHz cm^{-1} from the trap centre for $m_F = 1$ in the ground and excited states respectively.

The cuboidal compensation coils had a base field gradient of approximately 1 G/cm and were used to cancel out the Earth's magnetic field. As suggested, they were also used during experiments to define the local quantisation axis, either along or close to the beam propagation path. In this case, the applied field was only ever strong enough to break the degeneracy of the Zeeman projections, rather than to significantly changing the resonance frequency: where the level shifts were less than 2.5 % of the excited state's natural width.

Under absorption imaging conditions, both the compensation and quantisation fields are active and so optimisation of the absorption profile requires a delicate balance between these fields and the incoming optical probe detuning. Under normal operating conditions, the x(long) and y(short) axes of the compensation coils carried currents of 0.38 and 0.44 A respectively,

such that the quantisation field introduced a 2.5 MHz shift to the resonance peak.

The circular quadrupole and rectangular compensation coils can be seen in Figure 3.14, where a long-exposure time allows the atomic cloud to be seen in practice.

Locking and Driving electronics

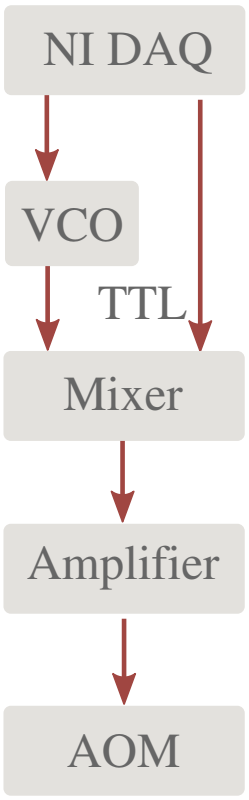

Figure 3.16: An overview of the driving electronics for the laser controlling AOMs.

The lasers have to be locked with precision and this is done electronically using a signal generator, phase lock-in amplifier and the photo-diode (PD) trace generated from the hyperfine pumping process.

The best signals from the photo-diode are usually a result of the cross-over between two transitions, where both red and blue detuned frequencies interact, and so these are the peaks used to lock the lasers. A lock-in amplifier was then used to create an error signal from a 10 kHz reference signal and the PD trace. The generated error signal is then used to modify the piezo, such that drifting of the laser frequency is met with a countering modulation of its cavity length. In turn, this modifies the frequency of the laser, enabling frequency stabilisation.

Locking the lasers to cross-over transitions however, in addition to the desire for detuning, means that the signal has to be further frequency modulated and this is done using an AOM.

The overall procedure is outlined in Figure 3.16, where the *National Instruments DAQ* was connected to a laboratory PC and controlled using the LabVIEW software environment. In essence, the AOM generates acoustic waves based on a radio frequency input (linearly to a good approximation) and so using an analogue output port, the acoustic frequency can be modulated at will to to create frequency deflections according to the methods outlined in § 2.4 (p. 47). The mixer simply combines the VCO output with a digital stream of TTL pulses, such that the AOM can be switched on and off independently. In practice, the mixer can also be replaced with voltage-controlled attenuators, which perform the same function and this was done subject to convenience.

Cloud Parameters

The combination of the above considerations allows the creation of a MOT. Releasing the Rubidium in the vacuum, then, in the presence of the compensation, quadrupole, trapping and repump beams; the atomic vapour forms a cloud. This takes on the order of 0.1 to 10 s in principle, as dictated by the background pressure. Unfortunately, the pressure gauge of the current system is broken, but the experimentally determined loading rate was approximately 6 s.

As suggested previously, the size can be inferred from a camera image and the number and temperature can be calculated through absorption imaging, where care is taken to ensure that the probe shadow reaches zero for maximum resolution and the quantisation axis is turned on 800 µs before the probe beam (allowing for the magnetic rise time). Consequently, it was possible to achieve a peak atom number and density of around 3×10^8 atoms and $4 \times 10^{10}\,\mathrm{cm}^{-3}$ respectively, where the parameters under normal operating conditions are listed[26] in Table 3.1.

MOT	Axis	
Parameter	x	y
N_a	$1.3(1) \times 10^8$	
Size/µm	1300(7)	850(7)
$N_\mathcal{V}/\mathrm{cm}^{-3}$	$9.3(8) \times 10^9$	
Temp./µK	388(7)	137(7)

Table 3.1: An overview of the key MOT parameters.

26. Here, we note that the measured temperature is significantly different between axes. The source of this discrepancy is currently unknown, but is likely to be a result of the asymmetry of the magnetic field between $\underline{\hat{x}}$ and $\underline{\hat{y}}$ (as mandated by Maxwell's equations) and the added presence of gravity in the latter.

3.4.3 *A holographically-shaped dark SpOT*

We have discussed how a MOT has been realised that approaches the theoretical density limit, but whether in the implementation of quantum memories, the loading of BEC[27]s or the enhancement of many non-linear effects in general, increasing the density further has many immediate applications.

The limitations of the cooling and trapping effectiveness are induced by high density collisions between atoms in the excited and ground states. After the MOT has been fully loaded, then unnecessary trapping forces still perturb the atoms, increasing the size and density that could otherwise be achieved. Ketterle, Davis, Joffe, Martin and Pritchard however, suggested a solution [84]. They pointed out that the two processes of one: capture and cooling and two: storage, benefit from different regimes and suggested the use of a repump beam with a hole in the centre. The original dark SpOT actually formed this hole by

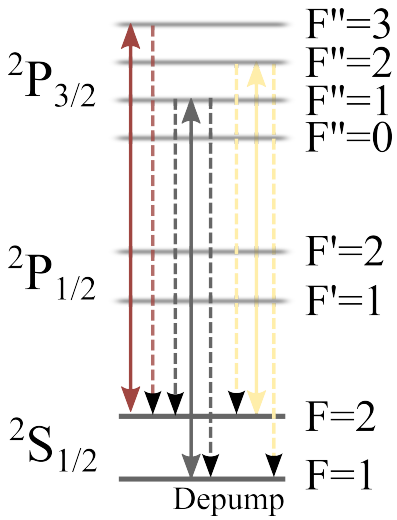

Figure 3.17: The beam configuration used for establishing a dynamic dark SpOT in Rubidium-87.

27 Bose-Einstein Condensate

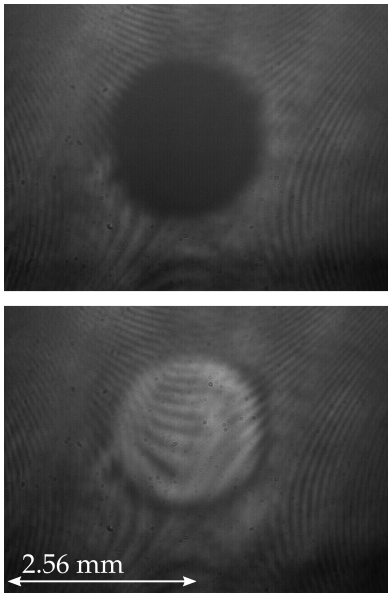

Figure 3.18: A camera image of both the Repump and the repump & depump beam profiles overlapped.

SpOT Parameter	Axis	
[Delay/µs]	x	y
N_a[2000]	$8.6(1) \times 10^7$	
N_a[3000]	$7.5(1) \times 10^7$	
Size [2000]	291(7)	315(7)
Size [3000]	291(7)	315(7)
$N_{\mathcal{V}}$[2000]	$2.1(7) \times 10^{11}$	
$N_{\mathcal{V}}$[3000]	$2.0(7) \times 10^{11}$	
Temp./µK	38(7)	114(7)

Table 3.2: An overview of the SpOT parameters, where the bracketed terms denote the probe delay and the units are consistent with the table above.

using a 10 mm spot on a glass plate, which was then imaged onto the atoms. Simply blocking the repump light worked for earlier experiments, which used different atomic species, but for Rubidium trapping the pumping rates make this approach prohibitively inefficient. Therefore, an extra beam has to be introduced that creates an extra relaxation path to the ground state, in order to induce more relaxation. And this is called the *depump* beam. Therefore, we have in a sense, gone full cycle. The repump beam was introduced to stop atoms going into the lower ground state, and now we consider having to take the repump away to stop atoms leaving the lower ground state.

The fixed vortex in dark SpOTs however, normally lead to severely reduced trap loading rates and become impractical even when the dark core approaches the size of the MOT. The system at Glasgow however, has overcome this problem with the introduction of dynamic switching. After first loading a MOT normally, a spatial light modulator can then be used to dynamically switch the repump and depump beams simultaneously, to form a dark SpOT, which allows the SpOT to work with already pre-cooled atoms.

This configuration then allowed for the first large-scale, systematic study of vortex size against trap density. The fascinating result of this experiment was that the best repumping beam size was deemed to be at 20times the SpOT radius [83]. Furthermore, the system at Glasgow demonstrated a preservation of the temperature on switching in combination with an atom number retention of approximately 75%. A rare example of a best of all worlds result. Furthermore, since the original study, the obtained temperature has been lowered further. A summary of the normal operating conditions can be found in Table 3.2.

Beam	Power/mW	
Trap	Before Splitting	Per Arm
	23.7	6.5
Repump	Before SLM	Shaped At Trap
	3.65	0.183
	Unshaped At Trap	
	1.00	
Depump	Before SLM	Shaped
	0.2	60×10^{-3}

Table 3.3: The beam powers for the SpOT under normal operation.

Beam	Radio Frequency/MHz	Manufacturer
Trap	58.1 (double passed)	Crystal Technologies Inc 3080-122
Repump	78.4	NEOS AOM 24080
Depump	54.8	Crystal Technologies Inc 3080-122

Table 3.4: The normal AOM radio frequencies for the three main coupling beams in the dark SpOT system, along with manufacturers.

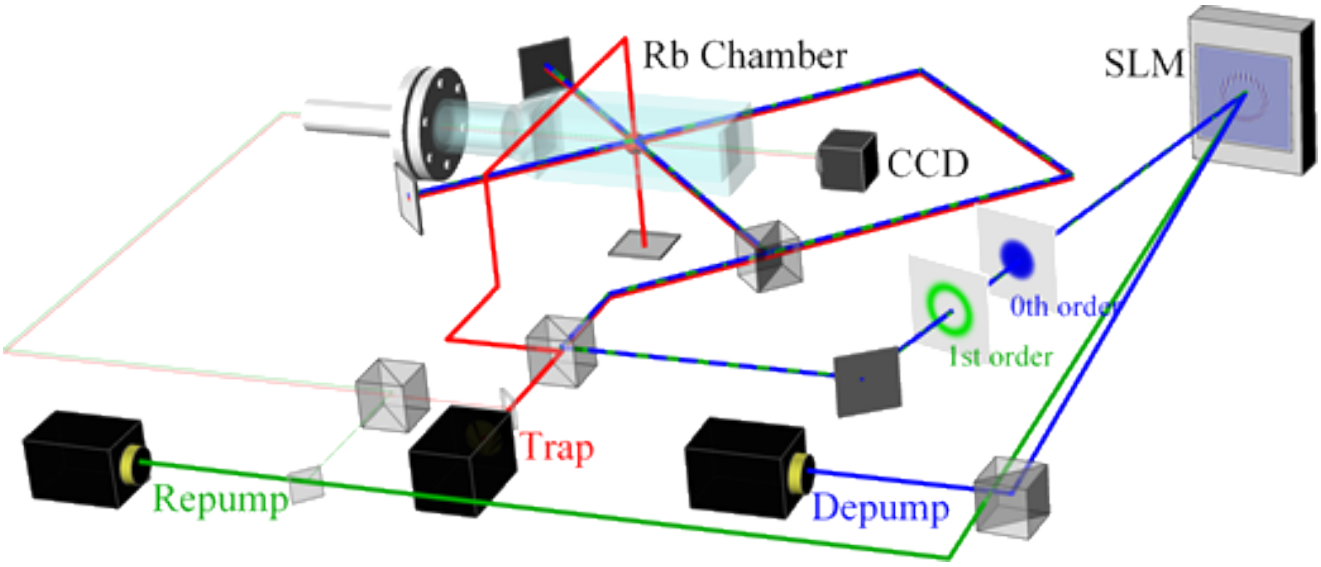

Figure 3.19: A simplified account of the spatial beam configuration needed to produce a dynamic dark SpOT (reproduced with the permission of the authors) [83].

SCULPTING SHADOWS: THE ARBITRARY CONTROL OF TRANSPARENCY IN ATOMS

4

Carl Gustav Jung, writing in *Modern Man in Search of a Soul*, famously asked the question:

> *How can I be substantial if I do not cast a shadow? I must have a dark side also if I am to be whole.*

A rhetorical question, with slight vampiric undertones, it is a powerful, if curious, testament to the depth and reach of mankind's attentions that such questions have now been answered.

First observed in 1991, it may be an inherent aptness of EIT[1], that its discovery carries revelation: how, with the careful application of light, matter need not cast a shadow after all. Following both the theme of this work and the challenge of Jung's questioning, we will see how the mechanism can be extended from a simple point interaction to that of the whole of atomic space. A discovery, which has opened a window on the future of many nonlinear interactions and through which we will shed light on this quantum puzzle; an optical mystery: neither maleficent nor benign.

Outline

[1] Electromagnetically Induced Transparency

4.1 Trapping & Transparency

Previously, first in our look at holograms and second, in the creation of a dynamically shaped dark SpOT, we have seen how coherence and cooperative behaviour respectively can have powerful effects. In this chapter however, rather than considering holography or the macroscopic coupling of population rates, we will consider the more fundamental mechanism of EIT: an effect that can be observed with only three atomic states.

4.1.1 Superpositions & Optical Coherence

Although it is possible to find classical analogies [85, 86], EIT is a profound consequence of quantum interference and its underlying mechanism is interwoven with the founding constitutions of quantum mechanics. Such is the case, and in order to emphasize its fundamental nature, we will consider it here from first principles, beginning with the curiously extrinsic concept of *superposition*.

Recalling the time-dependent Schrödinger equation in its most general form:

$$\hat{H}|\psi\rangle = i\hbar\frac{\partial}{\partial t}|\psi\rangle, \tag{4.1}$$

we note that, similarly to the case of electromagnetism, it is linear in ψ and as such, the principle of superposition applies[2]. To reiterate, this is a general property. At this stage in our discussion, we are of course familiar with the application of superposition in regards to electric fields, but it is important to realise that it is this very same principle that is behind so much of quantum's infamous controversy. The mysterious properties of this process arise from the notion that wavefunctions are never what are being measured, rather that they are the foundation from which states collapse by measurement. In practice therefore, the properties of a quantum superposition are uniquely different from the simple mathematical reality that a sum of solutions to Eq. 4.1 is also a solution.

2. (See § 2.1.5 (p. 21) and Eq. 2.25)

If we consider the position of an arbitrary body in two dimensions, we might intuitively describe it as the sum or super-

position of two weighted bases $|r\rangle = x|x\rangle + y|y\rangle$, or equally, we might consider it as a single state in a diagonal basis $|r\rangle = d|\text{Diag.}\rangle$, where d is simply a multiplicative constant. The importance here is that we are completely free to choose and, as such, it is our choice of perspective which determines whether or not a property is in a state of superposition.

This can be seen explicitly by considering the two simplest superposition states:

$$|\pm\rangle = \frac{1}{\sqrt{2}}\left[|0\rangle \pm |1\rangle\right]. \tag{4.2}$$

If we make measurements in the $\{|0\rangle, |1\rangle\}$ basis *i.e.* $\langle 0|\pm\rangle^2 = \langle 1|\pm\rangle^2 = \frac{1}{2}$, then we immediately see that there is no distinction between $|+\rangle\&|-\rangle$ states. Whereas if we make measurements in the $\{|+\rangle, |-\rangle\}$ basis, there of course would be no problem in distinguishing the states.

In general however, the situation is rather more complicated. Assuming that all physical properties have wave properties (these days a fairly safe assumption) then the two regimes can move from one to another depending on their relative phase. What distinguishes the two therefore, is the small matter of coherence...

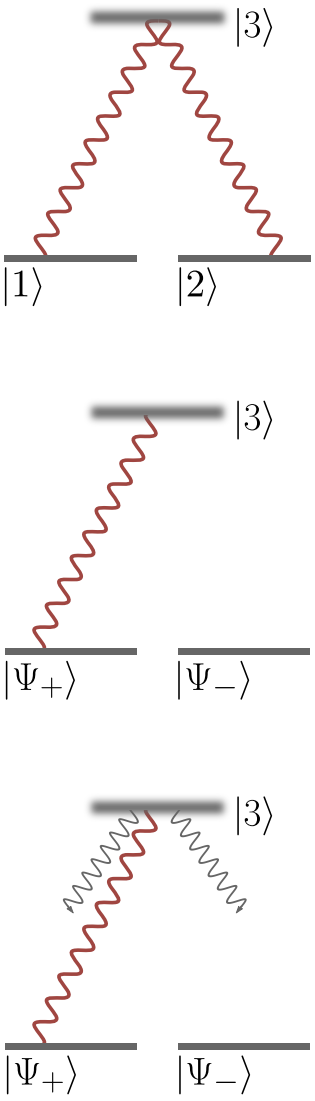

Figure 4.1: A schematic outline of a three level system under the influence of two electric-dipole allowed fields: in the eigenstates of the natural atomic energy levels (top); where the ground states are expressed in superposition (middle) and the superposition picture, including relaxation from the excited state to the two ground states (bottom).

4.1.2 *Coherent Population Trapping (CPT)*

With this understanding, expanding on the treatment by Grynberg, Aspect and Fabre [87], we can consider how atomic energy levels transform after the application of coherent light. Consider a three-level system of the style outlined in Figure 4.1(top). Such a system can be described in its most general form by the wavefunction:

$$|\Psi_0(\boldsymbol{r},t)\rangle = \alpha_1 e^{-i\frac{t}{\hbar}U_1}|1\rangle + \alpha_2 e^{-i\frac{t}{\hbar}U_2}|2\rangle + \alpha_3 e^{-i\frac{t}{\hbar}U_3}|3\rangle \tag{4.3}$$

where $\alpha_i = \alpha_i(\boldsymbol{r},t)\ \forall i \in [1,3]$ are the probability amplitudes. Following our previous discussion, the bare Hamiltonian of this system and that under interaction with a dipole allowed field,

can be written as

$$\begin{aligned}
\hat{H}_0 =& \hat{\mathbb{I}}\, \hat{H}_0\, \hat{\mathbb{I}} && (4.4)\\
=& \sum_i^3 U_i |i\rangle\langle i| \text{ and} && \left(\text{From Eq. 3.34}\right)\\
\hat{H}_{d_E} =& |1\rangle\langle 1|\hat{H}_{d_E}|3\rangle\langle 3| + |2\rangle\langle 2|\hat{H}_{d_E}|3\rangle\langle 3| + H.c. && \left(\text{From Eq. 3.38}\right)\\
\equiv& d_{13}|1\rangle\langle 3| + d_{23}|2\rangle\langle 3| + H.c.
\end{aligned}$$

respectively, where we have defined d_{i3} for convenience. Figure 4.1(top) therefore represents our usual perspective of this atomic interaction. Following our previous discussion however, we can consider a transformation to a new basis, such that the atomic ground states can be expressed as the two orthogonal superpositions:

$$|\Psi_+\rangle = \frac{1}{n}\left[d_{13}e^{-i\frac{t}{\hbar}U_1}|1\rangle + d_{23}e^{-i\frac{t}{\hbar}U_2}|2\rangle\right] \text{ and} \quad (4.5)$$

$$|\Psi_-\rangle = \frac{1}{n}\left[d_{23}^* e^{-i\frac{t}{\hbar}U_1}|1\rangle - d_{13}^* e^{-i\frac{t}{\hbar}U_2}|2\rangle\right], \quad (4.6)$$

where $n = \sqrt{d_{13}^2 + d_{23}^2}$[3]. Expanding the dipole interaction in this new basis, the interaction elements can then be expressed as

3. Where we have assumed real dipole matrix elements.

$$\langle\Psi_+|\,\hat{H}_{d_E}\,|3\rangle = \frac{1}{n}\left[d_{13}^2 e^{i\frac{t}{\hbar}U_1} + d_{23}^2 e^{i\frac{t}{\hbar}U_2}\right] \text{ and} \quad (4.7)$$

$$\langle\Psi_-|\,\hat{H}_{d_E}\,|3\rangle = \frac{d_{13}d_{23}}{n}\left[e^{i\frac{t}{\hbar}U_1} - e^{i\frac{t}{\hbar}U_2}\right]. \quad (4.8)$$

If we consider the Λ-configuration, where the two ground states are degenerate, then $U_1 = U_2 = 0$ and[4] we uncover the surprisingly concise result:

4. For $U_1 = U_2 \neq 0$, the result acquires a constant phase factor, but this can be set to zero without loss of generality.

$$\hat{H}_{d_E} = n\,|\Psi_+\rangle\langle 3| + H.c.. \quad (4.9)$$

Therefore, having not yet considered the *form* of the interaction, we can immediately see that the Λ system under coherent coupling is fundamentally equivalent to a simple two-level system. This is a profound statement and can be understood as the result of destructive interference between the transition probabilities. If we now consider relaxation from the excited state (Figure 4.1:bottom), we can see how under steady-state conditions, $|\psi_-\rangle$ becomes a *dark state* of interaction: only accessible by

spontaneous decay[5]. Therefore, simply by applying a monochromatic field; we can populate a coherent superposition of atomic ground states free from further interaction, hence *CPT*[6]. Such a configuration is illustrative of the quantum interference available with superposition states and is the basis for many trapping experiments, but the requirement of degenerate ground states is prohibitive for many applications. As pointed out by Grynberg *et al.*, this is particularly a problem when considering stray magnetic fields: something which we will consider in the next section.

5. The incoherent nature of spontaneous decay is what makes this transition possible in practice: as ultimately, decoherence will add extra phase terms to Eq. 4.7.

Therefore, to investigate the more general case, we consider the form of the interaction Hamiltonian for the same Λ system represented in Figure 4.1. We consider two fields, $\mathcal{E}_1 \cos(\omega_1 t)\hat{\underline{\varepsilon}}_1$ and $\mathcal{E}_2 \cos(\omega_2 t + \varphi)\hat{\underline{\varepsilon}}$, such that φ models the total relative phase between them and the symbols carry their usual meanings. Similarly to that done before, this then naturally leads to the Hamiltonian:

$$\hat{H}_{\mathrm{d_E}} = \hbar \begin{pmatrix} 0 & 0 & \Omega_{\mathrm{R1}} \cos\omega_1 t \\ 0 & 0 & \Omega_{\mathrm{R2}} \cos(\omega_2 t + \varphi) \\ \Omega_{\mathrm{R1}} \cos\omega_1 t & \Omega_{\mathrm{R2}} \cos(\omega_2 t + \varphi) & 0 \end{pmatrix} \tag{4.10}$$

where $\Omega_{\mathrm{Ri}} = -\mathcal{E}_{\mathrm{i}} \langle i \,\|\mathrm{d_E} \cdot \hat{\underline{\varepsilon}}_{\mathrm{i}}\|\, 3\rangle \;\forall\, i \in \{1,2\}$. Extending the state $|\Psi_-\rangle$ in this regime, then

$$|\Psi_-\rangle = \frac{1}{\sqrt{\Omega_{\mathrm{R1}}^2 + \Omega_{\mathrm{R2}}^2}} \left[\Omega_{\mathrm{R2}}^* e^{-i\frac{t}{\hbar}U_1}|1\rangle - \Omega_{\mathrm{R1}}^* e^{-i\frac{t}{\hbar}U_2 - i\varphi}|2\rangle\right] \tag{4.11}$$

and therefore

$$\langle \Psi_- | \hat{H}_{\mathrm{d_E}} | 3\rangle = \frac{\Omega_{\mathrm{R1}}\Omega_{\mathrm{R2}}}{\sqrt{\Omega_{\mathrm{R1}}^2 + \Omega_{\mathrm{R2}}^2}} \Big[\cos\omega_1 t e^{-i\frac{t}{\hbar}[U_3 - U_1]} - \cos(\omega_2 t + \varphi) e^{-i\frac{t}{\hbar}[U_3 - U_2] + i\varphi}\Big]. \tag{4.12}$$

This expression can then be simplified using familiar identities:

$$\cos(\omega_2 t + \varphi) e^{-i\frac{t}{\hbar}[U_3 - U_2] + i\varphi} = \frac{1}{2}\left[e^{-i\frac{t}{\hbar}[U_3 - U_2 - \hbar\omega_2 - 2\frac{\hbar}{t}\varphi]} + e^{-i\frac{t}{\hbar}[U_3 - U_2 + \hbar\omega_2]}\right]. \tag{4.13}$$

[6] Coherent Population Trapping

For optical frequencies near resonance, $(U_3 - U_{\mathrm{i}}) - \hbar\omega_{\mathrm{i}} \ll (U_3 - U_{\mathrm{i}}) + \hbar\omega_{\mathrm{i}}\ \forall i\ \in\ \{1,2\}$, we can then write:

$$\langle \Psi_- | \hat{H}_{\mathrm{d_E}} | 3 \rangle \simeq \frac{\Omega_{\mathrm{R1}}\Omega_{\mathrm{R2}}}{2\sqrt{\Omega_{\mathrm{R1}}^2 + \Omega_{\mathrm{R2}}^2}} \left[e^{-i\frac{t}{\hbar}[U_3 - U_1 - \hbar\omega_1]} - e^{-i\frac{t}{\hbar}[U_3 - U_2 - \hbar\omega_2 - 2\frac{\hbar}{t}\varphi]} \right]. \tag{4.14}$$

Therefore, destructive interference on the transition takes place when the two beams are both Raman resonant and temporally coherent *i.e.* when

$$\hbar \left[\omega_1 - \omega_2 - 2\frac{\varphi}{t} \right] = U_2 - U_1. \tag{4.15}$$

This more general condition allows the dark state to be maintained in the presence of stray fields[7] and other energising effects, simply by compensating the relative detuning of the lasers and this insight has proved very useful in the work undertaken. With some possible controversy, here we consider the phenomenon of EIT as the result of this fundamental effect.

7. To clarify, this only applies to stray fields that change the energy of the state, not the coupling in general.

4.1.3 *Electromagnetically Induced Transparency*

There is widespread disagreement in the literature on what distinguishes EIT from CPT. Generally speaking, if one of the two applied fields in a three-level system is very weak in intensity compared to the other one, then a drop in probe absorption at resonance is described as electromagnetically induced transparency. Such a configuration, which we will refer to as the *probe* regime, has many distinguishing features from the system described previously: where the key points of Khan *et al.* [88] are summarised below.

- *Beam Intensity* In the probe regime, by definition, the intensities are very different. Analytically, the equations remain the same, but the strong coupling between only two of the levels distorts the energy eigenstates largely independently of the probe features, whereas the narrowest features of CPT can be observed when the two beams are of equal intensity.
- *Coherence* The strong coupling then leaves the fields in the probe

regime mostly phase independent, in stark contrast to the reliance of CPT on phase coherence to produce dark states.

- *Fluorescence* The strong coupling in the probe regime means that the fluorescence of the system is largely unaffected by the presence or absence of the probe, whereas the dark state created by the CPT process of course has a dramatic effect on the excited state population.
- *Scan-Axis* In the probe regime, it is the frequency and associated detuning from atomic resonance of the probe beam that is the main source of experimental observation. In the case of traditional CPT configurations however, the relative detunings of the two beams is of more interest and is subsequently limited to a much narrower range.
- *Sub-natural resonance* The preceding difference also determines the relevant linewidth, highlighting that CPT can aid high-precision spectroscopy of the ground levels, whereas the probe regime can provide sub-natural measurements of the upper level.
- *Detuning* The linewidth dichotomy then has implications for how the systems behave with detuning. In the CPT regime, the excitation rate, and thus the decoherence, can be reduced by detuning the coupling from the upper level, while maintaining the resonance at the same relative detuning between the two beams. In the probe regime on the other hand, a detuning of the coupling field from the upper level results in a drastic shift in the absorption: where the Raman condition is preserved, but the resonance is shifted and the lineshape is altered.
- *Buffer gas* The two regimes also have different properties in the presence of a buffer gas. The marked increase in collisions broadens the absorption profile, which for the probe regime, washes out the frequency dependence of the transparency. The increased pressure however, constrains the atoms. Greatly reducing their mean free path, the coherence time of the ground states is increased and this narrows the linewidth of a CPT transition.

Although these features are distinctive, and highly useful for analysis and interpretation, they are not reliable filters in the use of the terms in the literature. Thus, given the extensive amount of work done under both headings, and the fact that, mathemat-

8. This is in general true, but, strictly speaking, we should note that the probe regime requires an optically thick medium.

ically, the probe regime can be regarded as a limiting case of the CPT[8], this work will not labour to separate the two terms. On the contrary, let us content ourselves to using the phrases literally, for, like the difference between a heavy screwdriver and a hammer, the distinction is situation specific.

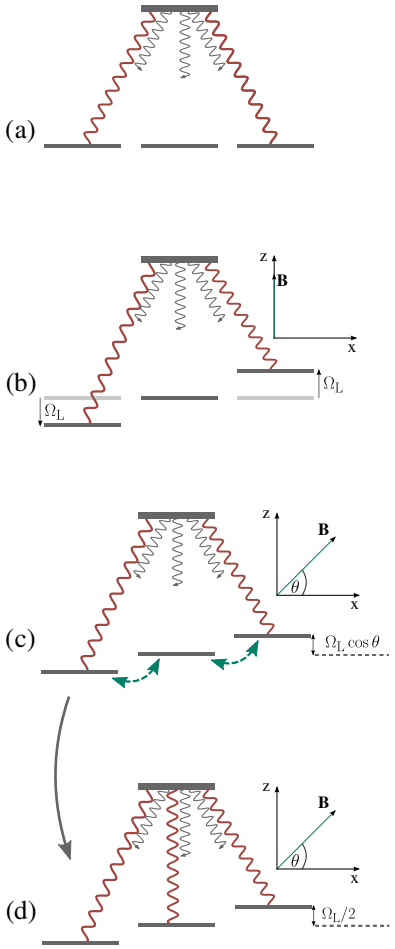

Figure 4.2: A schematic outline of a four-level system under the influence of two circularly-polarised fields. (a) without a magnetic field; (b) under the influence of a magnetic field aligned along the axis of beam propagation; (c) under the influence of a transverse magnetic field and (d) the same as (c), but where the basis states have been rotated to align the quantization axis with the applied field.

4.2 The Four-level Tripod

Having established the essential foundations of the CPT/EIT processes, we now prepare the way for more original discussion.

Following on from our discussion of the manipulation of light, we recall that the complete complex control of electric fields can be done purely through manipulation of the optical phase and in our quest to spatially regulate our atomic systems, we fill follow a similar procedure: utilising the atomic phase differences between the levels. As we will discover later however, the phase-dependent control of atomic systems requires a closed interaction contour and this limits our choice of atomic transitions and associated energy levels. The most convenient way to couple the ground states to one another is through the induced Zeeman coherences in the presence of a magnetic field and so, experimentally limited to rubidium, the closest states to a three level system with Zeeman ground levels, are the circular polarisation components of the rubidium-87 transition: $F = 1, 5s^2S_{1/2} \rightarrow F = 0, 5p^2P_{3/2}$.

Although this is a four-level configuration, the orthogonally polarised central ground state is not accessible to the driving laser: avoiding unwanted interference. Thus, we will consider this level structure in more detail.

4.2.1 Four-Level Λ

Illustrated in Figure 4.2, this system will be our focus of the remaining discussion and will thus prove instructive to analyse in full: from its most basic, to its most involved form.

The object of the chosen levels is to drive the two circularly polarised resonances and therefore our applied fields, in exponential notation, take the following form:

$$\boldsymbol{E}_{\mathrm{i}} = \mathcal{E}_{\mathrm{i}} \cos(\omega_{\mathrm{i}} t) \hat{\underline{e}}_{\mathrm{i}}, \tag{4.16}$$

where $i \in \{1, 2\}$ and $\hat{\underline{e}}_{\mathrm{i}} \in \{\sigma_+, \sigma_-\}$. This allows us to consider the total field:

$$\boldsymbol{E}_{\mathrm{Tot.}} = \frac{1}{\sqrt{2}} \begin{pmatrix} \mathcal{E}_1 e^{-it\omega_1} + \mathcal{E}_2 e^{-it\omega_2} \\ i\left[\mathcal{E}_1 e^{-it\omega_1} - \mathcal{E}_2 e^{-it\omega_2}\right] \\ 0 \end{pmatrix} \tag{4.17}$$

where we have used the Cartesian basis, $\left\{\hat{\underline{x}}, \hat{\underline{y}}, \hat{\underline{z}}\right\}$. Writing this explicitly, we see that our total field does not easily factor into the standard polarisation bases. Exactly as for the case of wavefunctions discussed previously, and for classical waves more generally, the combined field carries a beat frequency which mixes the two polarisation components; which has to be accounted for when modelling an atomic system. As our discussion is markedly polarisation dependent, we will consider this carefully. Based on the example from Budker *et al.* [89, 90], and standard wave theory, the field can be considered to oscillate at the average frequency $\frac{1}{2}[\omega_1 + \omega_2]$ and so by factoring out the high frequency oscillation and taking the real component of the remainder, we can model the time-dependent development of the polarisation *i.e.*

$$\hat{\underline{e}}(t) = \mathrm{Re}\left(\frac{\sqrt{2}}{\mathcal{E}_1 + \mathcal{E}_2} e^{\frac{it}{2}[\omega_1+\omega_2]} \boldsymbol{E}_{\mathrm{Tot.}}\right) = \begin{pmatrix} \cos\frac{1}{2}t[\omega_1 - \omega_2] \\ \sin\frac{1}{2}t[\omega_1 - \omega_2] \\ 0 \end{pmatrix}. \tag{4.18}$$

Therefore, we see that although the superposition of both circular components would otherwise create $\hat{\underline{x}}$-polarised light, any detuning $\omega_{\Delta 12} = \omega_1 - \omega_2$ between the beams causes the linear polarisation to rotate; spiralling faster with greater discrepancy.

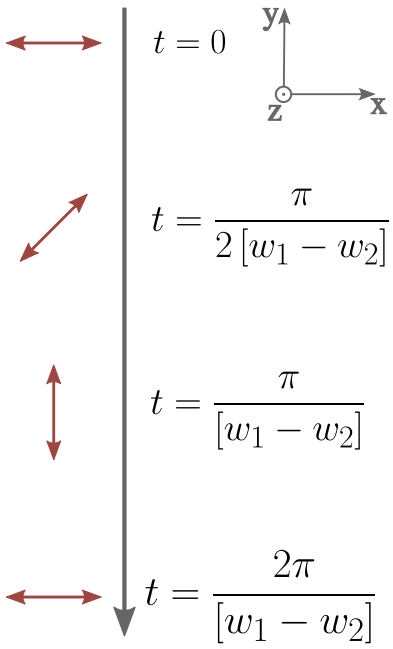

Figure 4.3: An overview of the development of degenerate field polarisation. The two circular components combine to produce linear polarisation that rotates at a rate equal to the difference in optical frequencies.

Hamiltonian

The system under discussion will be subject to the full Hamiltonian $\hat{H}$, similarly to previous sections, such that

$$\hat{H} = \hat{H}_0 + \hat{H}_\mathrm{E} + \hat{H}_\mathrm{B}, \tag{4.19}$$

and $\hat{H}_0 = \hbar\omega_\mathrm{e}|e\rangle\langle e|$ accounts for the unperturbed excited level. The interaction of this system with atomic vapour then follows *i.e.*

$$\hat{H}_\mathrm{E} = -\operatorname{Re}(\boldsymbol{E}) \cdot \boldsymbol{d}_\mathrm{E}, \tag{4.20}$$

where we remember that $\boldsymbol{d}_\mathrm{E}$ is a Hermitian operator. Therefore, from the *Wigner-Eckart theorem* [91, 92, 67], the dipole operator can be written as

$$\begin{aligned}\langle F_2 m_{F_2} | \, \mathrm{d}_{\mathrm{E}\pm} \, | F_1 m_{F_1} \rangle = &(-1)^{F_2 - m_{F_2}} \begin{pmatrix} F_2 & 1 & F_1 \\ -m_{F_2} & \pm 1 & m_{F_1} \end{pmatrix} \\ &\times \langle F_2 \, \| \mathrm{d}_\mathrm{E} \| \, F_1 \rangle \, .\end{aligned} \tag{4.21}$$

The Wigner-Eckart theorem is a profound mathematical separation of form and function. The theorem applies quite generally to tensor relations, but for our purposes its role is to break down the calculation of matrix elements into two parts: one that is entirely defined by the spatial orientation, and hence only depends on the angular momenta, and one that characterises the quantum operation, without specifying the spatial orientation. This is reflected in the statement above, where $\begin{pmatrix} \cdots & \cdots & \cdots \\ \cdots & \cdots & \cdots \end{pmatrix}$ is the *Wigner-3j symbol* characterising the spatial orientation of the atomic polarisations and $\langle \ldots \, \| \hat{\mathrm{O}} \| \, \ldots \rangle$ is known as the *reduced matrix element* of the given operator $\hat{\mathrm{O}}$.

For the case of hyperfine levels, the reduced dipole matrix element can then be further simplified by

$$\begin{aligned}\langle F_2 \, \| \mathrm{d}_\mathrm{E} \| \, F_1 \rangle = &(-1)^{J_2 + I + F_1 + 1} \sqrt{(2F_1 + 1)(2F_2 + 1)} \\ &\times \begin{Bmatrix} J_2 & F_2 & I \\ F_1 & J_1 & 1 \end{Bmatrix} \langle J_2 \, \| \mathrm{d}_\mathrm{E} \| \, J_1 \rangle\end{aligned} \tag{4.22}$$

and noting that the conjugate transforms according to

$$\langle F_1 \, \| T^\kappa \| \, F_2 \rangle = (-1)^{F_1 - F_2} \langle F_2 \, \| T^\kappa \| \, F_1 \rangle^* . \tag{4.23}$$

Here, the coupling of the angular momenta is further separated using the *Wigner-6j symbol* as represented by $\left\{ \begin{array}{ccc} \cdots & \cdots & \cdots \\ \cdots & \cdots & \cdots \end{array} \right\}$. The Wigner symbols are then real numbers that apply to any interaction of equivalent geometry, which can be calculated independently using software like *Mathematica*. The combination of these results means that the operator only has to be calculated once, for the general case of fine structure interaction, before it can be applied to any magnetic hyperfine interaction. For more details, see *Optically Polarized Atoms* [67].

This allows us to write

$$\hat{H}_{\mathrm{E}} = \frac{\hbar}{4\sqrt{6}}\Big[-\Omega_{\mathrm{R}1}e^{-it\omega_1} - \Omega_{\mathrm{R}2}e^{it\omega_2}|e\rangle\langle g_+| + [\Omega_{\mathrm{R}1}e^{-it\omega_1} + \Omega_{\mathrm{R}2}e^{it\omega_2}|g_-\rangle\langle e|\Big] + H.c.\Big], \tag{4.24}$$

The extra factor of two comes from the conversion to exponentials.

where the ground and excited states are identified by $|g\rangle$ and $|e\rangle$ respectively and $i \in \{,0,+\}$ reflects the possible m_F values of $-1, 0$ and $+1$. Then, under the rotating wave approximation and change to the interaction picture[9], the full Hamiltonian in the absence of a magnetic field becomes

$$\hat{H} = \frac{\hbar}{4\sqrt{3}}\Big[-\Omega_{\mathrm{R}2}|e\rangle\langle g_+| + \Omega_{\mathrm{R}1}|g_-\rangle\langle e|\Big] + \hbar\Big[\omega_{\Delta 10}|e\rangle\langle e| + \omega_{\Delta 12}|g_+\rangle\langle g_+|\Big] + H.c.. \tag{4.25}$$

9.

$$\hat{U}_{\mathrm{Rot.}} = 1|i\rangle\langle i| + e^{-it\omega_1}|4\rangle\langle 4| + H.c.;$$
$$\hat{U}_{\omega_\Delta} = 1|j\rangle\langle j| + e^{it\omega_{\Delta 12}}|1\rangle\langle 1| + H.c.$$
$$\forall\ i \in [1,3] \text{ and } j \in [2,4].$$

The Master Equation

Having obtained the Hamiltonian for the system, independent of magnetic fields, we can apply the master equation,

$$\frac{d\hat{\rho}}{dt} = -\frac{i}{\hbar}\left[\hat{H}, \hat{\rho}\right] - \frac{1}{2}\left(\hat{\Gamma}\hat{\rho} + \hat{\rho}\hat{\Gamma}\right) + \hat{\Lambda},$$

where for our $F = 1, 0$ states, we describe the relaxation and repopulation as

$$\hat{\Gamma} = \sum_i \gamma|g_i\rangle\langle g_i| + (\gamma + \Gamma)|e\rangle\langle e| \text{ and} \tag{4.26a}$$

$$\Lambda = \sum_i \frac{1}{3}(\gamma + \Gamma\hat{\rho}_{\mathrm{e}})|g_i\rangle\langle g_i| \tag{4.26b}$$

respectively[10]. The explicit form of these equations can be computed from substitution, but carry no extra physical insight than

10. These diagonal matrices are unchanged in the *'rotating'* frame.

that already described: both above and as depicted in Figure 4.4. For this Hamiltonian, such a system of equations can be solved analytically using the *Mathematica* software environment, where throughout the remaining discussion the *Atomic Density Matrix* package has been invaluable [93]. The solutions however, are punitively convoluted[11].

11. On the order of 30 lines per matrix element!

Observables

To interpret these complete, if in-concise, results, let us consider them in the context of experimental observables. There are many ways to parametrise our optical fields and this leaves us with a choice of how to model our measurable field properties. Our particular level configuration is covered in some detail in [67], but it is considered holistically and broken down by fractional change in field, phase, polarisation angle and ellipticity. As we will be investigating the effects of individual magnetic transitions however, we use the potentially more pleasing[12] approach of considering only the field loss and phase change for each component. The previous discussion then allows the recovery of fractional change in electric field and phase for both components of the applied field. For time independence, the solutions are calculated within the rotating wave approximation, and so the observables have to be rotated into this frame too. Thus, for left-circularly polarised light:

12. The two approaches are of course equivalent, but the chosen one arguably relies on fewer concepts and perhaps more neatly coincides with the fundamental energy level picture.

$$\frac{1}{\mathcal{E}_1}\frac{\partial}{\partial z}\mathcal{E}_1 = -2\sqrt{3}\pi\frac{\Gamma\omega_1}{\Omega_{\mathrm{R1}}U_{\mathrm{e}}^3}\,\mathrm{Im}(\hat{\rho}_{\text{-1,e}}) \quad \text{and} \tag{4.27a}$$

$$\frac{\partial}{\partial z}\varphi_1 = -2\sqrt{3}\pi\frac{\Gamma\omega_1}{\Omega_{\mathrm{R1}}U_{\mathrm{e}}^3}\,\mathrm{Re}(\hat{\rho}_{\text{-1,e}}); \tag{4.27b}$$

whereas for right-circularly polarised light:

$$\frac{1}{\mathcal{E}_2}\frac{\partial}{\partial z}\mathcal{E}_2 = +2\sqrt{3}\pi\frac{\Gamma\omega_2}{\Omega_{\mathrm{R2}}U_{\mathrm{e}}^3}\,\mathrm{Im}(\hat{\rho}_{\text{+1,e}}) \quad \text{and} \tag{4.28a}$$

$$\frac{\partial}{\partial z}\varphi_2 = +2\sqrt{3}\pi\frac{\Gamma\omega_2}{\Omega_{\mathrm{R2}}U_{\mathrm{e}}^3}\,\mathrm{Re}(\hat{\rho}_{\text{+1,e}}). \tag{4.28b}$$

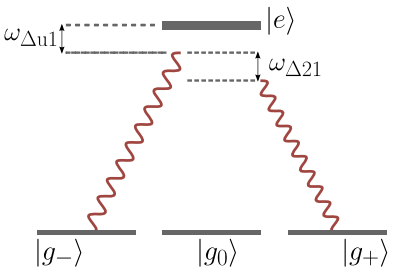

Figure 4.4: A schematic outline of the laser detunings.

As noted above, the solutions themselves are complete, but for ease of reporting, let us consider the relevant coherences in the limit of $\gamma \ll \Gamma$. In this limit,

$$\hat{\rho}_{\text{-1,e}} = i\frac{2\sqrt{3}}{\mathcal{D}}\left(\Gamma + 2i\omega_{\Delta 1}\right)\sqrt{\gamma\Gamma\kappa_1}\left(\Gamma^2(\kappa_2+12) + 48\left(\omega_{\Delta 1} - \omega_{\Delta 12}\right)^2\right) \text{ and} \tag{4.29a}$$

$$\hat{\rho}_{\text{+1,e}} = \frac{2\sqrt{3}}{\mathcal{D}}\left(-i\Gamma + 2\omega_{\Delta 1} - 2\omega_{\Delta 12}\right)\sqrt{\gamma\Gamma\kappa_2}\left(\Gamma^2(\kappa_1+12) + 48\omega_{\Delta 1}^2\right), \text{ where} \tag{4.29b}$$

$$\begin{aligned}\mathcal{D} = \Gamma^4(\kappa_1(\kappa_2+24) + 24(\kappa_2+18)) + 96\Big(\Gamma^2\omega_{\Delta 1}^2(\kappa_1+\kappa_2+36) - 2\omega_{\Delta 12}\omega_{\Delta 1}\Big(\Gamma^2(\kappa_1+18) \\ +72\omega_{\Delta 1}^2\Big) + \omega_{\Delta 12}^2\left(\Gamma^2(\kappa_1+18) + 72\omega_{\Delta 1}^2\right) + 72\omega_{\Delta 1}^4\Big)\end{aligned}$$

and we have introduced the saturation parameters, $\kappa_{\text{i}} = \frac{\Omega_{\text{R1}}^2}{\gamma\Gamma}$, for $i \in \{1,2\}$.

Now that we have a harness of the system dynamics, we can consider the steady-state solution of the system in the different regimes.

Equal-intensity: $\kappa_1 = \kappa_2$ For equal beam intensity, $\omega_{\Delta u1} = 0$, and setting the remaining parameters to convenient values ($\Omega_{\text{R1}} = \Omega_{\text{R2}} = \Gamma = 1$, $\gamma = 0.01$ and $U = 2\pi$), then we obtain the classic CPT/EIT result shown in Figure 4.5. As we are varying the intra-beam detuning, we immediately notice the asymmetry of the system. The left-circularly polarised light is continually on resonance and so experiences uniform and greater absorption, but in each polarisation component there is a dramatic drop in absorption around the Raman resonance discussed previously, the characteristic feature of EIT. Additionally, if we particularly consider the profile of σ_-, we note the clear accompaniment of a steep dispersion gradient around resonance and it is this feature that is responsible for the remarkable experiments involving the slowing and stopping and storage of optical fields, as listed in our introduction. Further considering the interaction of σ_-, we can catalogue the non-linear nature of the process. Increasing from saturation, we note how the contrast of the absorption dip can be increased with more intense optical fields, but this comes at the cost of power broadening: both of the overall profile, and the characteristic dip width, while the overall fractional absorption also drops.

Furthermore, considering the associated dispersion profiles, we see how sensitive the non-linear features can be to observation.

Probe Regime: $\kappa_1 \gg \kappa_2$ If instead we hold the power in σ_- at saturation and ramp that of σ_+ independently, we can consider the probe regime for σ_-. Considering Figure 4.7, we begin to see the particular value of this configuration. By making this change, it is noticeably easier to increase the fractional absorption while also greatly increasing the contrast of the central dip. Furthermore, we note the great simultaneous clarification of the dispersion features, where in both cases an increase in power is in general beneficial, with relatively much less loss. Regardless of the chosen configuration however, there are over-arching similarities and we use this opportunity to expand on a helpful mechanism for analysing later results.

4.2.2 EIT and the AMPS

Summarising the discussion by Rochester *et al.*[71], we take this opportunity to examine the mechanism of EIT in more detail before pre-emptively familiarising ourselves with the AMPS[13], briefly introduced previously.

13. Although this discussion is mostly unoriginal, we include it here for ease of contrast with our later results.

Looking again at our fractional observables, we can characterise the interaction by three different regimes: that of large values of detuning, where $\omega_{\Delta 12}$ is much larger than the power-broadened natural width (the asymptotic tails of the absorption spectrum); the regime characteristic of a two-level transition, where the detuning lies between the natural and transit widths and the central, near-resonant regime, where the intra-field detuning is within the power-broadened ground state width. The ubiquitous and fundamental nature of EIT however mean that there are many ways of interpreting these configurations. We could for example explicitly consider the populations of the appropriate atomic transitions, and compare the relative excitation rates, but for our purposes it is sufficient to note that in the near-resonant regime the pump and probe act coherently, whereas in the other regimes the coupling is incoherent. From our discussion at the beginning of the chapter therefore, we can re-describe the coherent excitation of the system in terms of superpositions and see how the creation of *dark* and *bright* states results in transparency. Of potentially some interest however, is

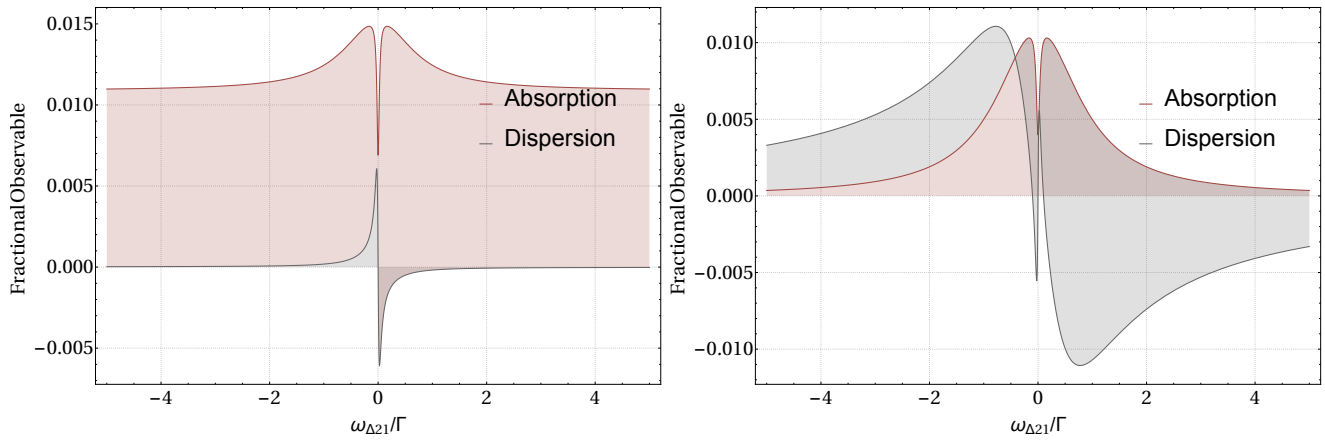

Figure 4.5: The absorption and dispersion profile for each of the left and right circularly polarised transitions respectively, where the beams are of equal intensity.

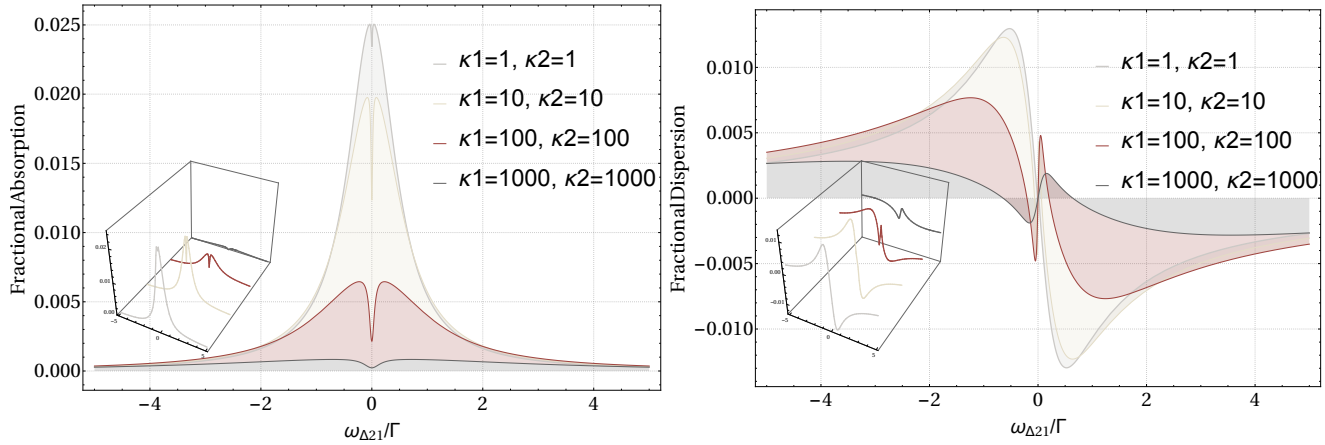

Figure 4.6: The absorption profile of the probe transition for varying levels of optical saturation, where each beam carries the same intensity.

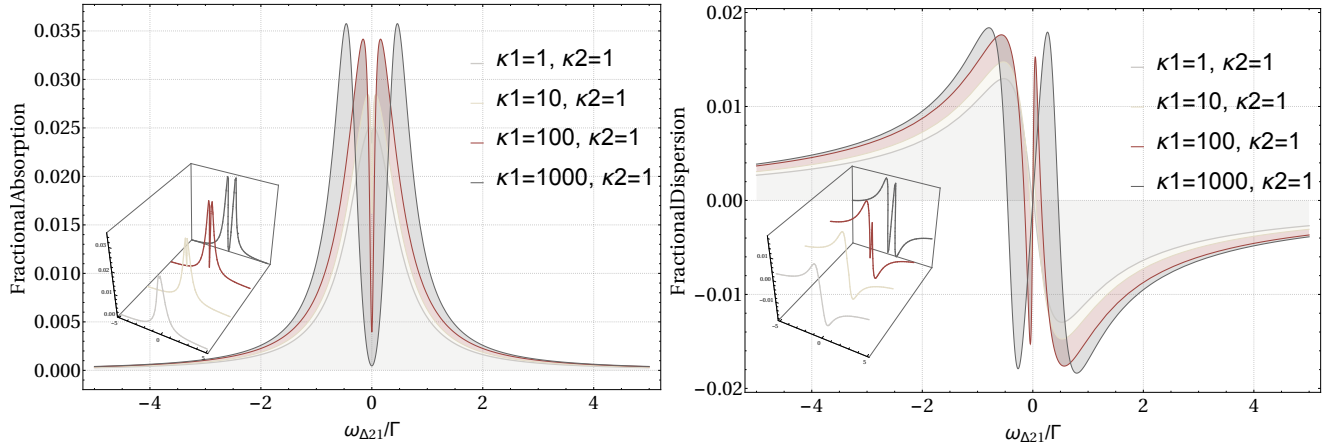

Figure 4.7: The absorption profile of the probe transition for varying levels of control beam saturation, where the probe beam is held constant and low.

how this coherence is created.

At the beginning of the section, we lingered on the effects of detuning and now we can see why. As our EIT profiles are functions of field detuning, then any discrepancy between the frequencies will introduce a temporal phase. As we move from greater to lower detuning therefore, the net polarisation rotates slower and slower, bringing its frequency scale closer to the characteristic interaction times of the atoms, as determined by the two widths. Therefore, although the outer regime is dominated by the probe frequency's distance from atomic resonance, limiting any interaction, the inner regimes are separated by the degree of coherence created by the rotating polarisation. When the detuning is between the transit and natural widths therefore the light is rotating faster than the atomic polarisation can adapt and so the field components pump the transitions incoherently. When the detuning is small enough however, the net polarisation is distinguishable and so the two field polarisations interact coherently[14]: acting as one linearly polarised field.

As briefly mentioned in the previous chapter, the angular-momentum probability surfaces (AMPS) offer a complementary way of interpreting the interaction. These diagrams allow us to directly and holistically visualise the ground state properties of the atoms. Indeed, as outlined by [67], the AMPS is a bijective mapping of the full ground state density matrix and moreover the surfaces are basis-independent.

Considering the surfaces under the condition of equal beam intensity (Figure 4.8), we see that for large detuning the polarisation bulges in the positive z-axis. This indicates an asymmetric depletion of the Zeeman states, such that the atoms now carry a positive angular momentum projection. This makes some sense, as the large detuning causes the probe to interact very weakly in comparison to the pump. As the detuning is decreased however, the interaction of the probe strengthens and this consequently reduces the momentum projection of the atoms until both components interact equally. This is represented by a gain in symmetry, such that there is no spatial orientation of the atoms and no alignment with a preferred axis. For the narrow band of detuning lying within the ground state coherence however, the light inter-

14. An intuitive way to understand this distinction is to simply imagine an old-fashioned propeller. When the propeller is at full speed, then for our purposes it interacts as one object, covering a circular area of space. If it is moving slowly enough however, then we can safely interact with it as a linear set of blades. Moreover, if all interactions are wave-like then it's interesting to wonder how far this analogy goes.

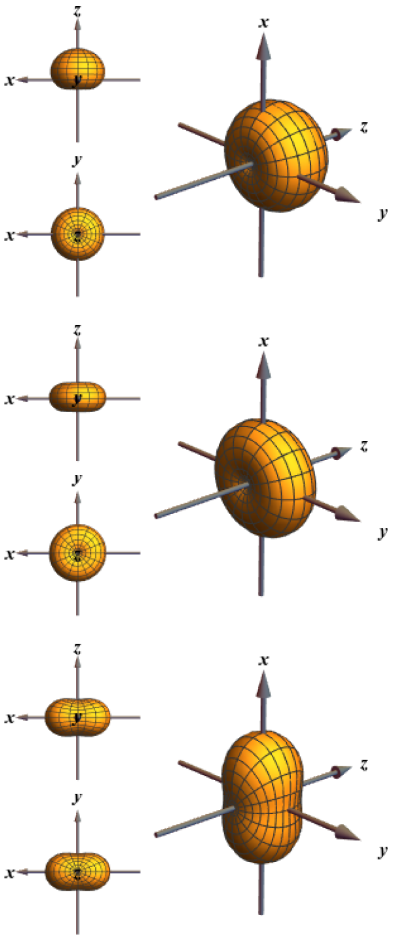

Figure 4.8: A schematic overview of the atomic ground states as the detuning is decreased towards resonance.

acts coherently and as such, is not averaged around the entire x, y plane. The atomic population thus reforms along a preferred axis, which is equal to the dark superposition state. The bright state is then efficiently depleted, such that the absorption of the probe drops dramatically.

In summary therefore, we see that by introducing the detuning we have brought a temporal phase to the system, whose adjustment can move the atomic cloud between three significantly distinguishable regimes and, expressing it this way, this will prove to be of fundamental importance in the next section.

4.2.3 *Longitudinal Magnetic Field*

Having considered the system in the absence of a magnetic field, we have seen how EIT can be observed in both absorption and dispersion as a function of internal beam detuning, but the presence of a magnetic field greatly disturbs the system: introducing additional ways of probing the atomic levels. Here, we first consider an additional longitudinal field and show that in this limit we can now meaningfully introduce the observables detailed in the last chapter, providing both a foundation and direction for our future discussions. To account for a field directed along the axis of propagation, we add an extra term to our Hamiltonian, such that

$$\hat{H}_{\mathrm{Bz}} = -\frac{1}{2}\Omega_{\mathrm{L}}|g_+\rangle\langle g_+| + \frac{1}{2}\Omega_{\mathrm{L}}|g_-\rangle\langle g_-| \tag{4.30}$$

and where the factors are properties of our chosen transition, as discussed previously. Re-evaluating the resulting master equation in the usual way, we can then consider the fractional observables (§ 3.3 (p. 82)) as both a function of atomic detuning and magnetic field, as summarised in Figure 4.10. For these plots, we are working in the same parameter regime as before, but where we now assume that the internal beam detuning is zero, and where we consider the interaction in the limits of both low and high beam intensity, as defined by the saturation. Under these conditions, then we see similar results to that reported by Auzinsh *et al.* [67], but where we have explicitly included the individual profiles of the two polarisation components. Follow-

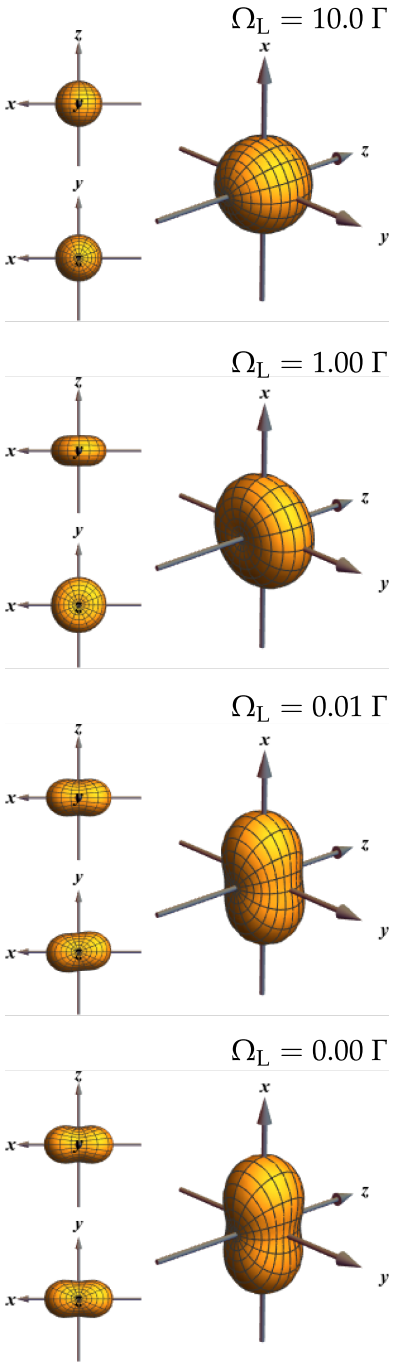

Figure 4.9: A schematic overview of the atomic ground states as the magnetic field strength is decreased towards zero.

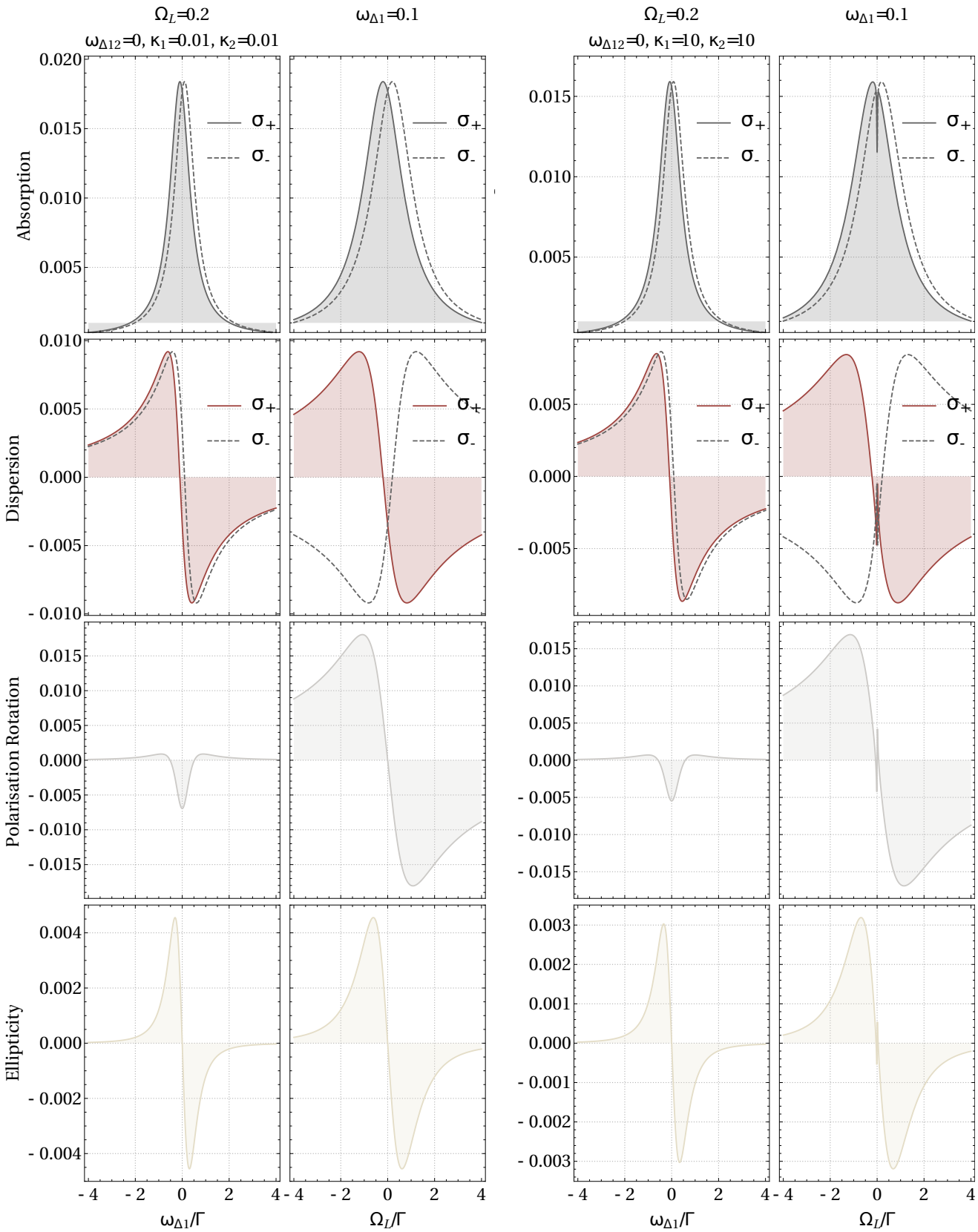

Figure 4.10: The absorption, dispersion, polarisation rotation and change in ellipticity profiles in the four-level system, where the beams are of equally (a) low and (b) high intensity.

ing the left-most column, we see that for both components, the characteristic absorption and dispersion curves of a two level system are recovered, but in the presence of a magnetic field (see Hamiltonian above) the level energies are shifted, offsetting their profiles with respect to one another. From their respective definitions, this phase offset then results in changes to both net polarisation angle and ellipticity. If we hold a fixed detuning and scan the magnetic field angle however, then the situation is similar, but the antisymmetric separation of the outer ground state energy levels results in a reflection of the component dispersions around resonance. In either case however, we note that without the magnetic field the ground states would be degenerate and the lack of symmetry breaking between σ_+ and σ_- leads to no change in net polarisation. Interestingly however, we note that we do not observe any of the characteristic features of EIT in these profiles. If we consider the same graphs under conditions of much higher beam intensity however, we gain more information about our choice of scan-axis in what follows. With increased power, we begin to see that EIT is imperceptible by simply scanning the atomic detuning, whereas it is clear while scanning the magnetic field strength. The explanation of this is to do with non-linearity. Although the shifting energy levels produce the same effects at higher fields (accounting for the same features in both sets of plots), higher intensities change the frequency scales of the system and so similarly to our previous discussion surrounding the AMPS, we now need to consider the development of the atomic polarisation, as outlined in Figure 4.9. Similarly to the case of explicit beam detuning, we see that by decreasing the magnetic field, we increase the asymmetry of the angular momentum distribution, but the exact form is somewhat different and can be considered in terms of Larmor precession. As the Larmor precession simply describes the rotation of these surfaces around the magnetic axis, we see that for large values *e.g.* 10 times the natural width, the distribution rotates quickly enough to average out any spatial dependence. Decreasing the strength however until the rotation frequency equals the natural line width, brings the system into the same regime as equal field detuning, where the momentum is distributed across the x, y plane. Just inside

the ground state coherence, but off of resonance, we see how the Larmor precession has rotated our expected resonant EIT profile, but of course in the limit of no field, then we return to our previous result. Such an analysis will be helpful in later discussion, but for our current purposes, it is enough to know that rather than scanning the internal field detuning, we can now switch between our EIT regimes by considering changes in the longitudinal field strength. It should be noted however, that the absence of an atomic detuning, even in the presence of a magnetic field, leads to indistinguishable absorption profiles, as each beam is detuned equally around the excited state, and thus changes in polarisation ellipticity necessitate some manner of explicit detuning. A full overview of the interplay of these two variables is included in Figure 4.11.

4.2.4 Transverse Magnetic Field: Four-Level Tripod

As detailed at the beginning of the last chapter, the application of a magnetic field is a fundamental way to break the symmetry of an atomic system. The ability to shift our atomic energies, without explicit detuning of the applied field, allows easy access to a host of previously hidden properties. As detailed in the last sub-section, we have seen how the application of a small longitudinal field has led not only to the frequency-dependent manipulation of atomic populations, but both to the subtle and dramatic manipulation of our applied fields: in the rotation and compression of polarisation, the manipulation of relative phase and the spectral hole-burning inherent in the EIT process.

Although the resonant nature of Faraday rotation and its relationship to the Zeeman effect has been known since the late 19th century, it is perhaps unfortunate that the great developments in atomic theory have since made these effects easy to describe without intuition. For the unwary experimentalist, it is easy to forget that the manipulation of angular momentum levels is a geometric exercise and as such, we can be forgiven for failing to notice that the effects described previously can simply be attributed to the spatial manipulation of atomic polarisation. As clarified by the AMPS plotted in Figure 4.9.

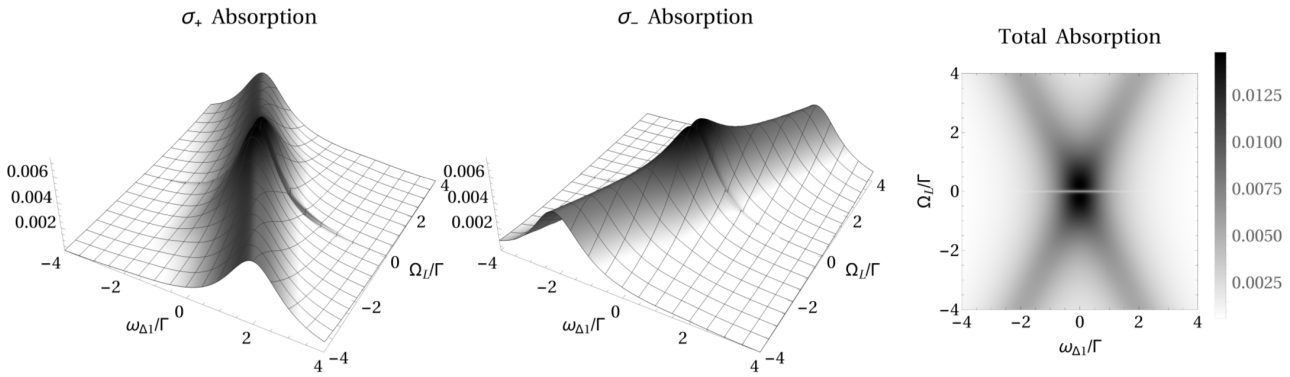

Figure 4.11: The absorption of transmitted light with atomic detuning and magnetic field strength.

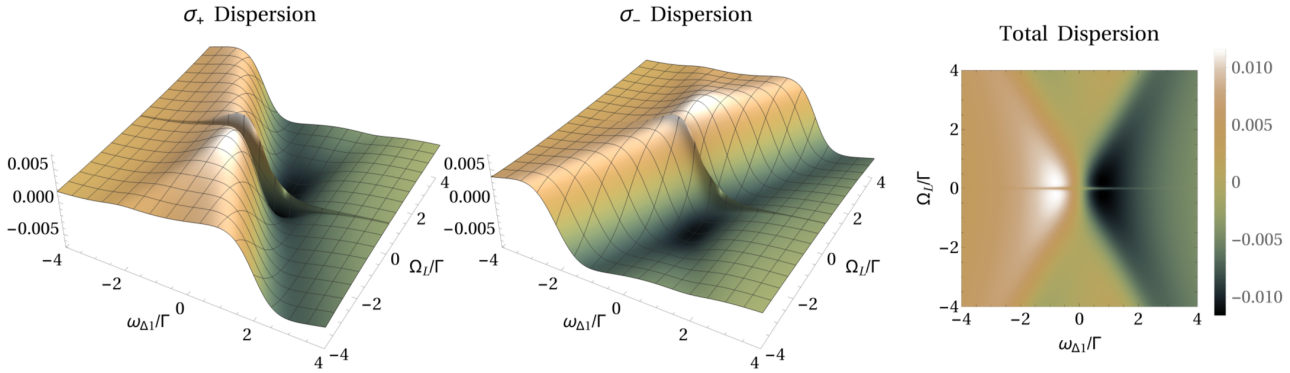

Figure 4.12: The change in circular and total phase of transmitted light as depending on the atomic detuning and the magnetic field strength.

Figure 4.13: The change in polarisation and ellipticity of transmitted light with atomic detuning and magnetic field strength.

The next step is, naturally, then to consider what happens when we apply a more general magnetic field, as considered spatially. The study of such two-dimensional fields is not original in nature, and has been carried out in many different systems in the cases of changing light polarisation, counter propagation, and where either the longitudinal or transverse field components are fixed, while the other is scanned. Particularly, we note that in the context of EIT/CPT systems the extra dimensionality can lead to either enhanced or reduced absorption amplitudes, and in the specific case of a Hanle resonance with σ polarised light, we expect both a reduction in amplitude and an increase in resonance width subject to normal saturation.

Following the developments outlined above, we will continue to develop our model of the four-level system, highlighting the two main bases normally used for such discussions and additionally, we will introduce another perspective on the system for the special case of Hanle resonance, where the use of superpositions allows us to greatly simplify the theoretical description. To the best of my knowledge, such a description is entirely, if modestly, novel, but in any case, it will prove useful for our later discussions and as such, we consider the implications here in some detail.

Following our previous discussion of the hyperfine Zeeman effect (Eq. 3.31(p. 69)), we recall that the most general form of the magnetic Hamiltonian in the weak-field limit is $\hat{H}_{\mathrm{B}} = \mathrm{g_F}\, d_{\mathrm{Bohr}} \boldsymbol{F} \cdot \boldsymbol{B}$, such that

$$\hat{H}_{\mathrm{B}} = \mathrm{g_F}\, d_{\mathrm{Bohr}} \hbar B \Big[\pm \cos\theta |g_{\pm}\rangle\langle g_{\pm}| + \frac{1}{\sqrt{2}} \sin\theta e^{i\phi} \big[\, |g_0\rangle\langle g_+| + |g_-\rangle\langle g_0| \, \big] + H.c. \Big] \tag{4.31}$$

and θ and ϕ are the standard polar and azimuthal angles respectively. The origin of the azimuthal angle is naturally ambiguous and as such, we define it to zero for the remainder of this discourse [15]. Furthermore, for our purposes we only need a two dimensional magnetic field, where we are more interested in the direction than in the magnitudes and as such we define for convenience the field $\boldsymbol{B} = B\left[\sin\theta \underline{\hat{x}} + \cos\theta \underline{\hat{z}}\right]$. Under these conditions, we can then write the most general form of the atomic

15. This angle will prove to be important again in later discussions, but for convenience we extend our definition of the origin of the magnetic field to coincide with the origin of any similarly denoted angle throughout this work.

Hamiltonian for our coupled rubidium system in the laboratory frame ($\{|g_+\rangle, |g_0\rangle, |g_-\rangle, |e\rangle\}$) as

$$\hat{H} = \frac{1}{2}\hbar \begin{pmatrix} -\Omega_{\mathrm{L}}\cos\theta & -\frac{1}{\sqrt{2}}\Omega_{\mathrm{L}}\sin\theta & 0 & -\mathrm{fld}_+ \\ -\frac{1}{\sqrt{2}}\Omega_{\mathrm{L}}\sin\theta & 0 & -\frac{1}{\sqrt{2}}\Omega_{\mathrm{L}}\sin\theta & 0 \\ 0 & -\frac{1}{\sqrt{2}}\Omega_{\mathrm{L}}\sin\theta & +\Omega_{\mathrm{L}}\cos\theta & \mathrm{fld}_- \\ -\mathrm{fld}_- & 0 & \mathrm{fld}_+ & 2U_{\mathrm{e}} \end{pmatrix} \tag{4.32}$$

$$\text{where} \quad \mathrm{fld}_- = \frac{1}{2\sqrt{6}}\left[e^{-i\omega_1 t}\Omega_{\mathrm{R1}} + e^{+i\omega_2 t}\Omega_{\mathrm{R2}}\right] \text{ and} \tag{4.33a}$$

$$\mathrm{fld}_+ = \mathrm{fld}_-^*. \tag{4.33b}$$

Tripod System

The resulting Hamiltonian has very few non-zero elements and in practise is very difficult to solve analytically without making limiting assumptions. Considering the Hamiltonian carefully, we see that the new transverse terms do nothing to change the bare energy levels themselves, but rather denote new interactions between the ground states. Following the thinking outlined above, we can simply interpret these complications as the result of further symmetry breaking of the system. Spatially, the magnetic field now interacts with the atoms outside of the z-axis and as such, our states describing the x, y plane reflect this. It stands to reason therefore that if we can reintroduce the spatial symmetry in the system then our Hamiltonian, which in itself still maintains degenerate elements, can be simplified. Therefore, we consider a spatial transformation such that our perspective is now aligned with the new magnetic field axis. The required transformation can be performed with the relevant Wigner rotation matrix $\mathcal{D}_W(\alpha, \beta, \gamma)$, where α, β, γ are the universal Euler angles. For our freely rotated magnetic field in the x, z-plane, the transformation can then be written as

$$\mathcal{D}_W = \frac{1}{2}\hbar \begin{pmatrix} \cos^2\frac{\theta}{2} & -\frac{1}{\sqrt{2}}\sin\theta & \sin^2\frac{\theta}{2} & 0 \\ \frac{1}{\sqrt{2}}\sin\theta & \cos\theta & -\frac{1}{\sqrt{2}}\sin\theta & \\ \sin^2\frac{\theta}{2} & \frac{1}{\sqrt{2}}\sin\theta & \cos^2\frac{\theta}{2} & 0 \\ 0 & 0 & 0 & 1 \end{pmatrix}, \tag{4.34}$$

16. Recall that for time-dependent transformations we use : $\hat{H}' = \hat{U}^{*T}\hat{H}\hat{U} - i\hbar\hat{U}^{*T}\frac{\partial}{\partial t}\hat{U}$.

which on application[16] converts our Hamiltonian to

$$\hat{H}_{\text{Tripod}} = \frac{1}{2}\hbar \begin{pmatrix} -\Omega_{\text{L}} & 0 & 0 & -\text{g}_+ \\ 0 & 0 & 0 & \text{g}_0 \\ 0 & 0 & +\Omega_{\text{L}} & +\text{g}_- \\ -\text{g}_- & \text{g}_0 & +\text{g}_+ & 2U_{\text{e}} \end{pmatrix}, \tag{4.35}$$

$$\text{where} \quad \text{g}_- = \frac{1}{2\sqrt{6}}\Big(\cos\theta \left[\Omega_{\text{R1}} \cos\omega_1 t + \Omega_{\text{R2}} \cos\omega_2 t\right] \tag{4.36a}$$
$$+ i\left[\Omega_{\text{R1}} \sin\omega_1 t - \Omega_{\text{R2}} \sin\omega_2 t\right] \Big),$$
$$\text{g}_0 = \frac{1}{2\sqrt{3}} \sin\theta \left[\Omega_{\text{R1}} \cos\omega_1 t + \Omega_{\text{R2}} \cos\omega_2 t\right] \text{ and} \tag{4.36b}$$
$$\text{g}_+ = \text{g}_-^*. \tag{4.36c}$$

Immediately, we recover some symmetry, but at the cost of introducing a third component to our combined field. This is a natural consequence of changing our quantisation axis. For propagation in z, the field can be completely decomposed into $\sigma_\pm$ components, but projections on another axis will of course include a perpendicular component.

In both bases however, taking the rotating wave approximation does not allow removal of the explicit time dependence. If we simplify our considerations to where the frequencies are equal, then the Hamiltonian retains a similar form,

(ω_2=ω_1)
$$\hat{H}_{\text{Tripod}} = \frac{1}{2}\hbar \begin{pmatrix} -\Omega_{\text{L}} & 0 & 0 & \text{g}_+ \\ 0 & 0 & 0 & \text{g}_0 \\ 0 & 0 & +\Omega_{\text{L}} & \text{g}_- \\ \text{g}_+ & \text{g}_0 & \text{g}_- & -2\omega_{\Delta 1e} \end{pmatrix} \tag{4.37}$$

, but with simplified fields:

$$g_\pm = \frac{1}{4\sqrt{6}} \left[\Omega_{\text{R1}} - \Omega_{\text{R2}} \mp \cos\theta \left(\Omega_{\text{R1}} + \Omega_{\text{R2}}\right)\right] \text{ and} \tag{4.38a}$$
$$\text{g}_0 = \frac{1}{4\sqrt{3}} \left[\Omega_{\text{R1}} + \Omega_{\text{R2}}\right] \sin\theta. \tag{4.38b}$$

Following our previous discussion, this is only a small constraint as we can mostly replicate the effects of beam detuning with the application of a magnetic field. The Hamiltonian itself however, remains unsolvable and so we consider an alternative approach.

Hanle Superposition

An alternative approach to restoring symmetry is to retain our natural quantisation axis and yet try to directly combine the coherences in the system. From our original Hamiltonian, we can consider superpositions of our outer ground states such that on transformation

$$\hat{H}_{\Xi} = \frac{1}{2}\hbar \begin{pmatrix} 0 & \Omega_{\mathrm{L}} \sin\theta & 0 & 0 \\ \Omega_{\mathrm{L}} \sin\theta & 0 & \Omega_{\mathrm{L}} \cos\theta & h_{-} \\ 0 & \Omega_{\mathrm{L}} \cos\theta & 0 & h_{+} \\ 0 & h_{-}^{*} & h_{+}^{*} & -2\omega_{\Delta 1 e} \end{pmatrix}, \qquad (4.39) \qquad \text{(Under RWA)}$$

$$\text{where} \quad h_{\pm} = \frac{1}{4\sqrt{3}} \left[\Omega_{\mathrm{R}1} \pm e^{it\omega_{\Delta 21}} \Omega_{\mathrm{R}2} \right]. \qquad (4.40)$$

Remembering that a *ket* represents a column vector in matrix mechanics, the transformation $\hat{\psi}$ is defined as

$$|\psi_1\rangle \equiv -|g_0\rangle; \;\; |\psi_{\pm}\rangle \equiv \pm\frac{1}{\sqrt{2}}|g_{+}\rangle + \frac{1}{\sqrt{2}}|g_{-}\rangle \text{ and } |\psi_4\rangle \equiv |e\rangle \qquad (4.41)$$

where $\hat{\psi} = \{\psi_1, \psi_{+}, \psi_{-}, \psi_4\}$.

From this perspective, not only have the ground states recovered their degeneracy, but the longitudinal and transverse components of the magnetic interaction have been collected and isolated from one another. Collecting the interactions in this form, we more readily observe how the on-axis dark state can be created by aligning the magnetic field with propagation and how it is only distinguishability in the polarised light fields which prevents the creation of an equivalent dark state in the presence of transverse magnetic interaction. If we consider the case of Hanle resonance however, which we define here as the equality of power and frequency in circular light, then we achieve a greatly reduced Hamiltonian *i.e.*

ω_2=ω_1

$$\hat{H}_{\Xi} = \frac{1}{2}\hbar \begin{pmatrix} 0 & \Omega_{\mathrm{L}} \sin\theta & 0 & 0 \\ \Omega_{\mathrm{L}} \sin\theta & 0 & \Omega_{\mathrm{L}} \cos\theta & 0 \\ 0 & \Omega_{\mathrm{L}} \cos\theta & 0 & \frac{1}{2\sqrt{3}}\Omega_{\mathrm{R1}} \\ 0 & 0 & \frac{1}{2\sqrt{3}}\Omega_{\mathrm{R1}} & -2\omega_{\Delta 1e} \end{pmatrix}. \tag{4.42}$$

The Hamiltonian now forms a set of degenerate energy levels that only interact in tandem; creating a four-level ladder configuration. To distinguish it from other bases, we shall refer to this new perspective subsequently as the *Hanle superposition*.

4.3 Spatially-dependent EIT (SEIT)

4.3.1 Overview

Now that we have investigated the spatial dependence of our chosen Rubidium levels in the presence of a directed magnetic field, and gone some way to simplify their description, we can begin to address how to spatially modulate our atoms in two dimensions: allowing spatial sculpting of their polarisation to a near-arbitrary degree.

Faced with the problem of trying to introduce spatial dependence, there are many paths we could follow, but ultimately we are concerned either with the manipulation of field amplitude or phase, as outlined in earlier chapters. With holographic control of our input field, amplitude shaping of the incident light would be the most direct method to mediate a region by region interaction, but this approach is fundamentally limited. Without introducing phase differences between the polarisation components, it would be difficult to access, control or preserve atomic phases and by nature would not involve an entire atomic cloud. In contrast, we consider in this section the application of Gaussian modes with only a spatial phase, and show how this can lead to fundamental manipulation of a vapour's angular polarisation: affecting the subsequent absorption and dispersion of incoming light and the consequent geometric manipulation of the field's polarisation structure.

4.3.2 Model

In 1986, Buckle, Barnett, Knight, Lauder and Pegg [94] demonstrated how cyclical excitation pathways depend on both optical and atomic phase, suggesting the use of multi-level systems as interferometers. The delicate phase-dependence of similar systems has also been investigated by many, but of particular interest is the work of Kosachiov, Matisov and Rozhdestvensky [95], where, extending the work of Buckle *et al.* to include relaxation, they conclude that for an arbitrary number of levels, steady-state phase-dependent population dynamics are only possible when the levels form a closed interaction contour (unlike the current

system, outlined in Figure 4.4). They similarly conclude that the stationary state of a closed multi-level system always depends on the total path phase and both of these observations are key to our spatial manipulation.

A Note on Optical Fields

With standard definitions, the optical fields that we have considered thus far have taken the form:

$$\boldsymbol{E}(\boldsymbol{r},t) = \mathcal{E}(\boldsymbol{r})e^{-i\omega t}\, e^{i\varphi(\boldsymbol{r})}\underline{\hat{e}}, \tag{4.43}$$

where $\underline{\hat{e}}$ has represented either horizontally or vertically polarised light respectively. When we consider composite fields acting on both branches of a Zeeman state however, we cannot naively use a linearly polarised basis as each transition may have a different spatial profile. In this section therefore, we will consider fields of the general form

$$\boldsymbol{E}(\boldsymbol{r},t) = \frac{1}{\sqrt{2}}\left[\mathcal{E}_1(\boldsymbol{r})e^{i[\varphi_1(\boldsymbol{r})-\omega t]}\,\sigma_+ + \mathcal{E}_2(\boldsymbol{r})e^{i[\varphi_2(\boldsymbol{r})-\omega t]}\,\sigma_-\right] \tag{4.44}$$

and most often, for the special case of equal power and frequency,

$$\boldsymbol{E}(\boldsymbol{r},t) = \frac{1}{\sqrt{2}}\mathcal{E}(\boldsymbol{r})e^{-i\omega t}\left[e^{i\varphi_1(\boldsymbol{r})}\sigma_+ + e^{i\varphi_2(\boldsymbol{r})}\sigma_-\right]. \tag{4.45}$$

Recalling that absolute phase is ultimately lost on measurement, then we are interested in fields with strictly *relative* phase differences between the circular transitions. The easiest ways to achieve this are naturally to consider the case where each component carries equal and opposite values with respect to one another and similarly, the case where the spatial profile is completely contained within one polarisation. In each case, subtle changes to the Hamiltonian can then arise, as we will see below.

The Hamiltonian

As described previously, our options are limitless when describing a field with spatial phase. Possibly the cleanest theoretical system however, is to again consider a plane wave with no amplitude modulation, but with the now familiar azimuthal winding in each component. For reasons of symmetry, we first consider

the case of equal and opposite OAM and for reasons of experimental concern, we consider the case where each polarisation component contains oppositely charged momentum:

$$\boldsymbol{E}(\boldsymbol{r},t) = \frac{1}{\sqrt{2}}\mathcal{E}e^{-i\omega t}\left[e^{-il\phi}\sigma_+ + e^{+il\phi}\sigma_-\right]; \tag{4.46}$$

a configuration that can easily be obtained with a *q plate* (see chapter 1).

Under the unlimiting assumption that the Zeeman ground level has no hyperfine energy (see chapter 3), and that the applied magnetic field $\boldsymbol{B}$ can be defined as previousy, then the bare state Hamiltonian for equal and opposite OAM has exactly the same form as Eq. 4.33b(p. 133). Where the electric coupling terms of course now carry the additional spatial structure, such that

$$\begin{aligned}\hat{H}_{\text{bare}} = -e^{-il\phi}\frac{1}{2\sqrt{6}}\left[e^{-i\omega_1 t}\Omega_{\text{R1}} + e^{+i\omega_2 t}\Omega_{\text{R2}}\right]|+\rangle\langle e| \\ +\ldots+e^{+il\phi}\frac{1}{2\sqrt{6}}\left[e^{+i\omega_1 t}\Omega_{\text{R1}} + e^{-i\omega_2 t}\Omega_{\text{R2}}\right]|-\rangle\langle e| + H.c.\end{aligned} \tag{4.47}$$

Naturally, the subtle addition to Eq. 4.33b(p. 133) does nothing to simplify the situation and so for our initial considerations we again consider the Hamiltonian with no intra-beam detuning and evenly powered fields. Even under these limitations however, the extra phase components make it more difficult to eliminate matrix elements. A transformation can be found though, such that the new Hamiltonian $\hat{H}_\Xi = \hat{U}^{*T}\cdot\hat{H}_{\text{bare}}\cdot\hat{U}$ is greatly simplified *i.e.*

$$\hat{H}_\Xi = \frac{\hbar}{2}\Big[-2\omega_{\Delta e}|e\rangle\langle e| + \Omega_{\text{L}}\cos l\phi\sin\theta|\psi_1\rangle\langle\psi_2| + \Omega_{\text{L}}N|\psi_2\rangle\langle\psi_c| + \frac{\Omega_{\text{R}}}{2\sqrt{3}}|\psi_c\rangle\langle e|\Big]. \tag{4.48}$$

Here, we note that the Hermitian conjugates have been omitted for conciseness, $N = \sqrt{\cos^2\theta + \sin^2\theta\sin^2 l\phi}$ and that the transformation $\hat{U} = \{|\psi_1\rangle, |\psi_2\rangle, |\psi_c\rangle, |\psi_e\rangle\}$ was applied before appyling the rotating wave approximation under conventional constraints.

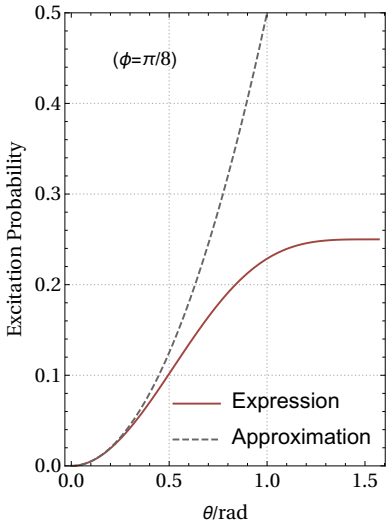

Figure 4.14: The absorption probability according to both the full golden ratio prediction and the same expression under the small angle approximation for $l = \mp 2$, where ϕ is chosen for peak absorption.

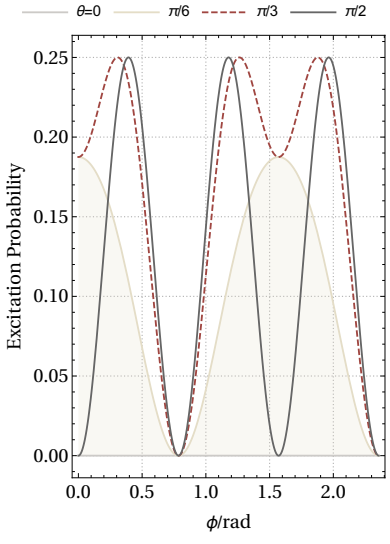

Figure 4.15: The excitation probability with azimuthal angle for different values of magnetic field angle and $l = \mp 2$.

The transformation states are defined according to

$$|\psi_1\rangle \equiv + \frac{ie^{-il\phi}\sin\theta\sin l\phi}{\sqrt{2}N}|+\rangle - \frac{\cos\theta}{N}|0\rangle + \frac{(e^{i2l\phi}-1)\sin\theta}{2\sqrt{2}N}|-\rangle \quad (4.49)$$

$$|\psi_2\rangle \equiv + \frac{e^{-il\phi}\cos\theta}{\sqrt{2}N}|+\rangle - \frac{i\sin\theta\sin(l\phi)}{N}|0\rangle + \frac{e^{il\phi}\cos\theta}{\sqrt{2}N}|-\rangle$$

$$|\psi_c\rangle \equiv - \frac{e^{-il\phi}}{\sqrt{2}}|+\rangle + \frac{e^{il\phi}}{\sqrt{2}}|-\rangle$$

$$|\psi_e\rangle \equiv |e\rangle.$$

We see that the Hamiltonian has now been reduced to the same form as Eq. 4.42(p. 136), such that the system is entirely degenerate on resonance and each level has only one connection; where the couplings themselves have an unusual form. Having transformed to a spatially dependent basis, we see that there is now no phase struture in the optical coherence; the lowest level (which we define as the level with the most linkages between it and the excited state) is coupled magnetically to $|\psi_2\rangle$ and this in turn is magnetically connected to the coupling state $|\psi_c\rangle$. It is perhaps unusual for a normalisation constant to play an active role in the process, but here we see that both the longitudinal magnetic field and a spatially-weighted transverse component is linked to the coupling state through N. Clearly however, we see that $|\psi_1\rangle$ plays the most significant role. In the absence of a magnetic field, then the state is equivalent to the unperturbed $|g_0\rangle$ state and as such doesn't interact with the optical fields, but in the presence of a transverse magnetic field, we see that there are values of ϕ for which the coherence still necessarily vanishes *i.e.* for $\phi = \frac{n}{2l}\pi \forall n \in \mathbb{N}_{\text{odd}}$. Hence, in this configuration we have a *spatially dependent dark state* where, similarly to the system described at the start of the chapter, in steady state there can be no absorption.

4.3.3 *Analytical Solutions*

The dynamics of the system are of course determined by the Schrödinger equation, but for initial insight we can consider cumulative absorption from $|\psi_1\rangle$ to $|\psi_e\rangle$ through *Fermi's golden rule*, $T_{\text{initial}\to\text{final}} \propto \frac{2\pi}{\hbar}\left|\langle i|\,\hat{H}_\Xi\,|f\rangle\right|^2$, where T is the transition proba-

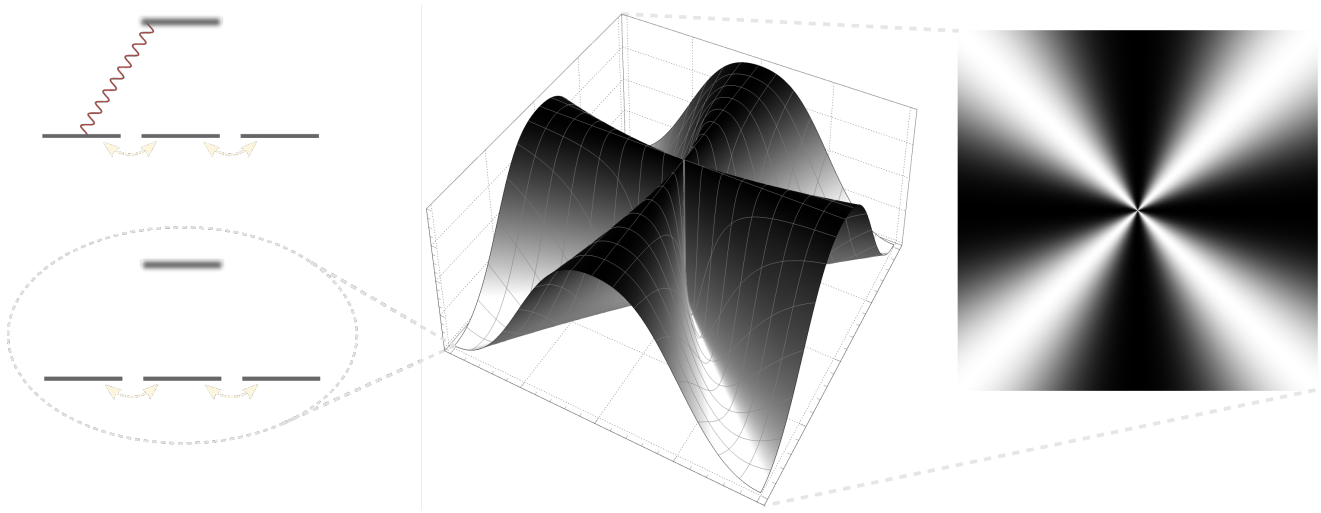

Figure 4.17: The qualitative absorption profile (centre and right) of light carrying orbital angular momentum $l = \mp 2$ in the respective $\sigma_\pm$ polarisation components, as predicted from Fermi's golden rule. In the superposition frame all excitation is mediated by a single field between the upper level and degenerate ground states (top), but for $\phi = \frac{n}{2l}\pi \forall n \in \mathbb{N}_{\text{odd}}$ the coupling vanishes (bottom left).

bility [17]. Although the golden rule is most commonly derived under interaction with a continuum, the concept also holds between discrete states [96] under the standard constraints: where the perturbation is much smaller than the unperturbed transition width and where the probability is quasi-time-independent with respect to the rate of interaction. For a steady-state with negligible excited state population, or for a time interval much shorter than the natural lifetime, the probability is then given by

$$T_{\psi_1 \to \psi_e} \propto \left[\frac{2\pi}{\hbar}\right]^3 \left|\frac{\Omega_\text{L}}{2}\sin\theta\cos l\phi\right|^2 \left|\frac{\Omega_\text{L}}{2}N(\phi)\right|^2 \left|\frac{\hbar\Omega_\text{R}}{4\sqrt{3}}\right|^2. \tag{4.50}$$

Expanding and simplifying, this can be re-expressed as

$$T_{\psi_1 \to \psi_e} \propto \frac{\hbar\pi^3}{96}\Omega_\text{L}^4\Omega_\text{R}^2 \sin^2\theta\cos^2 l\phi\left[\cos^2\theta + \sin^2\theta\sin^2 l\phi\right], \tag{4.51}$$

which in the limit of small magnetic field angle ($\theta \ll \pi/2$) becomes

$$T_{\psi_1 \to \psi_e} \propto \theta^2\cos^2 l\phi \left[\frac{\hbar\pi^3}{96}\Omega_\text{L}^4\Omega_\text{R}^2\right] + \mathcal{O}(\theta^4). \tag{4.52}$$

First of all, we consider the spatial dependence of the absorption without approximation, as plotted qualitatively for $l \mp 2$

17. Note that T is actually a constant probability *rate*.

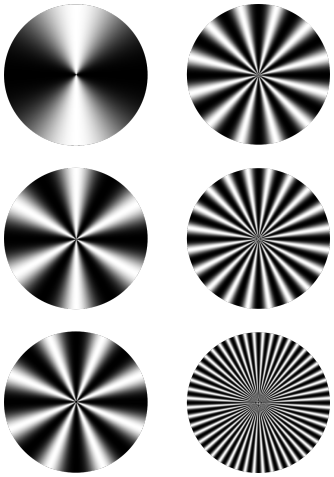

Figure 4.16: The normalised spatial absorption profile ($T_{\psi_1 \to \psi_e}$) of light carrying $\mp l$ in the $\sigma_\pm$ polarisation components respectively $\forall l \in \{1, 3, 4, 6, 10, 24\}$. The azimuth, φ, has been unwrapped according to $\arctan(y/x)$ and minimum to maximum absorption is represented by a linear colour change from white to black.

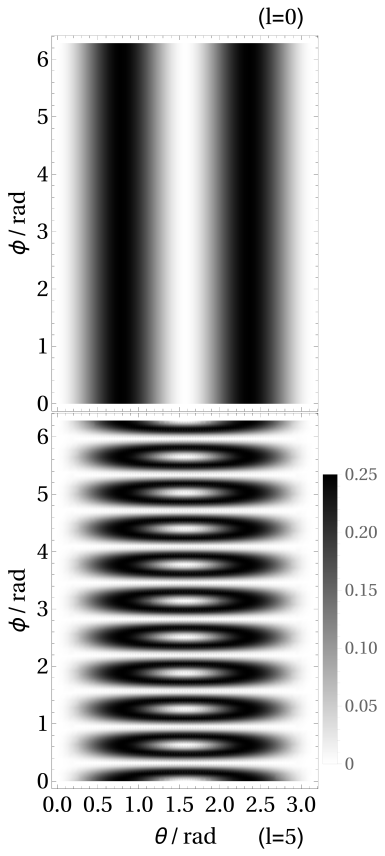

Figure 4.18: The absorption profile of light carrying orbital angular momentum $l = 0$ (top) and $l = \mp 5$ (bottom) as predicted from Fermi's golden rule.

in Figure 4.17. As suggested above, and as stated at the outset, we see that our spatially dependent dark states result in an absorption profile which is shaped around the propagation axis, where the minimum and maximum of absorption are white and black respectively. As an initial prediction under the limitations of Fermi's golden rule therefore, such a result is very encouraging; it is indeed possible to design an absorption profile: or to sculpt atomic shadows. In our discussion of dark states we noted that the coupling disappears when $\phi = \frac{n}{2l}\pi \forall n \in \mathbb{N}_{\text{odd}}$ and this suggests a $2l$ rotational symmetry as confirmed above and as illustrated in Figure 4.16 for higher values of l. Having considered the spatial distribution however, let us now consider the mathematical form of the absorption. In the small angle limit, we have a very concise expression for the absorption in the system, which is actually valid for relatively large angles. If we plot the approximation against the full expression above (Figure 4.14), we see that the two only begin to diverge meaningfully at approximately 30°. In any case, we note the strong dependence on both aspects of the magnetic field: quartic in the Larmor frequency and quadratic in the deviation angle. Such a result shows how relatively insignificant the optical coupling is, only equal in proportionality to the magnetic field angle and with quadratically smaller influence than the magnetic field strength. Refamiliarising ourselves with the system explored in the previous section however, we see that this is also true for when the applied light carries no spatial dependence. There are however some crucial differences. The most dramatic effect of adding the phase profile is of course the spatially dependent increase in transmission, as described by the extra factor of $\cos l\phi$ in $|\psi_1\rangle\langle\psi_2|$. The spatially dependent normalisation factor in the $|\psi_2\rangle\langle\psi_c|$ coupling however, also has a peculiar effect. If we follow the development of the absorption for larger and larger values of magnetic field angle (outside the small angle approximation), we find that each peak of the absorption profile flattens out by 45° and then begins to split. By 90°, the absorption peaks have each completely split in two, doubling the number of lobes (see Figure 4.15).

Such a splitting is a fascinating development, with attractive implications for magnetometry. Although the splitting of an ab-

sorption peak in the presence of a transverse field is not original, it was only in 2013 that Margalit, Rosenbluh and Wilson-Gordon [97] showed that it is possible to split an absorption peak in an $F_g = 1 \rightarrow F_e = 0$ transition. Such a splitting had been achieved with elliptically polarised light in an $F_g = 2 \rightarrow F_e = 1$ transition, but the phenomenon was attributed to the creation of high-order ground states and thus, was not deemed possible for excitations between transitions with lower total angular momentum. Margalit *et al.* however, showed that for their (and our) system, the splitting was proportional to B_x and along with the frequency shift attributed to the strength in B_z it was now possible to independently measure both the value of B_x and the sign and value of B_z. Importantly however, the rending of their absorption peak is a function of longitudinal magnetic field, not space. To the best of my knowledge, the splitting has never been observed spatially, and thus we begin to see the possibility of a visual magnetometer.

Directly comparing the absorption profile of a flat phased beam with that of a spatially dependent one, for all values of ϕ and where the magnetic field angle ranges from 0 to π (Figure 4.18), we can see what overall impact the optical winding has on the absorption profile. Notionally, we can observe the same overall regions: the pattern is symmetric around $\pi/2$, where increasing θ from 0 to $\pi/4$ increases absorption from a minium to a maximum, after which the absorption drecreases to another minimum. The presence of OAM in the beam however introduces a spatially dependent pattern, the frequency of which, in ϕ, can be tuned arbitrarily by changing l or doubled by tuning θ around $\pi/4$ (or equivalently at $\pi - \pi/4$). The spatial shape of the absorption profile can therefore probe the deflection of the magnetic field unambiguously up to $\pi/2$. Furthermore, a subtle effect is that in addition to *removing* the absorption for certain angles of ϕ, we can actually *introduce* absorption in regions that otherwise wouldn't absorb at all *i.e.* in the regions where $\theta = [\pi/4, 3\pi/4]$, through the spatial splitting. In terms of magnitude however we note that the peak values observed are unaffected.

These results pose many questions, but by not considering

the relaxation of the system, we limit their applicability to times much shorter than the lifetime of the upper state, as well as constraining them to within the applicability of Fermi's golden rule. Such is the case, we postpone deeper discussion until we have considered the full master equations.

The Master equations

Near the beginning of the chapter, we considered a model EIT system, where relaxations were introduced phenomenologically. The matrices used to describe them however, are just as applicable here, and don't change under any transformations that we have or will consider. Evaluating the master equation for our system in the usual way therefore, we arrive at the Maxwell-Bloch equations for our system in the rotating superposition frame *i.e.*

$$\frac{\partial}{\partial t}\widehat{\rho}_{1,1} = \frac{1}{3}\left[\gamma + \Gamma\widehat{\rho}_{e,e}\right] - i\left[\frac{1}{2}\Omega_L \cos l\phi \sin\theta\widehat{\rho}_{0,1} - \frac{1}{2}\Omega_L \cos l\phi \sin\theta\widehat{\rho}_{1,0}\right] - \gamma\widehat{\rho}_{1,1} \tag{4.53a}$$

$$\frac{\partial}{\partial t}\widehat{\rho}_{1,0} = -\gamma\widehat{\rho}_{1,0} - i\left[\frac{1}{2}\Omega_L \cos l\phi \sin\theta\widehat{\rho}_{0,0} - \frac{1}{2}N\Omega_L\widehat{\rho}_{1,-1} - \frac{1}{2}\Omega_L \cos l\phi \sin\theta\widehat{\rho}_{1,1}\right] \tag{4.53b}$$

$$\frac{\partial}{\partial t}\widehat{\rho}_{1,-1} = -\gamma\widehat{\rho}_{1,-1} - i\left[\frac{1}{2}\Omega_L \cos l\phi \sin\theta\widehat{\rho}_{0,-1} - \frac{1}{4\sqrt{3}}\Omega_{R1}\widehat{\rho}_{1,e} - \frac{1}{2}N\Omega_L\widehat{\rho}_{1,0}\right] \tag{4.53c}$$

$$\frac{\partial}{\partial t}\widehat{\rho}_{1,e} = \frac{1}{2}\left[-\gamma\widehat{\rho}_{1,e} - (\gamma+\Gamma)\widehat{\rho}_{1,e}\right] - i\left[\frac{1}{2}\Omega_L \cos l\phi \sin\theta\widehat{\rho}_{0,e} + \Delta\widehat{\rho}_{1,e} - \frac{1}{4\sqrt{3}}\Omega_{R1}\widehat{\rho}_{1,-1}\right] \tag{4.53d}$$

$$\begin{aligned}\frac{\partial}{\partial t}\widehat{\rho}_{0,0} =& \frac{1}{3}\left[\gamma + \Gamma\widehat{\rho}_{e,e}\right] - \gamma\widehat{\rho}_{0,0} \\ &- i\left[\frac{1}{2}N\Omega_L\widehat{\rho}_{-1,0} - \frac{1}{2}N\Omega_L\widehat{\rho}_{0,-1} - \frac{1}{2}\Omega_L \cos l\phi \sin\theta\widehat{\rho}_{0,1} + \frac{1}{2}\Omega_L \cos l\phi \sin\theta\widehat{\rho}_{1,0}\right]\end{aligned} \tag{4.53e}$$

$$\begin{aligned}\frac{\partial}{\partial t}\widehat{\rho}_{0,-1} =& -\gamma\widehat{\rho}_{0,-1} \\ &- i\left[\frac{1}{2}N\Omega_L\widehat{\rho}_{-1,-1} - \frac{1}{4\sqrt{3}}\Omega_{R1}\widehat{\rho}_{0,e} - \frac{1}{2}N\Omega_L\widehat{\rho}_{0,0} + \frac{1}{2}\Omega_L \cos l\phi \sin\theta\widehat{\rho}_{1,-1}\right]\end{aligned} \tag{4.53f}$$

$$\begin{aligned}\frac{\partial}{\partial t}\widehat{\rho}_{0,e} =& \frac{1}{2}\left[-\gamma\widehat{\rho}_{0,e} - (\gamma+\Gamma)\widehat{\rho}_{0,e}\right] \\ &- i\left[\frac{1}{2}N\Omega_L\widehat{\rho}_{-1,e} + \Delta\widehat{\rho}_{0,e} - \frac{1}{4\sqrt{3}}\Omega_{R1}\widehat{\rho}_{0,-1} + \frac{1}{2}\Omega_L \cos l\phi \sin\theta\widehat{\rho}_{1,e}\right]\end{aligned} \tag{4.53g}$$

$$\begin{aligned}\frac{\partial}{\partial t}\widehat{\rho}_{-1,-1} =& \frac{1}{3}\left[\gamma + \Gamma\widehat{\rho}_{e,e}\right] - \gamma\widehat{\rho}_{-1,-1} \\ &- i\left[\frac{1}{4\sqrt{3}}\Omega_{R1}\widehat{\rho}_{e,-1} - \frac{1}{4\sqrt{3}}\Omega_{R1}\widehat{\rho}_{-1,e} - \frac{1}{2}N\Omega_L\widehat{\rho}_{-1,0} + \frac{1}{2}N\Omega_L\widehat{\rho}_{0,-1}\right]\end{aligned} \tag{4.53h}$$

$$\begin{aligned}\frac{\partial}{\partial t}\widehat{\rho}_{-1,e} =& \frac{1}{2}\left[-\gamma\widehat{\rho}_{-1,e} - (\gamma+\Gamma)\widehat{\rho}_{-1,e}\right] \\ &- i\left[\frac{1}{4\sqrt{3}}\Omega_{R1}\widehat{\rho}_{e,e} + \Delta\widehat{\rho}_{-1,e} - \frac{1}{4\sqrt{3}}\Omega_{R1}\widehat{\rho}_{-1,-1} + \frac{1}{2}N\Omega_L\widehat{\rho}_{0,e}\right]\end{aligned} \tag{4.53i}$$

$$\frac{\partial}{\partial t}\widehat{\rho}_{e,e} = -\left[\gamma + \Gamma\right]\widehat{\rho}_{e,e} - i\left[-\frac{1}{4\sqrt{3}}\Omega_{R1}\widehat{\rho}_{e,-1} + \frac{1}{4\sqrt{3}}\Omega_{R1}\widehat{\rho}_{-1,e}\right] \tag{4.53j}$$

where we have omitted the Hermitian conjugates for conciseness and the normalisation factor is as defined previously. Considering the complexity of the original problem, we can see that our considered choice of transformation has greatly simplified the resulting equations, such that they are comparable to those for the bare EIT system in the previous section. Using a symbolic algebra engine such as the *Mathematica* programming environment, this set of equations can be solved analytically, allowing us unfettered access to the system dynamics in this regime. The

solutions however, far more so than before, are incredibly protracted, to the point that there is little value in presenting them here. It may prove that the solutions can be simplified under specific approximations, but simpler results have so far remained elusive. Furthermore, the solutions to this set of equations are only valid for the case of equal beam power and equal and opposite angular momentum, so for the sake of efficiency we will continue our analysis using a raw numerical simulation, in the rotating laboratory frame.

4.3.4 Numerical Solutions

To investigate our system numerically it is important to define our parameters from the very beginning. As we are primarily interested in experimentally relevant results, we will consider how our atomic variables relate to measurable quantities, converting them in general to SI units [18] according to the standard parameters listed in Table 4.1.

18. The only exception is $\boldsymbol{B}$, which is more conveniently measured in Gauss.

Constants and Parameters in SI units

Parameter	
d_E /10^{-29}C m	5.068 89
Width /MHz	$2\pi \times 6.06656$
Energy /10^{15}Hz	2.41419

Table 4.1: An overview of the parameters assumed for the $F = 1, 5s^2S_{1/2} \rightarrow F = 0, 5p^2P_{3/2}$ transition in Rubidium 87, as extracted from the Atomic Density Matrix package [93].

The Larmor and Rabi frequencies are then given by

$$\Omega_L = B \ \frac{d_{\text{Bohr}}}{\hbar} \tag{4.54}$$

$$= B \ 8.794\,11\,\text{MHz} \tag{4.55}$$

and

$$\Omega_R = \mathcal{E} \ \frac{d_E}{\hbar} \tag{4.56}$$

$$= \sqrt{\mathcal{I}} \ 41.7222\,\text{MHz} \tag{4.57}$$

respectively, where B is the magnetic field strength in Gauss and $\mathcal{I}$ is given in mW cm^{-2}.

Although we have previously considered a rigorous treatment of absorption, such that the absorbed light was proportional to the imaginary part of the density matrix only, the presence of spatial structure complicates the issue. Using the full form derived previously therefore, we can see that the absorption due

to structured light can be given by

$$\frac{1}{\mathcal{E}_{\pm}k}\frac{\partial}{\partial z}\mathcal{E}_{\pm 1} = N_{\mathcal{V}} z \ \frac{2\sqrt{3}\pi\Gamma}{\Omega_{\mathrm{R}\pm 1}U_{\mathrm{e}}^2}\left[\cos\varphi_{\pm}\,\mathrm{Im}(\widehat{\rho}_{\mp 1,\mathrm{e}}) + \sin\varphi_{\pm}\,\mathrm{Re}(\widehat{\rho}_{\mp 1,\mathrm{e}})\right] \tag{4.58}$$

where multiplying through by the density and the propagation length allows us to consider the absorption under pseudo-realistic conditions, subject to the thin-medium constraint, and where $\pm$ relates the absorption to the $\sigma_{\pm}$ polarisation components. The dispersion is defined similarly, but where the Real and Imaginary functions are interchanged and where the new Imaginary function picks up a preceding minus sign.

Absorption profiles and spatially structured atoms

With these expressions, we can now probe the system for arbitrary planar magnetic fields, where the additional, freely varying, parameters are beam intensity $\mathcal{I}_1, \mathcal{I}_2$, total detuning $\omega_{\Delta 1e}$, spontaneous emission rate Γ , transit decay rate γ , optical density $N_{\mathcal{V}}$, propagation length z and orbital angular momentum l.

The interplay of so many variables does present something of an analytical challenge: both conceptually and practically. In the face of so many considerations, we keep our focus on the cause and consequences of our spatial structure and begin by tracking the dramatic effects of a freely rotating magnetic field and an incoming beam with equal and opposite OAM. Assuming that the incoming field is carrying $l = \mp 2$, then the predicted absorption profiles for 6,50 and 90° can be plotted as before (Figure 4.19). These results confirm the qualitative expectations of Fermi's golden rule and thus, with some fanfare, we can conclude that it should indeed be possible to sculpt our atomic polarisation states in the steady-state under practical conditions: fundamentally, the result we've been looking for. As ϕ is one dimensional, density plots are not the most efficient way to monitor the spatial profile and so further analysis will unwrap the profile azimuthally and, where appropriate, include a momentum probability surface, which in itself highlights the level to which we can now sculpt our atomic system.

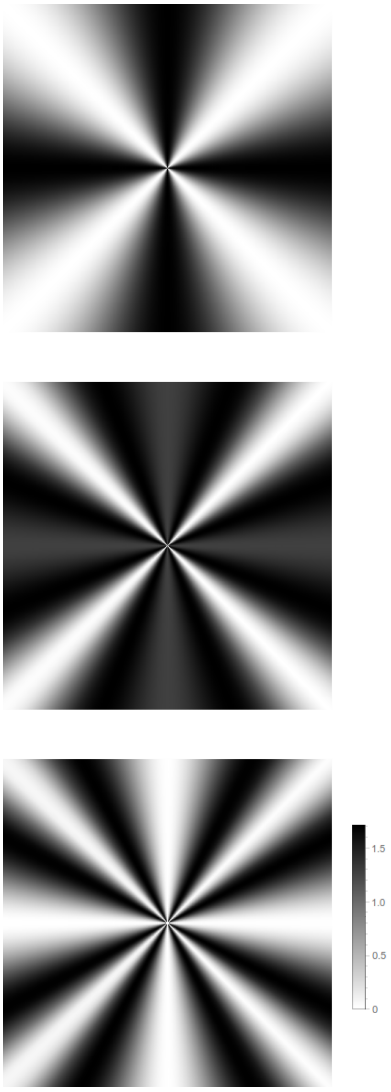

Figure 4.19: The predicted fractional change in transverse absorption for light carrying $l = \mp 2$ when $\theta = 6, 50$ and 90° respectively, where the spatial φ is unwrapped in x and y.

19. We note that on resonance there would be no change in ellipticity due to symmetry and thus, we consider the situation that there is a small total detuning $\omega_{\Delta 1e} = 10\,\text{MHz}$, unless otherwise stated.

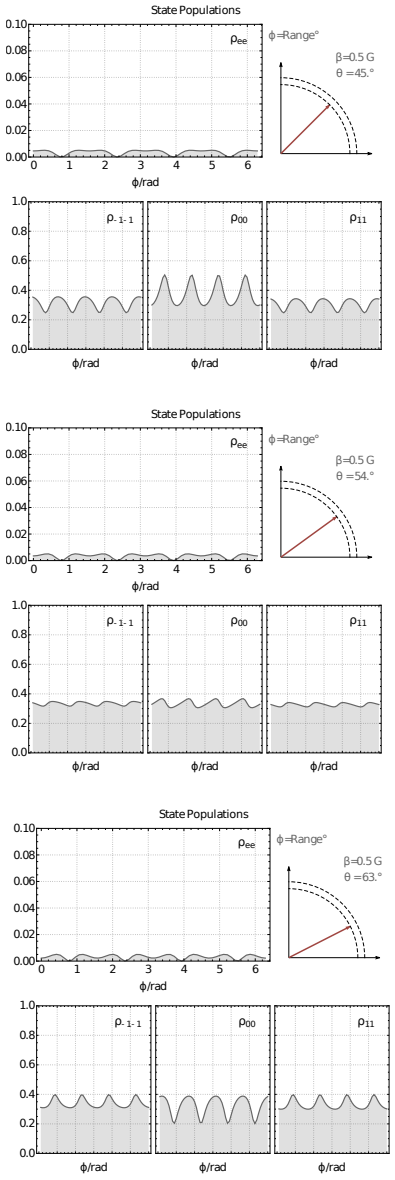

Figure 4.21: The change in state populations with magnetic field angle as the angle is increased around 45°.

Considering Figure 4.20, we observe how the state populations and fractional observables develop with increasing deviation of the magnetic field, under realistic laboratory parameters [19]. First of all, we can confirm that when the magnetic field is pointing along the axis of propagation, then there is no spatial dependence in any of the observables. Furthermore we see that, for these light powers, almost the entire population is driven into the central ground state due both to its lack of coupling and the insignificance of transit relaxation. A negligible transit decay is justified from the trapping parameters reported previously (Table 3.2), where the trap temperature is approximately six orders of magnitude smaller than room temperature. The specific figure of $\gamma = 100\,\text{Hz}$ was then chosen to avoid the numerical complications associated with setting parameters to zero. If we increase the magnetic field angle however, we see that the absorption jumps steeply in magnitude, but also obtains the spatial variance that we predicted previously. Furthermore, the fractional change in absorption is certainly large enough to be experimentally visible, reaching approximately 75% at both absolute and relative value, with the minimum approximately dropping to zero: allowing for experimentally perfect transmission.

If we regard the other observables too, then we see that the small detuning is enough to create a spatial offset between the absorption profiles of the polarisation components, changing the ellipticity, whereas the offset between the two dispersion curves is also enough to instigate rotation of the net incident polarisation. The shaped populations are also revealing, as after only a small angle, we see that the coupling between the ground levels is enough to appreciably distribute the population.

Confirming the prediction of Fermi's golden rule, we see that greatly increasing the angle causes further changes to the system. As the angle increases, the absoprtion peaks stretch linearly and then begin to flatten, but unlike the previous prediction this happens before 45°, suggesting that the balance of field strengths and relaxations must have an effect. Additionally, we begin to see splitting in the spatial profiles of the other observables

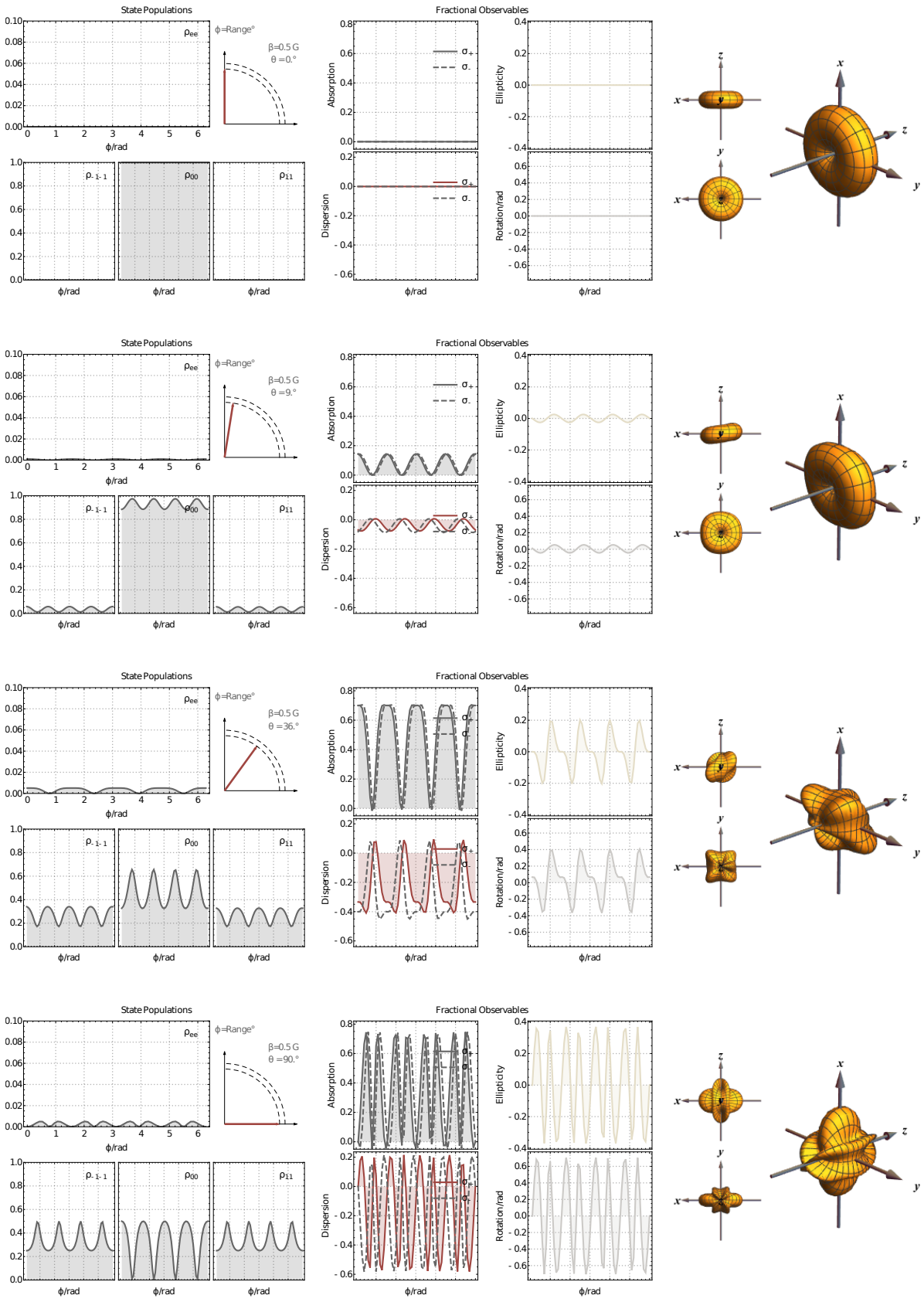

Figure 4.20: An overview of the state populations and observables of interest for a beam carrying $l = \mp 2$ in the absence of a transverse magnetic field. The parameters used in the simulation are $\mathcal{I} = 0.1\,\mathrm{mW\,cm^{-2}}, \gamma = 100\,\mathrm{Hz}, \omega_{\Delta 1e} = 10\,\mathrm{MHz}, N_{\mathcal{V}} = 2 \times 10^{11}\,\mathrm{cm^{-3}}, z = 400\,\mu\mathrm{m}$ and $l = 2$.

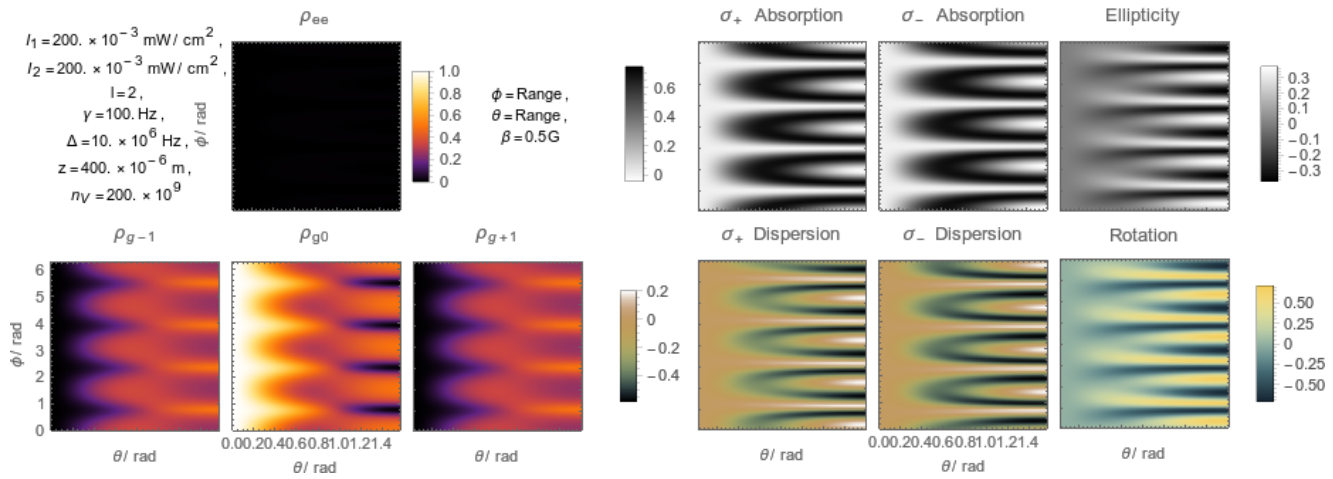

Figure 4.22: An overview of the state populations and observables of interest for a beam carrying $l = \mp 2$ in the presence of a magnetic field, $\forall \theta \in [0, \pi/2]$ and $B = 0.5G$.

and the state poulations have greatly diversified. The excited state has noticably increased its spatially dependent population, while the outer ground states have greatly increased both their base and peak populations: the base increase outstripping the modest gains in spatial contrast. Naturally, as we are considering a conserved system, the central ground state has in comparison lost population due to the increased coupling and has gained spatial contrast, along with an associated increase in gradient. Although the Cartesian dependence in itself is a tangible result, we mention here the change in optical and atomic gradients as this, if verified, could have significant applications in the context of dipole trapping: the dipole force being strongly reliant on the spatial gradient of the Rabi frequency.

Once the angle reaches 90° however, the splitting is complete. Similarly to earlier predictions, we see that after splitting, at least for these parameters, the absorption peak width is equal, but, interestingly, not uniform in the other profiles and not discernible at all in the ground state populations. The peak populations by this angle however, have levelled out completely, a result of maximal coupling between the ground states, while the central ground state has maximised the spatial contrast. A subtle feature however, is that by this angle, the ground state population profiles have completely inverted. Considering Figure 4.21, we can see how over the intervening field angles the profiles ini-

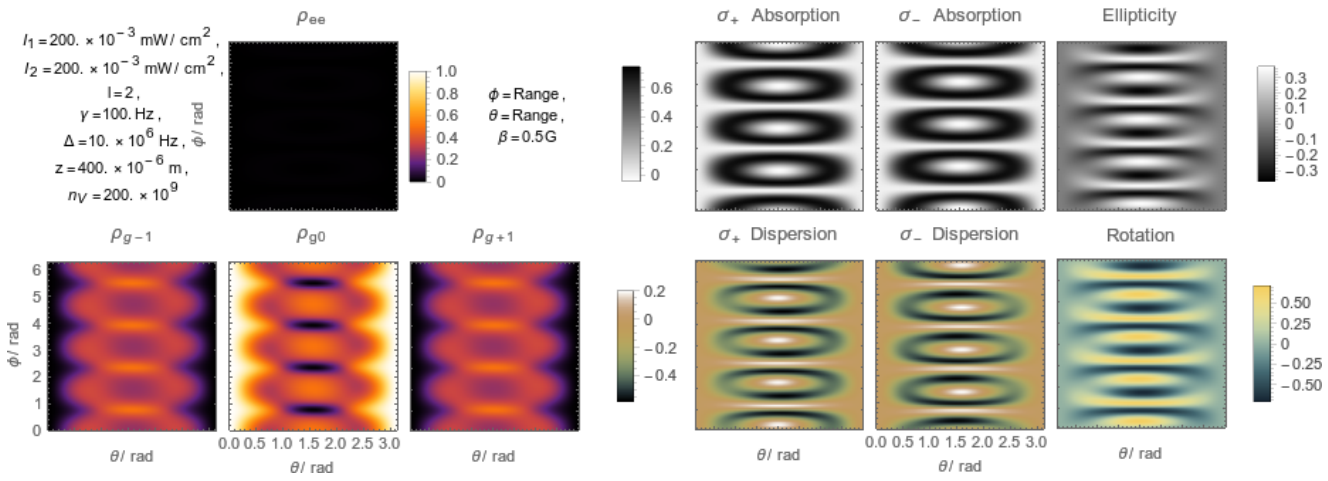

Figure 4.23: An overview of the state populations and observables of interest for a beam carrying $l = \mp 2$ in the presence of a magnetic field, $\forall \theta \in [0, \pi]$ and $B = 0.5G$.

tially pick up a slight skewness towards lower values of ϕ before revealing that the lines between peak and trough are gradually pivoting around their mid-point, with their spatial contrast decreasing and increasing accordingly. The combination of these considerations is illustrated in Figure 4.22.

The density plots in field angle and ϕ reveal the underlying symmetry of the system and suggest that, for this range of field angle, the spatial profile is uniquely specified by the angle of deflection. This appears to be true for every observable individually, although there is far greater uncertainty around $\theta = 0$ and $\pi/2$. In principle however, the transversality of the magnetic field can be discovered visibly by a single camera image of a phase-shaped beam. A natural next question therefore is, of course, how much can we know about the magnetic field from the optical observables? If we consider the system under the same conditions, but where θ extends from 0 to π, then we see that there appears to be a limit to what we can do to the beam structure purely by manipulating the magnetic field angle. The symmetry is such that the profiles appear reflected around $\pi/2$ and hence, very little information is gained. Examining the profiles closely however, we note that there are minor differences in magnitude under this reflection that suggest the symmetry may be avoidable. This is confirmed by observation under a changing magnetic field strength (Figure 4.23).

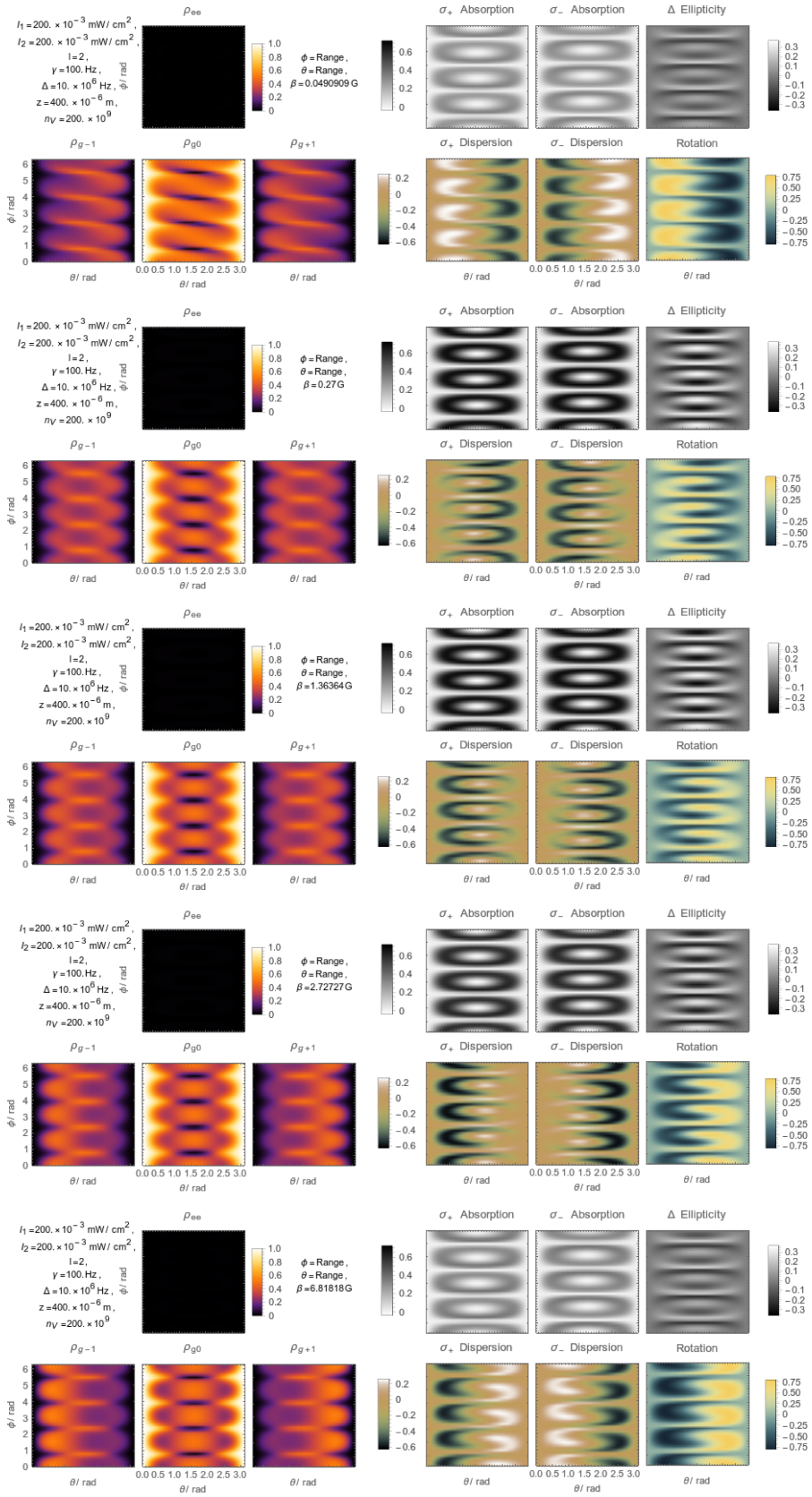

Figure 4.24: An overview of the state populations and observables of interest for a beam carrying $l = \mp 2$ in the presence of a transverse magnetic field.

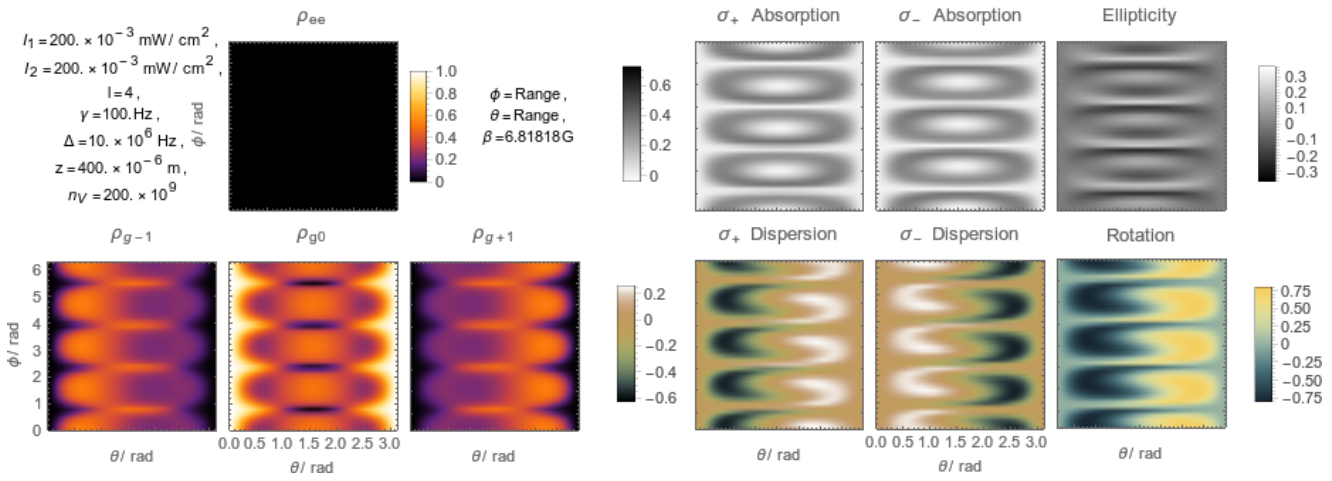

Figure 4.25: An overview of the state populations and observables of interest for a dual structured beam carrying $l = 0$ and $l = 4$ respectively in its $\sigma_\pm$ polarisation components.

Considering Figure 4.23, where the Larmor frequency ranges from approximately $1 - 150\%$ of the natural width, we see that for much lower magnetic field ($B \simeq 0.05G$), the reduced coupling leads to an increased helicity in the outer ground state populations. The slight weighting of peak population from $|+\rangle$ to $|-\rangle$ on increasing field angle is simply an effect of the beam detuning, but the shape of the profile is otherwise identical on resonance, indicating that the phase offset is purely a result of $\boldsymbol{B}$. This influence is also present in the central ground state, where the helicity in ϕ and θ narrows the range of $\boldsymbol{B}$ over which $|0\rangle$ is emptied. The reduced coupling between the ground states has the additionial effect of lowering the absorption in both polarisation states. The spatial structure however, is unaffected and both these properties are reflected in the acquired ellipticity profile, whose shape remains unchanged. The dispersion profiles in contrast, are dramatically altered by the magnetic field strength. Where previously these and the corresponding rotation profiles were degenerately symmetric around $\theta = \pi$, the symmetry has now been broken, such that the spatial dependence is almost unambiguous in θ; the exceptions being the two bounding values.

As we follow the increase in magnetic field, we see that the effect on the state populations is qualitatively weak. The increase in field unwinds the helicity proportionally until it is imperceptible and afterwards the form remains largely unchanged across

the full range, with the exception of the detuning effects, which become increasingly apparent. The effect on the dispersion profiles however is to non-linearly rotate the peaks and troughs around one another in a tightening orbit, stretching the regions of intensely high and low values all the while, until intersection: whereby they combine to form the previous plot. On further increase in magnitude, the curious rotation continues until the regions of low value have rotated 180° around $\theta = \pi/2$. The profile then maintains this form, but intensifies in contrast for a large value of magnetic field, before continuing to rotate in a similar way until the profile reaches its own inverse. Meanwhile, the absorption and corresponding ellipticity profiles grow and shrink in value according to the same pattern discussed for a spatially independent field.

Overall therefore, we see that there is a strong, non-linear dependence on the magnetic field in both strength and field angle, such that scanning either may provide information on the former, although as with all single-shot magnetometry, there are varying degrees of uncertainty depending on the the particular field configuration.

Atomic Shaping of Coupled Beams

So far in this section, we have worked under the simplifying assumption of antisymmetric phase profiles across σ_+ and σ_-. As we have seen, this leads to some startling results, but it is quite a limiting assumption. The next question therefore, is what happens when we remove this constraint?

For this investigation we initially consider a field where σ_+ carries no phase profile and where σ_- carries four units of OAM under the same parameters as previously, the reults of which are displayed in Figure 4.24. Having appropriately chosen our structured field, we immediately confirm that the state populations and fractional observables are only dependent on the *relative* phase difference between the polarisations and so exactly the same results are obtained.

Although not unexpected, considering a measurement's general independence from absolute phase, this is a compelling result. The presence of a spatially shaped beam in the atoms is

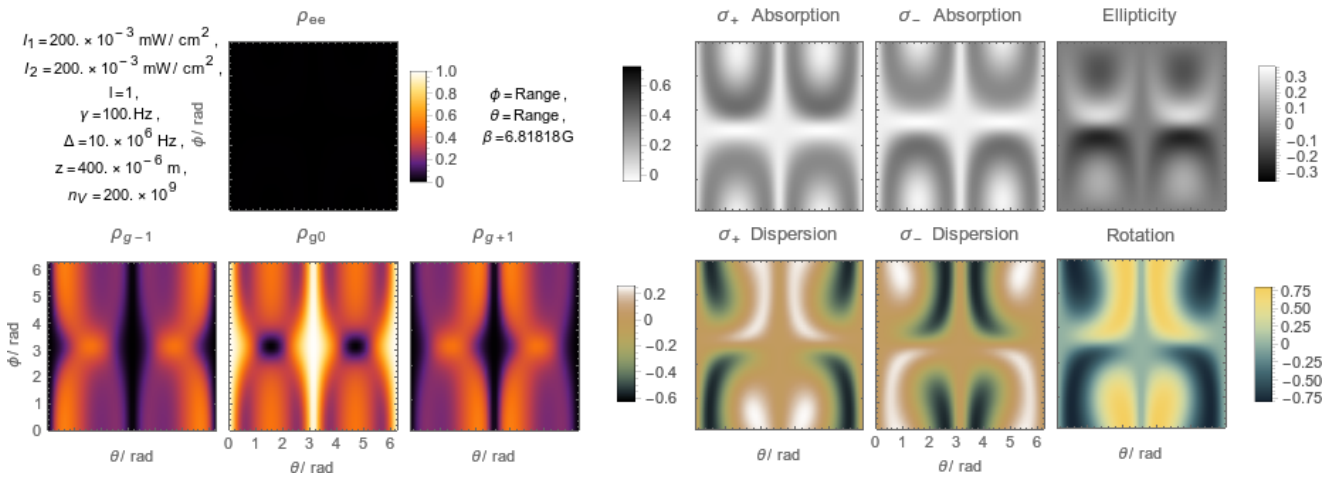

Figure 4.27: An overview of the state populations and observables of interest for a dual structured beam carrying $l = 0$ and $l = 1$ respectively in its $\sigma_\pm$ polarisation components.

enough to mould the atomic polarisation and in the steady-state, the now spatially-dependent interaction has a back effect on exiting planar light: creating large changes in absorption, dispersion, and exiting polarisation.

The presence of a planar field further serves to highlight the fundamental nature of the population trapping as unambiguously, all of the atoms are known to interact with the fields. The sculpting of the atomic polarisation is therefore holistic in nature, and potentially more stable than simple amplitude shaping. Additionally, the ability to create localised transparency, and its associated effects, while interacting with the entire cloud suggests that this technique may find particular use in the study of BEC systems, where the cloud can be described as a single wavefunction. Another salient feature of asymmetric phase profiles is, naturally, the freedom to implement more asymmetry. When considering the measurment of our change in observables, particularly when considering the measurement of rotations and spatial offsets, there is significant advantage in using asymmetric patterns. Indeed, each polarisation component can in principle undergo arbitrary phase-shaping through the use of an SLM and this suggests profound implications regarding the storage of arbitrary two-dimensional information. SLMs however, are in general expensive, and so the ability to create asymmetric patterns from the interaction of planar light with more fundamental

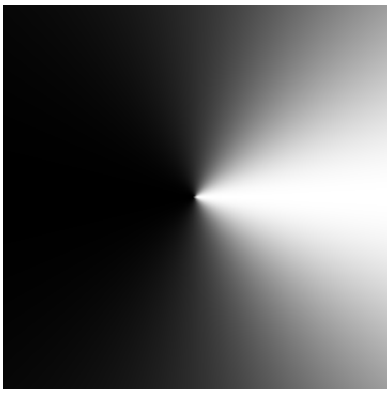

Figure 4.26: The qualitative predicted change in absorption profile for a field carrying $l = 0, 1$: B=5.45 G and $\theta = 25.5°$, where the grayscale changes linearly from white to black, representing minimum to maximum fractional absorption.

profiles may also be of interest. Recalling our discussions from chapter, we note that even a humble glass cone can create asymmetric vector vortex fields, and a beam with a single spiral phase plate could in principle be combined with a 0th-order Gaussian to produce an $l = 1, l = 0$ composite field. Using this combination as an example, we can replot our previous result to obtain a less ambiguous dependence on the magnetic field, as shown in Figure 4.27. For completeness, we have also here extended the range of magnetic field angle to 2πrad. Unfortunately, this clarifies that even with increased asymmetry in the optical fields, there is physical ambiguity for single-shot detection of magnetic field dependence. There is however a reflection around $\theta = \pi$ which makes close to 2πrad angle detection a real possibility for multiple measurements.

4.4 Experimental Tests

Having laid the theoretical ground work for creating our spatially varying atomic polarisations, we now demonstrate how such configurations can be created in practice, a summary of which has been published previously [12].

4.4.1 Overview

Following the work undertaken in the last section, we recall that spatially dependent interactions require a closed interaction, but otherwise there is great freedom in choosing how to account for the spatial phase. We recall however, that the simplest system is when we consider the combined Hamiltonian for both atomic energy states and field interactions under the conditions of equal beam intensity and frequency and where the polarised beam components carry equal and opposite angular momentum. Theoretically, this allowed us to find a complete analytical solution to the system for arbitrary planar magnetic fields, where the additional, freely varying, parameters are total beam intensity $\mathcal{I} = \mathcal{I}_1 = \mathcal{I}_2$, total detuning $\omega_{\Delta 1e}$, spontaneous emission rate Γ, transit decay rate γ and orbital angular momentum l.

As it happens, this result neatly matches the experimental limitations. We discussed in the second chapter that there are many ways of creating beams with orbital angular momentum or spatial structure more generally, but for our initial experiments we used a series of q-plates. As discussed, these novel birefringent waveplates can be used to efficiently convert spin to orbital angular momentum, such that for our purposes [20]

$$\mathcal{E}\hat{\sigma}_{\pm} \rightarrow \mathcal{E}e^{\pm i2q\phi}\hat{\sigma}_{\mp}, \tag{4.59}$$

where the overall phase factor is neglected and q is determined at manufacture. As q-plates twist each handedness of circular-polarisation in an opposing direction, it follows that passing a linearly polarised beam through the plate will produce a superposition of both right and left circularly polarised beams with equal and opposite angular momentum i.e.

$$\hat{Q} \cdot \boldsymbol{E}_{\text{in}}(\boldsymbol{r}) = \frac{1}{\sqrt{2}}\mathcal{E}(\boldsymbol{r})\left[e^{-il\phi}\sigma_{+} + e^{+il\phi}\sigma_{-}\right] \tag{4.60}$$

20. As can be seen in equation Eq. 2.32(p. 24), there is in principle an additional phase factor of α_0, but for our plates this was (in construction) set to zero.

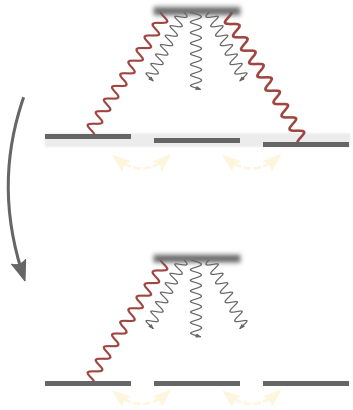

Figure 4.28: The energy level diagrams for the the laboratory and Hanle superposition frames of reference.

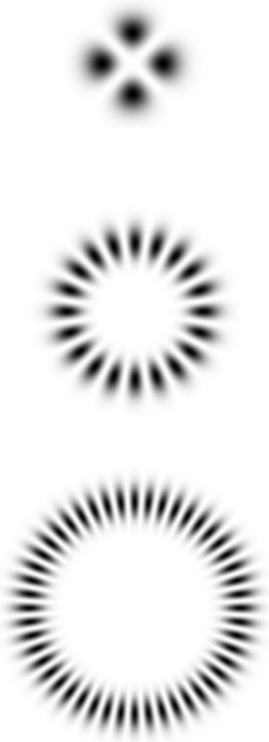

Figure 4.29: The golden-rule absorption predictions for $q = 1$, 5 and 12, accounting for the spatial amplitude of the incident light.

where we have explicitly identified $2q$ with l. Applying such a beam to our Zeeman-split transition results in the opposing polarisations being absorbed independently and thus, it is possible to drive two different transitions with a single dual-structured light field. Such is the case, we had the simplest possible setup for observing spatially dependent absorption: requiring only a single, linearly polarised Gaussian beam, a q–plate and a camera - not forgetting the atoms themselves. The polarisations drove different magnetic sublevels in cold Rb87 and whereas the cloud of atoms was opaque to each individual component, the combined light field generated patterns of transparency as shown in Figure 4.32 for q-plates with q = 1 to 100.

Such a system poses an elegant way of testing our analytical model, but of course is insufficient for testing beams with vastly different phase profiles or internal frequency detunings. There was an expectation of returning to the experiment after the initial findings, but construction work led to unexpected problems in the laboratory and, in the end, the entire atom-trapping apparatus had to be reassembled. The resulting time loss means we will only consider an incomplete collection of experimental findings. In summary however, we will conclusively demonstrate the shaping of absorption patterns for many different values of orbital angular momentum and their dependency on polarisation structure, although without considering their explicit dependence on magnetic field. Instead, the magnetic field is used only to close the atomic energy levels, and is perturbative, such that the Zeeman splitting of the energy levels is well within the natural width of the ground state.

Under these assumptions, the Hamiltonian can be faithfully described by Eq. 4.48(p. 139), with the relaxations described as per the rest of the chapter. For the waveplate results however, the theoretical comparisons were calculated numerically, using

$$\begin{aligned}\hat{H}_{\text{bare}} =& \frac{\hbar}{2}\Big[\mp \Omega_{\text{L}} \cos\theta |\pm\rangle\langle\pm| + 2U_{\text{e}}|e\rangle\langle e| \\ &- \frac{1}{\sqrt{2}}\Omega_{\text{L}} \sin\theta |+\rangle\langle 0| - \frac{1}{\sqrt{3}}\Omega_{\text{R}} \cos\omega t \, e^{-il\phi}|+\rangle\langle e| \\ &- \frac{1}{\sqrt{2}}\Omega_{\text{L}} \sin\theta |0\rangle\langle -| + \frac{1}{\sqrt{3}}\Omega_{\text{R}} \cos\omega t \, e^{+il\phi}|-\rangle\langle e| + H.c.\Big].\end{aligned} \tag{4.61}$$

4.4.2 Setup and Procedure

As highlighted above, the use of a q-plate to generate the optical field allows the experimental system to remain conceptually quite simple. Following the procedures outlined in the last chapter, the trapping system can be optimised normally to obtain a dual MOT & SpOT setup and once this has been established, all that is required is to extend the *repump probe* arm of the trap to allow for the additional wave plate and imaging optics.

The relevant arrangement of the imaging components can be seen in figure Figure 4.30. Here, what we will now refer to as, the *probe* beam is passed through a pinhole, collimated, and directed through the q-plate before being focused onto the atomic cloud. The positioning of the last lenses can then be used to determine the imaging conditions of the q-plate on the atoms. With one metre between the q-plate and the atoms, we use either an $f = 250$ or $f = 500\,\text{mm}$ lens such that the $2f/f$ imaging conditions are satisfied for near or far-field imaging respectively. With this configuration, and subsequently using the LabVIEW programming environment, the optical frequency is tuned to resonance with the hyperfine transition of interest $F = 1, 5s^2S_{1/2} \rightarrow F = 0, 5p^2P_{3/2}$ and the experimental timings are tailored programmatically to synchronise trap loading times, magnetic field configurations and beam switching. The following experimental procedure was then implemented accordingly, to obtain the three images required for absorption imaging, as laid out in Eq. 3.118(p. 94).

1 Image the probe beam to obtain $\mathcal{I}_{\text{input}}$.
2 Form a MOT (6 s).
3 Dynamically load a SpOT (250 ms).
4 Switch off the trapping lasers and quadropole field.
5 Allow cloud expansion (2-5ms).
6 Trigger the camera to obtain $\mathcal{I}_{\text{output}}$.
7 Trigger the quantisation coils (duration of probe).
8 Trigger the probe beam (.2-.5ms).
9 Trigger the camera to obtain $\mathcal{I}_{\text{background}}$.

MOT	Axis	
Parameter	x	y
N_a	$1.3(1) \times 10^8$	
Size/µm	1300(7)	850(7)
$N_\mathcal{V}/\text{cm}^{-3}$	$9.3(8) \times 10^9$	
Temp./µK	388(7)	137(7)

Table 4.2: An overview of the key MOT parameters.

SpOT Parameter	Axis	
[Delay/µs]	x	y
N_a[2000]	$8.6(1) \times 10^7$	
N_a[3000]	$7.5(1) \times 10^7$	
Size [2000]	291(7)	315(7)
Size [3000]	291(7)	315(7)
$N_\mathcal{V}$[2000]	$2.1(7) \times 10^{11}$	
$N_\mathcal{V}$[3000]	$2.0(7) \times 10^{11}$	
Temp./µK	38(7)	114(7)

Table 4.3: An overview of the SpOT parameters, where the bracketed terms denote the probe delay and the units are consistent with the table above.

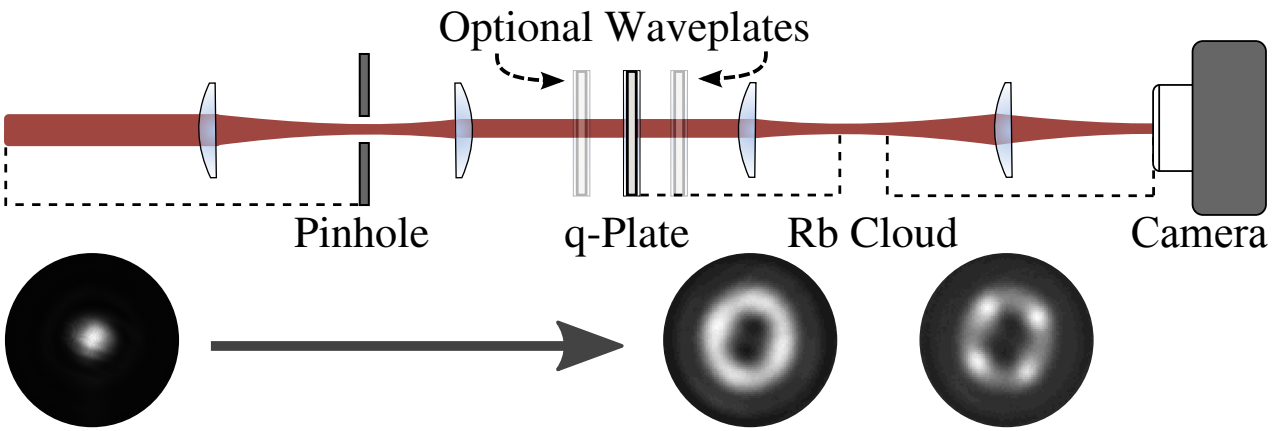

Figure 4.30: A simplified account of the imaging beam path, where the optional components are a combination of half- and quarter-wave plates, as described below. The insets are cropped images of the beam intensity, as observed on the camera under conditions of no q-plate (Left), no atomic cloud (Middle) and normal operation (Right) and serve to indicate the state of the beam at the regions indicated for $q = 1$.

The variation in pulse and expansion timings were performed on an adhoc basis to experimentally maximise the contrast in the patterns. It may seem counter intuitive to take the trouble to form a SpOT, only to let it expand outwards, but there are a few advantages to using the SpOT over a normal MOT. The main gain is that the SpOT allows for a drastically increased number density, which naturally allows for maximisation of the absorption and minimisation of collisional broadening and decoherence. The formation of a dark SpOT in particular however, means that not only is unpredictable repopulation minimised through the temperature gains, but also that we reliably load the atomic population into the $F = 1$ ground state: giving exceptional control over the polarisation of the system. A summary of the normal operating parametrs are given in Table 4.2 and Table 4.3 for the MOT and SpOT respectively. In regards to the magnetic field interaction, in Chapter 3 we discussed how the quantisation coils were used both to cancel the Earth's magnetic field and to define the quantization axis for absorption measurements and the same is largely true here. In this experiment however, the compensation field is slightly *misaligned* in order to provide the required closure of the atomic transitions. For these initial experimental

results, the full dependence of absorption on the magnetic field properties was not investigated, and so the field deviation θ from the propagation axis is assumed to have been small *i.e.* $\theta \ll \pi/2$, but not zero, while the magnetic field strength was set such that the Zeeman shift was within 1% of the excited state line width.

4.4.3 *Results and Discussion*

The insets of Figure 4.30 illustrate how a beam develops as it passes through the imaging setup, assuming action with a $q = 1$ q plate [21]. Initially a linearly polarised fundamental Gaussian, the beam picks up equal and opposite angular momentum in each component of its polarisation as it passes through the q-plate. As the momentum is carried within independent polarisation states, the associated electric fields do not interfere with one another and so on propagation to the camera the beam takes on a similar appearence to that of an $l = 2$ Laguerre-Gaussian beam[22]. The beam then passes through the atomic cloud and, as predicted, undergoes spatially dependent absorption.

21. For clarity, we stress that these images were not taken *in situ*, but rather by removing relevant components from the beam path, where the probe beam was measured in the far-field.

22. We recall here that a beam shaped only in phase is not a true LG beam.

Absorption and Phase

The final camera image above is a significant result in itself: as it was the first reported observation of spatially dependent electromagnetically induced transparency and we emphasise here that these camera images are single-shot and, other than cropping, haven't been altered in any way. Our theoretical predictions however concern absorption in the more technically constrained fashion. As outlined previously, one measure of absorption is the optical density/optical depth OD which can be expressed:

$$\mathrm{OD} = \ln\left(\frac{\mathcal{I}_{\mathrm{in}} - \mathcal{I}_{\mathrm{back.}}}{\mathcal{I}_{\mathrm{out}} - \mathcal{I}_{\mathrm{back.}}}\right),$$

where we have re-labeled the intensities to relate them to our experimental procedure. There is a problem with this approach however. As we are dealing exclusively with vortex beams, then, axiomatically, our camera images will contain areas of zero intensity. This equation therefore, suffers from singularities and

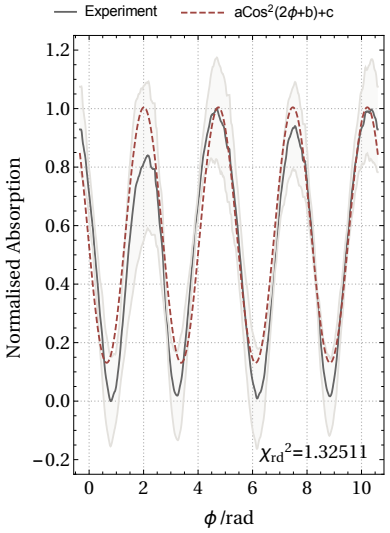

Figure 4.31: The mean absorption profile for $l = \mp 2$ transformed to polar coordinates and compared to $a\cos^2(2\phi + b) + c$: where a, b and c are fitting constants. The shaded region is the standard deviation in the mean.

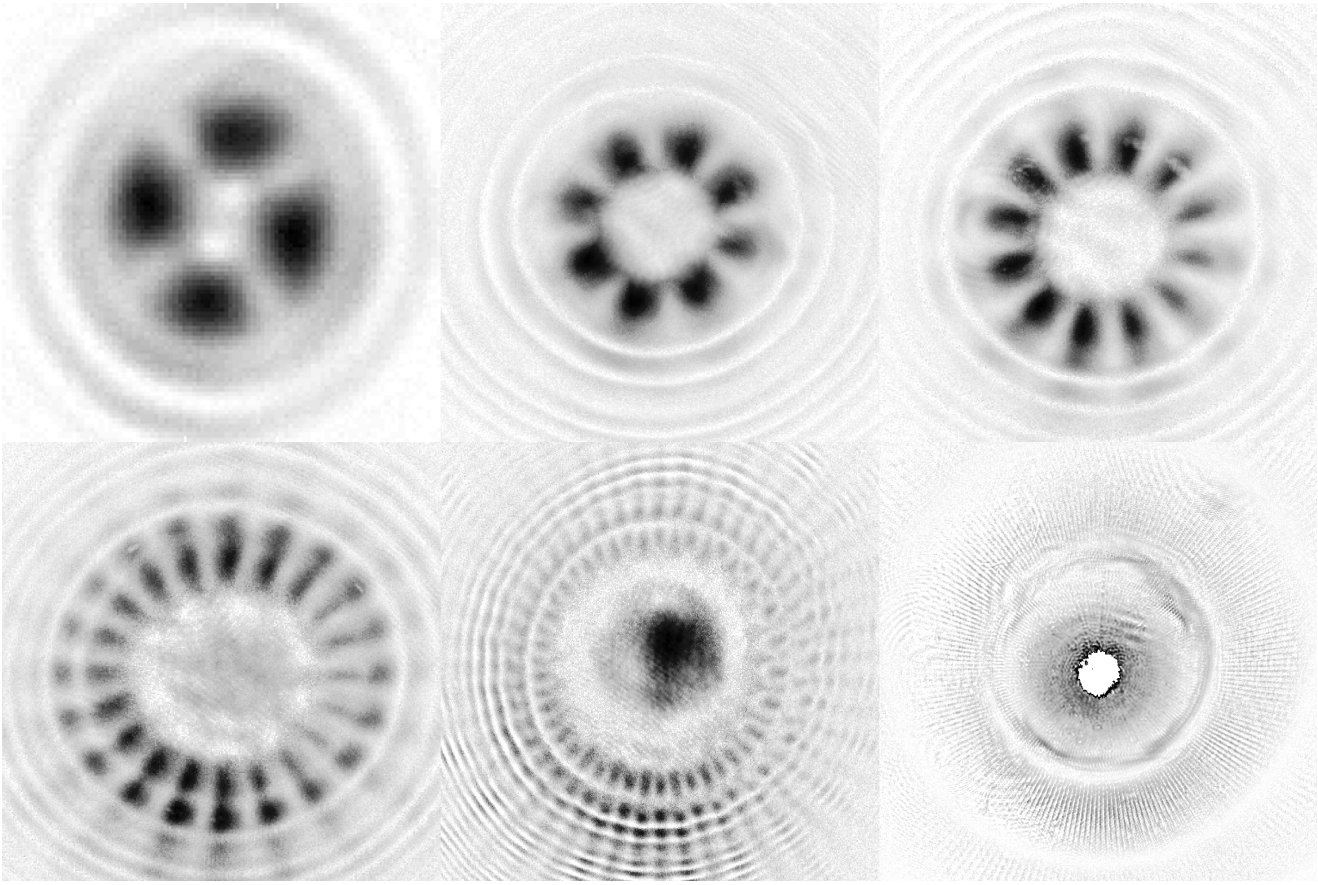

Figure 4.32: The calculated absorption profiles for beams with $l = 2, 4, 6, 10, 24$ and 200, where minimum to maximum absorption is represented by a linear gradient from white to black.

even where there is no *mathematical* problem, experimental fluctuations mean that significantly low intensity regions will still skew the image scaling. Such is the case, we now consider the calculated optical densities for varying values of orbital angular momentum, where each image is scaled by $\sqrt{\mathcal{I}_{\text{in}}}$ to enhance the meaningful areas of interest (see Figure 4.32). [23] Immediately, we see that the absorption patterns confirm the relevant discussions of the previous section. For the case of small magnetic field angle, with equally intense beam polarisations, we recover a petal pattern with $2l$ lobes: confirming that our atomic polarisations have been shaped. A result that extends throughout high-dimensional space in OAM. Furthermore, if we consider the absorption image for $l = \mp 2$ under a transformation to polar coordinates, then we can explicitly confirm the $\cos^2 l\phi$ spatial dependency, as shown in Figure 4.31 for $l = \mp 2$. Direct comparison with our earlier

23. Where we recall that maximum and minimum absorption are represented by black and white respectively, which we now see helps to avoid confusion with the camera images.

considerations is not strictly appropriate however, as the models don't take the radial profile of the incident beams into account. To compensate for this, the experimental curve was created by first unwrapping the absorption profile and cropping around the input-beam region. Each radial slice was then scaled to a common mean, before taking a final average. The standard deviation then provided an estimate of the azimuthally dependent uncertainty, and this allowed a reduced χ^2 comparison with the fit.

So far however, we have considered the absorption profile only for the case of far field imaging of the q-plates onto the atoms. As the q-plate is a phase-only modulator, this is a natural imaging condition as theoretically it is only on propagation that the beam will look any differently. For our purposes however, we are interested in whether the system can be modified independently of amplitude shaping and so we also consider the absorption in the case of near-field imaging. Changing the focal length of the imaging lens therefore, the experiment was conducted again and a summary of the results can be found in Figure 4.33. Bearing in mind that getting an optical component exactly in the imaging plane is incredibly sensitive and that the q plate is not 100% efficient, we see that the near-field images visually resemble the predictions made previously, with the exception of the decaying radial intensity. Aside from the experimental noise in the centre, we see that the depth of absorption is consistent, but the amplitude superpositions which are reminiscent of LG superpositions are gone. Thus, we can assume that even in the absence of beam shaping, a spatially dependent phase can mitigate spatially dependent transparency across a cloud of atoms.

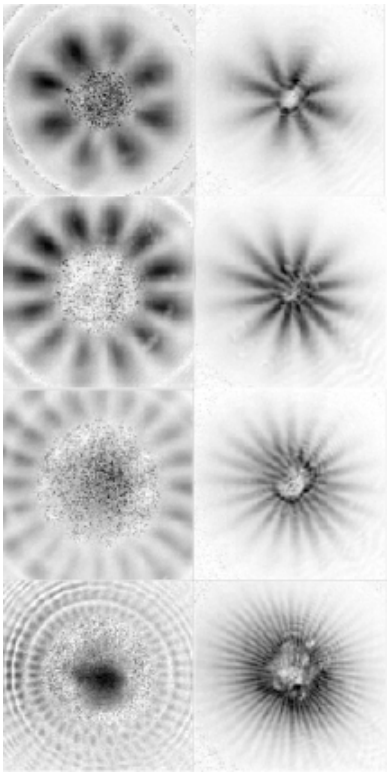

Figure 4.33: The calculated absorption profiles for beams with $l = \pm 4, 6, 10$ and 24 in both the far- (left) and near- (right) field imaging planes.

Absorption and Polarisation

Considering a response to the published paper, it is important to emphasise that the spatial phase dependence of fields is, in general, completely independent of the polarisation. As we stressed previously however, there is an intimate correlation between local polarisation and spatial dependence. In fact, if we

expand the composite field created by the q-plates in terms of Cartesian components, then the field factorises concisely:

$$\boldsymbol{E}(\boldsymbol{r},t) = \mathcal{E}(r,z,t) \begin{pmatrix} \cos l\phi \\ \sin l\phi \\ 0 \end{pmatrix}. \tag{4.62}$$

Therefore, this field can be equally well considered as an unshaped beam, whose linear polarisation rotates azimuthally with frequency $2l$. We can therefore predict the petal pattern from the local atomic interference of excitation amplitudes, where like polarisations interfere according to the quantisation axis. This can then be confirmed using waveplates (see Figure 4.34). Plotting the local polarisation as colour-coded ellipses, for the specific case of $l = \mp 2$, we see that the input field has the expected rotation from vertical to horizontal polarisation within $\phi = \frac{n}{2l}\pi \forall n \in \mathbb{N}_{\text{odd}}$. As the half-wave plate is turned, the input field picks up the associated rotation and so the absorption profile as a whole is seen to turn accordingly. This is summarised by the upper right inset, where the azimuhal pattern for 19 different measurements has been unwrapped by the same coordinate transform used previously. Replacing the half-wave plate with a quarter-wave plate however is perhaps more revealing. In this configuration, we see that the absorption profile moves from spatially dependent absorption at 0° to spatially independent absorption at about 45°, where we recall that the middle of the images is prone to noise. Confirming the spatially dependent transparency, these images show that both arms of the tripod must be present before we observe the patterns, as by rotating the quarter-wave plate through 45° we transform the input beam from dual structured linear polarisation to purely circular polarisation through the properties of the qplate. Extending these considerations further, we can see that if we examine instead the results of a quarter-wave plate after the q-plate, then the structured light picks up additional areas of interference, strongly absorbing the horizontally polarised components of the field - akin to an *inverse* polariser.

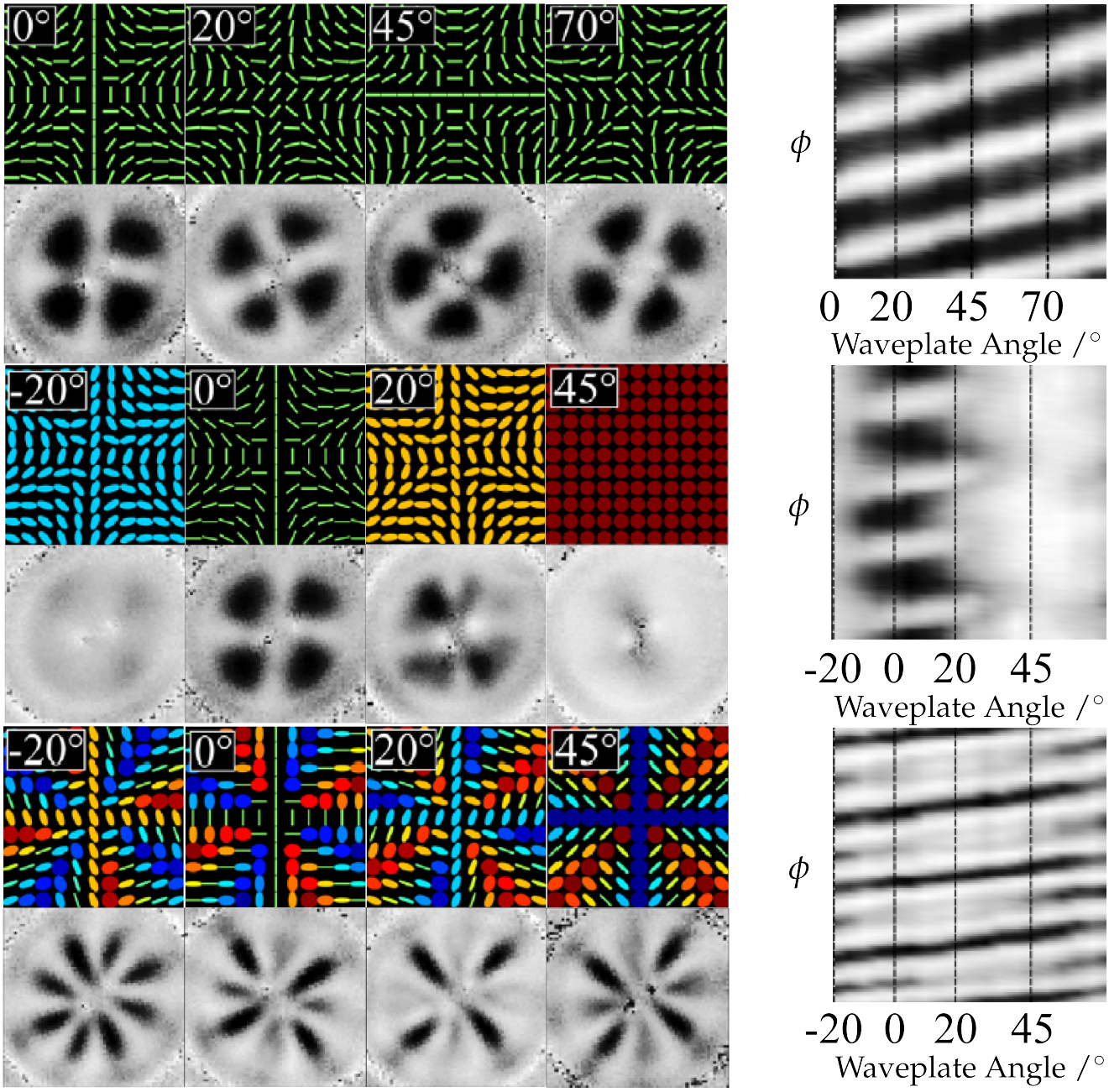

Figure 4.34: Absorption profiles as a function of input polarisation for a probe beam with $q = 1$. In the top row, we see the local polarisation and absorption profiles as a function of half-waveplate angle, where the half-waveplate is placed before the q-plate. In the middle row, we see the same plots, but where the quarter-waveplate is before the q-plate. In the bottom row, we see the same plots, but where the quarter-wave plate is placed after the q-plate. Throughout, the right-hand column is the polar coordinate representation of the absorption profiles in the same row.

4.4.4 Experimental Conclusions

In this section, we have seen how the founding principles of our theoretical discussions can be realised experimentally. We have not explicitly measured the atomic populations or considered the magentic field coupling and we have not studied the geometric manipulation of polarisation, either in rotation or change in ellipticity. That being the case however, we have reviewed explicit evidence of the spatial manipulation of an atomic cloud: specifically evidenced by the creation of spatial patterns of transparency. We have seen how this can be done very simply, using only one additional optical element, and have confirmed the phase-induced mitigation of spatial absorption for both very low and high values of orbital angular momentum. We have further demonstrated the shaping of atomic absorption without amplitude modulation, and shown how the polarisation structure of the input field affects the output: such that the symmetry of the former determines that of the latter and where the ratio of power in the excitation amplitudes is a key factor in the depth of the petal contrast.

In summary, having actualised our theoretical concerns, we are now forced to concede that the shaping of atomic absorption is a palpable possibility. Real enough to settle our past questionings; substantial enough to cast a shadow on what may lie ahead...

PART III

. . . IN THE END

ENDINGS

We shall not cease from exploration
And the end of all our exploring
Will be to arrive where we started
And know the place for the first time.

T.S. Eliot

5

And so, four years and four chapters later, we come right to the very end of our story: a tale that, I can honestly say, has grown much in the telling. At this point in our journey however, with both the end and the comforts of home in sight, I ask that you'd bear with me just a little longer, that we might chance a glance backwards and know how far we've come.

Summary

In summary, from arbitrary creation to considered absorption, we have demonstrated the sculpting of both light and atoms across an entire optical life span.

First considering the spatial properties of classical light fields in general, we categorised their core architecture and dependencies before focussing our attention on their relationship with amplitude and phase. With particular application to phase-only spatial light modulators, we then considered a detailed outline of how complex optical landscapes can be created in theory, before confirming the practice through both simulation and experiment. Comparing six different methods, we reflected on the strengths and weaknesses inherent in each, including a surprising triumph of simplicity over study. Of particular note in this section, was the inclusion of a new hologram creation method and the study

of the input beam in the hologram creation process. In particular, we saw the introduction of an original method for both measuring and accounting for the beam profile and highlighted how introducing a deliberate discrepancy between the known and the assumed incident light can be used to trade accuracy for power. Furthermore, the relation between aperture size, image quality and power was also studied, posing a possible tweak for optimising spatial modes.

Passing from creation to communication, we then considered how a simple assortment of optical components can be used for high-speed data transfer and reviewed the demonstration of 10 kHz character switching rates.

In the third chapter, we reviewed, in some depth, the theoretical tools and concepts required for the study of atomic structure and reported the re-creation of both a magneto-optical trap and a dynamically switched holographic dark SpOT.

Finally, in the previous chapter, we built a complete theoretical model of a magnetically-coupled four-level atomic system. This system was composed of two hyperfine levels, where the ground state was internally coupled by a two-dimensional magnetic field. Fundamentally, We saw how the application of oppositely polarised phase-shaped beams can dramatically alter the atomic coherences: extending the well-known results of EIT to the two-dimensional domain. Recalling the atomic system outlined previously, we then considered the experimental demonstration of this process where the application of differing spatial phases was used to selectively choose the shadows of our choice.

Future Outlook

It is with some sadness that a conspiracy of both the unexpected and the otherwise prevented the full completion of this work. The silver-lining to this non-atomic cloud however, is that there are many avenues for further adventure. And of the work re-

viewed so far, we could say it is the spatial shaping of atomic polarisations that has the brightest future.

The creation of two-dimensional dark states, particularly considering their derivation from CPT and EIT effects, raises the fascinating possibility of an entirely new way of creating a transverse atomic memory. Such a system would then have several advantages. Unlike for other memories, the spatial dark states derived in the fourth chapter are intrinsically decoupled from the environment and so there is already the potential for greater stability. Moreover, the ability to encode all of the transverse information in one transition would experimentally guarantee the phase coherence between probe and signal, increasing the potential of the spatial resolution. The predicted reliance of the dark states on the magnetic field would also then allow for precision control of the interaction: particularly during the reading and writing processes. In regards to the feasibility of these investigations, the current Bloch-equation model and associated software would require little extension for temporal analysis and so the immediate future is very promising. Additionally, the atomic trap is in the process of being rebuilt and so the experimental verification of the magnetic field dependencies is also not a distant prospect.

Overall therefore, there is both the means and motivation for future development and so the outlook for the future is encouraging.

Closing Remarks

It has been something of a historical preoccupation with the natural philosophers of the past: that laws and lemmas were formulated in terms of straight lines, stationary frames and the flattest, purest possible fields; with the curvature of space and the constant motion of particles however, maybe this was a mistake. Indeed it is a curious thing, that people like Fresnel, with all of the tools, theory and motivation, never encountered a vortex beam from a simple glass cone. But then, according to Jung, one does not become enlightened by imagining figures of light, but

by making the darkness conscious …

PART IV

BACK MATTER

BIBLIOGRAPHY

[1] Eivind Uggedal. Social navigation on the social web. https://github.com/dergachev/uggedal-thesis/blob/master/uggedal.pdf. Accessed: 2016-10-14. Cited on p. xvii.

[2] Neil V. Corzo, Baptiste Gouraud, Aveek Chandra, Akihisa Goban, Alexandra S. Sheremet, Dmitriy V. Kupriyanov, and Julien Laurat. Large bragg reflection from one-dimensional chains of trapped atoms near a nanoscale waveguide. *Phys. Rev. Lett.*, 117:133603, Sep 2016. Cited on p. 2.

[3] H. L. Sørensen, J.-B. Béguin, K. W. Kluge, I. Iakoupov, A. S. Sørensen, J. H. Müller, E. S. Polzik, and J. Appel. Coherent backscattering of light off one-dimensional atomic strings. *Phys. Rev. Lett.*, 117:133604, Sep 2016. Cited on pp. 2 and 3.

[4] Evangelos Theocharous, R Deshpande, AC Dillon, and J Lehman. Evaluation of a pyroelectric detector with a carbon multiwalled nanotube black coating in the infrared. *Applied optics*, 45(6):1093–1097, 2006. Cited on p. 2.

[5] Vantablack. https://www.surreynanosystems.com/media/images-videos. Accessed: 2016-10-14. Cited on pp. 2 and 3.

[6] HR Gray, RM Whitley, and CR Stroud. Coherent trapping of atomic populations. *Optics letters*, 3(6):218–220, 1978. Cited on p. 2.

[7] Claude Cohen-Tannoudji and Serge Reynaud. Dressed-atom description of resonance fluorescence and absorption spectra of a multi-level atom in an intense laser beam. *Journal of Physics B: Atomic and Molecular Physics*, 10(3):345, 1977. Cited on p. 2.

[8] S. E. Harris, J. E. Field, and A. Imamoglu. Nonlinear optical processes using electromagnetically induced transparency. *Phys. Rev. Lett.*, 64(10):1107–1110, March 1990. Cited on p. 2.

[9] K.-J. Boller, A Imamoglu, and S E Harris. Observation of electromagnetically induced transparency. *Phys. Rev. Lett.*, 66(20):2593–2596, May 1991. Cited on p. 2.

[10] Focus: Strong light reflection from few atoms. https://physics.aps.org/articles/v9/109. Accessed: 2016-10-14. Cited on p. 3.

[11] N Radwell, D Brickus, TW Clark, and S Franke-Arnold. High speed switching between arbitrary spatial light profiles. *Optics express*, 22(11):12845–12852, 2014. Cited on pp. 3 and 47.

[12] Neal Radwell, Thomas W Clark, Bruno Piccirillo, Stephen M Barnett, and Sonja Franke-Arnold. Spatially dependent electromagnetically induced transparency. *Physical review letters*, 114(12):123603, 2015. Cited on pp. 4 and 157.

[13] Thomas W Clark, Rachel F Offer, Sonja Franke-Arnold, Aidan S Arnold, and Neal Radwell. Comparison of beam generation techniques using a phase only spatial light modulator. *Optics express*, 24(6):6249–6264, 2016. Cited on pp. 4 and 31.

[14] Francesco Pampaloni and Jörg Enderlein. Gaussian, hermite-gaussian, and laguerre-gaussian beams: A primer. *arXiv preprint physics/0410021*, 2004. Cited on p. 13.

[15] P Hariharan and PA Robinson. The gouy phase shift as a geometrical quantum effect. *journal of modern optics*, 43(2):219–221, 1996. Cited on p. 14.

[16] Simin Feng and Herbert G Winful. Physical origin of the gouy phase shift. *Optics letters*, 26(8):485–487, 2001. Cited on p. 14.

[17] Paula B Monteiro, Paulo A Maia Neto, and H Moysés Nussenzveig. Angular momentum of focused beams: Beyond the paraxial approximation. *Physical Review A*, 79(3):033830, 2009. Cited on p. 17.

[18] N. Jhajj, I. Larkin, E. W. Rosenthal, S. Zahedpour, J. K. Wahlstrand, and H. M. Milchberg. Spatiotemporal optical vortices. *Phys. Rev. X*, 6:031037, Sep 2016. Cited on p. 23.

[19] George Goubau and F Schwering. On the guided propagation of electromagnetic wave beams. *IRE Transactions on Antennas and Propagation*, 9(3):248–256, 1961. Cited on p. 23.

[20] Les Allen, Marco W Beijersbergen, RJC Spreeuw, and JP Woerdman. Orbital angular momentum of light and the transformation of laguerre-gaussian laser modes. *Physical Review A*, 45(11):8185, 1992. Cited on p. 23.

[21] Chr Tamm and CO Weiss. Bistability and optical switching of spatial patterns in a laser. *JOSA B*, 7(6):1034–1038, 1990. Cited on p. 23.

[22] E Abramochkin and V Volostnikov. Beam transformations and nontransformed beams. *Optics Communications*, 83(1):123–135, 1991. Cited on p. 23.

[23] M.W. Beijersbergen, R.P.C. Coerwinkel, M. Kristensen, and J.P. Woerdman. Helical-wavefront laser beams produced with a spiral phaseplate. *Opt. Commun.*, 112(5-6):321–327, December 1994. Cited on p. 23.

[24] N Radwell, RD Hawley, JB Götte, and S Franke-Arnold. Achromatic vector vortex beams from a glass cone. *Nature communications*, 7, 2016. Cited on p. 23.

[25] LORENZO Marrucci, C Manzo, and D Paparo. Optical Spin-to-Orbital Angular Momentum Conversion in Inhomogeneous Anisotropic Media. *Phys. Rev. Lett.*, 96(16):163905, April 2006. Cited on p. 23.

[26] Stacy Wise, V Quetschke, AJ Deshpande, G Mueller, DH Reitze, DB Tanner, BF Whiting, Y Chen, A Tünnermann, E Kley, et al. Phase effects in the diffraction of light: beyond the grating equation. *Physical review letters*, 95(1):013901, 2005. Cited on p. 24.

[27] C. Palmer and E. Loewen. *Diffraction Grating Handbook*. Milton Roy, 1994. Cited on p. 25.

[28] Pierre-Alexandre Blanche. *Field Guide to Holography*. SPIE Press, 2014. Cited on pp. 25, 28, and 48.

[29] Dionys Gabor. Microscopy by reconstructed wave-fronts. In *Proceedings of the Royal Society of London A: Mathematical, Physical and Engineering Sciences*, volume 197, pages 454–487. The Royal Society, 1949. Cited on p. 27.

[30] Lcos-slm x13138-01. http://www.hamamatsu.com/jp/en/X13138-01.html. Accessed: 2016-10-14. Cited on p. 28.

[31] Jeffrey A Davis, Don M Cottrell, Juan Campos, María J Yzuel, and Ignacio Moreno. Encoding amplitude information onto phase-only filters. *Applied optics*, 38(23):5004–5013, 1999. Cited on p. 32.

[32] Eliot Bolduc, Nicolas Bent, Enrico Santamato, Ebrahim Karimi, and Robert W Boyd. Exact solution to simultaneous intensity and phase encryption with a single phase-only

hologram. *Optics letters*, 38(18):3546–3549, 2013. Cited on p. 32.

[33] Victor Arrizón, Ulises Ruiz, Rosibel Carrada, and Luis A González. Pixelated phase computer holograms for the accurate encoding of scalar complex fields. *JOSA A*, 24(11):3500–3507, 2007. Cited on pp. 32 and 33.

[34] Gordon D Love. Wave-front correction and production of zernike modes with a liquid-crystal spatial light modulator. *Applied optics*, 36(7):1517–1524, 1997. Cited on p. 34.

[35] Richard W Bowman, Amanda J Wright, and Miles J Padgett. An slm-based shack–hartmann wavefront sensor for aberration correction in optical tweezers. *Journal of Optics*, 12(12):124004, 2010. Cited on p. 34.

[36] Neal Radwell, Kevin J Mitchell, Graham M Gibson, Matthew P Edgar, Richard Bowman, and Miles J Padgett. Single-pixel infrared and visible microscope. *Optica*, 1(5):285–289, 2014. Cited on p. 34.

[37] Stephen S Welsh, Matthew P Edgar, Richard Bowman, Phillip Jonathan, Baoqing Sun, and Miles J Padgett. Fast full-color computational imaging with single-pixel detectors. *Optics express*, 21(20):23068–23074, 2013. Cited on p. 34.

[38] L Allen and MJ Padgett. The poynting vector in laguerre–gaussian beams and the interpretation of their angular momentum density. *Optics Communications*, 184(1):67–71, 2000. Cited on p. 35.

[39] Sonja Franke-Arnold, Jonathan Leach, Miles J Padgett, Vassilis E Lembessis, Demos Ellinas, Amanda J Wright, John M Girkin, P Ohberg, and Aidan S Arnold. Optical ferris wheel for ultracold atoms. *Optics Express*, 15(14):8619–8625, 2007. Cited on p. 35.

[40] Quan Huynh-Thu and Mohammed Ghanbari. Scope of validity of psnr in image/video quality assessment. *Electronics letters*, 44(13):800–801, 2008. Cited on p. 37.

[41] R Liu, DB Phillips, F Li, MD Williams, DL Andrews, and MJ Padgett. Discrete emitters as a source of orbital angular momentum. *Journal of Optics*, 17(4):045608, 2015. Cited on p. 38.

[42] R Liu, F Li, MJ Padgett, and DB Phillips. Generalized photon sieves: fine control of complex fields with simple pinhole arrays. *Optica*, 2(12):1028–1036, 2015. Cited on p. 44.

[43] Mt250-ir6-fio-pm-ic fibre pigtailed modulator. http://www.aaoptoelectronic.com/Documents/MT200-250-IR6-IR10-Fio-Ic-2015.pdf. Accessed: 2016-01-17. Cited on p. 48.

[44] Norman J Berg and John N Lee. Acousto-optic signal processing: theory and implementation. In *New York, Marcel Dekker, Inc.(Optical Engineering. Volume 2), 1983, 496 p. No individual items are abstracted in this volume.*, volume 2, 1983. Cited on p. 48.

[45] Chiara Vitelli, Nicolo Spagnolo, Lorenzo Aparo, Fabio Sciarrino, Enrico Santamato, and Lorenzo Marrucci. Joining the quantum state of two photons into one. *Nature Photonics*, 7(7):521–526, 2013. Cited on p. 48.

[46] Mikhail I. Kolobov and Claude Fabre. Quantum limits on optical resolution. *Phys. Rev. Lett.*, 85(18):3789, 2000. Cited on p. 49.

[47] G. Brida, M. Genovese, and I. Ruo Berchera. Experimental realization of sub-shot-noise quantum imaging. *Nature Photonics*, 4(4):227–230, 2010. Cited on p. 49.

[48] Robert W.Boyd, Anand Jha, Mehul Malik, Colin O'Sullivan, Brandon Rodenburg, and Daniel J.Gauthier. Quantum key distribution in a high-dimensional state space: exploiting the transverse degree of freedom of the photon. *Proceedings of the SPIE*, 7948:79480L, 2011. Cited on pp. 49 and 55.

[49] Adetunmise C. Dada, Jonathan Leach, Gerald Buller, Miles J. Padgett, and Erika Andersson. Experimental high-dimensional two-photon entanglement and violations of generalized bell inequalities. *Nature Physics*, 7(9):677–680, 2011. Cited on p. 49.

[50] Martin P.J. Lavery, David J. Robertson, Anna Sponselli, Johannes Courtial, Nicholas K Steinhoff, Glenn A Tyler, Alan E. Willner, and Miles J. Padgett. Efficient measurement of an optical orbital-angular-momentum spectrum comprising more than 50 states. *New J. Phys.*, 15:013024, 2013. Cited on p. 49.

[51] Nenad Bozinovic, Yang Yue, Yongxiong Ren, Moshe Tur, Poul Kristensen, Hao Huang, Alan E. Willner, , and Siddharth Ramachandran. Terabit-scale orbital angular momentum mode division multiplexing in fibers. *Science*, 340(6140):1545–1548, 2013. Cited on p. 49.

[52] Jian Wang, Jeng-Yuan Yang, Irfan M. Fazal, Nisar Ahmed, Yan Yan, Hao Huang, Yongxiong Ren, Yang Yue, Samuel Dolinar, and Moshe Tur et al. Terabit free-space data transmission employing orbital angular momentum multiplexing. *Nature Photonics*, 6(7):488–496, 2012. Cited on p. 49.

[53] D.J.Richardson, J.M.Fini, and L.E.Nelson. Space-division multiplexing in optical fibres. *Nature Photonics*, 7(5):354–362, 2013. Cited on p. 49.

[54] Gregor Thalhammer, Richard W Bowman, Gordon D Love, Miles J Padgett, and Monika Ritsch-Marte. Speeding up liquid crystal slms using overdrive with phase change reduction. *Optics express*, 21(2):1779–1797, 2013. Cited on p. 49.

[55] Mohammad Mirhosseini, Omar S Magana-Loaiza, Changchen Chen, Brandon Rodenburg, Mehul Malik, and Robert W Boyd. Rapid generation of light beams carrying orbital angular momentum. *Optics Express*, 21(25):30196–30203, 2013. Cited on p. 49.

[56] Sergei Slussarenko, Ebrahim Karim, Bruno Piccirillo, Lorenzo Marrucci, and Enrico Santamato. Efficient generation and control of different-order orbital angular momentum states for communication links. *JOSA A*, 28(1):61–65, 2011. Cited on p. 49.

[57] Gregorius C. G. Berkhout, Martin P. J. Lavery, Johannes Courtial, Marco W. Beijersbergen, and Miles J. Padgett. Efficient sorting of orbital angular momentum states of light. *Phys. Rev. Lett.*, 105:153601, Oct 2010. Cited on p. 55.

[58] Nicolas J. Cerf, Mohamed Bourennane, Anders Karlsson, and Nicolas Gisin. Security of quantum key distribution using d-level systems. *Phys. Rev. Lett.*, 88(12):127902, 2002. Cited on p. 55.

[59] S. Etcheverry, G. Cañas, E. S. Gómez, W. A. T. Nogueira, C. Saavedra, G. B. Xavier, and G. Lima. Quantum key distribution session with 16-dimensional photonic states. *Scientific Reports*, 3:2316, 2002. Cited on p. 55.

[60] Benjamin P. Lanyon, Marco Barbieri, Marcelo P. Almeida, Thomas Jennewein, Timothy C. Ralph, Kevin J. Resch, Geoff J. Pryde, Jeremy L. O'Brien, Alexei Gilchrist, and Andrew G. White. Simplifying quantum logic using higher-dimensional hilbert spaces. *Nature Physics*, 5:134–140, 2009. Cited on p. 55.

[61] Wolfgang Ketterle. 8.421 atomic and optical physics i. spring 2014. massachusetts institute of technology: Mit opencourseware. https://ocw.mit.edu. License: Creative Commons BY-NC-SA, Accessed: 2016-10-14. Cited on p. 59.

[62] Baoqing Sun, Matthew P Edgar, Richard Bowman, Liberty E Vittert, Stuart Welsh, A Bowman, and MJ Padgett. 3d computational imaging with single-pixel detectors. *Science*, 340(6134):844–847, 2013. Cited on p. 60.

[63] David J Griffiths. Introduction to electrodynamics. *Prentice Hall*, 93:95, 1999. Cited on p. 62.

[64] Christopher J Foot. *Atomic physics*, volume 7. Oxford University Press, 2005. Cited on pp. 65, 67, 68, 94, 96, 97, and 100.

[65] Rubidium 87 d line data. http://steck.us/alkalidata/. Accessed: 2016-08-20. Cited on pp. 66 and 69.

[66] Rubidium 85 d line data. http://steck.us/alkalidata/. Accessed: 2016-08-20. Cited on p. 66.

[67] Marcis Auzinsh, Dmitry Budker, and SM Rochester. Optically polarized atoms. *Physics of Atoms and Molecules (Oxford University Press, New York, 2010)*, 2010. Cited on pp. 73, 79, 93, 120, 121, 122, 126, and 127.

[68] Stephen M Barnett and Paul M Radmore. *Methods in theoretical quantum optics*, volume 15. Oxford University Press, 2002. Cited on p. 76.

[69] Stig Stenholm. *Foundations of laser spectroscopy*. Courier Corporation, 2012. Cited on p. 76.

[70] Marcis Auzinsh. Tutorial/article didactique: Angular momenta dynamics in magnetic and electric field: Classical and quantum approach. *Canadian journal of physics*, 75(12):853–872, 1997. Cited on p. 79.

[71] SM Rochester and D Budker. Atomic polarization visualized. *American Journal of Physics*, 69(4):450–454, 2001. Cited on pp. 79 and 124.

[72] John S Toll. Causality and the dispersion relation: logical foundations. *Physical Review*, 104(6):1760, 1956. Cited on p. 84.

[73] Quantum and atom optics. http://atomoptics-nas.uoregon.edu/~dsteck/teaching/quantum-optics/. Accessed: 2016-08-20. Cited on p. 84.

[74] Igor I Sobelman. Radiative transitions. In *Atomic Spectra and Radiative Transitions*, pages 200–302. Springer, 1992. Cited on p. 93.

[75] Thomas G. Mayerhöfer, Harald Mutschke, and Jürgen Popp. Employing theories far beyond their limits—the case of the (boguer-) beer–lambert law. *ChemPhysChem*, 17(13):1948–1955, 2016. Cited on p. 93.

[76] Miroslav Gajdacz, Andrew J Hilliard, Mick A Kristensen, Poul L Pedersen, Carsten Klempt, Jan J Arlt, and Jacob F Sherson. Preparation of ultracold atom clouds at the shot noise level. *arXiv preprint arXiv:1604.05087*, 2016. Cited on p. 95.

[77] Aidan Arnold. *Preparation and Manipulation of an ^{87}Rb Bose-Einstein Condensate*. PhD thesis, University of Sussex, 1999. Cited on p. 95.

[78] David S Weiss, Erling Riis, Yaakov Shevy, P Jeffrey Ungar, and Steven Chu. Optical molasses and multilevel atoms: experiment. *JOSA B*, 6(11):2072–2083, 1989. Cited on p. 95.

[79] David A Smith and Ifan G Hughes. The role of hyperfine pumping in multilevel systems exhibiting saturated absorption. *American Journal of Physics*, 72(5):631–637, 2004. Cited on p. 96.

[80] AS Arnold, JS Wilson, and MG Boshier. A simple extended-cavity diode laser. *Review of Scientific Instruments*, 69:1236, 1998. Cited on p. 96.

[81] Aline Vernier. *Phase dependent atom optics*. PhD thesis, University of Glasgow, 2011. Cited on p. 103.

[82] Graeme Walker. *Trans-spectral transfer of orbital angular momentum and creation of an ultra high density cold atom trap*. PhD thesis, University of Glasgow, 2013. Cited on pp. 103 and 105.

[83] N Radwell, G Walker, and S Franke-Arnold. Cold-atom densities of more than 10 12 cm- 3 in a holographically shaped dark spontaneous-force optical trap. *Physical Review A*, 88(4):043409, 2013. Cited on pp. 103, 108, and 109.

[84] Wolfgang Ketterle, Kendall B Davis, Michael A Joffe, Alex Martin, and David E Pritchard. High densities of cold atoms in a dark spontaneous-force optical trap. *Physical review letters*, 70(15):2253, 1993. Cited on p. 107.

[85] JA Souza, L Cabral, RR Oliveira, and CJ Villas-Boas. Electromagnetically-induced-transparency-related phenomena and their mechanical analogs. *Physical Review A*, 92(2):023818, 2015. Cited on p. 112.

[86] CL Garrido Alzar, MAG Martinez, and P Nussenzveig. Classical analog of electromagnetically induced transparency. *American Journal of Physics*, 70(1):37–41, 2002. Cited on p. 112.

[87] Gilbert Grynberg, Alain Aspect, and Claude Fabre. *Introduction to quantum optics: from the semi-classical approach to quantized light*. Cambridge university press, 2010. Cited on p. 113.

[88] Sumanta Khan, M. P. Kumar, Sapam Ranjita Chanu, Vineet Bharti, and Vasant Natarajan. Coherent population trapping (CPT) versus Electromagnetically induced transparency (EIT). *arXiv Prepr. arXiv ...*, 2015. Cited on p. 116.

[89] Dmitry Budker, Derek F Kimball, and David P DeMille. *Atomic physics: an exploration through problems and solutions*. Oxford University Press, USA, 2004. Cited on p. 119.

[90] Electromagnetically induced transparency and atomic polarization. http://rochesterscientific.com/ADM/AtomicDensityMatrix/tutorial/ElectromagneticallyInducedTransparencyAndAtomicPolarization.html. Accessed: 2016-10-14. Cited on p. 119.

[91] Eugene Wigner. *Group theory: and its application to the quantum mechanics of atomic spectra*, volume 5. Elsevier, 2012. Cited on p. 120.

[92] Carl Eckart. The application of group theory to the quantum dynamics of monatomic systems. *Reviews of modern Physics*, 2(3):305, 1930. Cited on p. 120.

[93] The atomic density matrix package. http://rochesterscientific.com/ADM/AtomicDensityMatrix/guide/AtomicDensityMatrix.html. Accessed: 2016-10-14. Cited on pp. 122 and 146.

[94] S.J. Buckle, S.M. Barnett, P.L. Knight, M.A. Lauder, and D.T. Pegg. Atomic Interferometers. *Opt. Acta*, 33(9):1129–1140, September 1986. Cited on p. 137.

[95] D V Kosachiov, B G Matisov, and Y V Rozhdestvensky. Coherent phenomena in multilevel systems with closed interaction contour. *J. Phys. B At. Mol. Opt. Phys.*, 25(11):2473–2488, June 1992. Cited on p. 137.

[96] Rodney Loudon. *The quantum theory of light*. OUP Oxford, 2000. Cited on p. 141.

[97] L Margalit, M Rosenbluh, and AD Wilson-Gordon. Degenerate two-level system in the presence of a transverse magnetic field. *Physical Review A*, 87(3):033808, 2013. Cited on p. 143.